DESIGN AND DEVELOPMENT OF A HIGH-SPEED AXIAL-FLUX PERMANENT-MAGNET MACHINE

DESIGN AND DEVELOPMENT OF A HIGH-SPEED AXIAL-FLUX PERMANENT-MAGNET MACHINE

PROEFSCHRIFT

ter verkrijging van de graad van doctor aan de
Technische Universiteit Eindhoven, op gezag van de
Rector Magnificus, prof.dr. M. Rem, voor een
commissie aangewezen door het College voor
Promoties in het openbaar te verdedigen
op woensdag 16 mei 2001 om 16.00 uur

door

Funda Sahin

geboren te Van, Turkije

Dit proefschrift is goedgekeurd door de promotoren:

prof.dr.ir. A.J.A. Vandenput
en
prof.dr.ir. J.C. Compter

CIP-DATA LIBRARY TECHNISCHE UNIVERSITEIT EINDHOVEN

Sahin, Funda

Design and development of a high-speed axial-flux permanent machine / by Funda Sahin. - Eindhoven :
Technische Universiteit Eindhoven, 2001.
Proefschrift. - ISBN 90-386-1380-1
NUGI 832
Trefw: elektrische machines ; permanente magneten / electrische machines ; verliezen / hybride voertuigen / elektrische machines ; warmte.
Subject headings: permanent magnet machines / losses / electric vehicles / thermal analysis.

Contents

Foreword

Many people have contributed to the completion of this dissertation, both directly, by providing me with useful comments, thoughts and suggestions, as well as indirectly, by creating a stimulating and pleasant working environment. I would therefore like to express my gratitude to all my friends and my (ex-)colleagues that I have been working with over the last four years. I am not giving a full list of names here, but I am sure that all the people to whom these acknowledgments are addressed are aware of their inclusion.

A number of people deserve special attention here, though. First of all I would like to thank Andre Vandenput for his fascinating supervision over the whole Ph.D. period in all aspects, which can be listed with pages from the technical problems to funding. I would also like to express my appreciation to his management skills and character, which led to a friendly and almost stress-free working environment independent of the work load.

I would also like to thank John Compter, for his supervision and especially for his guidance by his industry experience. For any mind boggling issue, he always had a real life example ready in mind.

During the four years of this project, Jaques van Rooij has been contributing to this project first by supplying the application and then sparing the time to solve mechanical problems, finding suppliers for materials, and giving ideas voluntarily. It was a treat to have him as an advisor with his always kind and refined attitude during the whole period of the project.

Almost two years I shared an office with Andrew Tuckey, who was a post-doc researcher at that time, working on the development of the test bench in which the measurements of the machine designed for this project are carried out. I would like to thank him not only for his advices and direct help in manufacturing and testing of the machine, but also for his existence that created extra stimuli and a nice friendship. We had hours of conversations even for tiny technical aspects, and his ambition was really contagious. I will never forget his optimism and his everyday sentences starting with a : "Hey Funda, we can also do ...".

I would also like to express my gratitude to Jorge Duarte, for his helps in many aspects such as power electronics and programming DSPs, which are not my strongest points, for letting me use and manipulate his old Assembler codes, his latest advices

in LaTeX and most of all for his friendship. Marijn Uyt de Willigen deserves many thanks. For almost a year he did loads of work on the test bench. I can not remember anymore how many times he coupled and decoupled the machine to the belt drive, changed pulleys, belts and couplings. He was also very careful about the safety aspects. I would also like to thank Wim Thirion for his support during measurements and Joke Verhoef for her help in administrative work. I would also like to express my pleasure of working in the same group with Elena Lomonova, Johanna Myrzik and Melanie Mitchon. It was a very lucky coincidence not being the only woman engineer around. I also would like to thank them for their support, and for amiable company.

Especially during the last year of this study, I couldn't spare my friends and my family the time they deserve. I would like to apologize them and also thank them for their being patient and understanding. These appreciation and apologies specially go to my close friends Isil Aras and John Hird who proved that a Ph.D. student may as well have friends.

Last but not the least, special thanks go to my computer troubleshooter, domestic brainstorming partner, editor, cook, composer, chauffeur and best friend, who are one and the same person with my beloved husband Önder.

Funda Sahin

Chapter 1

Introduction

1.1 Rationale and approach

> *... even objects that had been lost for a long time appeared from where they had been searched for most and went dragging along in turbulent confusion behind Melquiades' magical irons. "Things have a life of their own" the gypsy proclaimed with a harsh accent. "Its simply a matter of waking up their souls". José Arcadio Buendia whose unbridled imagination always went beyond the genius of nature and even beyond miracles and magic, thought that it would be possible to make use of that useless invention to extract gold from the bowels of the earth.....*[1]

From the earlier days of its invention onwards, the phenomenon of the "magical irons" that attract other metallic objects has been a major source of astonishment, magic, inspiration, and imagination, all of which led to scientific and technological discovery and progress, of course with the exception of many futile and frustrating attempts such as the fictitious case of *José Arcadio Buendia* of Márquez. Even the introduction of the word *electricity* by William Gilbert around 1600, was due to the magnetic properties of lodestone. Although Gilbert himself believed magnetism to be a purely occult force and did not even dream of machines that could generate or harness electricity based on magnetism, fortunately his followers did. It did not take more than two centuries before the first electrical-mechanical converter that relies on the principles of magnetism was introduced. Yet, it took a bit more than another century before the "magical irons", which we refer as "permanent magnets (PM)" today, and which are the oldest evidences of the magnetism concept, were brought into actual use in electrical machines.

[1] From Gabriel Garcia Márquez's "One Hundred Years of Solitude"

The idea of energy transmission between the rotor and the stator based on "excitation by permanent magnets", was anticipated as the future alternative to technologies that rely on "brushes". This (eventually) self fulfilling prophecy has been burdened with the shortcomings of the PM material technologies and also the level of advancement in power- and micro-electronics which stood in the way of efficient applications offering a high power range. Therefore, the fulfillment of the prophecy has been progressing parallel to advancements in these two fields as evidenced by the literature on PM (brushless) machines, almost all of which mention the rapid diffusion of permanent magnet technologies into the field of electrical machines.

In a typical industrial country of today, between a half and two thirds of the electrical energy is consumed by electrical machines. Therefore given this volume, even a slight increase in the efficiency of electrical drives amounts to a huge energy economization on the global scale. In this context, PM brushless machines offer a lot with their high efficiency, high power factor, and high power density These are apparently the dominant underlying reasons for their rapid diffusion into electrical machine applications, which could soon turn into a case of non-surprising and deserved predominance.

This study follows this trend which already proved to be more than a promising avenue to explore. In doing that, it aims to contribute to this field by a real application that draws on the so called "axial-flux machine" concept, which is another -more than promising- trend in electrical machine literature and applications. As the name implies, the "axial-flux machines" refer to a set of various structures sharing one common feature which is the running of flux in the axial rather than the radial direction. The usage of permanent magnets in combination with the axial-flux architecture leads to a combined concept referred as the "axial-flux permanent-magnet" (AFPM) machines. The machines in this class offer advantageous features such as compact machine construction with a short frame, high power density, high efficiency (no rotor copper losses due to PM excitation).

The electric machine application pertaining to this study is not hypothetical and is embedded in an existing "Hybrid Electrical Vehicle" (HEV) application. This particular HEV application that is called as "Hybrid Driving System" holds a European patent and is characterized by a novel framework for a total drive system that aims to introduce a feasible and efficient solution to a collection of specific demands and core problems in HEV applications.

The "Hybrid Driving System" provides the study with two inputs. The first input is of a technical nature and gives the study a context in terms of constituting a system in which the electrical machine is to be made to fit. In other words, the design of the electric motor is based upon the technical requirements and the constraints of the particular HEV application. A design is, by definition, the introduction of an internally consistent system, which works in a way that constitutes a feasible (and an as optimum as possible) solution to a well defined set of problems and

requirements. Therefore, the ready existence of such a system with rather challenging demands not only provided us with a challenging real-life project definition, but saved us the trouble of making up a hypothetical problematic as well. The main challenges imposed by the "Hybrid Driving System" were a dire constraint on machine volume, given this low volume, a rather high torque density requirement, which comes together with a rather high rotational speed requirement. Already at the outset, these constraints pointed to the direction of tapping on the well-known advantageous features that are offered by AFPM machines.

The second input is more of a personal and cognitive nature. Among the alternative solutions to the enormous pollution due to the hydrocarbon emissions of internal combustion based vehicles, electric vehicle (EV) and in particular HEV technologies are currently high on academic and industrial research agendas. As a matter of fact, almost all electric machine applications, to some extent aim to increase efficiency which reduces electrical energy consumption. Yet, in the HEV context, any efficiency improvement in any subsystem indirectly implies a reduction in fossil fuel consumption and thus in hydrocarbon emission and pollution. Therefore, the idea of involvement in the design of an electrical machine as a part of a system that serves for this purpose introduced an extra source of stimuli.

1.2 Organization of the thesis

The study constitutes an overall approach to the design, manufacturing and testing of an electric machine. Naturally, such an approach involves the making of a series of choices and decisions, some mandated at the outset by the requirements and constraints of the surrounding system, and some gradually introduced in due course by the accompanying technical analyses. The former are mainly about the basic structure of the machine and the latter are on the specifics of the design parameters and other auxiliary issues such as the power electronic drive.

After making these choices and decisions, the actual manufacturing becomes an issue and is followed by the testing and measurement phase. Thus, the organization of the chapters of this thesis is arranged to follow the actual historical course of the 4 year study.

First, chapter 2 presents a discussion on the particular HEV that encompasses the electric machine application. Before going into the details, some background information on the EVs, the HEVs and the underlying components such as energy storage devices in general (and flywheel concept in particular) are provided. The chapter concludes with an overview of the essential requirements and constraints imposed by the particular HEV application.

Chapter 3 is basically a justification of the choice of the AFPM concept in relation to the specifications presented in the previous chapter. As mentioned before, the AFPM concept underlies a broad range of various structures (which are also discussed

in the chapter) and towards an initial design, the first natural step to be taken is an initial choice on the basic structure among the AFPM machine class. The choice requires a comparative analysis and for this purpose a set of generic equations is derived. The basic issues of comparison are sizing, magnetic design and type of excitation with regard to torque, emf, power and reactance. Drawing on the basic equations derived in this chapter, a general comparison between axial- and radial-flux permanent-magnet machines is also provided. The results of this comparative analysis, together with the requirement of embedding the rotor within the flywheel, rationalize the basic choice on a sinusoidal current excited AFPM machine that incorporates a single rotor structure on which the magnets are attached.

Chapter 4 is an extension of chapter 3, where further potential variations in the structural design are compared and contrasted. Based on the basic choice made in chapter 3, chapter 4 introduces an analysis mainly with regard to the number of stator slots, the magnet span, winding configuration, skewing and the stator offset. A discussion on the design procedure and the presentation of machine data follow the derivation of the underlying equations.

Chapters 3 and 4 can be seen as an initial screening and a raw elimination among many alternatives, which lead to a candidate design. Nevertheless, this effort relies on a set of analytical equations which lack the precision and accuracy that a final analysis deserves. Although such accuracy and precision can be maintained by the use of *Finite Element Method* (FEM), the obvious limitations (time and effort) make it infeasible to be employed for the purposes of chapter 3 and 4, which accordingly resort to analytical approximations. Yet, it is the most appropriate tool to verify and finalize (fine tuning and optimization) the raw design provided by the analytical approximation approach.

The finite element method allows the modelling of complicated geometries in 2D and 3D, non-linearities of materials and gives accurate results without standing on many restricting assumptions as the analytical approach does. An overview of the FEM and the way it is utilized in this study, are presented in chapter 5. The main issues regarding the usage of the FEM are the analyses of flux density, emf, torque ripples, inductances and eddy current losses.

The calculation of losses is essential in terms of an accurate prior estimation of the efficiency and the thermal behavior of the machine. The major types of losses can be categorized into copper losses, core losses, rotor losses and mechanical losses, and a detailed discussion on the analysis of each type is presented in chapter 6. The chapter also provides an efficiency map and concludes with a discussion on the effects of the design parameters on the efficiency.

The dependence of the safe operating conditions and overloading capabilities on the temperature rise makes a prior estimation of the thermal behavior of any electrical machine a very important issue. It is obvious that an exact determination of the thermal behavior of the machine is impossible due to many variable factors,

such as unknown loss components and their distribution, and the three dimensional complexity of the problem. Yet, a prior knowledge on the order of magnitude of the temperature rises in various parts of the machine is crucial, especially in the case of a high-speed machine design. It is also important for the designer to know the magnitudes of the thermal parameters and to choose a suitable cooling strategy that will enhance the machine performance. Therefore, based on the estimated loss components that are made available by the analysis in chapter 6, an analytical estimation approach is pursued. The thermal behavior of the machine is modelled in terms of an equivalent electrical circuit and various scenarios that simulate various combinations of evacuation, cooling and load conditions, are analyzed. Chapter 7 is dedicated to this analysis and the major findings.

The theoretical design and analysis of the AFPM machine is followed by the actual manufacturing practice. Chapter 8 describes the manufacturing process in relation to the material choices, problems encountered and the final mechanical design that follows the analyses of mechanical forces and stresses on components, as well as the dynamical analyses of the rotating parts.

Chapter 9 presents the final essential stage of the application which is measurement and testing. Since it was not feasible to accomplish this in the natural environment in which the machine is meant to be (the HEV), a test bench is used that allows the testing and measurement of the machine under varying (load, speed) conditions. Various experiments are carried out, mainly focusing on measurements of stationary performance and thermal behavior. Chapter 9 also includes a comparison of measured and calculated results together with a discussion on the possible causes of discrepancy between the two.

Finally, chapter 10 concludes this dissertation by summarizing the main results and presenting some concluding remarks. Further, some directions for future research are recommended.

Chapter 2

Hybrid electric vehicle application

2.1 Introduction

The ambitious attempts to fulfil the human aspirations for faster mobility have a long history in civilization. The starting of the automobile industry with the development of a gasoline engine was in 1860s and 1870s mainly in France and Germany, although there were steam-powered road vehicles produced earlier. After the first success of the gasoline engine, came widespread experimentations with steam and *electricity.* For a short period of time, the electric automobile actually has great acceptance because it was quiet and easy to operate, but the limitations imposed by the battery capacity proved competitively fatal.

After the first introduction of the cars in the cities, it looked like an enormous improvement in the environment. According to historians, when autos replaced horses in 1920s tuberculosis rates decreased [1]. Before, the polluted air loaded with bacteria-carrying dust transmitted respiratory diseases. In retrospect, it looks now quite ironic that almost a century ago, the introduction of cars was thought to be the solution of cities' transportation related pollution problems while the health conditions of millions of people living in big cities are threatened by vehicle emission as today (Fig.2.1).

Although in the last two decades hydrocarbon emissions of the cars were reduced by 35% due to the introduction of more efficient cars and cleaner leadfree fuel and catalysts, the increasing number of new cars and less cleaner aging ones made the overall picture more tragic [2].

Nowadays, it is unequivocally accepted that the cars propelled by internal combustion engines (ICEs) are making the air in big cities unhealthy to breathe and increasing the atmospheric carbon dioxide density which jeopardizes the life in the whole planet. Hence, the introduction and rapid diffusion of vehicles propelled by alternative energy sources (Fig.2.2) are inevitable and electricity is the most promising and feasible medium term alternative.

Political and public pressures to improve the environment funding helped a lot to generate interest to develop practical and efficient electric vehicles (EVs). All of the major automobile manufacturers produced their prototypes. Although many have been done, EVs are still not mature and feasible enough to go into streets. Historically, the major problem preventing the commercialization of EVs is the lack of suitable batteries. Industry experts have concluded that practical EVs must have energy storage devices capable of a minimum specific energy of 200 Wh/kg, a relatively high life expectancy at a cost of around US $75/kWh and a 40% to 80% recharge capability in less than 30 minutes [3]. These figures are not met yet. It still takes time and research to improve them.

Figure 2.1: History of transportation.

Figure 2.2: Future of vehicles.

Under these circumstances the hybrid electric vehicles (HEVs) seem to be the most promising stage in this transition period. Hybrid electric vehicles, as their name implies, draw their operating power from two or more sources of energy. Typically, these sources are an electric drive train, consisting of an electric motor and a battery and an internal combustion engine. HEVs are currently under development by auto manufacturers throughout the world and lots of research is devoted to

further improvement of them. This persistent activity is also directly related with the concerns about global warming. HEVs are without any doubt only short-term or even mid-term solution to reduce the worldwide carbondioxide emissions by an acceptable level [4].

The research project discussed in this thesis deals with a part of an already existing HEV design and aims to develop an optimal electrical machine that would satisfy the technical specifications demanded by this particular design. The HEV design under consideration proposes to use two types of energy storage devices, a battery and a flywheel. This combination has its own advantages as will be discussed in section 2.4.

This chapter is devoted to explain this application and the constraints and requirements determining the specifications of the electric machine. In the following two sections, possible energy storage devices and hybrid electric vehicles will be briefly outlined. Afterwards, in section 2.4 the properties of a particular hybrid electric vehicle design will be given. Finally, the specifications of the electric machine required will be dealt with in the last section.

2.2 Energy storage devices

There are four types of energy storage units which can be provided to EVs and HEVs. They are identified as [5]:

- electrochemical (batteries);
- hydrogen;
- electromechanical (flywheel);
- molten salt heat storage (fusion).

2.2.1 Batteries

"*Batteries are the Achilles' heel of electric vehicles. In fact of all the technologies used in electric vehicles, this one remains the sole barrier to success* [6]" Although plenty of improvement has been done battery technology did not achieve required levels. Newer technologies have also been introduced in the last few years, particularly lithium-ion offers better characteristics, but the higher cost of these batteries makes their use in EVs infeasible [7].

A simple comparison reveals that the energy content of gasoline is around 44 megaJoules per kilogram ($\sim$12 kWh/kg), while a conventional lead-acid battery can store 30 Wh/kg which is almost 400 times less than does gasoline [6]. Of course, many types of batteries offer a better specific energy than the lead-acid, but they all

Parameter	*Goals for EVs*	*Goals for HEVs*	Lead-acid battery
Specific energy (Wh/kg)	80-200	8-80	25-35
Energy density (Wh/l)	135-300	9-100	∼70
Specific power (W/kg)	75-200	625-1600	80-100
Life expectancy (cycles)	600-1000	103-105	200-400
Life expectancy (years)	5-10	5-10	2-5
Cost (US $/kWh)	100-150	170-1000	∼100

Table 2.1: Goals of battery properties for EVs and HEVs in comparison with typical lead-acid battery properties.

Parameter	*Advanced lead-acid*	*Nickel-methal hybrid*	*Lithium-ion*	*Lithium-polymer*
Specific energy (Wh/kg)	35-40	50-60	80-90	100
Energy density (Wh/l)	70	175	200	-
Specific power (W/kg)	100-150	200	<1000	200
Life expectancy (cycles)	300-500	600-1000	-	200-300
Cost US $/kWh	100-150	300-400	-	-

Table 2.2: Comparison of batteries.

cost more, some perform less, and some have environmental risks or safety problems. Table 2.1 illustrates some representative battery targets for electric and hybrid electric vehicles (extracted from the joint government-industry program US Advanced Battery Consortium and the partnership of New Generation of Vehicles [6]) in comparison with some typical lead-acid battery figures.

As seen from Table 2.1, the battery requirements for EVs and HEVs differ. For example, EVs require a higher specific energy while the specific power is more important for HEVs. It is because of the fact that the required batteries are smaller for HEVs than those for EVs. Batteries for HEVs can be recharged from another source and they only need to be used for a certain fraction of the driving times. Hence, a different type of battery can be suitable for EVs and HEVs.

Table 2.2 shows the list of recent prominent types of batteries. With their impressive energy performance and their high power capability Nickel-metal hybrid (NiMH) batteries seem to be suitable for HEV applications [8].

2.2.2 Hydrogen

Fuel cells are electrochemical conversion devices that produce electricity directly by oxidizing hydrogen [9]. Hydrogen seems to be an ideal nonpolluting fuel. It burns cleanly and leaves just plain H_2O as a result of the oxidation process. Hydrogen is very attractive since it has the highest energy density of all the fuels [5].

The existing methods of storing hydrogen are suitable for industrial use but are unacceptable for vehicles yet. Another disadvantage of hydrogen as a fuel is that no infrastructure for the distribution of hydrogen exists and a large investment is required to establish it. On the other hand, the cost is still a very big issue that must be solved.

2.2.3 Flywheels

The working principle of the flywheel as an energy storage device is quite simple. The faster the flywheel rotates, the more energy it retains. Energy can be withdrawn from it as needed by reducing the speed of the flywheel. The kinetic energy stored in a flywheel is

$$E = \frac{1}{2} J\omega^2, \tag{2.1}$$

where J is the moment of inertia and ω is the angular rotation speed.

The stored energy is proportional to the speed squared, but limited by the stress in the material. When the maximal tensile strength is exceeded, the flywheel disintegrates. Flywheels are made of materials that have relatively higher tensile strength such as glass fibres, Kevlar fibres, maraging steel. The specific energy of a flywheel is proportional to the ratio of tensile strength/specific density of the used material [5].

The flywheel rotates in a reduced air pressure condition. In addition, the flywheels are generally designed with an integrated electrical machine to extract energy from it. This machine should be capable of rotating with high speed in a medium (reduced air pressure) that is very difficult to be cooled. Four types of electric machines can be used for this purpose:

- permanent-magnet machines;
- claw-pole machines;
- reluctance machines;
- induction machines.

All of these machines have brushless rotors which are suitable for high speeds. The apparent advantage of permanent-magnet machines is their significantly higher efficiency than that of the other types [5]. Hybrid electric vehicles with a flywheel and a permanent-magnet machine can be found in [10], [11], [12], [13], [14], [15], [16].

Due to the conditions in which the flywheel is proposed to be used in a vehicle, safety should also be guaranteed. The flywheel must be properly encased. Otherwise, in the event that the system breaks down, debris would fly outwards with considerable force. In case of a crash, the containment structure should remain intact by designing it to withstand the forces if the flywheel disintegrates [17].

2.3 Hybrid electric vehicles

A HEV is mainly an electric car supplemented with a small or medium size combustion engine. Since the electric machine operating as a generator, can charge the battery, the vehicle's driving range is extended. Thus, HEVs do not suffer from EVs limited ranges between charges. This means that HEVs can function as a pure electric vehicle while retaining the capability of a conventional automobile to make long trips. Properly designed HEVs can achieve several times the fuel efficiency of gasoline powered vehicles [18].

Although there are many HEV design alternatives, they can be mainly categorized as series and parallel as indicated in Fig.2.3 [18]. In a series hybrid the internal combustion engine drives a generator which charges the batteries. In this case, the vehicle is always driven by means of an electric motor.

On the other hand, in the case of a parallel hybrid both the electric machine and the internal combustion engine may power the drive shaft. Parallel hybrids do not need an external generator. When the engine turns the drive shaft, it also spins the electric machine's rotor. The machine thus works as a generator. The most advantageous point of this type is that a relatively smaller engine and an electric machine can be used, since they can work together.

The HEV concept will be further discussed in relation to a particular application in the following section.

2.4 The particular HEV application

The electrical machine of which the design, manufacturing aspects and testing are the subjects of this dissertation, is based upon the technical requirements and constraints of an existing HEV application. It is called as "Multiple Drive System" and is characterized by a novel framework for a total drive system that aims to introduce a feasible and efficient solution to a collection of specific demands and problems of

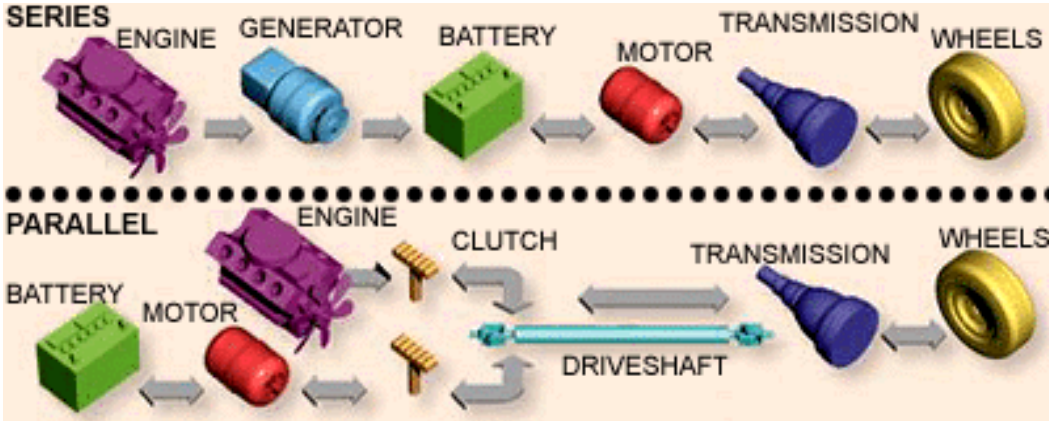

Figure 2.3: Main categories of hybrid electric vehicles.

HEV applications in general. The application holds a European patent [19] since April 1997.

As mentioned before, one of the direst constraints that has been restricting the progress in HEV applications is the energy storage device, especially the battery cell. Therefore the rate of progress of HEV (and/or EV) applications that heavily depend on the usage of a battery cell as the main or only device of energy storage is obviously bounded by the progress rate in battery technologies. Historically as well, this fact has been a major source of frustration and pessimism in the pure EV studies, and also a reason for the emergence of HEVs as an intermediate solution to the world energy and pollution problem.

The main issues surrounding the battery problem were briefly discussed in section 2.2.1. Among these, the high peak power demands [20], and the battery specific power which determines the recharge rate of the battery in regenerative braking, are of specific concern. A brief look at the European standard driving cycles (Fig.2.4), which indicate the patterns of acceleration and deceleration in typical driving cycles of a passenger car/bus/truck, is enough to reveal the underlying reason. In short, a typical urban utilization of a vehicle is far from a constant speed cruise and involves a long series of repetitive accelerations and decelerations which accounts for the bulk of the inefficiencies and the consequent energy waste and pollution by fossil fuel based vehicles. Similarly, the procurement of the peak power that matches the acceleration requirements, and an efficient system of braking energy recuperation are the major goals and challenges of any vehicle that deviates from the fossil fuel based propulsion. In the case of pure EVs, a good deal of this burden falls on the battery cell.

In the case of pure fossil fuel propulsion, given the typical urban acceleration/ deceleration requirements the major source of energy inefficiency is the consequent diversion from the efficiency interval that characterizes the IC engine. That is, it is

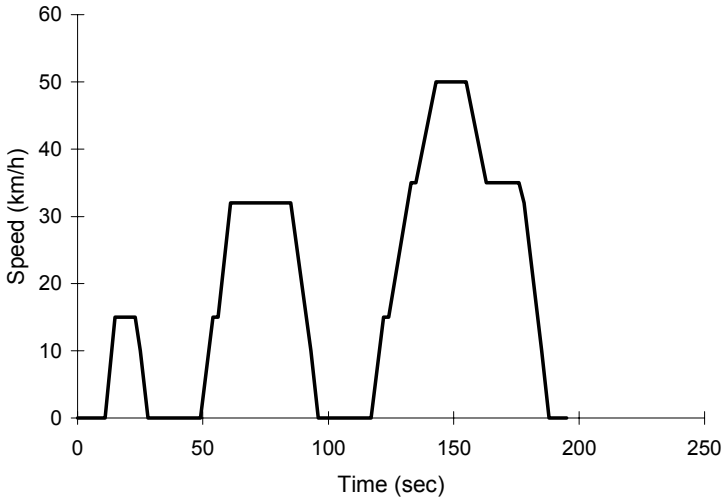

(a) City cycle.

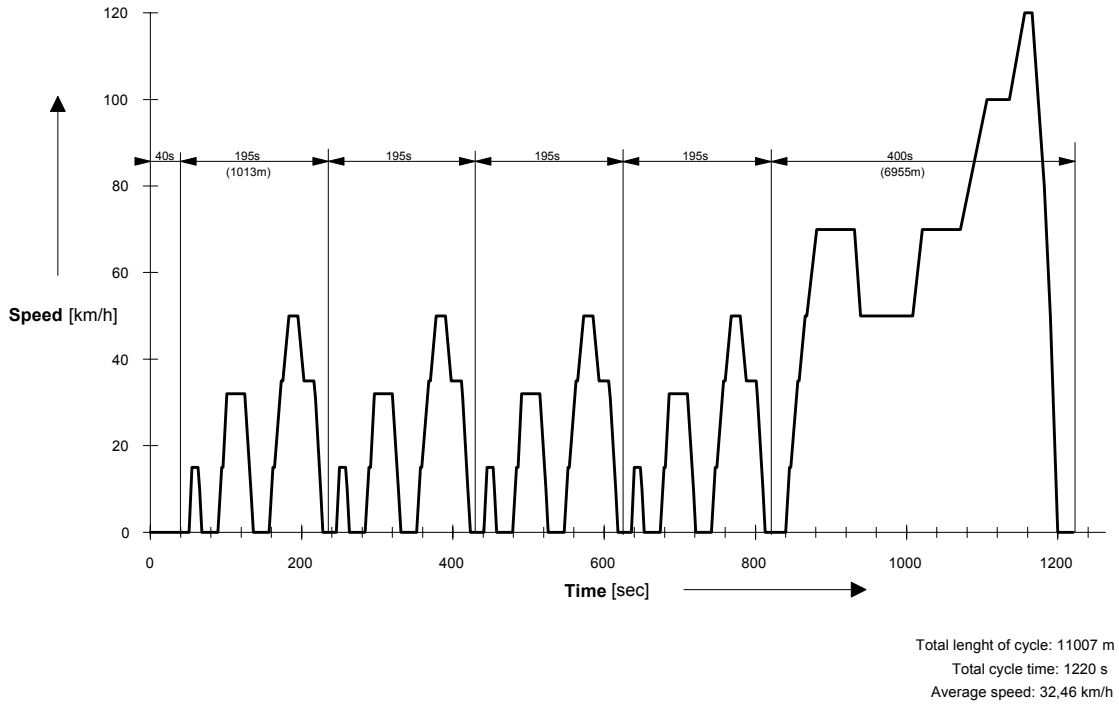

(b) Extra urban cycle.

Figure 2.4: European city and extra urban driving cycles.

theoretically possible to construct highly efficient IC engines, but only to the extent that the engine operates at specific torque/speed combinations without significant divergences. Nevertheless, the typical IC operation requirements imposed by the urban driving cycles demand a rather broad operation interval and make this option infeasible. This is the main reason that justifies HEVs.

The HEV concept is based upon the idea of enabling an efficient operating point for the IC, by utilizing a secondary propulsion system integrated with a secondary (and in some cases a tertiary) energy storage device in addition to fossil fuel. As the name HEV implies this secondary propulsion system relies on an electrical machine or two. The electrical machine(s) is/are responsible not only for supplying power for propulsion but also for intermediate storage of the braking energy that would otherwise be lost. In some applications these two functions are served by two separate electrical machine, whereas in others one electric machines operates in two modes on a need basis.

Since the storage and procurement of energy in this secondary system are electrical, the HEVs, just like EVs, are potentially dependent on the characteristics and thus vulnerable to the shortcomings of battery cells as well. The electric machine that supplies the required acceleration power, is fed by the battery and the recuperated braking energy is stored in the battery. Therefore, the peak power characteristic and the specific power of the battery are still key factors in determining the overall performance of the HEV.

Another complication regarding HEVs is of mechanical nature. The power transmission system between the wheels and the electrical machine which should be capable of working in both directions constitutes huge mechanical complications.

The design titled "Multiple Drive System" (MDS) upon which this study is based, introduces a simultaneous solution to the above mentioned problems inherent in HEV design. The design is a combination of three building blocks [19]:

An electrical machine embedded in a flywheel: An electrical machine that operates in both motoring and generating mode is responsible for the mechanical/electrical power conversion. Furthermore, the machine (more precisely the rotor of the machine) is embedded in a flywheel which can store and emit mechanical energy both through the shaft and the integrated electrical machine. The flywheel introduces a relaxation to the constraints imposed by the commonly known potential shortcomings of batteries as explained before. The peak powers at acceleration are supplied directly by the flywheel (mechanically) and also the recuperated energy from braking is mechanically stored in the flywheel. Furthermore, during city driving, the vehicle is mainly propelled by the mechanical energy transmitted from the flywheel. The flywheel rotates at constant speed and the variations around this speed are steadily regulated by the battery via the electrical machine, which significantly reduces the severe characteristics usually demanded from the battery otherwise. In other words, the battery is loaded at steady-state power only and thus peak cur-

rents are avoided which significantly improves the battery efficiency and extends the electrical range. Besides, internal heat production is reduced and battery durability is considerably improved. Since the flywheel introduces a third storage device, this parallel system (see Fig.2.3) is referred to as a "3-fold hybrid drive" which is the reason why the system is named "Multiple Drive System" [19].

A continuous variable transmission system (CVT): The introduction of a second drive system into the vehicle causes a series of potential complications and complexities regarding mechanical transmission and its coordination, efficiency and cost. The core of that system consists of an electronically regulated mechanical Continuous Variable Transmission (CVT) which facilitates the transmission of energy in both ways between the flywheel and the wheels. Although a CVT is already utilized in some existing passenger cars, it is a rather new technology.

In steady state the flywheel operates between specified minimum and maximum speeds, whereas the vehicle must be able to drive between zero and a maximum velocity. Therefore, for an efficient transmission, an infinite number of transmission ratios must be possible between the wheels and the flywheel and this can only be achieved by using a CVT. Besides, the CVT enables the control of the direction of transmission in a rather simple and efficient way.

The working principle of the CVT is depicted schematically in Fig.2.5. It consists of two parallel conical pulleys with an endless V-chain connecting the two. The centre-to-centre distance of the pulleys is fixed. Each pulley consists of a fixed conical disc and a conical disc that can move in the axial direction. The movable conical discs are located crosswise to each other. When the chain runs on the input pulley on a small radius r, it will run on the output pulley on a large radius R. By reducing the disc gap of the input pulley, the chain on this side starts to run on a larger radius and on the output side on a smaller radius. Therefore, by adjusting the relative axial position of the movable discs (by p_1 and p_2 which stand for hydraulic pressure), it is possible to maintain infinitely many transmission ratios between the utmost positions r/R and R'/r'.

Fig.2.6 shows the flywheel, CVT and driving shaft system in action. During acceleration (Fig.2.6a), the spindle sharing the shaft with the flywheel moves in, which increases the radius and thus the transmission ratio. Therefore, energy flows from the flywheel to the wheels, accelerating the vehicle and decelerating the flywheel rotating speed in exchange. Similarly, deceleration (Fig.2.6b) is made possible by decreasing the transmission ratio so that the kinetic energy of the vehicle is transmitted back to the flywheel, which slows down the vehicle and accelerates the flywheel. The excess kinetic energy is absorbed by the battery via the electrical machine which operates in generating mode for this purpose.

A switchable clutch set: The flywheel stores mechanical energy and provides this energy to accelerate the car. In case of braking, the energy is mainly recuperated in the flywheel. During emission-free city traffic, the battery supplies the energy to

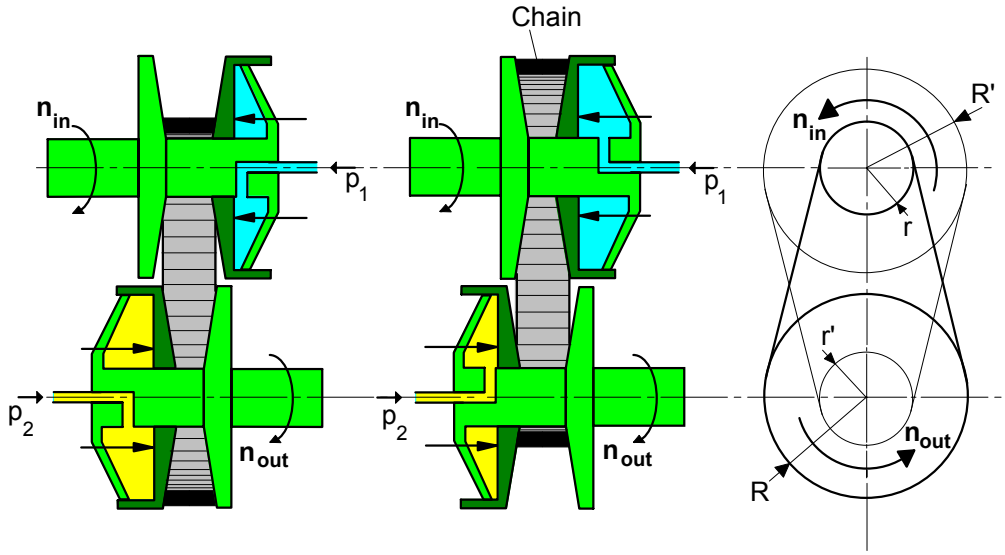

Figure 2.5: CVT working principle.

propel the car. As during accelerations the flywheel supplies the power. On highway, the power is supplied by the ICE.

All this implies various operating modes for the overall system and involves clearly a matter of coordination and control. This problem is solved with a set of switchable clutches and a planetary gear set, operated partially manually and partially automatically.

Fig.2.7a depicts the overall drive system which combines the IC engine, the electrical machine integrated in the flywheel, the CVT, the differential and the 5 clutch-gear set combination.

There are 5 clutches: K, $V1$, $V2$, $M1$ and $M2$. Except for K the clutches are all in connection with the planetary gear set (shown in purple color). The main function of the planetary gear set is to reduce the flywheel speed. The CVT input speed is maximum 5000 rpm and the flywheel speed is maximum 16000 rpm. However, the same gear set can be used to realize a reverse driving mode. In this way only one gear set on the input side of the CVT is sufficient. The clutch K is used to connect the combustion engine to the system. All clutches can be engaged or disengaged which is done hydraulically. Detailed information about the operation of the clutches can be found in [19].

A flywheel speed sensor determines the energy content of the flywheel. When the speed becomes too low, the electric machine (motor mode) is switched on. When it becomes too high (during driving down hill), the electric machine is switched on as well, but in generator mode to recuperate the braking energy to the battery.

When the flywheel is fully loaded and the generator has insufficient power to

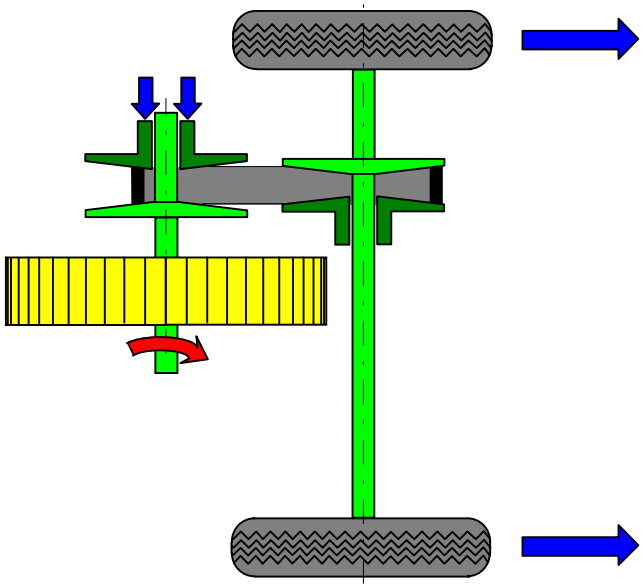

(a) Acceleration by shifting up.

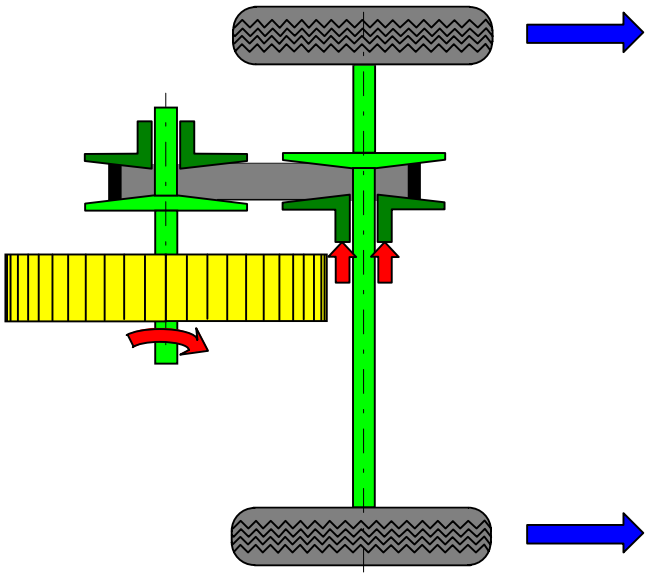

(b) Decelaration by shifting down.

Figure 2.6: Combination of flywheel, CVT and driving shaft.

Energy capacity	300 Wh
Outer and inner diameter	400×250 mm
Width	70 mm
Mass	28.2 kg
Speed	16000 rpm
Inertia	0.77 kgm^2

Table 2.3: Specifications of the flywheel.

brake the car, the mechanical wheel brakes are activated. The battery has insufficient energy to drive the car over very long distances on highway and thus the IC engine starts up facilitating a small quantity of flywheel energy. Highway accelerations still make use of the energy from the flywheel, reducing the IC engine's peak power requirement. The IC engine is only designed to reach a maximum highway speed of 130 km/h and is considerably smaller than the engine used in conventional cars. However, thanks to the flywheel, the acceleration performance of the vehicle is no worse than that of conventional pure IC engine based vehicles.

While driving below maximum highway speed, the engine power surplus is used to drive the electric machine as a generator and thus to reload the battery. Hence, after the highway trip the batteries are fully loaded and contain sufficient energy to start a new city trip.

The packaging of the overall system in a passenger car is depicted in Fig.2.7b. It already gives an idea on one major specification that the MDS imposes on the underlying electric machine; the space allocation. This and the other technical requirements imposed on the electrical machine that can be utilized in this particular HEV application, are discussed in the following section.

2.5 Required electrical machine

The existing design of the total drive system for a hybrid electric vehicle puts specific requirements on the electrical machine, which can be summarized as follows:

1. *Space allocated to the electrical machine:* From the prototype technical drawings it may be seen that the electrical machine must be integrated with the flywheel: it is proposed to be placed inside the flywheel. The flywheel specifications are shown in Table 2.3. The machine (including its frame) should be designed small enough to fit in a cylindrical volume of 150 mm height and 240 mm diameter.

2. *Torque requirement:* The machine is supposed to supply a mechanical torque of 18 Nm in the motoring mode under rated conditions. Short-time overloading can be necessary, e.g. if the vehicle is starting on a hill or in the case of a coupled trailer. In generating mode (the flywheel energy is recuperated) the machine should be able to supply a power of 30 kW.

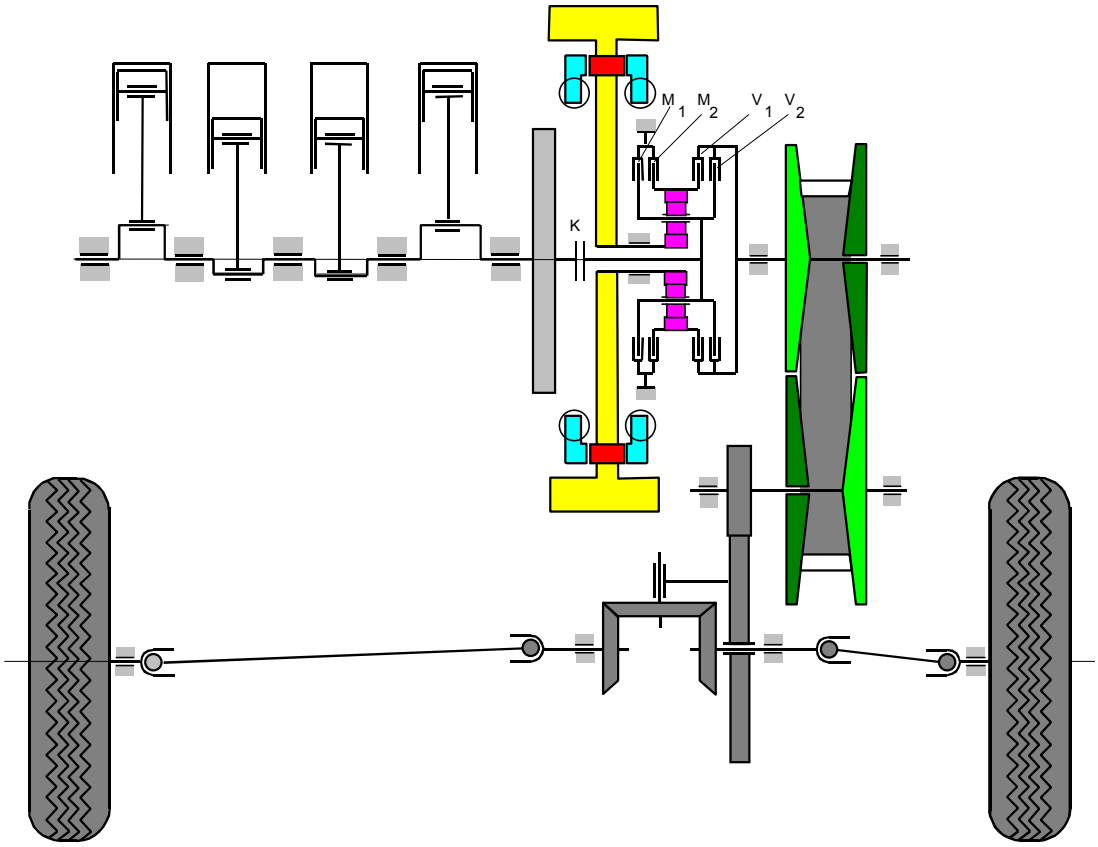

(a) Layout.

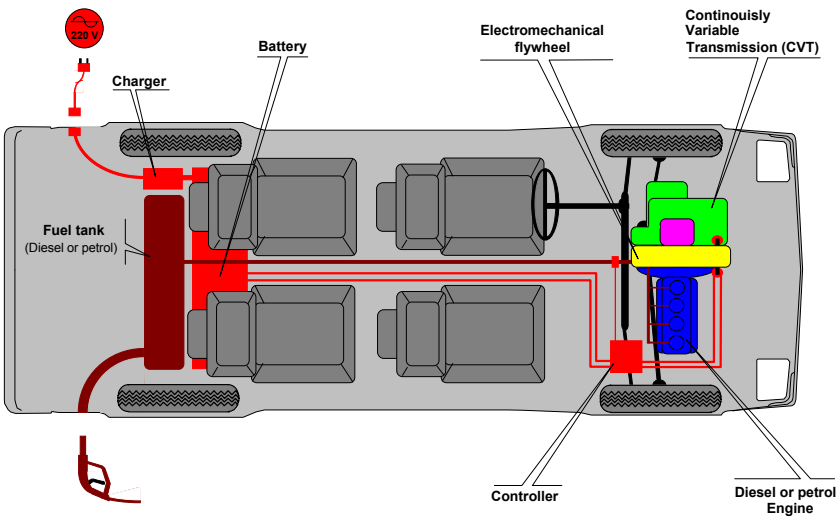

(b) Packaging in a passenger car.

Figure 2.7: Multiple drive system (MDS).

3. *Rotational speed:* Since the electrical machine is integrated with the flywheel, the rotational speed of the machine is the same as that of the flywheel which corresponds to 7000 rpm in city driving and a maximum of 16000 rpm while recuperating the brake energy.

In this hybrid drive system a high-speed axial-flux permanent-magnet (AFPM) machine which will be mounted inside the flywheel unit is proposed, mainly because of its shape and compactness. As a matter of fact, AFPM machines are becoming quite acceptable in electric vehicle applications [21]. For instance, Zhang et. al. [21] investigated several possible structures of AFPM wheel machines for electric vehicles. Acarnly et. al. [13] proposed a double-stator AFPM machine flywheel energy storage system and compared it with other machine types.

Here, a comparison with other possible machine types is briefly given to clarify the choice of an AFPM machine in this application.

- Switched reluctance machines also have a high torque density [13], but the use of a laminated rotor is not suitable. High strength rotor material is necessary in this application.

- Synchronous reluctance motors have some advantages such as low iron losses and ideally no rotor losses. But, as also studied and outlined in [13], they have low torque density, low power factor, and much higher windage losses.

- Induction machines have high rotor losses which can not be tolerated in reduced air pressure conditions.

- A radial-flux permanent-magnet machine with outer rotor could also be an alternative, considering the fact that the magnets are naturally protected against centrifugal forces. On the other hand, the required width of the machine is so small that the torque density will be lower than that of an AFPM machine. The comparison between radial- and axial-flux type permanent-magnet machines will be further discussed in section 3.6.

2.6 Conclusions

In this chapter background information regarding HEVs and the underlying components such as energy storage devices in general (and flywheel concept in particular) are provided. Based upon an existing design of the total drive system for a HEV, the requirements on the electrical machine are derived. An AFPM machine is proposed for the application. The following chapter is devoted to the description, theory and application of AFPM machines.

Chapter 3

Axial-flux permanent-magnet machines

3.1 Introduction

Following the introductory description of the application constraints and requirements, this chapter introduces the axial-flux permanent-magnet (AFPM) machine, which is the proposed machine type for the application in question. The relatively recent emergence of this type of machine structure made it possible to present a literature survey on existing AFPM applications with a rather broad coverage.

Unlike the radial-flux machines, the AFPM machine category actually incorporates a large set of various possible structures, sharing in common only the two simultaneous features that give the category its name: flux running in the axial direction and having permanent magnets on the rotor. Accordingly, the overview covers a set of different applications. Fortunately, thanks to their additional distinguishing features, it is also possible to further classify these applications (machine structures) and the overview follows a structure based on such a standard classification. Several design aspects and variations proposed by other researchers for each subcategory are included in section 3.2.

In section 3.3 the derivation of the basic AFPM machine sizing equations which relate to the machine power and volume, is presented and is followed by, magnetic design aspects in section 3.4. The derivations at this level are basic and therefore independent of the structural type.

Section 3.5 discusses some essential issues regarding the excitation type for the machine with regard to the specific requirements and restrictions that characterize the given application

From the sizing equations, the torque density estimations for AFPM machines are compared with those of conventional radial-flux machines in 3.6. The comparisons clearly show why an AFPM machine is more appropriate for applications where the

machine volume is a critical constraint.

In the light of the comparative analysis that draws on the derived sizing equations, the chapter finalizes with a re-evaluation of the basic decisions regarding the structural choices of the design.

3.2 Applications and types of AFPM machines

This section presents a survey of the most recent literature on various types of AFPM machines. It also aims to form a basis for further discussions regarding the choice and design of an appropriate type of electrical machine for the proposed hybrid vehicle, by comparing the advantages and the disadvantages offered by each type.

3.2.1 Existing applications

AFPM machines are being used in various applications in recent years. Some prominent examples of these applications are listed below together with the corresponding machine operating speeds, power ranges and types:

- High-speed generator driven by a gas turbine in a hybrid traction system: Three types of multi-disk (2,4,6-rotors versus 1,3,5-stators, respectively) AFPM machines were investigated for 10, 30, 50 kW at 60000 rpm [22].
- Hybrid electric vehicle with flywheel-electrical machine combination: Single-rotor, double-stator arrangement, toroidally-wound stator windings, 25 kW peak power (for motoring or generating), speeds in excess of 30000 rpm [13].
- Wheel direct drive for electric vehicles: Rated speed less than 1000 rpm, double-sided configuration with internal stator, slotless toroidal winding arrangement, with surface-mounted permanent magnets [23], [24] or internal permanent magnet rotors [21], [25], or multistage type slotless toroidal winding arrangement with surface-mounted permanent-magnet rotors and water-cooled ironless stator [26], [27], [28].
- Engine driven generator and starter motor: Slotless toroidal stator, two rotor disks, 2.5 kW at 3000 rpm [29], [30].
- Adjustable-speed pump applications: A slotless stator core with concentrated coils, surface-mounted permanent magnets (ferrite for cost minimization) on rotor disks, 880 W at 2800 rpm [31].
- Two direct-driven counterrotating propellers in ship propulsion system: AFPM machine with counterrotating rotors, slotless toroidally-wound stator iron core, surface-mounted permanent-magnet rotor disks, 510 W at 195 rpm [32].

- Low-torque servo and speed control applications for fans and robots [33].
- In computer peripherals, office equipment and storage devices [34].
- Innovative applications including the use of soft magnetic composite materials: Combined axial-radial permanent-magnet machine as the drive motor in an electric bicycle. This can be considered as a pioneering application offering a three-dimensional design capability [35].

3.2.2 Some common features of AFPM machines

Axial-flux machines are different from conventional electrical machines in terms of the direction of the flux which runs parallel with the mechanical shaft of the machine. The current flowing through each stator coil interacts with the flux created by the magnets on the rotor, producing a force tangential to the rotor circumference. Despite the large variety in the existing AFPM machines which are categorized and discussed in the next subsections, it is still possible to mention some common features which can be categorized as advantages and disadvantages with respect to conventional electrical machines.

Advantageous features:

- Compact machine construction and short frame.
- High power density.
- High efficiency; no rotor copper losses due to the permanent-magnet excitation.
- Having a short rotor in axial direction with the ability of the construction without rotor steel.
- More robust structure than cylindrical type [22].

Disadvantageous features:

- High windage losses at high-speed applications (which can be decreased to some extent by placing the machine in a vacuum seal, especially when combined with a flywheel).
- Complicated machine topology with two airgaps

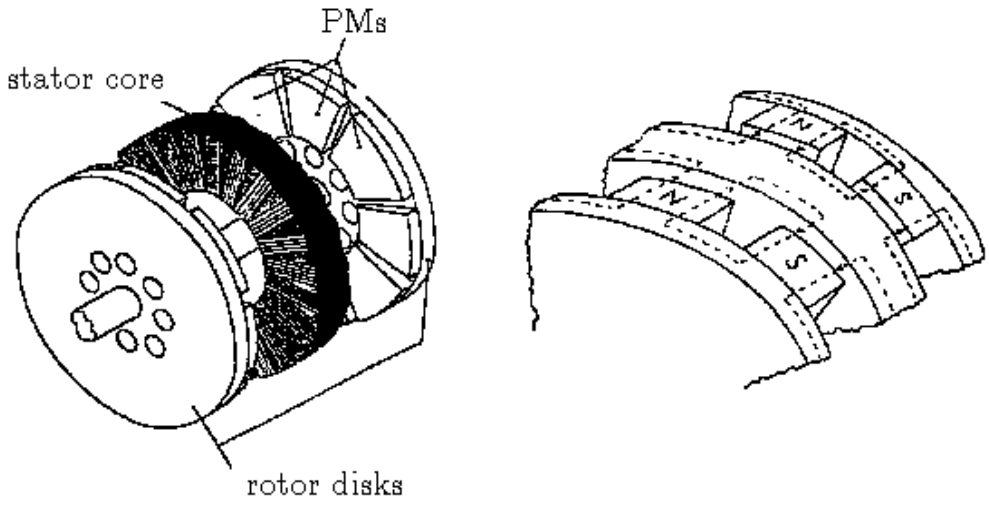

Figure 3.1: Double rotor/single stator AFPM machine and magnet flux distribution.

3.2.3 AFPM machine types

As it may be observed from the list of existing applications, AFPM machine types are basically different combinations of various features which can be classified as:

1. Stator-rotor arrangement:
   (a) Multi-disk structure.
   (b) Single-sided structure (Fig. 3.3 [36]).
   (c) Double-sided structure.
      i. Internal stator (Fig.3.1 [23]).
      ii. Internal rotor.
2. The technique to integrate the permanent magnets to the rotor:
   (a) Surface-mounted permanent magnet type (Fig. 3.3 [36]).
   (b) Internal or buried permanent magnet type (Fig.3.4).
3. Existence of armature slots:
   (a) Slotted stators (Fig.3.2 [37]).
   (b) Toroidally-wound slotless stators.

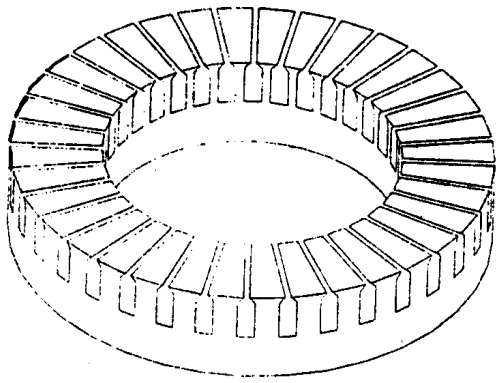

Figure 3.2: Slotted stator.

This classification is explained in detail below.

Stator-rotor arrangement: AFPM machines can be designed as double-sided, single-sided, or even as multi-disk configurations. Naturally, the easiest and the cheapest construction is the single-sided (only one rotor and one stator disk) type, but due to the relatively low torque production and bearing problems caused by the high attractive force normal to the plane of the airgap which tends to bring the two parts together [38], this type is not very popular.

However, the high attractive force between the rotor and the stator can be counterbalanced by the use of a second stator/rotor mounted as the mirror image of the first. This construction is called the double-sided arrangement. Double-sided motors are the most promising and widely used types [37].

Double-sided motors can be constructed with an internal stator or an internal permanent-magnet disk rotor. A double-sided motor with an internal permanent-magnet disk rotor has two stator cores and a disk rotor with permanent magnets sandwiched between them. In this construction the stators are surrounded by a considerable amount of end windings which results in a poor utilization of the machine copper [23]. The flux return paths are in the stators and relatively large iron losses are more pronounced in this configuration with respect to the other type [13]. On the other hand, having stators adjacent to the axial end surfaces of the device facilitates in providing a good thermal path for cooling the windings [13]. Stator windings of this configuration can be connected either in parallel or in series, which is an issue to be considered in the design. In parallel connection, the motor can operate even if one stator winding is broken, while series connection provides equal magnitudes of opposite axial attractive forces [33]. If the windings are connected in series, then one stator may be rotated over a certain angle with respect to the other which results in reduced cogging torque and space harmonic components [37]. Besides, with such a

configuration, a flywheel motor arrangement can be made as in [13], by embedding the permanent magnets in the wings of the flywheel.

The double-rotor configuration on the other hand has the main advantage of reduced copper and iron losses (the flux return paths are in the rotor disks) and increased power density. According to [23], cooling is much easier for this type of machine, since the rotors with surface-mounted permanent magnets rotating next to the sides of the windings, act as a fan, especially when holes are located near the machine shaft as shown in Fig.3.1. On the other hand, this structure is more difficult to manufacture. Besides, in high-speed applications, due to four rotating faces windage losses are more pronounced than in the other type.

In spite of the fact that the double-sided motors are suitable, multi-disk types can be the most attractive solution for certain applications, where a large power requirement is accompanied by a severe limitation on the external diameters of the disks. In such cases, increasing the number of disks is a good alternative [22], [26], [27], [28]. For example, in [22] three types of test machines are described with the same diameter but different power ratings; two rotors/one stator at 10 kW, four rotors/three stators at 30 kW, and six rotors/five stators rated at 50 kW. Apparently, mechanical stresses and windage losses are both higher for multi-disk type machines. On the other hand, as far as the cost of the machine is concerned, multi-disk motors having many rotor disks with expensive permanent magnets, can doubtlessly be eliminated from the very outset.

The technique to integrate the permanent magnets to the rotor: AFPM machines can be designed with surface-mounted (Fig.3.3 [36]) or interior (or buried) type permanent magnets (Fig.3.4 [21]) on the rotor disks. For interior permanent magnet type machines having permanent magnets embedded in the iron, the structure is mechanically quite robust; i.e. the magnets are very well protected against centrifugal forces which are more pronounced especially in high-speed operation. The major drawback of the interior permanent-magnet motor type may be its constructional difficulties.

For surface-mounted permanent-magnet motors, since the permeance of the magnets is nearly equal to that of free space, the effective airgap is larger, the stator winding inductance is very low and (in the constant power speed region, without oversizing the inverter kVA) the motor has limited capability to operate above its base speed, which is the main disadvantage of this type [21]. For high-speed applications surface permanent-magnet motors are generally used with an external rotor can [33].

Existence of armature slots: AFPM machines can be constructed with or without armature slots. In a slotless design, the permeance components of the flux ripple, tooth iron losses, tooth saturation and tooth related vibrations are eliminated [21]. Due to the relatively short end windings, copper losses are also lower [24]. But a slotless type is not suitable for applications where the motor is subjected to any

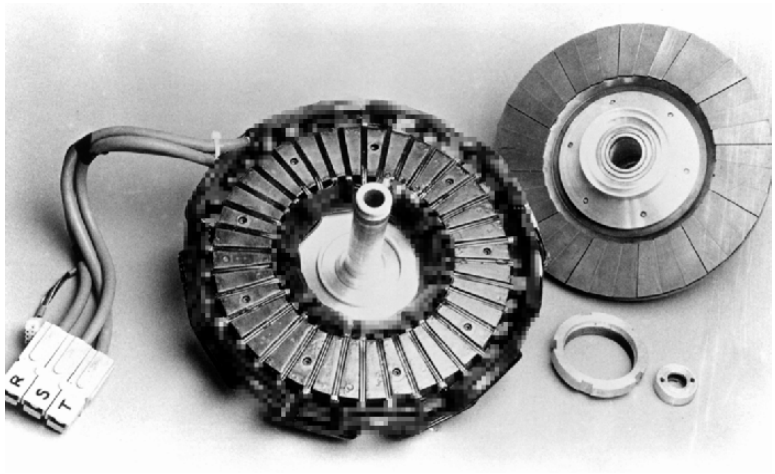

Figure 3.3: Single-sided machine structure with surface-mounted PM rotor.

type of mechanical stress [21].

A motor with armature slots is more robust and the effective airgap is much smaller. Another advantage is the allowance for different winding structures, which will result in different flux distributions as shown in Fig.3.5 [21]. The NN and NS type structures are explained in [21] for an internal stator structure. A NN type configuration economizes in the end windings length which is almost equal to the stator yoke axial length, resulting in low copper losses. But the stator yoke through which the flux passes should be made larger, which leads to relatively large iron losses. In the case of NS the opposite is true. It has small yoke dimensions, but long end windings (more than one pole pitch), which means smaller iron losses, but higher copper losses [21].

3.2.4 Design variations

As discussed by several researchers, stator inner and outer diameters are the two most important design parameters. Hence, for cases where the stator outer diameter is limited or imposed by the rest of the system, the ratio of inner to outer diameter, K_r is the key parameter to consider and it has a crucial impact on the determination of the machine characteristics, such as torque, torque to weight ratio, iron losses, copper losses, and efficiency. Caricchi et. al. [31], [24], [26] show the dependency on K_r for designs with various numbers of pole pairs.

Other important design parameters are the pole number, magnet thickness, conductor size, number of turns and material types. On the other hand, every design has its particular constraints and they differ with the type of application. Generally, one tries to obtain the maximum torque for a given motor diameter at a given

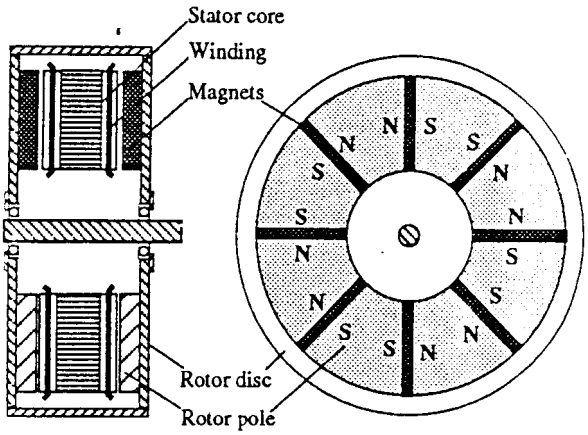

(a)

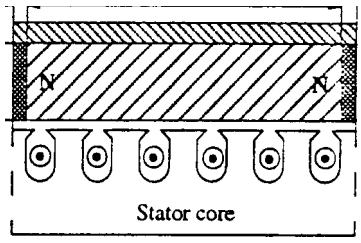

(b)

Figure 3.4: AFPM machine, with interior PMs (a) radial (b) axial view.

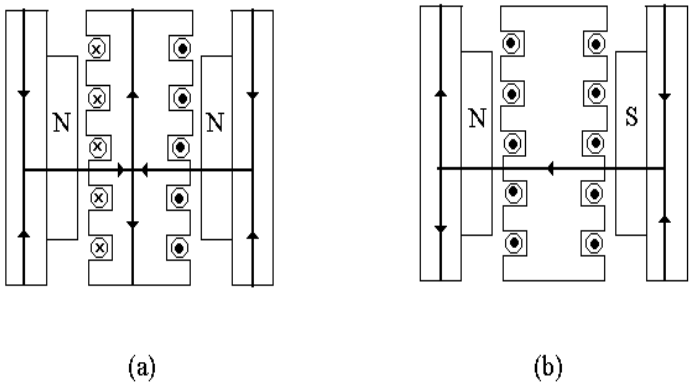

Figure 3.5: Configuration of (a) NN and (b) NS type double-sided, internal stator AFPM machines.

speed. Mostly for small machines, the number of poles is limited due to the reduced space available for the windings. Nevertheless, the most restricting limitation for the number of poles is the motor operating speed. If the speed is high, a large number of poles will bring about an increase in the frequency, which directly leads to higher stator core losses and higher converter losses.

The volume, thickness, shape and type of the permanent magnets also affect both the performance and the cost of the machine. The relationship between magnet volume and torque is explained in detail in [39]. In reference [27], a design based on the optimization of the width of the permanent magnets for a surface-mounted permanent-magnet type axial-flux machine is explained. The choice of the permanent magnet width to pole pitch ratio is discussed. For higher values of this ratio, 1 for instance, flux linkage is maximum, but also flux leakage due to adjacent permanent magnets is high. By decreasing the permanent magnet width, linkage and leakage fluxes are both decreased though not proportionally.

An example of a design based on cost minimization can be found in [31]. Since the permanent magnets are the most expensive part of the machine, instead of Nd-Fe-B, ferrite magnets are used in this work. Also, ferrites having small conductivity, do not suffer from eddy current problems which emerge in sintered rare-earth magnets [40]. But, of course, ferrite has poor characteristics when compared with Ne-Fe-B, and its usage makes it impossible to obtain high airgap flux densities. Magnet protection must also be considered as a constraint together with the dimensional machine parameters [41].

Throughout the design the improvement of the machine efficiency must always be kept in mind. For AFPM machines the most pronounced loss mechanisms are: Joule losses, eddy current, iron, and windage losses. With permanent magnets the rotor hardly suffers any losses at low speeds. In relation to conventional machines, the copper losses in a toroidal configuration are relatively low. As discussed in the previous section, with an appropriate selection among different types of AFPM machine structures the iron or copper losses can be reduced, though at high-speed operations higher eddy current losses are inevitable. Windage losses, which are relatively high for disk type machines, are also increased with speed. Loss mechanisms are dependent on the materials used. In the work of Jensen [40] amorphous iron, which is difficult to manufacture and very expensive, is chosen for the stator core to reduce iron losses.

The thermal behavior of the machine and consequent cooling requirements must also be studied in the design stage. For a certain power rating, high speed forces down the external diameter of the rotor, and together with the high frequency, causes large Joule losses and cooling problems. In [29] a thermal model of an AFPM machine is discussed. In some articles different cooling methods can be found [27], [28]. Additionally, high temperature introduces extra constraints on the choice of the materials.

Other constraints to be considered are mainly of mechanical nature. The centrifugal force acting on a rotating mass is proportional to the velocity squared and inversely proportional to the radius of rotation. Consequently, for high-speed applications (speeds in excess of 10000 rpm) the rotor must be designed with a small diameter in order to reduce tensile stress, and must have a very high mechanical integrity [33]. A dynamic analysis of the rotor, shaft and bearings must be made.

For every motor design an accurate analysis of the magnetic field preferably by means of finite element method (FEM) is essential. FEM applications on AFPM machines can be found in [37], [21], [38]. Due to the structure of AFPM machines (unlike radial-flux machines) it is very difficult to find a representative 2D cross-section which may accurately approximate the machine at each point along the third dimension as well. But relying on the fact that the flux path in the airgap runs along the mechanical axis of the machine, the analysis can be reduced to 2D by investigating the field in an axial cross-section, at the mean radius of the permanent magnets, and after the analysis the calculated magnitudes are integrated along the radial direction for the actual length. For some other researchers [38] the 2D analysis discussed above is carried out only for the aligned positions of the machine parts, and a 3D analysis is claimed to be necessary for investigating the effect of the displacements on torque and induced EMF.

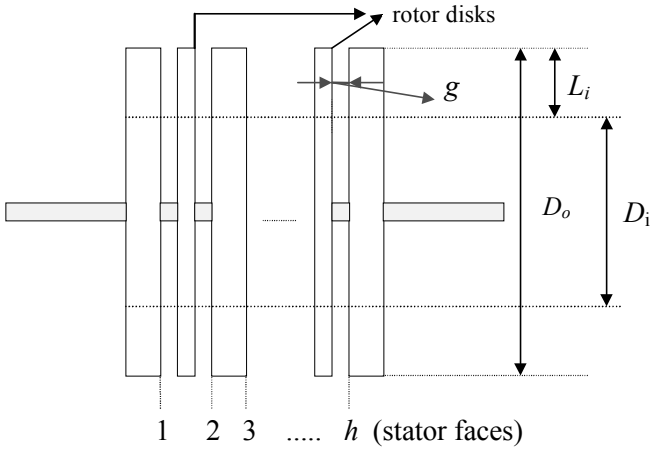

Figure 3.6: Simplified representation of an AFPM machine.

3.3 Derivation of the sizing equations

This section presents the basic design of an AFPM machine and the derivations of the basic electrical and magnetic parameters. There are several types of AFPM machines which were discussed in section 3.2, where the selection of the machine type is mostly based on the application. Hence, the derivation of the basic equations for quantities such as torque, back emf, inductance, which are valid for all these types of AFPM machines is included in this section. The differences of the sizing equations of the radial and axial flux machines will also be emphasized.

3.3.1 Dimensional design parameters

The basic dimensions related to the sizing of the AFPM machine are categorized and summarized as follows.

The number of stator faces (h)**:** This parameter is defined to obtain generalized sizing equations which also include the effect of the number of disks used. Since torque is produced as a result of the interaction between the magnetic field of the permanent magnets on the rotor and the current in the stator conductors, it is obvious that by increasing the number of stators, the torque of the machine will be increased proportionally. And this relation is also independent of the location of the rotor, i.e. either the rotor is in between two stator disks or the stator is in between the two rotor disks; h is equal to 2 and there is no difference between them in terms of torque. It may only affect the level of some losses due to the amount of copper (copper losses) and the amount of iron (iron losses) in the machine as discussed in section 3.2. In Fig.3.6 a simplified AFPM structure is shown.

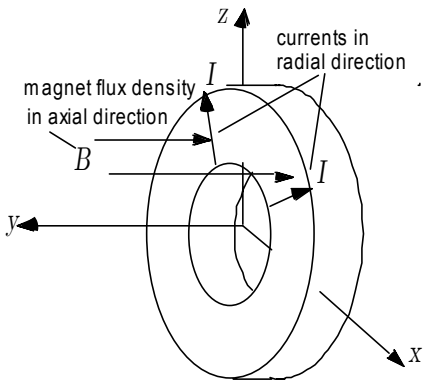

Figure 3.7: Stator conductors and the interacting magnet flux density on the stator disk.

Airgap length (g) is also indicated in Fig.3.6.

Stator dimensions: In Fig.3.6 the outside and inside diameters of the stator (D_o and D_i), and the effective length of the stator core in radial direction L_i are shown. For the sake of simplicity, the outside and inside radii of the stator, r_o and r_i, can also be defined. Other important parameters are the average diameter of the stator which is indicated with D_{av} ($(D_o + D_i)/2$), and the pole pitch at the average diameter τ_p ($D_{av}\pi/2p$ where p is the number of pole pairs). These dimensions are the ones which play an important role in the torque production of the machine.

3.3.2 Torque

As in the case of radial-flux machines, the torque equation of AFPM machines can be derived through Lorentz force equations. Force and torque can be written for one conductor of length ℓ, carrying a current i as

$$\overrightarrow{F} = \ell.\left(\overrightarrow{i} \times \overrightarrow{B}\right), \tag{3.1}$$

$$\overrightarrow{T} = \overrightarrow{r} \times \overrightarrow{F}, \tag{3.2}$$

where r is the radius at which the torque is produced and B is the flux density. Using these basic formulas the sizing equation may be written in terms of the magnet flux and the stator ampere-conductor distribution.

In Fig.3.7 the stator conductors on a radial cross-section (in x-y plane) and the interacting magnet flux, which is in axial direction, are shown on a disk stator unit. Since Eq.3.1 and 3.2 are only valid for one conductor, first the sinusoidal ampere-conductor distribution must be formalised in order to determine the total amount of torque.

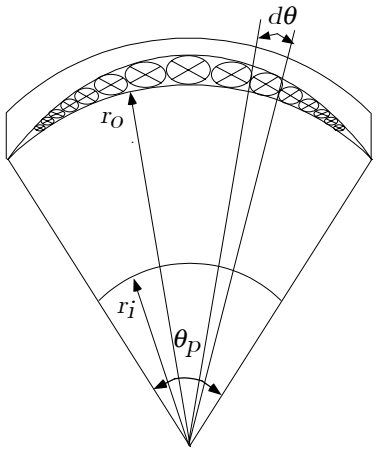

Figure 3.8: Sinusoidally distributed conductors of a phase on the stator pole section.

Assuming that a sinusoidal flux density distribution in the airgap is created from the stator current sheet as indicated in Fig.3.8, at any incremental angle $d\theta$, the number of conductors considering only one phase is

$$\frac{N_s}{2}\sin p\theta d\theta, \tag{3.3}$$

where p is the number of pole pairs and N_s is the sinusoidally distributed series turns per phase. Since the total number of turns per pole is

$$N_p = \frac{N_s}{2p}, \tag{3.4}$$

and in one pole there are $2N_p$ conductors, the integration of Eq.3.3 over a pole pitch should give the total number of conductors per pole, which is equal to N_s/p.

Now, considering three phase windings, whose axes are 120 electrical degrees apart and with pure sinusoidal currents, the total amount of current flowing through an incremental angle $d\theta$ at time t can be derived by adding up the contributions of all three phases [42],

$$\left\{\begin{array}{l} \text{Phase A: } \widehat{i}\cos\omega t\dfrac{N_s}{2}\sin p\theta d\theta \\ \\ \text{Phase B: } \widehat{i}\cos(\omega t-\dfrac{2\pi}{3})\dfrac{N_s}{2}\sin(p\theta-\dfrac{2\pi}{3})d\theta \\ \\ \text{Phase C: } \widehat{i}\cos(\omega t+\dfrac{2\pi}{3})\dfrac{N_s}{2}\sin(p\theta+\dfrac{2\pi}{3})d\theta \end{array}\right\}, \tag{3.5}$$

which results in

$$\frac{3}{2}I\sqrt{2}\frac{N_s}{2}\sin(p\theta-\omega t)d\theta, \tag{3.6}$$

where I is the rms value and $\widehat{i}$ is the amplitude of the phase currents.

The fundamental component of the airgap flux density due to the permanent magnets is

$$B_{g1}(\theta)=\widehat{B}_{g1}\cos(p\theta-\omega t-\alpha), \tag{3.7}$$

where $\widehat{B}_{g1}$ is the amplitude of the fundamental component and α is the electrical angle between the rotor and the stator magnetic axes.

Since the magnet flux density and the ampere-conductor distribution are already calculated, the only work left is to determine the torque for an AFPM machine structure using Eqs.3.1 and 3.2. As can be understood from Fig.3.9, for AFPM machines torque is produced at a continuum of radii from r_i to r_o unlike the radial-flux machines. Hence, the torque which is produced by the interaction of the stator conductors and permanent magnets should be calculated by integrating the incremental torque at radius r from r_i to r_o. Considering the area $(d\theta.dr)$ in Fig.3.9, the "incremental force" and torque can be derived as follows.

The total amperes entering the angular distance $d\theta$ of the stator surface is derived in Eq.3.6 and the length of the conductors in this small area is apparently dr. Hence, the small area can be considered as a conductor of length dr, in which the current determined by Eq.3.6 is flowing. Since the direction of the flux is perpendicular to the current as it is shown in Fig.3.7, the "cross product" in Eq.3.1 is eliminated and the amount of incremental force can be written as

$$dF_1(r,\theta)=\widehat{B}_{g1}\cos(p\theta-\alpha)\frac{3}{2}I\sqrt{2}\frac{N_s}{2}\sin(p\theta)d\theta dr, \tag{3.8}$$

after the elimination of the time dependent term ωt from the equations, i.e. anchoring the time to zero. The total force at radius r for one pole can be found by integrating Eq.3.8, from angle 0 to π/p (i.e. the angular pole pitch) and for the whole stator unit the equation must be multiplied by the number of poles $2p$:

$$F_1(r)=2p\int_0^{\pi/p}\widehat{B}_{g1}\cos(p\theta-\alpha)\frac{3}{2}I\sqrt{2}\frac{N_s}{2}\sin(p\theta)d\theta dr. \tag{3.9}$$

Finally, using Eq.3.2

$$T_1(r)=2p\int_0^{\pi/p}\widehat{B}_{g1}\cos(p\theta-\alpha)\frac{3}{2}I\sqrt{2}\frac{N_s}{2}\sin(p\theta)d\theta r dr, \tag{3.10}$$

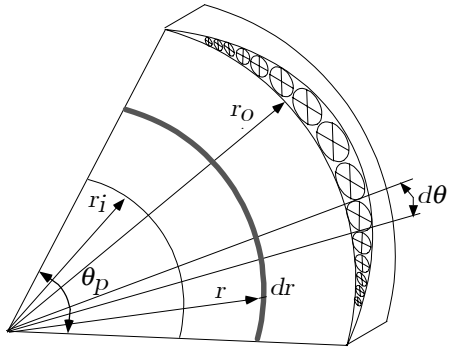

Figure 3.9: Geometry for torque calculation.

and the fundamental torque for one stator face of the AFPM machine is found by solving the integral equation as

$$T_1 = 2p \int_{r_i}^{r_o} \int_{0}^{\pi/p} \widehat{B}_{g1} \cos(p\theta - \alpha) \frac{3}{2} I\sqrt{2} \frac{N_s}{2} \sin(p\theta) d\theta r dr, \tag{3.11}$$

$$T_1 = \frac{3}{8}\sqrt{2}\pi \widehat{B}_{g1} N_s I (r_o^2 - r_i^2) \sin(\beta), \tag{3.12}$$

where $\beta = -\alpha$, which is known as the torque angle of a synchronous machine.

Practically, it is quite impossible to place the conductors sinusoidally. For a more realistic and practical equation, the actual number of series turns per phase, N_{ph}, is included in the equation by defining the effective number of sinusoidally distributed series turns per phase N_s as [43]

$$N_s = \frac{4}{\pi} k_{w1} N_{ph}, \tag{3.13}$$

where k_{w1} is the fundamental winding factor which contains the effects of distributed, shortened and skewed windings. The torque formula reduces to

$$T_1 = \frac{3}{2}\sqrt{2} \widehat{B}_{g1} k_{w1} N_{ph} I (r_o^2 - r_i^2) \sin(\beta). \tag{3.14}$$

The torque equation can also be written in terms of the average diameter and the effective length of the stator as

$$T_1 = \frac{3}{2}\sqrt{2} \widehat{B}_{g1} k_{w1} N_{ph} I D_{av} L_i \sin(\beta), \tag{3.15}$$

where $D_{av} = r_o + r_i$, and $L_i = r_o - r_i$.

In order to simplify the design calculations, a parameter "stator surface current density" or "specific electric loading" as it is called in the literature, should be inserted in the equations, because typical values of the surface current density for different applications are practically known, which helps for identifying initial design parameters. The amplitude of the surface current density K_1 ranges from 10000 A/m for small motors to 40000 A/m for medium power motors [33]. This parameter shows how many amperes can be packed together in each unit length of the stator circumference. The value is limited of course by several factors such as cooling, slot depth and slot fill factor [43].

Since there are 3 phases, $2N_{ph}$ conductors in each phase and $\sqrt{2}I$ as the peak current, the fundamental component of the surface current density K_1 is defined as

$$K_1 = \frac{\text{total max. ampere-conductors}}{\text{armature circumference}} = \frac{3\sqrt{2}I2N_{ph}}{D_{av}\pi}, \tag{3.16}$$

Due to the particular structure of the AFPM machines the average diameter of the stator is used for the calculation of the armature circumference. Yet it should be noted that some researchers [23], [44] are using the inside diameter of the stator where the space limitation is more pronounced, instead of the average diameter in the surface current density equations.

By eliminating $N_{ph}I$ in Eq.3.15 using Eq.3.16, the torque equation becomes

$$T_1 = \frac{1}{4}\pi \widehat{B}_{g1} k_{w1} K_1 D_{av}^2 L_i \sin(\beta). \tag{3.17}$$

Since this torque equation is calculated only for one stator face, it can be generalized by multiplying the expression with parameter h to obtain the total torque of an AFPM machine with h stator faces as

$$T_1 = \frac{h}{4}\pi \widehat{B}_{g1} k_{w1} K_1 D_{av}^2 L_i \sin(\beta). \tag{3.18}$$

In order to express the torque just in terms of the outside radius of the stator r_o, the factor K_r (r_i/r_o), which is the ratio of inside to outside radius of the stator, is inserted in the equation as[1]

$$T_1 = \frac{h}{4}\pi \widehat{B}_{g1} k_{w1} K_1 r_o^3 (1 - K_r^2)(1 + K_r) \sin(\beta). \tag{3.19}$$

This is the most important sizing equation of AFPM machines. It clearly shows the effect of the outside radius of the stator and the factor K_r on the torque production of the machine.

[1] $D_{av}^2 L_i = (r_o + r_i)^2 (r_o - r_i) = r_o^3 (1 - K_r^2)(1 + K_r)$

3.3.3 EMF and power

Considering the voltage e induced in a conductor with length ℓ moving with velocity v in the magnetic field B

$$e = \oint \left(\overrightarrow{v} \times \overrightarrow{B} \right) \cdot d\ell. \tag{3.20}$$

the emf induced in the stator windings from the rotor excitation system can be expressed. As it is seen from Fig.3.7, the rotor excitation system rotates with velocity v with respect to the stator conductors which are perpendicular to the direction of the magnetic field. To calculate the phase emf, again the elementary group of conductors for one phase in Fig.3.8 which was determined in Eq.3.3, should be considered. Using the fundamental component of the airgap flux density Eq.3.7 and assuming the conductor length L_i, the emf induced in the conductors can be written as

$$de = B_{g1}(\theta) L_i v \frac{N_s}{2} \sin p\theta d\theta. \tag{3.21}$$

If the mechanical speed of the rotor is ω_m, the average circumferential speed of the conductor is

$$v = \omega_m \frac{D_{av}}{2}. \tag{3.22}$$

Replacing Eq.3.22 in Eq.3.21 yields

$$de = B_{g1}(\theta) L_i \omega_m \frac{D_{av}}{2} \frac{N_s}{2} \sin p\theta d\theta, \tag{3.23}$$

Using Eq.3.7,

$$de = \widehat{B}_{g1} \cos(p\theta - \omega t - \alpha) L_i \omega_m \frac{D_{av}}{2} \frac{N_s}{2} \sin p\theta d\theta, \tag{3.24}$$

which results in

$$de = \widehat{B}_{g1} \omega_m \frac{D_{av}}{2} L_i \frac{N_s}{2} \frac{1}{2} \left[\sin(2p\theta - \omega t - \alpha) + \sin(\omega t + \alpha) \right] d\theta. \tag{3.25}$$

Integrating this equation over all the elementary groups of conductors, the fundamental component of the instantaneous phase emf for a machine with p pole pairs can be calculated

$$e_1 = 2p \int_0^{\pi/p} de = 2p \int_0^{\pi/p} \widehat{B}_{g1} \omega_m \frac{D_{av}}{2} L_i \frac{N_s}{2} \frac{1}{2} \left[\sin(2p\theta - \omega t - \alpha) + \sin(\omega t + \alpha) \right] d\theta. \tag{3.26}$$

After some manipulation

$$e_1 = \frac{\pi}{2} \int_0^{\pi/p} \widehat{B}_{g1}\omega_m \frac{D_{av}}{2} L_i N_s \sin(\omega t + \alpha). \tag{3.27}$$

It should be noted that all equations derived so far are valid for an idealized sinewave machine. Therefore the quantities such as torque or emf derived in this section only represent the fundamental components. The effects of the harmonic contents on these variables will be studied in section 4.12.

Using Eq.3.13 the rms phase emf equation can be written as

$$E_{ph} = \frac{\sqrt{2}}{2} \widehat{B}_{g1}\omega_m k_{w1} N_{ph} D_{av} L_i. \tag{3.28}$$

Regardless of the connection type of the stators (series or parallel), the inside apparent electromagnetic power of the machine with a 3-phase stator-system can be calculated using Eq.3.16 as

$$S_{elm} = 3hE_{ph}I = \pi \frac{h}{4} \widehat{B}_{g1}\omega_m k_{w1} K_1 D_{av}^2 L_i, \tag{3.29}$$

which can also be derived from Eq.3.18.

3.4 Basic magnetic design

The flux in the machine is mainly established by the magnets in most applications. Since the torque production is directly proportional to the flux, the design of the rotor has the utmost importance. As categorized before, the rotor can be designed with surface-mounted or interior permanent magnets. Here, the simplified calculation of the required lengths of the permanent magnets for both constructions are shown. The required length of the stator yoke is also derived in this section.

3.4.1 Rotor with surface-mounted permanent magnets

In Fig.3.3 the radial and axial cross-sections of the 2-stators/1-rotor AFPM machine with surface-mounted PM-rotor is shown [45]. Using the axial cross-section shown in Fig.3.10 where the flux paths are shown, the airgap flux density equation can be derived using

$$\nabla \times \overrightarrow{H} = \overrightarrow{J}. \tag{3.30}$$

By assuming that the stator iron has infinite permeability, neglecting magnet leakage flux and using a simple circuit approximation

$$2H_m L_m + 4H_g g = 0, \tag{3.31}$$

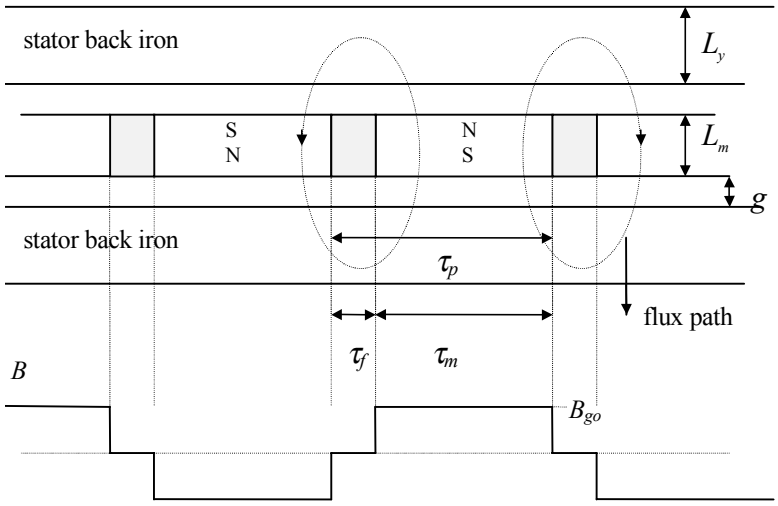

Figure 3.10: Axial cross-section of the surface-mounted PM rotor AFPM machine and airgap flux density waveform.

$$H_m = \frac{-2B_{g0}g}{\mu_0 L_m}, \tag{3.32}$$

$$B_m = \mu_0 \mu_r H_m + B_r, \tag{3.33}$$

where B_m, H_m, B_{g0}, and H_g, are the magnet and airgap flux densities and field strengths, respectively. B_r and μ_r are the magnet remanence and relative permeability. Here the term B_{g0} corresponds to the average airgap flux density as seen in Fig.3.10. Inserting Eq.3.32 into Eq.3.33 and assuming that there is no tangential flux density component ($B_{g0} = B_m$), the airgap flux density is derived as

$$B_{g0} = \frac{B_r}{1 + \dfrac{2g\mu_r}{L_m}}. \tag{3.34}$$

Although this formulation is sufficient for the initial design, it should be noted that, the calculation method can be improved to give more accurate results by the inclusion of the magnet leakage factors and slot coefficients [33]. The calculation of the magnet leakage factors for several magnet shapes can be found in [33]. Besides, if there are no slots in the stator, the airgap length effectively increases such that it covers the winding width as well. If there are slots, the airgap length g can be

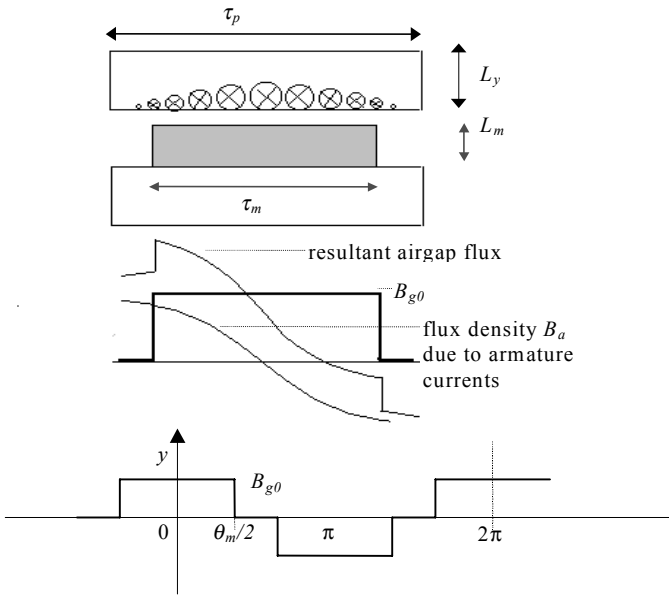

Figure 3.11: Flux density distribution of a sinusoidal current sheet and a rectangular magnet.

multiplied by the slot coefficients [33], [45]. In this thesis the detailed magnetic analysis is left to the FE analysis, where the effects of the magnet leakage and the slotting can be studied more accurately (see chapter 5).

With surface-mounted PMs, in order to obtain a better distribution of the flux density around the airgap, the magnet thickness can be shaped at the pole edges or a shorter magnet pole arc can be used. In Fig.3.11, the flux density distribution of a rectangular magnet, as well as the armature reaction and the resultant flux density waveforms are shown. In Fig.3.11, θ_m is the magnet span in electrical degrees. As an illustrative example, the amplitude of the first harmonic component is calculated from the Fourier analysis below.

The full Fourier-series representation of the function $f(\theta)$ is

$$
\begin{aligned}
f(\theta) &= \sum_{n=1}^{\infty}(a_n \cos n\theta + b_n \sin n\theta) \\
a_n &= \frac{1}{\pi}\int_0^{2\pi} f(\theta)\cos n\theta d\theta \\
b_n &= \frac{1}{\pi}\int_0^{2\pi} f(\theta)\sin n\theta d\theta.
\end{aligned}
$$

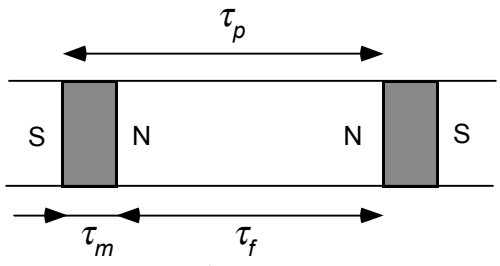

Figure 3.12: Interior-magnet rotor.

Since the airgap flux density distribution is symmetric with respect to the orthogonal axis, the sine terms (in the function) are zero. Hence, for the amplitude of the first harmonic component, only the calculation of a_1 is necessary, which results in

$$\widehat{B}_{g1} = \frac{1}{\pi}\left(\int_{\frac{-\theta_m}{2}}^{\frac{\theta_m}{2}} B_{g0}\cos\theta d\theta + \int_{\pi-\frac{\theta_m}{2}}^{\pi+\frac{\theta_m}{2}} B_{g0}\cos\theta d\theta\right), \tag{3.35}$$

$$\widehat{B}_{g1} = \frac{4}{\pi}B_{g0}\sin\frac{\theta_m}{2}. \tag{3.36}$$

3.4.2 Rotor with interior permanent magnets

The flux density equation, which is dependent on the airgap length, the magnet length and the magnet properties, can also be written for machines with an interior-PM rotor (as shown in Fig.3.4, [25]). The simplified drawing and the necessary dimensions such as pole pitch (τ_p) and axial magnet pitch (τ_m) are shown in Fig.3.12. The flux directed through the N-pole of the magnet first flows "radially" in the rotor, then it turns to the axial direction and crosses the airgap. So the magnet and the airgap areas ($A_m = L_m L_i$ and $A_g = \tau_f L_i$), in which the flux is flowing, are different from the previous case.

Considering as an example the double rotor/single stator construction as in Fig.3.4, assuming the permeability of the rotor and stator iron infinite,

$$\tau_m H_m = -2gH_g = \frac{-2gB_{g0}}{\mu_0}, \tag{3.37}$$

$$H_m = \frac{-2gB_{g0}}{\mu_0\tau_m}, \tag{3.38}$$

and further assuming the magnet and gap fluxes being equal,

$$B_m = \frac{B_{g0}\tau_f}{L_m}, \tag{3.39}$$

the airgap flux density is derived as

$$B_{g0} = \frac{B_r}{\frac{\tau_f}{L_m} + \frac{2g\mu_r}{\tau_m}} \tag{3.40}$$

where τ_f can be defined alongside the average radius as $\tau_f = \tau_p - \tau_m = \frac{D_{av}\pi}{2p} - \tau_m$.

3.4.3 Stator yoke

Since the iron does not have unlimited capacity to carry flux, in any design the maximum allowable flux density in the iron should be determined. It can not exceed a certain level determined by the steel saturation characteristics, since the permeability of the iron decreases rapidly. This fact should be considered in the determination of both the stator yoke and tooth widths. As understood from Fig.3.3, in the stator the flux directed from the magnets splits into two paths in the back iron to return through adjacent magnets. The approximate stator yoke length L_y (see Fig.3.11) can be determined considering the approximate airgap flux

$$\phi_g = \tau_p L_i B_{g0}, \tag{3.41}$$

and yoke flux

$$\phi_y = L_y L_i B_{\max}, \tag{3.42}$$

where $B_{\max}$ is the maximum allowable flux density in the steel. The minimum required stator yoke length is written as, assuming $\phi_g = 2\phi_y$

$$L_y = \frac{\tau_p B_{g0}}{2B_{\max}}. \tag{3.43}$$

3.5 Comparison of AFPM machines with sinewave and squarewave current excitations

Although the permanent magnet machines studied here are synchronous machines in their nature, according to [42], [43] permanent magnet motors can also be classified into two categories with respect to their modes of operation as brushless DC and brushless AC motors.

"*The characteristic features of brushless DC motors are*

1. *rectangular distribution of magnet flux in the airgap;*
2. *rectangular current waveforms;*
3. *concentrated stator windings.*

The sinewave motor (brushless AC) differs in all three respects, It has;

1. *sinusoidal or quasi-sinusoidal distribution of magnet flux in the airgap;*
2. *sinusoidal or quasi-sinusoidal current waveforms;*
3. *quasi-sinusoidal distribution of stator conductors; i.e. short-pitched and distributed or concentric stator windings* [42]*".*

AFPM machines can thus be designed to operate with squarewave or sinewave currents. Their operation principles are quite similar, but they can be chosen for different types of applications. For example, when a higher torque and/or a simpler drive system is necessary, brushless DC machines can be a better alternative [43]; a smoother torque and a reduction in audible noise can be obtained with brushless AC machines. In this section, the AFPM machines with sinewave (brushless AC machine) and squarewave current (brushless dc machine) excitations are compared in terms of the efficiency, the torque density and the drive circuit requirements for the given application. These machines will be called as *sinewave and squarewave machines* in the following parts, for the ease of understanding. Squarewave machines are also referred as trapezoidal machines in the literature.

For the given electric vehicle application the most important constraint related with the design is the space limitation in both axial and radial directions as discussed in section 2.5. Besides, the whole drive system should be as efficient as possible due to the usage of the battery. The efficiency of the converter part should also be considered.

Taking these facts into account, sinewave and squarewave machines are focussed on. Machine dimensions for the given ratings obtained from analytical formulations were used to compare the performances of these two machines. At first torque, emf and inductance equations, which were derived for sinewave machines before, are derived for the squarewave machine. Using these equations, these machines were compared in terms of torque, efficiency and the drive system requirements.

3.5.1 Sizing equations for squarewave-current driven AFPM machine

By following the same procedure as in the previous sections, the equations are rewritten for the idealized squarewave machine. In this "ideal" case, only two of the three

phases are excited at any given time, and currents are assumed to be continuous for 120° electrical of each period. The machine is assumed to have full pitched windings. By further assuming that the phase EMF waveform has at least a 120° electrical flat-top peak value, it can be said that this machine can theoretically develop a ripple-free output torque.

Considering the magnet span as 180° electrical, the peak-phase emf equation of the single stator unit can be found with the methods as discussed in section 3.3

$$E_{ph-sq} = B_{g0}\omega_m k_{w1} N_{ph} D_{av} L_i \tag{3.44}$$

where the idealized torque equation can be deduced as

$$T_{sq} = 2hB_{g0}k_w N_{ph} I_{sq} D_{av} L_i \tag{3.45}$$

where I_{sq} is the peak value of the squarewave current.

The self inductance of the phase winding is derived by using the same equivalent circuit that will be used for the synchronous reactance calculation in section 4.4. The 3-phase sinusoidal ampere-conductor distribution in the synchronous reactance calculation is here replaced by the concentrated winding of a single phase. The resulting phase self-inductance equation is derived as

$$L_s = \frac{\pi k_w N_{ph}^2 \mu_0 D_{av} L_i}{2p^2(2g + \frac{L_m}{\mu_r})}. \tag{3.46}$$

It should be noted that, for the 3-phase system which is considered here, the mutual inductance with the other excited phase should also be taken into account by $M_s = L_s/3$ [43]. The total phase inductance is the sum of these two terms plus the leakage inductance term.

3.5.2 Torque comparison

The stator rms phase emf and the torque equations of the idealized sinewave AFPM machine are,

$$E_{ph-\sin} = \frac{\sqrt{2}}{2}\widehat{B}_{g1}\omega_m k_{w1} N_{ph} D_{av} L_i, \tag{3.47}$$

$$T_{\sin} = \frac{3}{2}\sqrt{2}h\widehat{B}_{g1}k_{w1}N_{ph}I_{\sin}D_{av}L_i \sin(\beta), \tag{3.48}$$

where $\widehat{B}_{g1}$ is the peak value of the fundamental component of the airgap flux density and $I_{\sin}$ is the rms value of the sinusoidal phase current. The peak emf and the torque equations for the squarewave machine are given in Eq.3.44 and Eq.3.45.

According to [46] by designing machines with a nonsinusoidal winding distribution in which a prescribed nonsinusoidal current flows, the power density is improved and the machine iron is better utilized. In [46], [47], and [48], a generalized analytical approach for deriving the sizing equations including the effect of nonsinusoidal currents, is presented. Using their approach it is possible to compare machines with various shapes of current excitations.

These machines can be compared on the basis of several assumptions. The main assumption here is that the two machines have the same stator inner and outer diameters. A simple method of comparison which is applied for radial-flux machines as described in [42], is used. The comparisons can be made in terms of the magnet flux and the phase current.

Condition 1 *The peak magnet flux densities of the sinewave and the squarewave machines are the same*

This means that, independent of the amount of magnet volume, the peak value of the sinusoidal flux density $\widehat{B}_{g1}$ for the sinewave machine is equal to the peak value of the squarewave flux density B_{g0} of the squarewave machine .

1. *If they are compared in terms of peak currents*

   When the peak current values of the squarewave and the sinewave machines are the same ($\sqrt{2}I_{\sin} = I_{sq}$), the torque ratio of the two machines can be found by dividing Eq.3.45 by Eq.3.48 as $T_{sq}/T_{\sin}$ =1.33.

2. *If they are compared in terms of rms currents*

   When the rms current values of the squarewave and the sinewave machines are the same ($I_{\sin} = \sqrt{2/3}I_{sq}$), the ratio is found to be 1.15. This comparative number can also be found in [46].

It should be noted that, in order to obtain an equal peak magnet flux density in the airgap, the squarewave machine needs more magnet volume than the sinewave machine. Besides, since the flux per pole of the squarewave-machine will be higher than that in the sinewave machine, the axial length of each stator unit should be chosen larger. As a result, a squarewave machine will utilize a higher amount of steel and magnet volume. It can be concluded that this is not a very realistic way of comparison since the machines simply don't have the same dimensions.

Condition 2 *The fluxes per poles of the sinewave and the squarewave machines are the same*

This simply means that both machines have the same amount of magnets on their rotor poles. It is also assumed that the magnet pitches are equal for a fair comparison.

Similar comparisons in terms of the currents can be made by considering the peak value of the fundamental flux density of the sinewave machine ($\widehat{B}_{g1} = \frac{4}{\pi} B_{g0}$) and assuming the magnet pitch for both machines to be equal to the pole pitch .

1. *If they are compared in terms of peak currents:* $\dfrac{T_{sq}}{T_{\sin}} = 1.05.$

2. *If they are compared in terms of rms currents:* $\dfrac{T_{sq}}{T_{\sin}} = 0.906.$

Apparently there is actually no real torque density difference between these two machines. By considering the last comparison for the same amount of flux per pole and for the same rms currents a sinewave machine even seems to produce a higher torque density.

3.5.3 Efficiency comparison

For obtaining the same amount of torque out of the same machine (with the same amount of copper, stator iron and magnet) the squarewave machine requires a higher peak current implying higher copper losses. Assuming that both machines have the same amount of magnets on their rotors (where the airgap flux is the same), it was initially assumed that both machines have the same amount of core losses.

However, these machines also differ in terms of core losses. The reason is that the squarewave machine needs a larger magnet arc, i.e. generally 180° electrical, to guarantee a smooth torque. As a result, it has higher frequency harmonic flux components in the airgap. Therefore, the sinusoidal airgap flux distribution in the sinewave machine is preferred. It is achieved by reducing the harmonics. Parallel-magnetized magnet pieces can also be used as a solution. As a result of this effort, core losses may be reduced.

Nevertheless, at higher operating speeds the nonsinusoidal distribution of the windings in practice create higher order asynchronous space harmonic components which induce eddy currents in the rotor steel and magnets.

Based on the presented considerations it can be concluded that, the sinewave machine can be designed to be more efficient than the squarewave machines considering the effects of these loss components.

3.5.4 Comparison in terms of drive system requirements

For both machines a standard three-phase inverter with six transistor switches can be used, with different operating schemes. For an idealized squarewave machine, at any moment only two switches are active, as opposed to the PWM technique used in sinewave operation. This is the most important advantage of using the squarewave machine instead of the sinewave one. As a result, the switching losses are reduced

to one third of the sinewave operation. The other advantages of the squarewave machine is the requirement of a less expensive and simple position sensor, instead of an expensive and sensitive one. The control for squarewave operation is also simpler.

But the most significant problem related with the squarewave machine is the difficulty of obtaining a sufficient torque at high speeds due to commutation [49]. At higher speeds the difference between the supply voltage and the emf is getting smaller and due to this fact the current may not reach the required peak value, so that the torque decreases and the torque ripple increases. This problem may be solved by introducing some modifications into the drive circuit, but that increases both the losses and the price. So, at higher speeds a squarewave machine can not be considered as the advantageous one.

The phase inductance is very important due to its direct proportionality to the rise time of the current. As understood from Eq.3.46, the methods to decrease the inductance are decreasing the number of turns and increasing the airgap length. But either method has limitations, since decreasing the number of turns results in an increase of the supply current and increasing the airgap length results in an increase of the magnet length and price, and additionally, mechanical limitations can occur.

Another way to decrease the rise time of the current is a higher supply voltage. But especially for the applications where the voltage is supplied by a battery, a higher voltage may be unattainable. High di/dt may also be a problem for sinewave machines. Yet, sinewave machines don't need 120° electrical degrees continuous peak current. As a result, all of the design improvements mentioned above can be applied easier to the sinewave machines. A comparative study done by Friedrich and Kant, [50] presents the pros and cons of the two excitation schemes (sinusoidal and squarewave) also taking into account the limitations of the power supply.

3.5.5 Choice of excitation

The choice between the sinewave and the squarewave machine should be made according to the requirements of the application. The decision can not taken by solely considering the machine side; the converter and the controller parts should also be taken into account. The findings of this work can be summarized as follows.

1. There is no remarkable torque density difference between the sinewave and squarewave machines.

2. Sinewave machines can be designed to be more efficient than the squarewave machines.

3. Sinewave machines have the capability of producing a smooth torque at higher speeds as well.

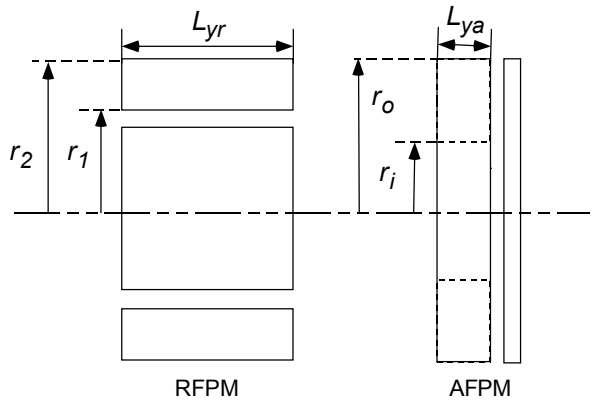

Figure 3.13: AFPM and RFPM machines.

4. The torque of squarewave machines decreases at high speed or with a low supply voltage because of the distortion of the phase current.

5. Sinewave machines need a high precision and expensive position transducer.

6. The control of sinewave machines is more complicated.

7. The converter switching losses are higher in sinewave operation.

It can be concluded that for high speed, high torque and low supply voltage applications sinewave machines offer more advantages.

3.6 Comparison of axial and radial-flux permanent-magnet machines

Having the sizing equations for the AFPM machine (sinewave machine with surface-mounted PM rotor) at hand, a general comparison in terms of torque density of axial and radial-flux machines can be made. Simplified structures of the two machines as shown in Fig.3.13, and the sizing equations for both machines as listed below will be the basis for the comparison.

The related sizing equations for AFPM machines can be summarized as follows.

Torque:

$$T_a = \frac{h}{4}\pi \widehat{B}_{g1} k_{w1} K_1 r_o^3 (1 - K_r^2)(1 + K_r) \sin(\beta)\,. \tag{3.49}$$

Electric loading:

$$K_{1a} = \frac{3\sqrt{2}I2N_{ph}}{D_{av}\pi}. \tag{3.50}$$

Stator yoke length:

$$L_{ya} = \frac{D_{av}\pi B_{g0}}{4pB_{\max}}c_\tau = \frac{r_o\left(1+K_r\right)\pi B_{g0}}{4pB_{\max}}c_\tau, \tag{3.51}$$

where c_τ is the ratio of the magnet pole pitch to the pole pitch.

The magnet length L_m and airgap length g can be expressed in terms of L_{ya} as

$$L_m + g = k_{mg}L_{ya}, \tag{3.52}$$

where k_{mg} is a proportion coefficient.

Motor volume (excluding end windings)

$$\nu_a = h\pi(r_o^2 - r_i^2)(L_{ya} + L_m + g) = h\pi r_o^2\left(1 - K_r^2\right)L_{ya}\left(1 + k_{mg}\right). \tag{3.53}$$

Torque density:

$$\zeta_a = \frac{T_a}{\nu_a} = \frac{\widehat{B}_{g1}k_{w1}K_{1a}r_o(1+K_r)}{4\left(1+k_{mg}\right)L_{ya}} = \frac{\widehat{B}_{g1}k_{w1}K_{1a}p}{\pi c_\tau(\frac{B_{g0}}{B_{\max}})\left(1+k_{mg}\right)}. \tag{3.54}$$

These equations can also be expressed for RFPM machines [43] considering the dimensions as shown in Fig.3.13.

Torque:

$$T_r = \pi\widehat{B}_{g1}k_{w1}K_1r_1^2L_{yr}\sin\left(\beta\right), \tag{3.55}$$

where L_{yr} is the stator yoke length.

Electric loading:

$$K_{1r} = \frac{3\sqrt{2}IN_{ph}}{r_1\pi}. \tag{3.56}$$

Stator yoke thickness:

$$r_2 - r_1 = \frac{r_1\pi B_{g0}c_\tau}{2pB_{\max}}, \tag{3.57}$$

which yields

$$r_2 = r_1(1 + \frac{\pi}{2p}c_\tau\frac{B_{g0}}{B_{\max}}), \tag{3.58}$$

Motor volume (excluding end windings):

$$\nu_r = \pi r_2^2 L_{yr}, \tag{3.59}$$

Torque density:

$$\zeta_r = \frac{T_r}{\nu r} = \frac{\widehat{B}_{g1} k_{w1} K_{1r} r_1^2}{r_2^2} = \frac{\widehat{B}_{g1} k_{w1} K_{1r}}{(1 + \frac{\pi}{2p} c_\tau \frac{B_{g0}}{B_{\max}})^2}. \tag{3.60}$$

Assuming that both machines have the same magnet pitch to pole pitch ratio, the same airgap flux density and the maximum allowable flux density is the same in the stators of both machines and that they also have simple airgap winding structures, the ratio of the torque densities of the axial and radial-flux machines becomes

$$\frac{\zeta_a}{\zeta_r} = \frac{p}{(1 + k_{mg})\, \pi c_\tau (\frac{B_{g0}}{B_{\max}})} (1 + \frac{\pi}{2p} c_\tau \frac{B_{g0}}{B_{\max}})^2. \tag{3.61}$$

As seen from Eq.3.61, there are three variables which may affect this ratio: the number of pole pairs p, the ratio of the airgap flux to maximum allowable flux density in the stator $B_{g0}/B_{\max}$, and the ratio of the magnet pitch to pole pitch c_τ. Since the last two variables are more or less in well-defined ranges, the torque density ratio of the two machines can be investigated based on the pole pair numbers. For the coefficient k_{mg}, a value of 0.2 is taken, which can be a bit higher or lower according to the design. The variation of the torque density ratio of both machines with respect to the number of pole pairs at various c_τ and $B_{g0}/B_{\max}$ are shown in Fig.3.14. As it is seen from this figure, the ratio of the torque densities of the axial and radial-flux machines increases with the number of poles. Considering the fact that, with the increased number of poles, the flux per pole of the machine decreases, consequently the required axial length of the stator core decreases. Hence, the torque density advantage of AFPM machines becomes more apparent in a design with a high number of poles. The choice of magnet span to pole pitch ratio, and the flux densities in the airgap and in the core also affect the torque density differences between the two machines. A comparative study presented in [51] shows the torque density differences between the two machine structures for small power applications and also includes the dimensional details of the machines. The same study also compares various types of AFPM machines in terms of torque density.

3.7 Towards an initial design

Amongst the many alternatives outlined in section 3.2.3, the double-stator/internal rotor type AFPM machine was considered to be the best choice. The main reason

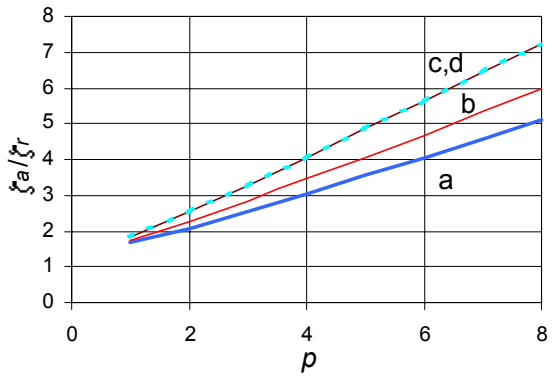

Figure 3.14: Torque density ratio with respect to number of pole pairs for cases (a) $c_\tau = 1$, $(B_{go}/B_{\max}) = 0.5$, (b) $c_\tau = 0.83$, $(B_{go}/B_{\max}) = 0.5$, (c) $c_\tau = 0.667$, $(B_{go}/B_{\max}) = 0.5$, (d) $c_\tau = 1$, $(B_{go}/B_{\max}) = 0.33$.

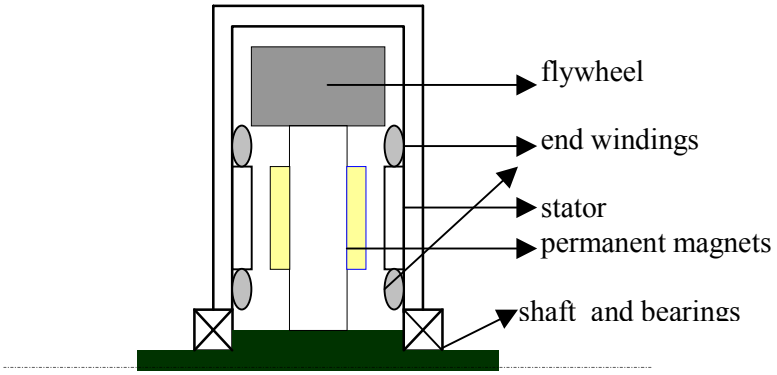

Figure 3.15: AFPM machine and the flywheel arrangement.

underlying this conclusion is the fact that the machine is to be mounted inside the flywheel with the rotor as an integral part of the flywheel. The resulting compact machine and the flywheel arrangement is sketched in Fig.3.15. The permanent magnets are placed on the rotor and the stators are fixed to the housing.

Since the inside diameter of the flywheel is fixed, due to the space limitation in the car, the outside diameter of the stators can not be chosen larger than 190 mm taking the end turns into account. The most important requirement of the application is the high efficiency in both load and no-load conditions that will improve the total drive system efficiency, especially in inner city operation.

On the other hand, slotted stators and surface-mounted permanent magnets are proposed as basic design choices. The surface-mounted permanent magnets are preferred mainly due to the constructional convenience. The slotted stators are advan-

tageous in terms of robustness. It is also possible to reach higher airgap flux density levels using a relatively smaller amount of permanent magnets compared with a slotless design. Furthermore, at higher speeds eddy current losses in the conductors are not as high as in the case of airgap windings.

By increasing the number of poles, the axial length of the stator and the length of the end windings and consequently the copper losses can be reduced, and the efficiency of the machine, especially at lower speed levels, may increase. The constraint on the number of poles is the frequency. Both frequency dependent loss components in the machine and the converter losses increase with the frequency. Additionally, the cost of the magnets increases. Therefore, the final decision was made in favor of the 4-pole machine with the frequency limited to 533 Hz [52]. The basic 4-pole AFPM machine with slotted stators and surface-mounted permanent magnets is shown in Fig.3.16. Having determined these basic properties of the machine, other design aspects are discussed in the following chapter.

3.8 Conclusions

The AFPM concept covers a broad range of various structures and towards an initial design, the first natural step to be taken is an initial choice of the basic structure. This choice requires a comparative analysis and for this purpose basic sizing equations are derived. The fundamental issues of comparison in this chapter are related with sizing, magnetic design and the type of excitation. Based on the derived equations, a general comparison between axial and radial-flux permanent-magnet machines is also provided. The results of this comparative study, together with the requirement of embedding of the rotor within the flywheel, rationalize the basic choice of a sinusoidal current excited AFPM machine that incorporates a single rotor structure on which the magnets are attached.

The following chapter will contain an analysis mainly with regard to the number

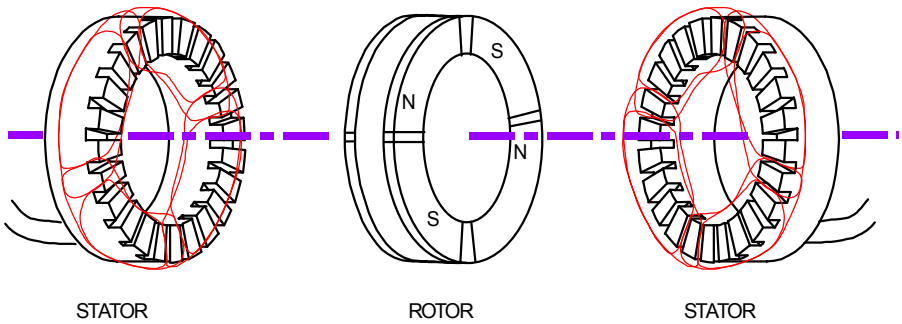

Figure 3.16: Proposed machine structure.

of stator slots, the magnet span, winding configuration, skewing and the stator offset. A discussion on the design procedure and the presentation of machine data follow the analyses.

Chapter 4

Design variations

4.1 Introduction

The previous chapter is devoted to the analytical derivation of the basic equations, such as torque, emf, power for the AFPM machine and a comparative discussion on the various types of AFPM machines. The final choice based on this discussion incorporates a single rotor structure on which the magnets are placed; this is mainly justified by the flywheel-electrical machine arrangement. The magnets are located in between two slotted stator disks, each having three-phase windings excited with sinusoidal currents.

This chapter extends the previous discussion to the design of the stators with slots. The advantages and disadvantages of slots will be outlined in comparison with the slotless construction. The derivation of the armature reaction reactance which is a very critical parameter in synchronous machine design, is included. The leakage reactances which are the components of the synchronous reactance are also derived.

The number of slots, the magnet span, and the winding configuration are the most important design parameters. In permanent-magnet synchronous machines excited by sinusoidal currents, the better the back-emf waveform approximates a perfect sinus, the less ripple the output torque exhibits. Therefore, the performance of the machine, especially emf and torque waveforms is, to a larger extent, dependent on these choices. Hence, the determination of these parameters is crucial.

With a computer program especially developed for the design and the analysis of the AFPM machine, a wide array of alternative structures are analyzed, back-emf and torque waveforms (torque v.s. position) are obtained and the results of this comparative study (in terms of harmonic contents, torque variations and losses) are presented in the following sections. The variables which are considered in this work, are the number of stator slots, the magnet span, the coil pitch, skewing and the stator offset.

At the end of the chapter, which finalizes with the machine data, the design

procedure is explained in detail.

4.2 Slotted stator design

Before the design details related with the slots are given, slotted and slotless arrangements should be compared.

The advantages of stator slots in comparison with airgap windings are

1. The required length of the magnet is smaller for the slotted structure. In the slotless structure, the airgap windings increase the effective airgap length, which causes a reduction in the airgap magnetic loading (airgap flux density).

2. With airgap windings, the rotor magnets induce eddy currents in the conductors, which is another source of loss. With slots, the windings are more protected.

3. In the slotted stator structure magnets are better protected against the high temperature caused by the stator currents.

4. With a slotted structure, the inductance of the windings is much higher. So, it can be easier to manipulate the required per unit synchronous reactance with slots since there is more freedom with respect to the airgap length. In the slotless structure the default space for the windings and the mechanical clearance should be considered as a minimum effective length.

5. Windings in slots present a more robust structure.

Advantages of the airgap windings in comparison with the slotted structure are:

1. Slots produce cogging torque which increases the vibration and the noise.

2. Manufacturing of the slotted disk stator can be more tedious than that of the slotless stator because of the specific shapes of the lamination segments.

3. By considering the amount of space occupied by the slots, the axial length of the stator will be much larger than that of the slotless structure.

4. The saturation of the teeth is a problem in the slotted structure.

The benefits of the slots apparently outweigh the disadvantages for the application especially since the magnet temperature and the robustness are major concerns.

The semi-closed rectangular slot is shown in Fig.4.1 with related dimensions. Due to the disk structure of the stator, the width of the tooth increases with increasing (from inside to the outside) diameter. Apparently, the tooth width is minimum

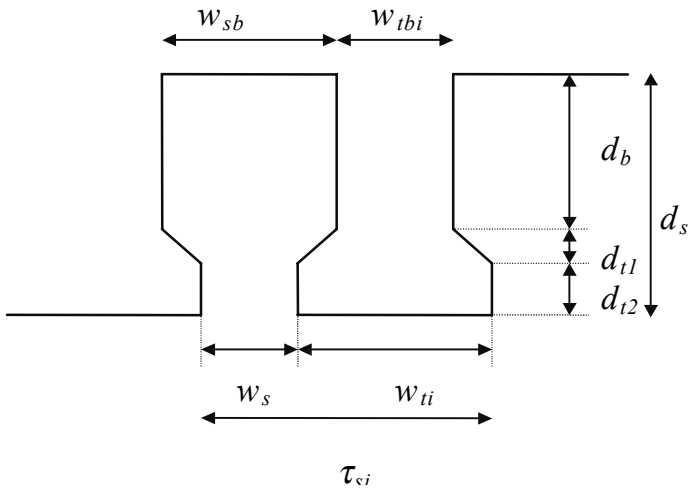

Figure 4.1: Slot dimensions at the inner diameter of the stator axial cross-section.

at the inside diameter of the stator disk. For this reason, the minimum necessary dimensions of the slot should be determined at the inside diameter of the stator. In Fig.4.1, τ_{si} is the slot pitch, w_{tbi} and w_{ti} are the tooth bottom and the tooth top widths at the inside diameter of the stator respectively, which is indicated by the subscript "i". Subscripts "i", "a" and "o" will be used to describe these parameters respectively at the inside, the average and the outside diameter.

The number of conductors per slot n_{cs}, the phase current I, the maximum tolerable slot current density $J_{s\,\max}$, which is limited by the cooling possibilities, the slot filling or the conductor packing factor k_{cp}, and the saturation of the teeth are the most important factors determining the dimensions of the slot. Assuming that none of the slots are left empty and the phases do not share the same slots, the dimensions are determined as follows.

Following the decision made on the "number of slots per pole per phase" n_{spp}, which depends on many other factors such as harmonics, number of poles, cogging torque etc., the number of conductors per slot can be calculated as

$$n_{cs} = \frac{N_{ph}}{p n_{spp}}, \tag{4.1}$$

where N_{ph} is the number of series turns per phase per stator, and p is the number of pole pairs. Since the number of conductors per slot can not be a fractional number, the number of series turns per phase N_{ph} should be chosen as an integer multiple of the number of pole pairs times the number of slots per pole per phase, which is an another constraint in the calculations.

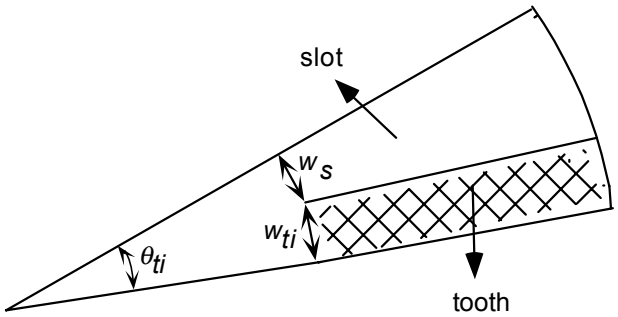

Figure 4.2: A slot pitch.

Accordingly, the total slot current I_s is expressed as

$$I_s = n_{cs} I, \tag{4.2}$$

where I is the rms value of the rated phase current. The area of the slot A_s can be constrained as

$$A_s \geq \frac{I_s}{J_{s\,\max} k_{cp}}, \tag{4.3}$$

where the conductor packing factor k_{cp} takes into account the physical space occupied by the insulation, the space between the conductors, and the slot liners (insulation around the stator periphery) in the total slot area. Hence, the conductor area calculated for the rated current value and for the minimum possible slot area becomes

$$A_c = \frac{I}{J_{s\,\max}} = \frac{A_s k_{cp}}{n_{cs}} = \frac{w_{sb} d_b k_{cp}}{n_{cs}}. \tag{4.4}$$

As it is indicated by the radial cross-section of the slot geometry shown in Fig.4.2, the proposed tooth dimensions do not change along the stator radially. Since the saturation of the teeth has a negative influence on the performance, first the minimum required tooth bottom width at the inner diameter of the stator should be calculated by considering the maximum tolerable flux density in the teeth $B_{t\,\max}$.

The slot pitch at the inner diameter of the stator is

$$\tau_{si} = \frac{D_i \pi}{2 p n_{spp} m} = w_{sb} + w_{tbi}, \tag{4.5}$$

where m is the number of phases. Considering the fact that the total airgap flux per pole will flow through the teeth (the pole area is reduced proportional to the ratio of

the tooth bottom width and the slot pitch), the minimum tooth bottom width can be expressed as

$$w_{tbi} = \tau_{si} \frac{B_{go}}{B_{t\,\max}} \tag{4.6}$$

Having calculated the tooth bottom width and the slot bottom width, the slot depth d_b can be calculated using Eq.4.4 and Eq.4.5.

The slot-top dimensions w_s, d_{t1} and d_{t2} should be properly selected by considering the fact that with decreasing slot-top width the amount of slot leakage increases and by increasing it, the amount of cogging torque increases. So the best compromise can be determined by using FE analysis after preliminary analytical calculations. Besides, d_{t1} and d_{t2}, which contribute to the total slot depth, should be kept as small as possible in order not to increase the axial length of the stator disks.

Finally, the important aspects, which should be kept in mind while designing the slots, can be summarized as follows:

1. If the current density is too high, the copper losses will increase and cooling problems will occur.

2. If the current density is too low, the amount of steel used for the teeth (so the core losses) and the axial length of the stator disks will increase.

3. If the slot is too deep and too narrow, slot leakage will increase.

4. If the slot width is too large, the teeth can saturate.

5. If the slot top is too open, cogging torque will increase.

6. If the slot top is too closed, the tooth-top slot leakage will increase.

4.3 Winding factors

Winding factors take into account the reduction of the fundamental and other harmonic components due to the actual distribution of the windings [43] as

$$E_n = \frac{\sqrt{2}}{2} \widehat{B}_{gn} \omega_m k_{wn} N_{ph} D_{av} L_i, \tag{4.7}$$

where E_n is the rms value of the n^{th} order emf harmonic component. For instance, the coils can be deliberately underpitched or overpitched to reduce certain harmonics, or the coils of the same phase are distributed (where the vectorial sum is necessary),

or skewing of the windings or magnets can be facilitated to reduce the cogging torque [43]. The winding factor k_{wn} has three components

$$k_{wn} = k_{dn} k_{pn} k_{sn}, \tag{4.8}$$

of which the equations are described below.

Distribution of the coils of a phase is very advantageous, but it means that the mmf, and consequently the induced voltage gets smaller when compared with concentrated windings. This reduction is represented by the distribution or the spread factor[43]

$$k_{dn} = \frac{\sin\left(n\frac{n_{spp}\theta_s}{2}\right)}{n_{spp}\sin\left(n\frac{\theta_s}{2}\right)}, \tag{4.9}$$

where n is the number of the harmonic component, θ_s is the slot pitch in electrical degrees if it is an integral slot winding, and n_{spp} is the number of slots per pole per phase.

The windings of the coils can be made under or overpitched to eliminate some of the higher harmonic components, but the fundamental component also reduces. The reduction is represented by the pitch factor

$$k_{pn} = \frac{\mathrm{n}^{th} \text{ mean flux for the pitched coil}}{\mathrm{n}^{th} \text{ mean flux for the full pitched coil}} = \sin n\frac{\theta_c}{2}, \tag{4.10}$$

where θ_c is the coil pitch in electrical degrees where the full pitch equals 180°.

Skewing of the windings or the magnets can be necessary to reduce the cogging torque, where the reduction of the induced voltage can be represented by the skew factor

$$k_{sn} = \frac{\mathrm{n}^{th} \text{ mean flux of the skewed design}}{\mathrm{n}^{th} \text{ mean flux of the unskewed design}} = \frac{\sin n\frac{\gamma}{2}}{n\frac{\gamma}{2}}, \tag{4.11}$$

where γ is the electrical angle of the skew. For AFPM machines however, the effect of changing the tooth width with the diameter of the disk should be taken into account when the magnets are skewed.

4.4 Synchronous reactance

If the magnets are placed on the rotor surface, the machine is a non-salient-pole type, and the synchronous reactance is given as

$$X_s = X_a + X_l, \tag{4.12}$$

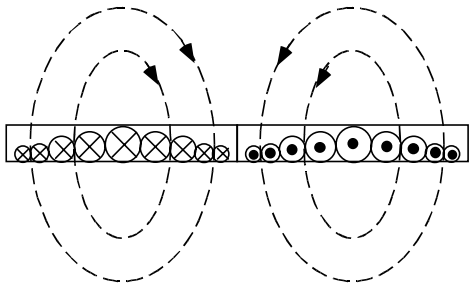

Figure 4.3: Sinwave windings.

where X_a is the armature reaction reactance and X_l is the per-phase leakage reactance which consists of slot, end turn, and differential leakage reactances. For rotor constructions with interior magnets, $d-axis$ and $q-axis$ armature reaction reactances are different and can be calculated using form factors [33].

4.4.1 Armature reaction reactance

In order to calculate the armature reaction reactance, a pole pair with sinusoidal winding distribution (as seen in Fig.4.3) is considered. The sinusoidal winding distribution represented in Eq.3.6 sets up a rotating flux density wave as

$$\widehat{B}_a \cos(p\theta - \omega t), \tag{4.13}$$

where the peak flux density $\widehat{B}_a$ can be found from the analysis of the magnetic circuit of the AFPM machine. Here the subscript a denotes that the airgap flux density is generated by the armature current. By considering only a single pole pair as shown in Fig.4.3, the mmf drop which corresponds to the contribution of a single stator disk can be found as

$$F_g = \frac{3}{2} I\sqrt{2}\frac{N_s}{2}\int_0^{\pi/p} \sin p\theta d\theta = \frac{3}{2} I\sqrt{2}\frac{N_s}{p}. \tag{4.14}$$

Now, considering the case of a double stator/single rotor with surface-mounted permanent magnets, the reluctance corresponding to the mmf drop can be determined by using the magnetic circuit representation shown in Fig.4.4. It should be noted that the airgap flux density in this structure is affected by two airgaps and two flux sources unlike the case of radial-flux machines.

From its equivalent magnetic circuit the reluctance can be calculated as

$$\Re = 2\Re_g + \Re_m = \frac{2g}{\mu_0 A_g} + \frac{L_m}{\mu_0 \mu_r A_g} = \frac{2g + \dfrac{L_m}{\mu_r}}{\mu_0 A_g} = \frac{g\prime}{\mu_0 A_g}, \tag{4.15}$$

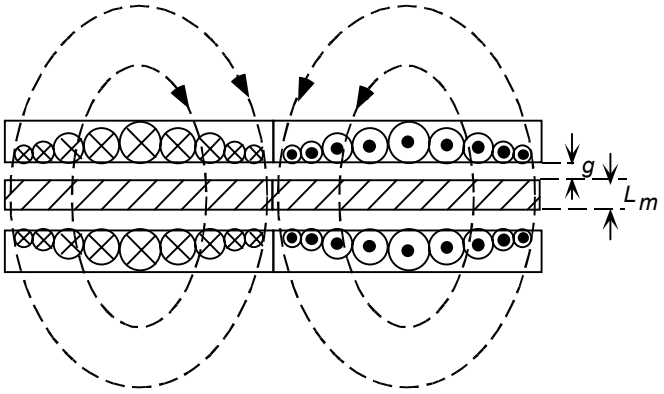

(a) Double-airgap structure.

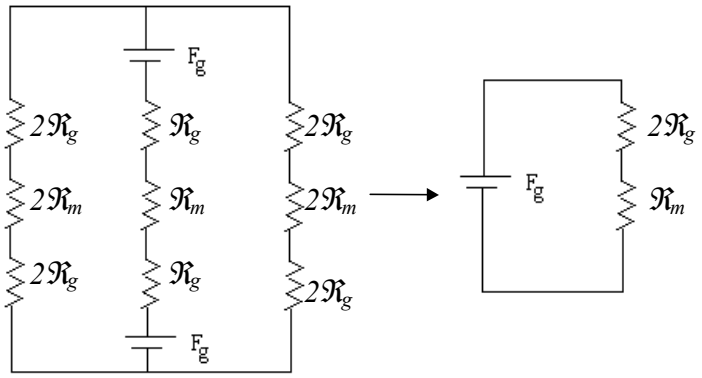

(b) Magnetic circuit.

Figure 4.4: Double-airgap structure and its equivalent magnetic circuit.

where $\Re_g$, $\Re_m$ and A_g are the airgap and the magnet reluctances and the airgap cross-sectional area, respectively. Here, the magnet is not represented as a flux source since it does not contribute to the airgap self inductance. In Eq.4.15, the effective length of the airgap corresponding to the given structure is represented as

$$g\prime = 2g + \frac{L_m}{\mu_r}. \tag{4.16}$$

The mmf and the reluctance formulas for the magnetic circuit are

$$F_g = \phi_a \Re = \widehat{B}_a A_g \Re, \tag{4.17}$$

where F_g is the mmf, ϕ_a is the armature reaction flux per pole, and $\widehat{B}_a$ is the armature reaction flux density in the airgap. Substituting Eq.4.17 into Eq.4.14 yields

$$\widehat{B}_a = \frac{\mu_0}{g'} \frac{3}{2} I \sqrt{2} \frac{N_s}{p}. \tag{4.18}$$

The rotating flux wave generates voltages in all three phases, and over the reactance there would be a voltage drop $X_a I$. Relying on this fact, the armature reaction reactance per stator unit can be calculated by subsequently substituting the peak flux density of Eq.4.18 into Eq.3.28, using Eq.3.13, dividing by I and substituting ω_m with $2\pi f/p$ as

$$X_a = \frac{12 f \mu_0 L_i D_{av} k_{w1}^2 N_{ph}^2}{p^2 g\prime} = \frac{24 f \mu_0 L_i \tau_p k_{w1}^2 N_{ph}^2}{\pi p g\prime}, \tag{4.19}$$

where the pole pitch τ_p is equal to $D_{av}\pi/2p$.

Substituting Eq.4.16, the armature reaction reactance per stator unit reduces to

$$X_a = \frac{24 f \mu_0 L_i \tau_p k_{w1}^2 N_{ph}^2}{\pi p \left(2g + \frac{L_m}{\mu_r}\right)}. \tag{4.20}$$

4.4.2 Slot leakage reactance

The slot leakage flux paths are shown in Fig.5.19. For the determination of the slot leakage inductance only the flux which is not crossing the airgap but circulating around the conductors along the slot is considered. For the semi-closed rectangular slot as shown in Fig.4.1, three different regions are contributing to the slot leakage inductance:

I The rectangular part of the slot uniformly filled with conductors. The area of this region is $d_b \times w_{sb}$.

II The area between the conductors and the slot top ($d_{t1} \times \frac{w_s + w_{sb}}{2}$).

III The rectangular slot-top region ($d_{t2} \times w_s$).

The magnetic field intensity $H(y)$ along the slot depth (see Fig.5.19) can be calculated using

$$\oint Hdl = n_{cs}i. \tag{4.21}$$

Since there are uniformly distributed conductors in the rectangular area I, for this region the magnetic field intensity is a linear function of the slot depth y, which can be written by assuming that the steel has infinite permeability as

$$H(y) = \frac{n_{cs}i}{w_{sb}} \left(\frac{y}{d_b}\right), \tag{4.22}$$

where the expression (y/d_b) takes into account the fraction of the total slot ampere-conductors at distant y along the slot depth. Knowing the magnetic field intensity, the slot leakage inductance for region I can be calculated using the stored magnetic energy as

$$\frac{1}{2}L_{sl-I}i^2 = \int\limits_{vol} \frac{1}{2}\mu_0 H^2(y)dV. \tag{4.23}$$

By inserting Eq.4.22 into Eq.4.23 and introducing the incremental volume as

$$dV = L_i w_{sb} dy, \tag{4.24}$$

one yields

$$\frac{1}{2}L_{sl-I}i^2 = \int\limits_0^{d_b} \frac{1}{2}\mu_0 \frac{n_{cs}^2 i^2}{w_{sb}} \left(\frac{y^2}{d_b^2}\right) L_i dy, \tag{4.25}$$

which results in

$$L_{sl-I} = \mu_0 n_{cs}^2 L_i \frac{d_b}{3w_{sb}}. \tag{4.26}$$

In the regions II and III, the magnetic field intensity equation can be written independently of y, since the total number of conductors seen from these regions is n_{cs}. By solving the integral equations as in the case of region I, the two other slot leakage inductance components can be obtained as

$$L_{sl-II} = \mu_0 n_{cs}^2 L_i (\frac{2d_{t1}}{w_s + w_{sb}}), \tag{4.27}$$

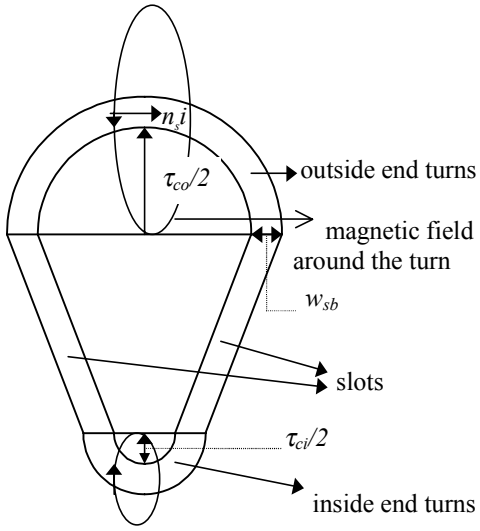

Figure 4.5: End turns over a folded coil pitch of the stator disk.

$$L_{sl-III} = \mu_0 n_{cs}^2 L_i (\frac{d_{t2}}{w_s}). \tag{4.28}$$

The sum of these inductance components is the total slot leakage inductance

$$L_{sl} = \mu_0 n_{cs}^2 L_i (\frac{d_b}{3w_{sb}} + \frac{2d_{t1}}{w_s + w_{sb}} + \frac{d_{t2}}{w_s}), \tag{4.29}$$

where the terms in the parenthesis are the permeance coefficients of the slot. Eq.4.29 is the leakage inductance corresponding to a single slot. For determining the total slot leakage reactance per phase, this equation should be multiplied with the number of slots per phase. In order to obtain a more general equation, the number of conductors per slot n_{cs} in Eq.4.29 is defined in terms of the number of turns per phase, N_{ph} using Eq.4.1, and the resultant slot leakage reactance per phase per stator disk is found as

$$X_{sl} = 4\pi f \mu_0 \frac{N_{ph}^2}{p n_{spp}} L_i (\frac{d_b}{3w_{sb}} + \frac{2d_{t1}}{w_s + w_{sb}} + \frac{d_{t2}}{w_s}). \tag{4.30}$$

4.4.3 End-turn leakage reactance

The analytical calculation of the end-turn leakage inductance can only be a rough approximation since neither the exact length of the end turns nor the distribution of the field around it, is exactly known.

Initially, the length of the end turns should be approximated. Fig.4.5 shows the folded forms of two slots and the coil pitch in a radial cross-section of the disk. τ_{ci}

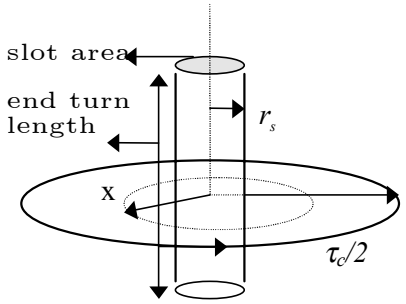

Figure 4.6: Cylindrical representation of an end turn.

and τ_{co} are the coil pitches at the inside and the outside diameters of the stator disk. It is assumed that the end turns are half circles with diameters τ_{ci} and τ_{co}. So the lengths of the outside and inside end turns can be calculated as

$$\ell_{oend} = \frac{\tau_{co}\pi}{2}, \tag{4.31}$$

$$\ell_{iend} = \frac{\tau_{ci}\pi}{2}. \tag{4.32}$$

The total length of the end turns for a slot pair is

$$\ell_{end} = (\tau_{co} + \tau_{ci})\,\frac{\pi}{2}. \tag{4.33}$$

The second assumption is that the slot conductors form a circular area equal to the area of the slot, which implies that the end turns can be considered as a cylindrical cable carrying the current $n_{cs}i$. The magnetic field is distributed around the end turns within the radius of half the coil pitch as shown in Fig.4.5 and Fig.4.6.

At radius x the magnetic field intensity can be calculated using Eq.4.21 as

$$H(x) = \frac{n_{cs}i}{2\pi x}, \tag{4.34}$$

and the magnetic flux density is

$$B(x) = \mu_0 \frac{n_{cs}i}{2\pi x}. \tag{4.35}$$

By integrating the flux density along the surface, the total flux can be found as

$$\phi = \int_{r_s}^{\tau_c/2} \mu_0 \frac{n_{cs}i}{2\pi x}\frac{\tau_c\pi}{2}dx = \frac{\mu_0 n_{cs} i \tau_c}{4} \ln\left(\frac{\tau_c}{2r_s}\right), \tag{4.36}$$

where r_s can be found by representing the rectangular conductor area as an equivalent circular area as

$$A_s = w_{sb}d_b = r_s^2\pi \Longrightarrow r_s = \sqrt{\frac{w_{sb}d_b}{\pi}}, \tag{4.37}$$

and the inductance of the single end-turn coil becomes

$$L_{end} = \frac{n_{cs}\phi}{i} = \frac{\mu_0 n_{cs}^2 \tau_c}{4} \ln\left(\frac{\tau_c}{2r_s}\right). \tag{4.38}$$

The total end-turn leakage inductance for a slot pair is the sum of the contributions of the upper and the lower end turns. For obtaining the total end-turn leakage inductance of the phase winding, it should be multiplied by the number of slot pairs per phase. Finally, the end-turn leakage reactance per phase per stator is

$$X_{end} = \frac{\pi f \mu_0 N_{ph}^2}{2pn_{spp}} \left(\tau_{co} \ln(\frac{\tau_{co}}{2r_s}) + \tau_{ci} \ln(\frac{\tau_{ci}}{2r_s})\right). \tag{4.39}$$

4.4.4 Differential leakage reactance

The differential leakage reactance takes into account the contributions of the higher order harmonics. The formula can be derived directly from the armature reaction reactance equation. Since the armature reaction flux density is not perfectly sinusoidal in reality, the armature reaction flux per pole can be expressed for each harmonic component. The fundamental component is

$$\phi_{a1} = \frac{2}{\pi} L_i \tau_p \widehat{B}_{a1}. \tag{4.40}$$

Since the pole pitch length of the higher harmonic component is the actual pole pitch divided by the harmonic number n, the harmonic components of the flux per pole can be deduced as

$$\phi_{an} = \frac{2}{\pi} \frac{L_i \tau_p}{n} \widehat{B}_{an}, \tag{4.41}$$

where in reference to Eq.4.18

$$\widehat{B}_{an} = \frac{\mu_0}{g'} \frac{3}{\pi} I\sqrt{2} \frac{2k_{wn}N_{ph}}{np}, \tag{4.42}$$

where the n^{th} order harmonic has n times p pole pairs. In the same manner as with the armature reaction reactance calculation, the harmonic reactances can be found as

$$X_{an} = \frac{24 f \mu_0 \tau_p L_i k_{wn}^2 N_{ph}^2}{\pi n^2 p g\prime}, \tag{4.43}$$

where

$$X_{an} = X_{a1}\frac{k_{wn}^2}{k_{w1}^2 n^2}. \tag{4.44}$$

The differential leakage reactance is the sum of all harmonic leakage reactances as

$$X_{dif} = \frac{X_a}{k_{w1}^2}\sum_{n=2}^{\infty}\frac{k_{wn}^2}{n^2}. \tag{4.45}$$

Due to the square of the harmonic number in the denominator, the differential leakage reactance will be a small part of the armature reaction reactance.

4.5 Magnet span

The magnet span θ_m is dependent on the harmonic components of the magnet flux density waveform and consequently the emf waveform. Optimum magnet spans are different for various number of stator slots and winding configurations. Hence, it should be optimized with the given number of slots and winding configuration.

The surface-mounted permanent magnet and the approximate flux density waveform is shown in Fig.3.11. Since the flux density distribution is a symmetric function, the sine-terms in the Fourier expansion reduce to zero. The magnet flux density waveform can be written in terms of a Fourier series by

$$B_m(\theta) = \sum_{n=1}^{\infty}\widehat{B}_n \cos n\theta, \tag{4.46}$$

where the general form for each harmonic component can be written as

$$\widehat{B}_n = \frac{B_{g0}}{n\pi}\left\{\sin(n\frac{\theta_m}{2}) - \sin n(\pi + \frac{\theta_m}{2}) + \sin n(\pi - \frac{\theta_m}{2}) - \sin n(2\pi - \frac{\theta_m}{2})\right\}. \tag{4.47}$$

It is obvious from the previous equation that the magnitude of the flux density harmonic components is directly dependent on the magnet span. The minimization of these higher order harmonic components is essential considering the fact that all the flux components are rotating asynchronously with respect to the rotor and therefore cause losses in the stator. Other effects of the harmonic fluxes are investigated in the following sections.

number of slots-n_s	number of slots per pole per phase-n_{spp}
9	0.75
12	1
15	1.25
18	1.5
21	1.75
24	2

Table 4.1: Possible slot numbers and the corresponding number of slots per pole per phase.

4.6 EMF waveforms

The generated no-load emf waveform is represented as

$$e(\theta) = \sum_{n=1}^{\infty} \widehat{E}_n \sin(n\theta), \tag{4.48}$$

where

$$\widehat{E}_n = \widehat{B}_{gn} \omega_m k_{wn} N_{ph} D_{av} L_i. \tag{4.49}$$

The magnitude of the n^{th} harmonic no-load emf depends upon two variables: the nth order harmonic component of the magnet flux and the n^{th} order harmonic component of the winding factor k_{wn}.

4.7 Number of stator slots

In section 3.7, the choice for a 4-pole structure was justified. For a 4-pole AFPM machine, 9, 12, 15, 18, 21, and 24, which are multiples of 3 for phase symmetry, are considered as possible numbers of stator slots. 36 slots could also be a good alternative, in order to avoid extra complications in manufacturing, 24 was chosen as the maximum possible slot number. For a 3-phase and 4-pole machine, the number of slots per pole per phase n_{spp} values for various n_s (9, 12, 15, 18, 21, 24) are shown in Table 4.1.

As it is seen from Table 4.1, the number of slots per pole per phase corresponding to 9, 15, 18 and 21 slots are fractional numbers. These fractional-slot stators are not commonly used. Probably some of them have never been constructed, but are still worth considering because of their reduced harmonic contents and reduced pulsating and cogging torque [53]. It should be noted that the winding arrangement of the fractional slot stators are not as straight forward as in the case of integral-slot stators, and there can be more than one way for the designer to place the coils optimally [43].

4.8 Maximum coil span-short pitching

The maximum coil span is simply the next lower integer number obtained from the division of the number of slots by the number of poles. For example, for a 24 slot structure 6 is the maximum coil span, while for 15 slots it is 3.

However, the maximum coil span for a given structure is not the only alternative, a lower integer number can be chosen, which is called short-pitching. For a 24 slot structure, if 5 slots are chosen as a coil span, it is 5/6 full-pitched (θ_c is 150° electrical). One of the reasons of short pitching is reducing some of the harmonic components in the emf waveform. For example, in the case of 2/3 (or 4/6) full-pitched structure (θ_c is 120° electrical), it is obvious and also well-known that the pitch factor will be zero for the 3^{rd} harmonic component. It is not actually useful considering the fact that the third order harmonic component disappears in the line-emf voltage when the phases are star connected.

The fractional-slot structures are already short-pitched in their nature. For a 15 slot structure the number of slots per pole is 3.75 and the possible alternatives for coil pitches are 3 (144°) and 2 slots (96°). It will certainly reduce some of the harmonic components, which will be shown in the following sections.

The other advantage of short pitching is that it reduces the length of the end windings and consequently the copper losses. Yet, it is not as linear as it looks. For example, a 5/6 full-pitched winding doesn't necessarily imply that the copper losses will be reduced by a factor of 1/6 compared with those of a full-pitched winding. The reason is the fact that the fundamental emf value also decreases with the first harmonic pitching factor (around 0.96), so the current necessary to yield the same output torque increases.

4.9 Distribution of the coils

The determination of the coil arrangement with fractional-slot windings is not as straightforward as in the case of integral-slot windings. The coils can be seen as groups or sections on the circumference (particular repetitive patterns). For example, the number of coils per group is 2 in the case of 24 slots (equal to the number of slots per pole per phase), while for 15 slot stators it is 5. Because there are no other patterns except the number of coils per phase (15/3). For a 18 slot stator the coils per group is 3, since the number of coils per section can also be divided into 2 more sections. Examining the winding schemes, this fact can be observed better.

4.10 Winding configurations

The winding configurations for integral-slot windings are rather obvious, so that only the configurations for fractional-slot structures will be discussed. A method described in [43] is used to place the coils. The coil arrangements for some particular coil pitches (indicated below) are shown in Fig.4.7 for 9, 15, 18 and 21 slot stators. Here, capital letters A, B, and C represent the phases, and signs "+" and "-" represent the direction of the windings.

A	-C	-A	C	-B	A	B	-A	-B
A	-C	B	C	-B	-C	B	-A	C

a. 9-slot double-layer stator winding (coil span=2)

A	A	B	-A	-A	C	-B	A	A	-C	B	-A	-A	-B	-B
A	-C	-C	B	-A	C	C	-B	-C	-C	B	B	C	C	-B

b. 15-slot double-layer stator winding (coil span=3)

A	A	-C	B	B	-A	C	-B	-B	A	A	-C	B	-A	-A	C	-B	-B
A	-C	-C	B	-A	-A	C	C	-B	A	-C	-C	B	B	-A	C	C	-B

c. 18-slot double-layer stator winding (coil span=4)

C	-B	A	A	-C	-C	B	B	-A	C	C	-B	-B	A	A	-C	B	B	-A	-A	C
-B	-B	A	A	-C	-C	B	-A	-A	C	C	-B	-B	A	-C	-C	B	B	-A	-A	C

d. 21-slot double-layer stator winding (coil span=5)

Figure 4.7: Winding constructions for 9, 15, 18, and 21-slot stators.

The number of alternatives for the winding configuration can also be increased by short pitching the fractional-slot structures. The 15 slot stator was designed with a 3 slot coil span, but 2 is also an alternative and can be reconfigured easily. For the 18 slot structure 3, and for the 21 slot structure both 3 and 4 slot coil span can be considered.

Considering the 13 stator configurations presented in Table 4.2, and the possible magnet spans (a number between 120° and 180° electrical), which are integer values, there exist 60×13 alternatives. These possibilities will be investigated in terms of losses, harmonic contents of their emf waveforms, and pulsating torque components.

configuration number	number of slots	coil-pitch/pole-pitch
1	9	2/2.25
2	12	2/3
3	12	full-pitch
4	15	2/3.75
5	15	3/3.75
6	18	3/4.5
7	18	4/4.5
8	21	3/5.25
9	21	4/5.25
10	21	5/5.25
11	24	4/6
12	24	5/6
13	24	full-pitch

Table 4.2: Possible winding configurations.

4.11 Comparison of winding schemes in terms of machine efficiency

Copper losses and efficiency values are computed and compared for the designs with the winding structures summarized in Table 4.2. It should be noted that the line-current values for these structures are not kept the same, because short-pitching reduces the fundamental emf-component and, consequently, the current must be increased to obtain the same amount of torque as mentioned before.

It is found that the efficiency values don't differ considerably. But, the differences are more pronounced at lower speeds due to the copper losses. The worst structure in terms of copper losses is found to be the 24 slot full-pitched one, and the best is the 15 slot, 2/3.75 short-pitched structure.

4.12 Percentage harmonic contents of the emf waveforms

In order to facilitate comparisons of the emf-harmonic contents of various structures, a new coefficient is introduced. This new coefficient measures the percentage harmonic content of the line-emf waveform as

$$\%E_{harm} = \sqrt{2}\frac{\sqrt{\sum_{n=5}^{\infty} \widehat{E}_{n-line}^2}}{\widehat{E}_{1-line}}, \tag{4.50}$$

which excludes the harmonic components of the multiples of the 3^{rd} order.

For the combinations of slot structures listed in Table 4.2 and various magnet span values between 120° and 180° electrical, this coefficient is calculated and the results are shown in Fig.4.8. 2000 harmonic components were used for the computational construction of the emf waveforms and derivation of the graph shown in Fig.4.8. The 12 slot structure is not included since its harmonic content is too high for a sinusoidal-current driven machine.

It is observed from the figure that some of the structures produce better sinusoidal back-emf waveforms than the others. Also the effect of the magnet span is observable. The harmonic contents of the 21 and 15 slot structures are very low (less than 10%) so their back-emf waveforms are quite sinusoidal. For these structures a 150° magnet span seems to be the best alternative. On the other hand, the 9 slot structure at 150° or 170°seems very promising, considering the fact that the stators have only 9 slots, which is very simple. The 18 slot structure is not better than the 9 slot one, yet outperforms the 24 slot structure.

The 24 slot structure, which is the most common, has its own advantages compared to fractional-slot structures, such as having a symmetrical armature reaction flux density which will be discussed later. It can also be observed that except for the reduction of the end-turn length, 2/3 short-pitched windings are not sufficiently justifiable for the 24 slot structure. The 5/6 short-pitched structure is an option for the 24 slot structure. This structure can be further improved by magnet skewing, which will be discussed in section 4.14.

In Appendix B, the percentage amounts of harmonic emf values (from 5th to 23th) with respect to magnet span values are shown for the structures mentioned above. Hence, this study covers the whole space harmonic analysis for all possible structures, and can be used for optimization. It should be noted that this analysis is also valid for radial-flux machines having surface-mounted permanent magnets.

In Fig.4.9 the resultant phase and line-emf waveforms for various structures, and magnet spans are shown as representative examples of this analysis.

4.13 Pulsating torque components due to space harmonics of windings and PMs

In [54] torque ripple components of permanent-magnet motors are categorized very clearly. Hence, the same terminology for defining torque ripple components according to their origin will be used here as well.

Four types of torque ripple are described:

1. Pulsating torque: torque ripple component produced by the space harmonic components of the windings and permanent magnets.

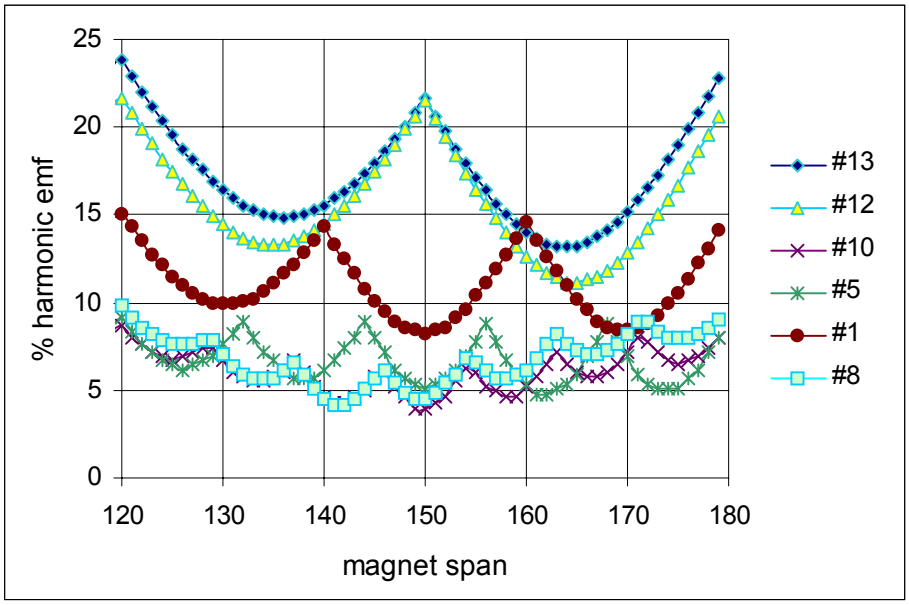

(a)

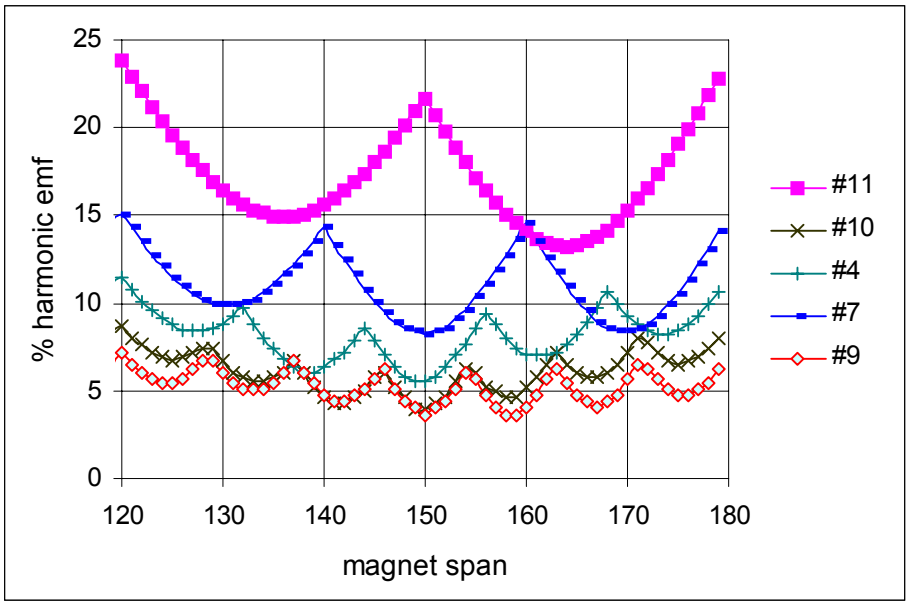

(b)

Figure 4.8: Percentage emf-harmonic contents of various structures (with configuration numbers in reference to Table 4.2) as a function of the magnet span θ_m (in electrical degrees).

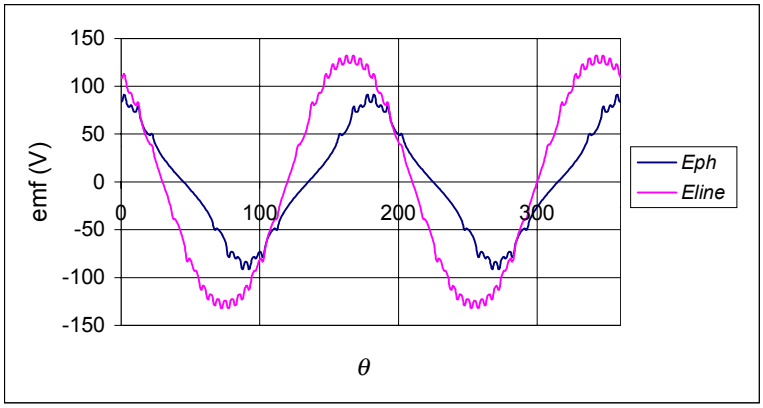

(a) 9-slot structure, $\theta_m = 150°$

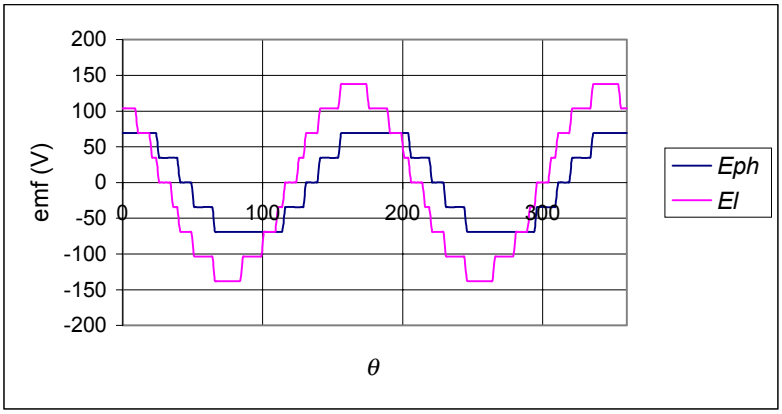

(b) 24-slot structure, full-pitched windings, $\theta_m = 130°$

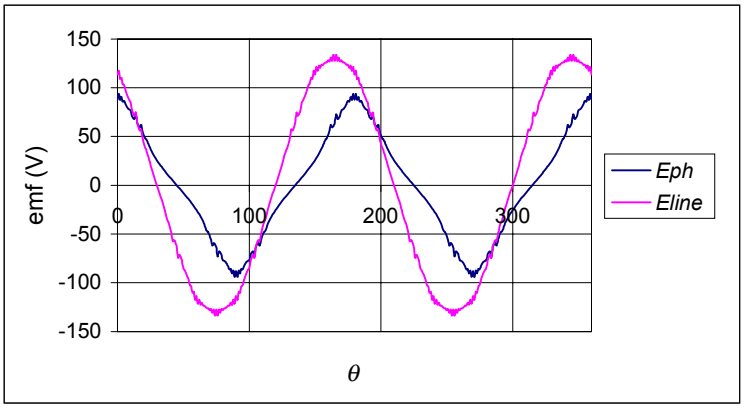

(c) 21-slot structure, coil-span=5 slots, $\theta_m = 150°$

Figure 4.9: Simulated line and phase-emf waveforms of some example structures.

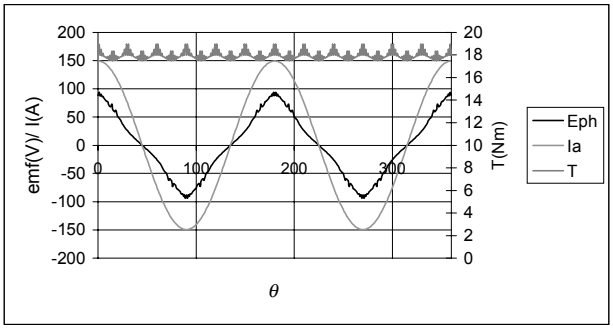

(a) 21 slots /magnet span=150 °.

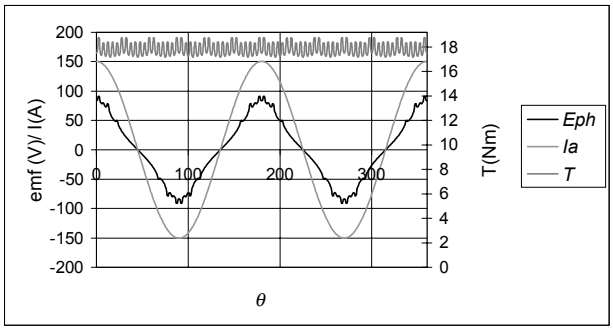

(b) 9 slots / magnet span=150°.

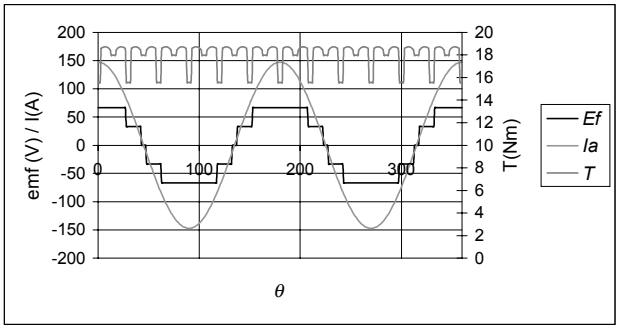

(c) 24 slots /magnet span=140°.

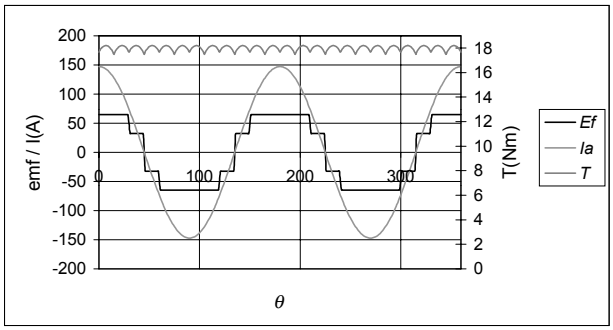

(d) 24 slots /magnet span=150°.

Figure 4.10: Phase emf, (sinusoidal) phase current, and output torque waveforms for some representative structures.

2. Fluctuating torque: torque ripple component produced by the time harmonic components of the input current (non-sinusoidal current components or ripple current).

3. Cogging torque: torque ripple component due to the reluctance variations in the airgap, mainly because of slotting. This component also exists when there is no armature excitation, so it can be determined easily with the FEM by calculating the torque for several positions of the rotor as will be explained in section 5.7.

4. Inertia and mechanical system torque.

The fluctuating and the mechanical system torques can not be improved during the design stage. The pulsating and the cogging torque components should be studied. Cogging torque can be removed by skewing the magnet by one slot pitch [55]. Also odd numbers of slots are known to reduce the cogging torque to an acceptable level [55]. Here, the most important torque ripple component of the PM synchronous machines namely the pulsating torque, will be investigated.

Having obtained the emf waveforms of various structures, the output torque waveforms can be derived by assuming the stator current waveform to be perfectly sinusoidal, which reduces the fluctuating torque component to zero. It is also assumed in the calculations that the stator current is in phase with the fundamental component of the emf waveform, which is the required angle for maximum torque production. Some examples of phase emf, phase current and spatial torque waveforms are shown in Fig.4.10 for some representative structures. Fig.4.10 demonstrates the dependence of the torque ripple on the winding scheme and the magnet span.

Among others, torque ripple minimization is an essential objective of the design. Nevertheless, torque is a continuous time variable and in order to compare various designs (combinations of winding schemes and magnet-span values) with regard to the torque ripple, a comparable (between designs) measure is required. The torque ripple is an essentially undesirable variation and thus the comparable measure should be defined. One possibility is to use the percentage distance between global peak values as done in [56]. Nevertheless, this measure while being appropriate for a rather discrete time process (such as in a switched reluctance machine), is not the best for a continuous process. Therefore, a RMS type measure which considers the mean of the variation throughout the entire process would apparently constitute a more useful proxy for the ranking of the undesirability of torque ripples among various designs.

For this purpose, a measure based on the standard deviation formula which is nothing but the rms value of the distance of sampled observation points from the process mean (18 Nm) is adopted.

The standard deviation of the torque (SDT) for 11 structures as a function of the magnet span values, are shown in Figures 4.11 to 4.14. In Appendix C, the SDT values are presented in a table.

As it is seen from the graphs and the table, the SDT values for the 21 slot structures are very low, especially at 150° magnet span. SDT values for 9 and 15 slot structures are also very low at 150° magnet span. The 24 slot full-pitched structure which has large amount of harmonic components, has also very low SDT at 150° magnet span. However, it doesn't mean that this particular construction is ripple free. For the same structure for example, a few degrees phase shift of the current (which is always possible in synchronous machine operation) will create a certain amount of torque ripple. The harmonic contents of the structures should also be considered for the optimum choice.

4.14 Effect of magnet skewing

In [55], it is stated and proved that, independently from the magnetic structure is for RFPM machines, one slot pitch magnet skew eliminates the cogging torque. One slot pitch magnet skew can also be introduced to an AFPM machine. Yet, the magnet shape becomes complicated especially for the structures with low number of slots.

Magnet skewing has also a filtering effect on the emf waveform. The skew factor as mentioned in section 4.3 is

$$k_{sn} = \frac{\sin n\frac{\gamma}{2}}{n\frac{\gamma}{2}} = \frac{\sin n\frac{\alpha\theta_s}{2}}{n\frac{\alpha\theta_s}{2}}, \tag{4.51}$$

where γ is the electrical angle of the skew, θ_s is the slot pitch, and α is the normalized skew amount in terms of slot pitch (i.e. α=1 means 1 slot-pitch skew). Fig.4.15 shows the effect of the skew in two stator structures. It is observable from the figure that the skew eliminates the high-frequency components. Hence, magnet skewing is essential for sinewave-current driven machines.

4.15 Effect of the stator offset

The stator offset is an additional flexibility of the double-stator AFPM machines. One stator can be offset with respect to the other by some degrees, if they are connected in series. Since the total emf of the phase is the sum of the emf values of the two stators, a properly chosen offset will result in an elimination of some higher order harmonic components.

The stator offset is not a permanent design decision. It can always be tested after the machine is constructed, by rotating one of the stators with respect to the other by various angles.

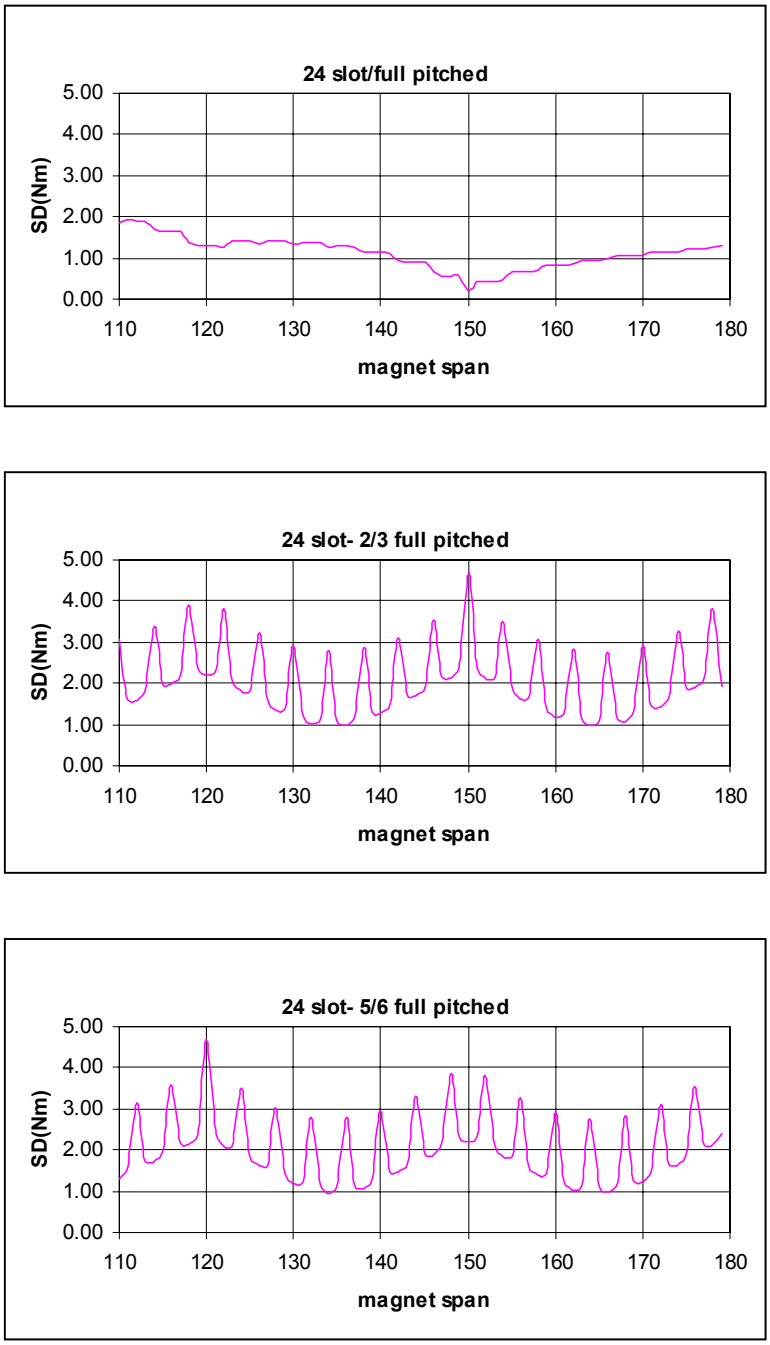

Figure 4.11: Standard deviation of the torque in various structures as a function of magnet span in electrical degrees.

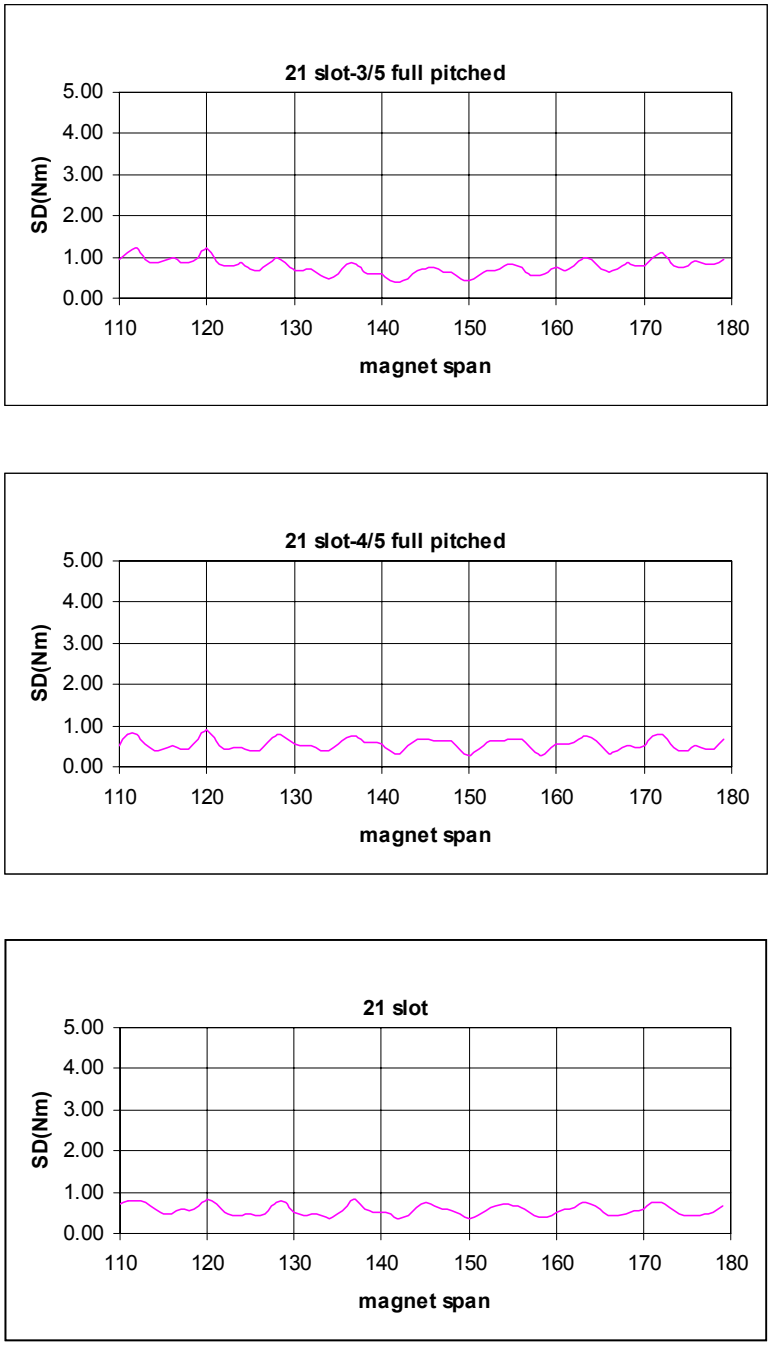

Figure 4.12: Standard deviation of the torque in various structures as a function of magnet span in electrical degrees.

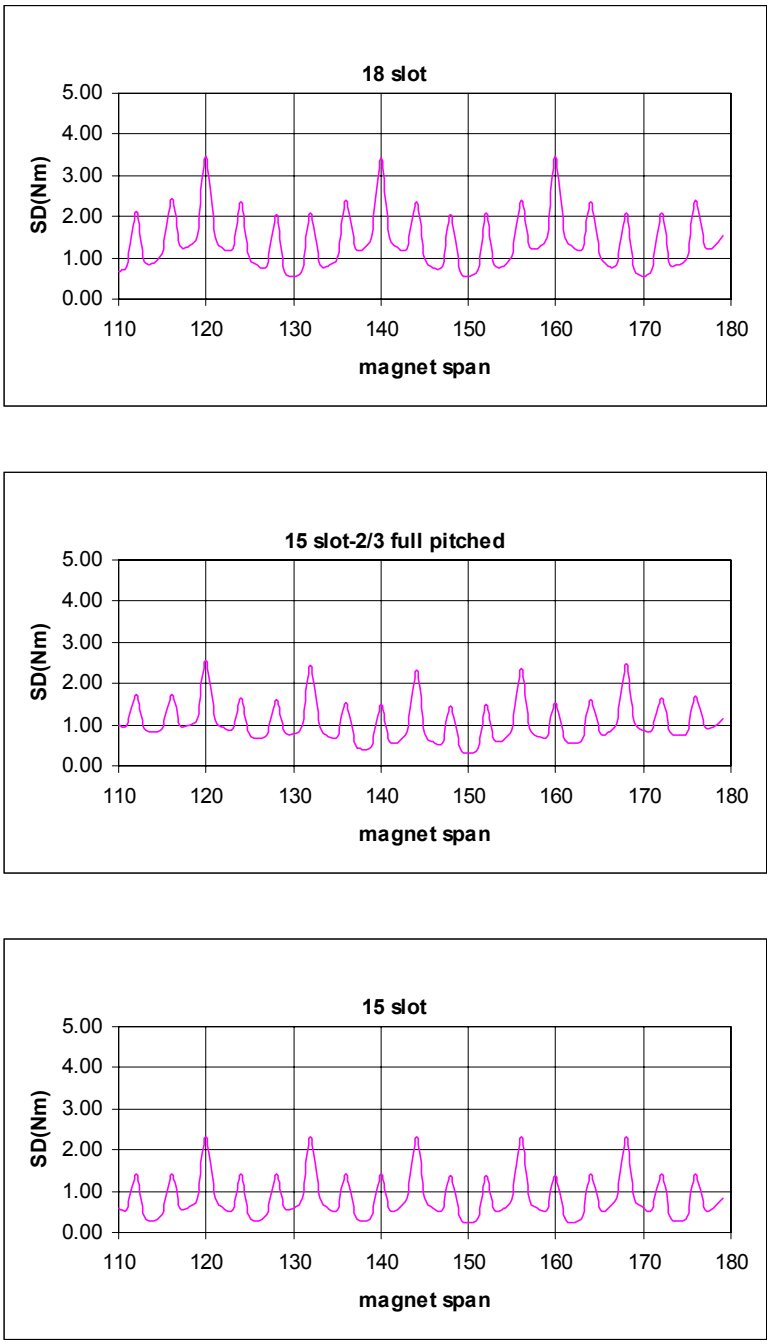

Figure 4.13: Standard deviation of the torque in various structures with respect to magnet span in electrical degrees.

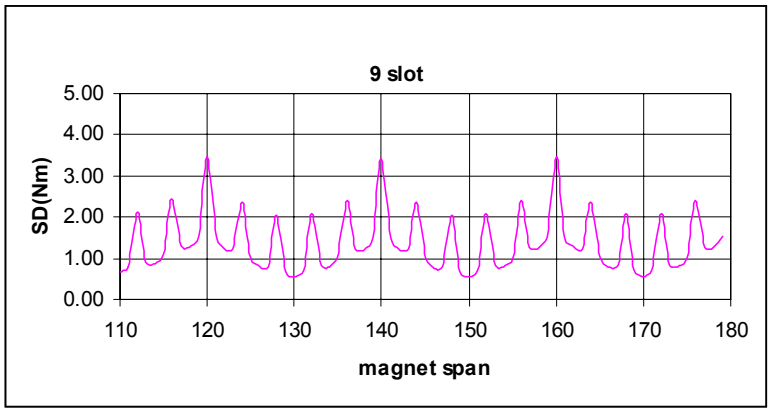

Figure 4.14: Standard deviation of the torque in various structures as a function of magnet span in electrical degrees.

The phase-emf equation can be rewritten as the emf equation of the two series connected stators with an offset angle β

$$e_2(\theta) = \sum_{n=1}^{\infty} \widehat{E}_n \sin(n\theta + n\frac{\beta}{2}) + \sum_{n=1}^{\infty} \widehat{E}_n \sin(n\theta - n\frac{\beta}{2}). \tag{4.52}$$

By using trigonometric equalities, Eq.4.52 can be rewritten as

$$e_2(\theta) = \sum_{n=1}^{\infty} 2\widehat{E}_n \sin(n\theta) \cos(n\frac{\beta}{2}). \tag{4.53}$$

The effect of the stator offset can be represented as a factor (like a winding factor), which may be included in the emf and the torque formulas as

$$k_{off-n} = \cos(n\frac{\beta}{2}). \tag{4.54}$$

For example, if the elimination of the 11^{th} harmonic component is essential, β should be chosen as $(90.2/11 =)\ 16.4°$. Naturally, it does not only eliminate the 11^{th}, but filters the other higher harmonic components as well. The fundamental component also reduces with the factor $cos(8.2) = 0.989$. An example is given in Fig.4.16. As can be seen in appendix C, the eleventh harmonic component of the 24 slot full-pitch stator at 120° magnet span is quite high. With 16.4° stator offset, the line-emf waveform in this structure is shown in Fig.4.16 in comparison with the one without offset.

One possible disadvantage of the stator offset is that it can cause an axial asymmetry in the machine. Since the armature reaction flux densities in the airgap will be shifted with an offset angle, the resultant flux densities of the airgaps can differ and it can cause a certain amount of pulsating axial force.

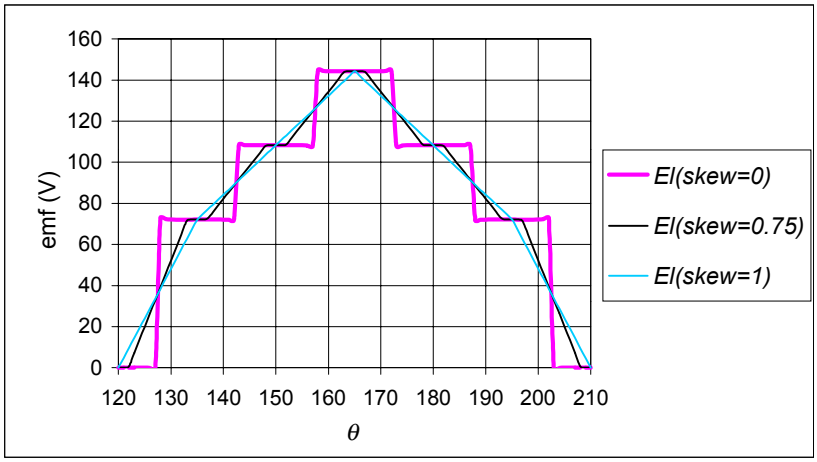

(a) 24-slot full-pitched winding, $\theta_m = 120°$, with skew values α =0, 0.75, and 1.

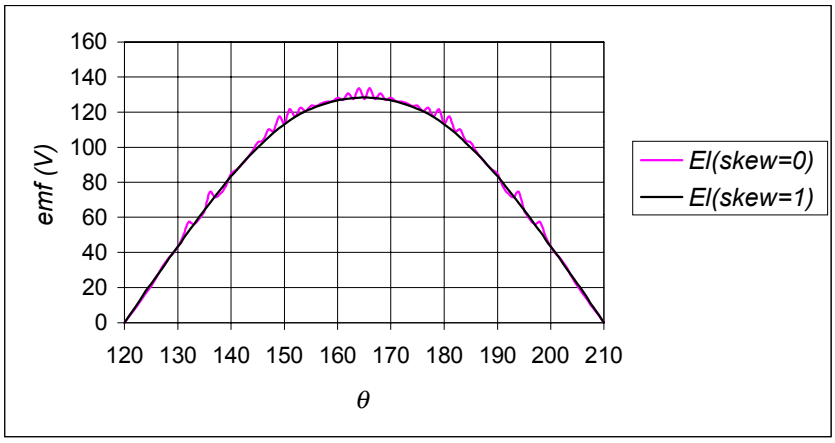

(b)21-slot, $\theta_m = 150°$, with skew values α =0, and 1.

Figure 4.15: The effect of magnet skewing in various structures.

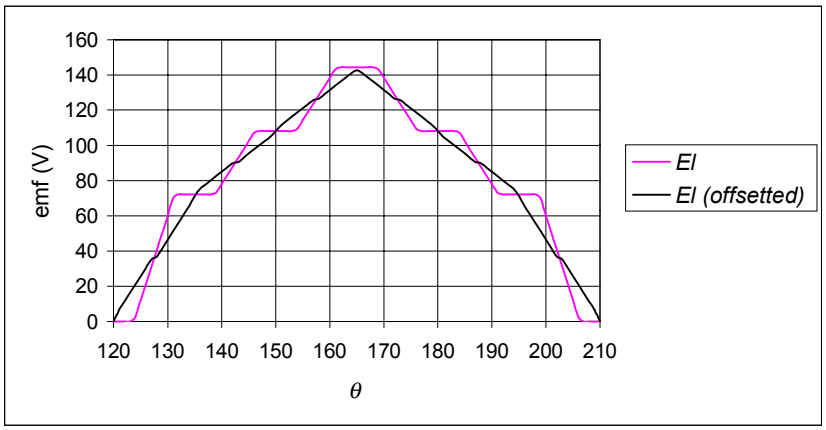

Figure 4.16: Line-emf waveforms for the 24 slot full-pitched structure, and $\theta_m = 120°$, with and without stator offset.

4.16 Results of space harmonics analysis

In the previous sections, a comparative study of various design variables was presented by means of space harmonics analysis. The results of this work can be summarized as follows.

1. The higher order harmonic contents of the emf highly depend on the choice of magnet span.

2. The optimum magnet span values are different for different number of slots and winding schemes.

3. 150° magnet span seems to be the best alternative for fractional-slot structures; it not only minimizes the harmonic contents of the emf but the level of pulsating torque as well.

4. The amount of pulsating torque is minimum at 150° magnet span for the 24 slot full-pitched structure, but only when the current is in phase with the emf. 135° or 165° magnet spans for 24 slot structures may also be good choices considering the harmonic contents.

5. Magnet skewing filters higher order harmonic components.

6. Stator offset filters higher order harmonic components.

7. Stator offset causes axial asymmetry, so an unbalanced pulsating axial force.

8. The axial asymmetry caused by fractional-slot structures is not as important as in radial-flux machines, since these forces will be neutralized by two stators from both sides if there is no stator offset.

9. Short-pitching increases the machine efficiency by reducing the end-turn lengths.

A proper winding scheme, magnet span and number of slots can be determined from these results. It should be noted again that a higher number of slots, i.e. a 36 slot structure is not included to this study due to the complications caused by a higher number of slots, i.e. increased space for the end turns, constructional difficulties, and the design difficulty related to the increased number of turns per phase.

The fractional-slot structures seem very promising considering their no-load emf waveforms with reduced higher harmonic contents and their low pulsating torques. Yet, the disadvantage is the fact that the odd number of slots introduces an asymmetrical mmf. The asymmetry in the armature reaction field can be observed in Fig.4.17a,b, which is obtained from Finite Element Analysis (FEA) when there is only current excitation. The concept and application of FEA will be further discussed in chapter 5. The effect of the asymmetry can also be observed on the resultant airgap flux density waveform (Fig.4.17.c,d). This mmf asymmetry will introduce even order harmonic components in the airgap. Although these components don't contribute to the output torque of the machine, they run asynchronously with respect to rotor and eventually will create losses in the rotor at higher speeds.

This kind of asymmetry also creates an unbalanced axial (normal) force which is the main reason why fractional-slot structures are not preferable in radial-flux machines [55]. In the case of an AFPM machine, there is already a huge amount of axial force between the stator and the rotor, but the axial force is balanced with the existence of two stators, if the rotor is located precisely in the middle. Accordingly, the axial force caused by an asymmetrical mmf is also balanced from both sides if there is no stator offset. On the other hand, it is obvious that this axial force caused by asymmetry can only amount to a few percentage points of the force caused the magnets, as it can be understood by investigating the flux density waveforms in Fig.4.17. It should also be noted that there are AFPM machines with a single rotor and stator, where the bearings tolerate all axial forces. The conclusion is that the axial forces are not the major problem related with fractional-slot stators in AFPM machines as in the case of radial-flux machines but, the even order harmonic components in the resultant mmf, introduced by the asymmetry, is the main reason why this structure is ruled out for this high-speed machine.

In the light of the conclusions of the analysis made so far, the AFPM machine is designed with 24 slots and 5/6 short-pitched stator windings, which together reduce both the harmonic content and the length of the end windings. The machine is designed torque ripple free by choosing a 150° magnet span (plus a small span to compensate fringing) and with one slot pitch magnet skewing. These methods

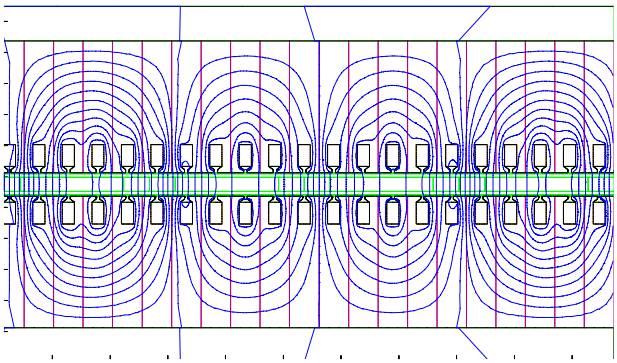

(a) Armature reaction field distribution.

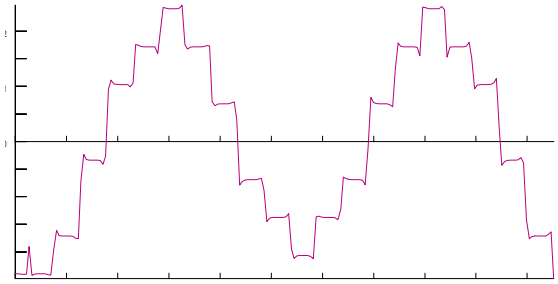

(b) Armature reaction flux density waveform.

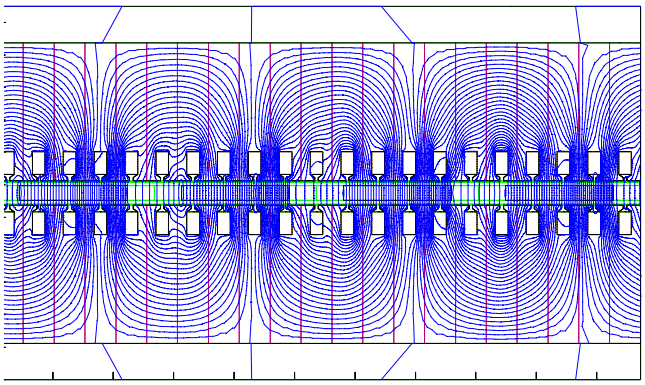

(c) Resultant flux distribution.

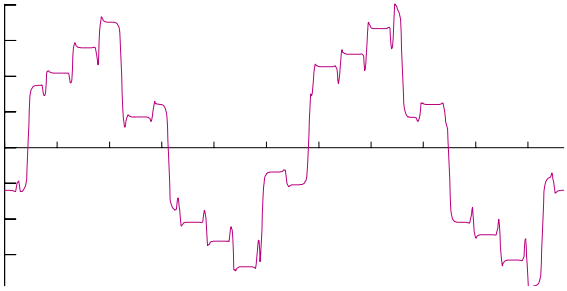

(d) Resultant airgap flux density waveform.

Figure 4.17: FE analysis of a 21 slot structure.

(distribution and short pitching of the windings, and magnet skewing) decrease the output torque of the machine. Nevertheless, they are advantageous in decreasing the losses brought about by the higher order winding and slot harmonics. This fact becomes more important at higher speeds where the rotor losses become a major concern as will be discussed in section 5.9.

4.17 Design procedure

The rest of the design is a multi-dimensional optimization problem concerning the maximization of the efficiency while satisfying several constraints, such as thermal conditions, magnet demagnetization, leakages, etc. The whole procedure facilitates the loss calculations, FE analysis and thermal analysis which will be discussed in detail in the chapters 5, 6, and 7. Here only the design procedure and the final machine data are given and the details will be left to the following chapters.

The steps of the design procedure can be summarized as follows:

1. Determine the application requirements.
2. Make structural decisions.
3. Determine the electric and magnetic loadings.
   (a) Maximum allowable stator surface current density (in relation to the cooling system).
   (b) Airgap flux density.
   (c) Maximum allowable flux density.
4. Determine the mechanical constraints.
5. Choose the tentative dimensions:
   (a) Airgap length.
   (b) Stator outside diameter.
   (c) Ratio of the inner and outer diameters of the stator.
6. Determine the specifications of the magnet.
7. Determine the dimensions of the stator.
8. Determine the magnet and stator yoke dimensions.
9. Check the mechanical constraints, if not satisfied, GO TO #5.

Stator outside diameter	D_o	190 mm
Stator inside diameter	D_i	110 mm
Stator yoke length	L_{st}	30 mm
Total stator axial length	L_y	45 mm
Number of poles	$2p$	4
Number of slots/pole/phase	n_{spp}	2
Number of turns/phase/stator	N_{ph}	16
Airgap length	g	1.5 mm
Total ($\times 2$) magnet axial length	L_m	6 mm
Slot bottom width	w_{sb}	6 mm
Slot top width	w_s	1.5 mm
Slot depth	d_b	11 mm
Slot top depth 1	d_{t1}	2 mm
Slot top depth 2	d_{t2}	2 mm
Total slot depth	d_s	15 mm

Table 4.3: Machine data.

10. Determine the required phase current.

11. Check the conditions of magnet demagnetization, if not satisfied GO TO #5.

12. Determine the losses.

13. Determine the efficiency, if too low GO TO #5.

14. Check the thermal constraints, if not satisfied GO TO #5.

15. Verify the results with FE analysis, if not satisfactory GO TO #5.

4.18 The machine data

After the implementation of the design procedure, the following machine data is achieved, which is summarized in Tables 4.3 and 4.4. The data will be used in the following chapters for further analyses.

4.19 Conclusions

In this chapter, various design alternatives were compared and contrasted in relation to the number of stator slots, the magnet span, winding configuration, skewing

Mechanical torque	18 Nm
Maximum speed	16000 rpm
Power	30.16 kW
Stator current (rms)	53 A
Max. inverter frequency	533 Hz
Line to line emf (rms)	330 V
Terminal voltage	345 V
Phase synchronous inductance,	0.115 mH
Per-unit synchronous reactance	0.203
Airgap flux density (at 60° C), B_{g0}	0.735 T

Table 4.4: Machine properties.

and the stator offset. Space harmonics analysis was performed on competing structures. The design procedure was discussed and the presentation of machine data was presented.

Chapters 3 and 4 can be seen as an initial screening and a raw elimination among many alternatives, which leads to a candidate design. Nevertheless, this effort relies on a set of analytical equations which lack the precision and accuracy that a final analysis deserves. Although, such accuracy and precision can be achieved by the use of *Finite Element Analysis* (FEA), the obvious resource limitations (time and effort) make it infeasible to be employed for the preliminary design, which accordingly resort to analytical approximations. Yet, it is the most appropriate tool to verify and finalize (fine tuning and optimization) the raw design provided by the analytical approximation approach.

Chapter 5

Finite element analysis

5.1 Introduction

Finite element analysis and optimization of electromagnetic devices became a commonly used tool for designers since the seventies. The recent introduction of the more complicated machines, such as permanent-magnet and reluctance, and even complicated geometries rendered the use of numerical techniques unavoidable. Analytical methods are mainly based on many assumptions, although it is possible to improve them to a certain complicated level [57], [58], [59], [60] (in 2-D), [61] (in 3-D), yet the obtained accuracy is limited. However, the finite element analysis allows modelling of complicated geometries, nonlinearities of the steel, in 2-D and in 3-D, and gives accurate results without standing on many restricting assumptions.

In this chapter, the finite element analysis results of the designed machine are presented. In section 5.2, the underlying theory is given. The description of the method is summarized in section 5.3. In section 5.4 the finite element modelling is explained. The results of the analysis of the AFPM machine are presented in the following sections and deal with armature reaction and leakage reactances, airgap, teeth and yoke flux density values at various load conditions, magnet flux leakage, analysis with respect to rotor position, EMF, cogging torque and pulsating torque, ripple flux in the magnets and in the rotor steel caused by asynchronous harmonic components and stator slotting, and finally the eddy current loss analysis.

5.2 Relevant theory

The most essential parameters in the analysis of an electrical machine are the magnitude and the distribution of flux density $\overrightarrow{B}$, magnetic field intensity or magnetizing force $\overrightarrow{H}$, and the flux linkages of the windings ϕ. These quantities are solved with FE methods in terms of potentials: scalar magnetic potential Ω, in terms of ampere-turns

(mmf, which corresponds to the voltages in the electrical analogue) and magnetic vector potential, $\overrightarrow{A}$ which is expressed in Wb/m, [62].

When the region of interest has no current carrying conductors, the magnetizing force $\overrightarrow{H}$ is related to the scalar magnetic potential, Ω as

$$\overrightarrow{H} = -\nabla\Omega, \tag{5.1}$$

where for a two dimensional isotropic region,

$$\begin{aligned} H_x &= -\frac{\partial\Omega}{\partial x}, \quad B_x = -\mu_0\mu_r\frac{\partial\Omega}{\partial x}, \\ H_y &= -\frac{\partial\Omega}{\partial y}, \quad B_y = -\mu_0\mu_r\frac{\partial\Omega}{\partial y}. \end{aligned} \tag{5.2}$$

Considering the three dimensional case, where there is no net loss or gain of flux

$$\nabla.\overrightarrow{B} = 0, \tag{5.3}$$

and in scalar form

$$\frac{\partial B_x}{\partial x} + \frac{\partial B_y}{\partial y} + \frac{\partial B_z}{\partial z} = 0. \tag{5.4}$$

Substituting Eq.5.2 into Eq.5.4 yields

$$\frac{\partial}{\partial x}(-\mu_0\mu_r\frac{\partial\Omega}{\partial x}) + \frac{\partial}{\partial y}(-\mu_0\mu_r\frac{\partial\Omega}{\partial y}) + \frac{\partial}{\partial z}(-\mu_0\mu_r\frac{\partial\Omega}{\partial z}) = 0, \tag{5.5}$$

simplifies as

$$\frac{\partial^2\Omega}{\partial x^2} + \frac{\partial^2\Omega}{\partial y^2} + \frac{\partial^2\Omega}{\partial z^2} = 0, \tag{5.6}$$

which is the Laplace's equation, [62].

Besides

$$\overrightarrow{B} = \nabla \times \overrightarrow{A}, \tag{5.7}$$

where

$$\begin{aligned} B_x &= \frac{\partial A_z}{\partial y} - \frac{\partial A_y}{\partial z}, \\ B_y &= \frac{\partial A_x}{\partial z} - \frac{\partial A_z}{\partial x}, \end{aligned} \tag{5.8}$$

$$B_z = \frac{\partial A_y}{\partial x} - \frac{\partial A_x}{\partial y},$$

and

$$\nabla \times H = \overrightarrow{J}, \tag{5.9}$$

where

$$\frac{\partial H_z}{\partial y} - \frac{\partial H_y}{\partial z} = J_x,$$

$$\frac{\partial H_x}{\partial z} - \frac{\partial H_z}{\partial x} = J_y, \tag{5.10}$$

$$\frac{\partial H_y}{\partial x} - \frac{\partial H_x}{\partial y} = J_z.$$

Using $\overrightarrow{B} = \mu_0 \mu_r \overrightarrow{H}$, and substituting Eq.5.7 into Eq.5.9, one finds

$$\nabla \times \left(\frac{1}{\mu_0 \mu_r} \nabla \times \overrightarrow{A} \right) = \overrightarrow{J}. \tag{5.11}$$

Considering the case where the only current density is J_z, (A_x and A_y are constant), consequently only A_z is considered as

$$B_x = \frac{\partial A_z}{\partial y}, \quad B_y = -\frac{\partial A_z}{\partial x}. \tag{5.12}$$

Using Eq.5.11 and assuming isotropy,

$$\frac{\partial}{\partial x}\left(\frac{1}{\mu_0 \mu_r} \frac{\partial A_z}{\partial x} \right) + \frac{\partial}{\partial y}\left(\frac{1}{\mu_0 \mu_r} \frac{\partial A_z}{\partial y} \right) = -J_z, \tag{5.13}$$

yields

$$\frac{\partial^2 A_z}{\partial x^2} + \frac{\partial^2 A_z}{\partial y^2} = -\mu_0 \mu_r J_z, \tag{5.14}$$

which is called the Poisson's equation. It should be noted that the components of the flux density vector $\overrightarrow{B}$ depend only on the gradients of the components of the magnetic vector potential, not on the magnitude of it [62].

5.3 Finite element method

The Finite Element Method (FEM) is used to solve partial differential or integral equations which otherwise, can not be solved accurately. The method is applicable to problems with any type of nonlinearity. The idea is based on the division of the volume or domain in which the equation is valid, into smaller volumes or domains or so-called finite elements. Within each element a simple polynomial is used to approximate the solution. In other words the discritization transforms the partial differential equation into a large number of simultaneous nonlinear algebraic equations containing the unknown node potentials. Iterations such as Newton-Raphson and conjugate-gradient methods are used.

Partial differential equations describe the magnetic field by means of a potential functional [63]. The resulting partial differential equation is written in terms of the vector potential $\overrightarrow{A}$, as in the case of Poisson's equation (Eq.5.14), and the important field quantities such as flux density are derived from it. Within one element the vector potential is assumed to vary according to a simple shape function, which may be linear, i.e. the potential is assumed to vary linearly between the nodes and the flux density is constant within each element. The shape function can be quadratic or a higher-order function of the three sets of node coordinates for the vertices of the triangular element [43].

The FEM is mainly based on the minimization of the so-called energy functional F, which is the difference between the stored energy and the input energy applied to the system. For electromagnetic systems the energy functional is

$$F = \int_V \left(\int_0^B \overrightarrow{H} \cdot \overrightarrow{dB} - \int_0^A \overrightarrow{J} \cdot \overrightarrow{dA} \right) dV. \tag{5.15}$$

Minimization of the energy functional over a set of elements leads to a matrix equation that has to be solved for the magnetic vector potential $\overrightarrow{A}$, throughout the mesh [63], [64], [33].

Contemporary finite element packages have mainly three components: pre-processor, solver and post-processor [65]. In the pre-processor the finite element model is created. First, the geometric outlines are drawn, which is similar to the available mechanical engineering packages. Then, material properties are assigned to the various regions of the model. Next, the current sources and the boundary conditions are applied to the model. Finally, the finite element mesh is created. In the solver part, the finite element solution is conducted. Some of the packages have adaptive mesh options, where an error estimate is produced from the solution; the mesh is refined and the solution is repeated again. The procedure goes on iteratively until the required accuracy level is achieved. In the post-processor, magnetic field quantities are displayed, and it allows to calculate quantities, such as, force, energy and flux.

The subsequent steps in the finite element analysis will be discussed in the following sections with an example, i.e. the analysis of the designed AFPM machine. The finite element package Opera-2D is used throughout the study. The static-field analysis program (ST) is utilized to solve the time invariant magnetic field problems with linear or nonlinear permeability values. The steady-state AC analysis program (AC) is also used to solve the eddy current problems, in cases of sinusoidally time varying driving currents [63].

5.4 Modelling

The problem of modelling starts with the definition of the coordinates, consequently the dimensions. Each part of the motor is represented with different materials, such as steel, magnet and copper. The definition of the materials involves the curve fitting of the B-H characteristics of the steels and magnet materials, and linear permeability values for other components. It follows with the application of the boundary conditions, imposing the current densities into the winding elements, and the definition of the direction of magnetization of the magnets. Periodic boundary conditions are used to reduce the model into a small fraction of it.

The AFPM machine is modelled in two dimensions by representing it with a two pole axial cross-section at a certain radius. In order to enhance accuracy, the two dimensional analysis was repeated at several selected cross-sections (radii) lying between the inside and outside radius of the stators. In this way a 3-D approximation that ignores the end-turn effects is obtained. The dependence of the slot to tooth pitch ratio on the selected radius (i.e. the teeth and yoke flux density values vary from the inside to outside radius of the stator) renders the modelling of the machine at different cross-sections necessary. Moreover, modelling at different cross-sections also facilitates the investigation of the effect of magnet skewing.

In Fig.5.1, the magnetic vector potential distribution is shown at full load and 90 degrees load angle and average radius as a representative example showing the direction of flux as well as the model. The model includes the surrounding air, a two pole stator section (which corresponds to 360° electrical), the airgap, magnets and half of the rotor from bottom to top, respectively. In this model the symmetry boundary conditions are used to simplify the finite elements model by representing the machine only with one pole-pair as seen in Fig.5.1.

5.4.1 Boundary conditions

The boundary conditions imposed on this model can be divided in three categories:

- *Dirichlet boundary condition:* This condition fixes the magnetic vector potential at a particular point to a prescribed value. Dirichlet boundaries force the flux

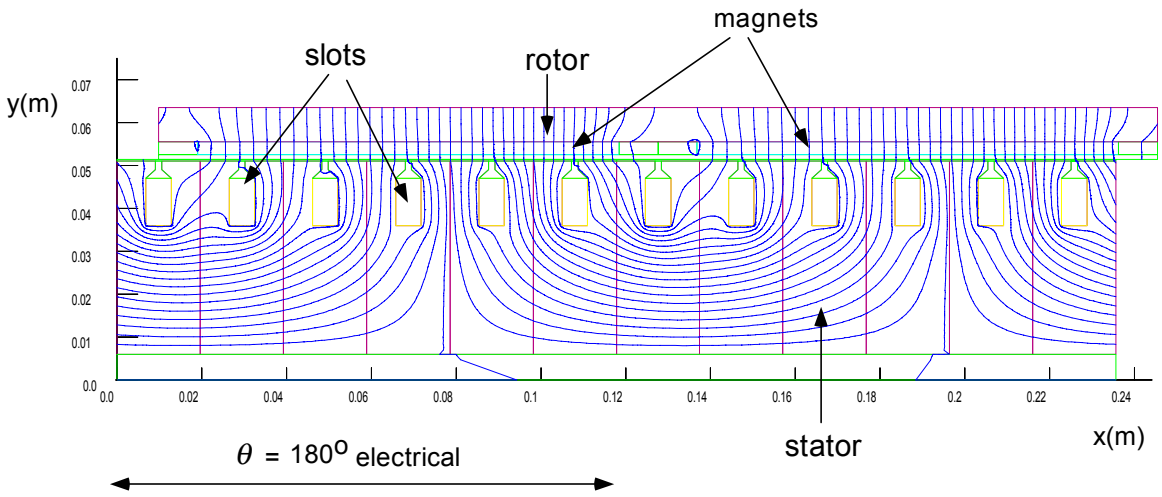

Figure 5.1: Magnetic vector potential distribution at over a two pole symmetry model at full load and average radius.

lines to be parallel to the boundary edges. In the model, the outer line of the surrounding air defined adjacent to the stator (lowest parallel line to the $x-$axis in Fig.5.1) has the $\overrightarrow{A} = 0$ Dirichlet boundary. This condition implies that there is no leakage flux beyond this line.

- *Neumann boundary condition:* This condition imposes the normal derivative of the magnetic vector potential to zero ($\partial \overrightarrow{A}/\partial n = 0$). Flux lines cross the Neumann boundary orthogonally. Neumann boundary is applied to the upper parallel line to the $x-$axis in the model, where there is a symmetry cut over the model, and the flux lines are orthogonal.

- *Symmetry boundary condition:* The symmetry boundaries (left and right) in the model, as seen in Fig.5.1 force the condition that the vector potentials are the same or negative of those on the other side (for single pole symmetry).

5.4.2 Finite element mesh and accuracy

The accuracy of the results of a finite element problem is mainly based on the correct discretization (mesh) of the considered region. Opera generates the mesh according to the geometric outline created by the user. It is done by means of discretization of the outer lines of the geometry. So it is essential to divide some material areas into smaller fractures. After obtaining a solution it is possible to observe the error plot showing the local error over the model. Having this feedback, it is possible to enhance the mesh by further decreasing the size of the elements in the regions where

the error is high. It is also possible to use quadratic elements instead of linear ones to enhance the accuracy with the cost of solution time. Quadratic elements give of course more accurate results for regions where the field is changing fast, such as corners, small airgaps etc. The software also has an adaptive mesh option, which offers a better and fast option of enhancing the solution. With the adaptive mesh option, an initial solution which is obtained from the user-defined starting mesh, the program automatically iterates on by dividing the elements in the regions where the local error is high. This iterative process continues until the required accuracy defined by the user is obtained. Nevertheless, the initial mesh should be accurate enough in regions such as airgap sliding surfaces, on which the post-processing calculations mainly depend. Fig.5.2 shows the initial and final meshes around the slot region respectively: the mesh refinement can clearly be observed from the two figures.

5.4.3 Modelling rotation

In order to model the rotor rotation, the airgap is defined with a sliding surface splitting the airgap into two layers. One of these layers is fixed to the rotor while the other one is fixed to the stator. The node spacing in the sliding layer is made such that the rotor can be rotated by an integer multiple of this constant. The positional variation of the flux density distribution at full load corresponding to 6 and 9 mechanical degrees of rotor rotation are seen in Fig.5.3 as representative examples.

The positional (i.e. time varying) information is obtained by shifting the rotor in position and the corresponding stator currents in time. In this manner the EMF waveform, cogging and pulsating torques, and magnet flux ripple are calculated. In order to compute these, the static field analysis is repeated 30 times (each at another position of the rotor over one pole pitch) at various stator cross-sections (inner, outer, average radius and two other radii in between) for the following operating conditions: at no-load, 25% full-load, 50% full-load, 75% full-load and full-load. In this way, the degree of nonlinearity involved in the machine is detected. The results are presented in the following sections.

5.5 Flux density

The value of the flux density in various machine parts is an important variable in the design as discussed in section 3.4. It is the determining parameter in both core losses and the amount of saturation to which the machine is exposed. The exposure of the varying flux density at various machine parts is studied with the use of FEM.

In Fig.5.4 full-load flux density distributions at the inner, average and outer radii are shown. It is clearly seen that the flux density values at different cross-sections of the machine are not equal. As will be explained and implemented in section 6.3,

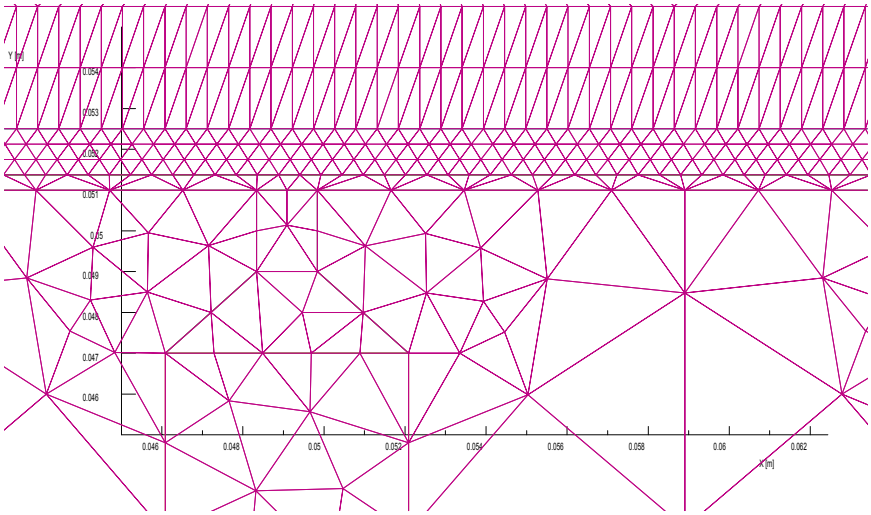

(a) Initial mesh.

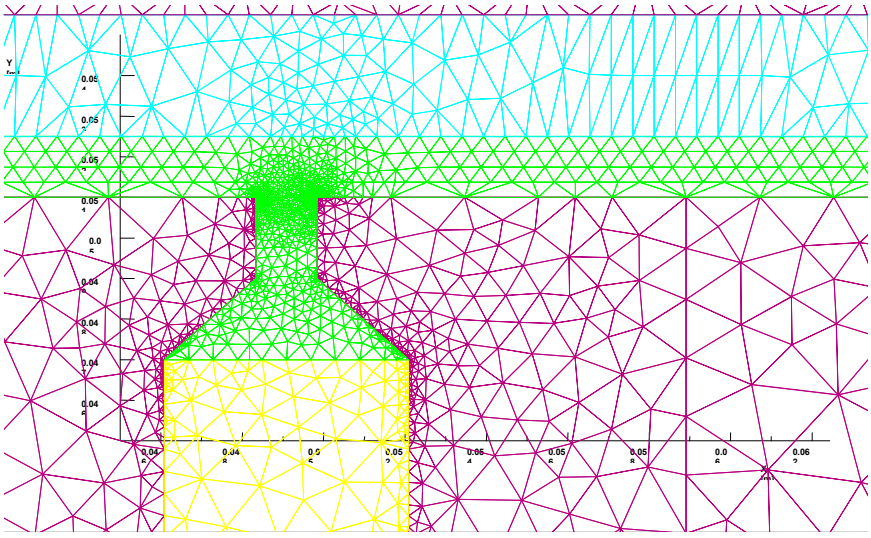

(b) Final mesh.

Figure 5.2: Initial and final discritizations.

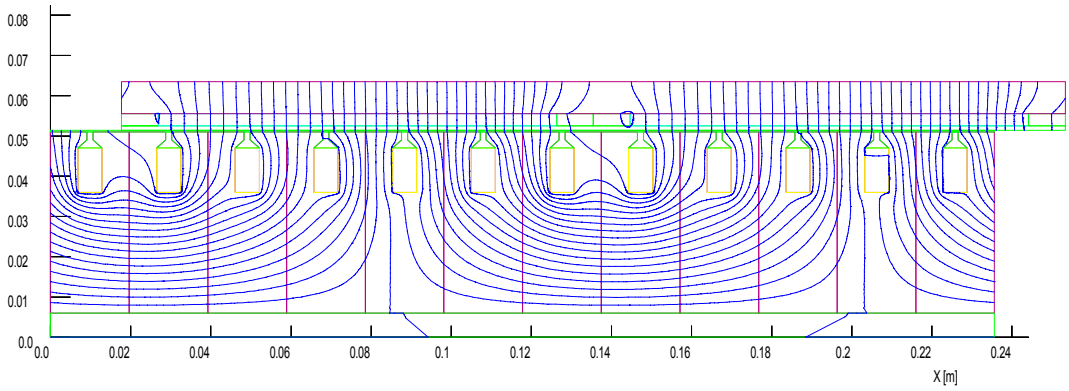

(a) 6° mechanical rotor shift.

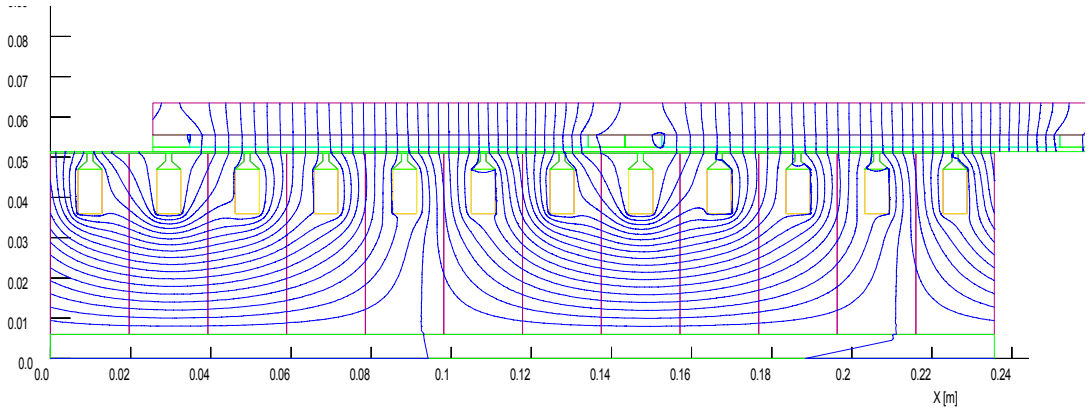

(b) 9° mechanical rotor shift.

Figure 5.3: Magnetic vector potential distribution at different rotor positions.

these differences are taken into account in the core loss calculations, as well as in the prediction of the machine performance.

5.5.1 Airgap flux density

The airgap flux density is directly related to the produced torque. The machine is continuously exposed to the magnet flux, where the armature reaction flux is dependent on the amount of stator current.

Fig 5.5 shows the airgap flux density waveform (over a two pole cross-section in electrical degrees θ as indicated in Fig. 5.1) at full-load and at no-load corresponding to the average radius. The discontinuities due to slotting and the effect of the armature reaction may be clearly seen. The armature reaction flux plot (when the magnet flux is off) over the model and the armature reaction flux density distribution in the airgap and corresponding harmonic amplitudes are shown in Figs. 5.6 and 5.7.

5.5.2 Stator flux density

The exposure of the stator core to the time-varying flux density is investigated by repeating the analysis several times for different positions of the rotor over a pole pitch and at different radii and different load conditions. The results are presented here and can be used for the detailed calculations of the core losses which will be explained in section 6.3.

The stator is divided into several regions, each having similar flux density variations. The points indicating these regions are shown in Fig.5.8 on a flux density plot of the part of the model. The flux density values at several points (A, B, C, ..I) with respect to rotor position and several load conditions, are shown in Fig.5.9. The waveforms obtained from these analyses will be used in detail analyses of the core losses (see section 6.3).

Due to the nature of the application, as low as possible no-load losses are preferred. Since the rotor is integrated into a flywheel, no-load losses always exist and keep on reducing the overall system efficiency. Reduction of the no-load losses can only be made possible via the reduction of the stator core losses, since the air friction losses are suppressed by means of reduced air pressure. On the other hand, especially due to the rotor losses (as will be discussed in sections 5.9 and 6.4) armature excitation should be kept in modest levels because of the critical thermal constraints.

In order to decrease stator core losses, the magnet excitation may be kept very low and a very low flux density may be permitted in the stator cores. In this design, both of these contradicting conditions were tried to be satisfied, by both keeping the magnet excitation dominant (around 0.73 T), and designing the stator cores with lower maximum flux density levels, with the cost of a relatively (to the extent permitted by the volume constraint) thicker stator back-iron. As it is seen from

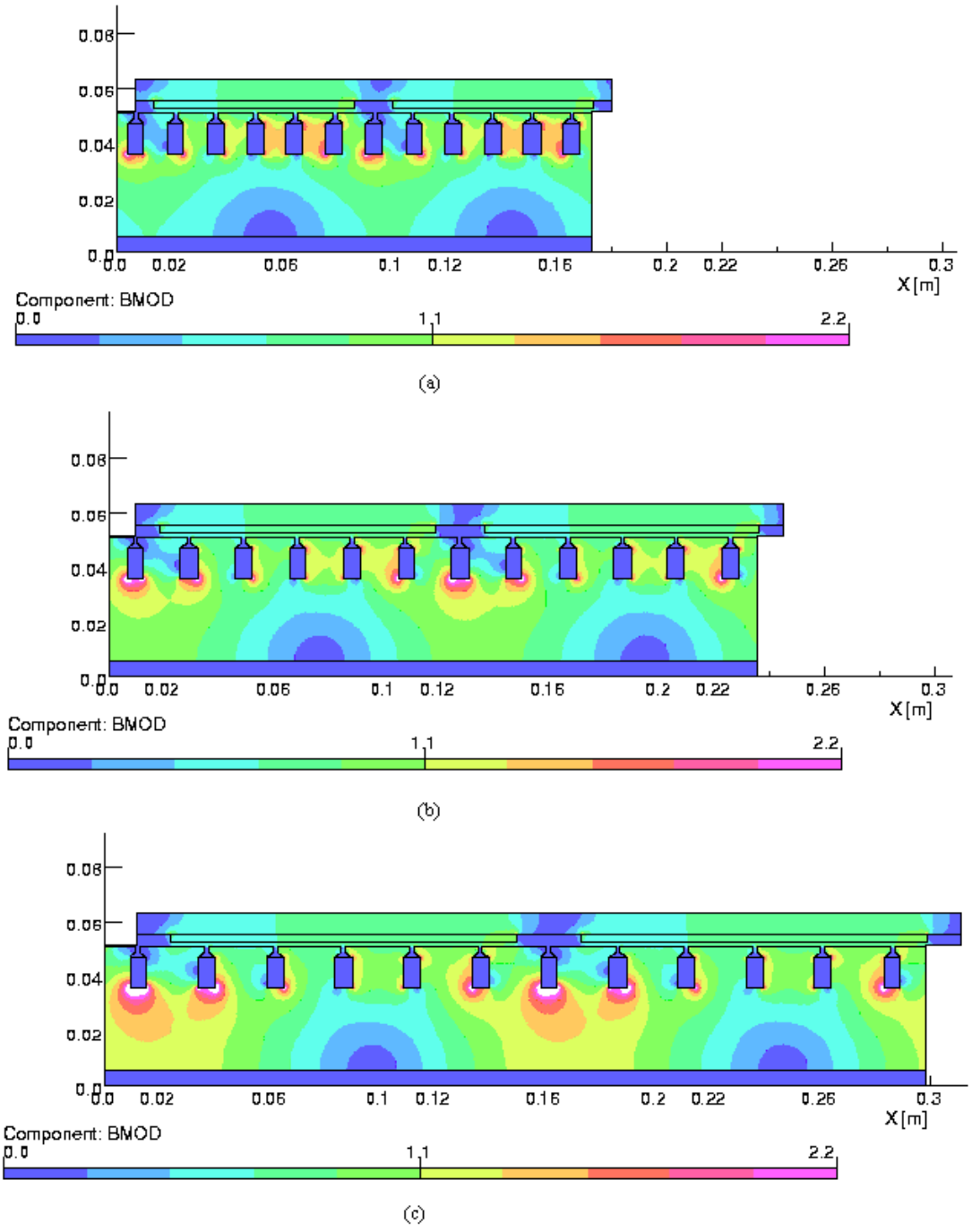

Figure 5.4: Flux density distributions at full load at the axial cross-sections corresponding to inner (a), average (b), and outer (c) radius.

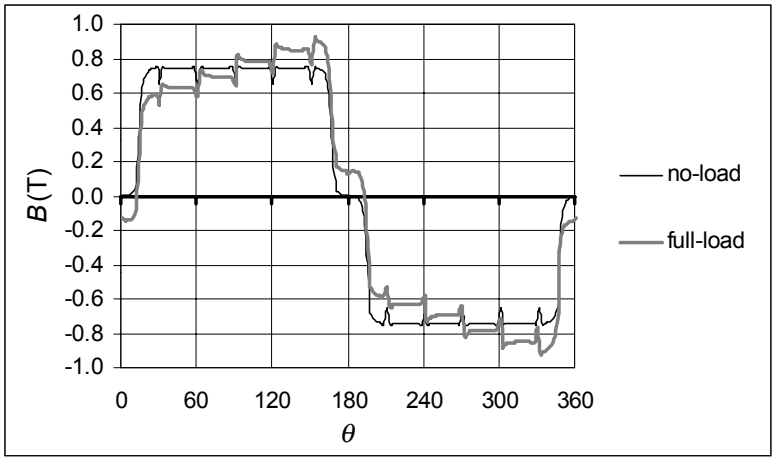

Figure 5.5: Airgap flux density waveforms at no-load and full-load conditions.

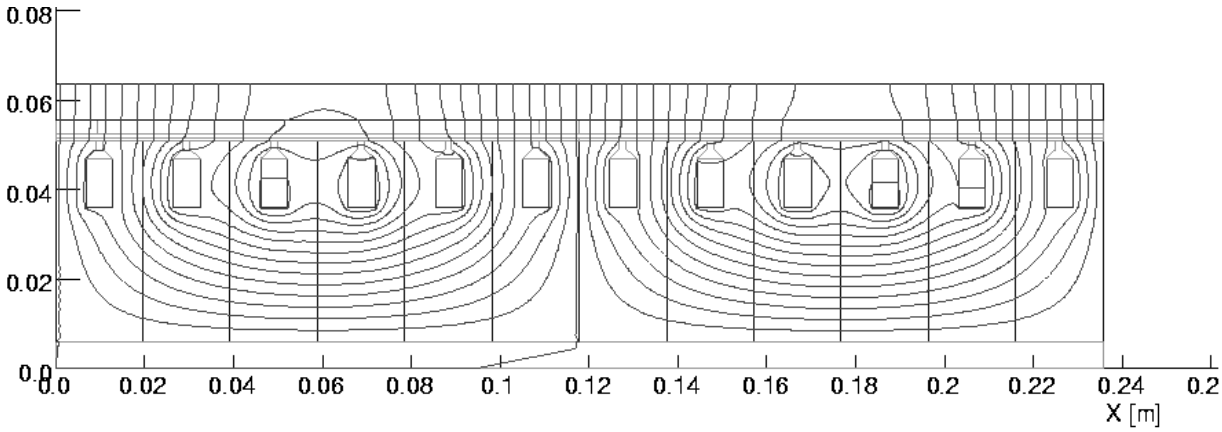

Figure 5.6: Armature reaction flux plot.

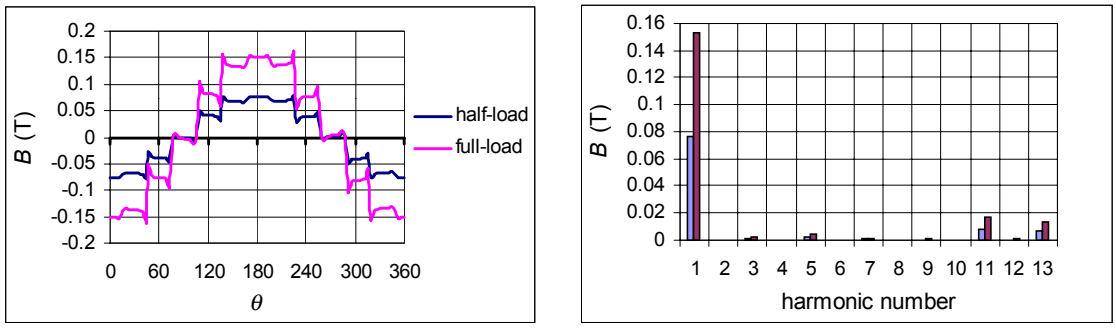

(a) (b)

Figure 5.7: (a) Armature reaction flux density distributions at full- and half-load conditions, (b) corresponding harmonic amplitudes.

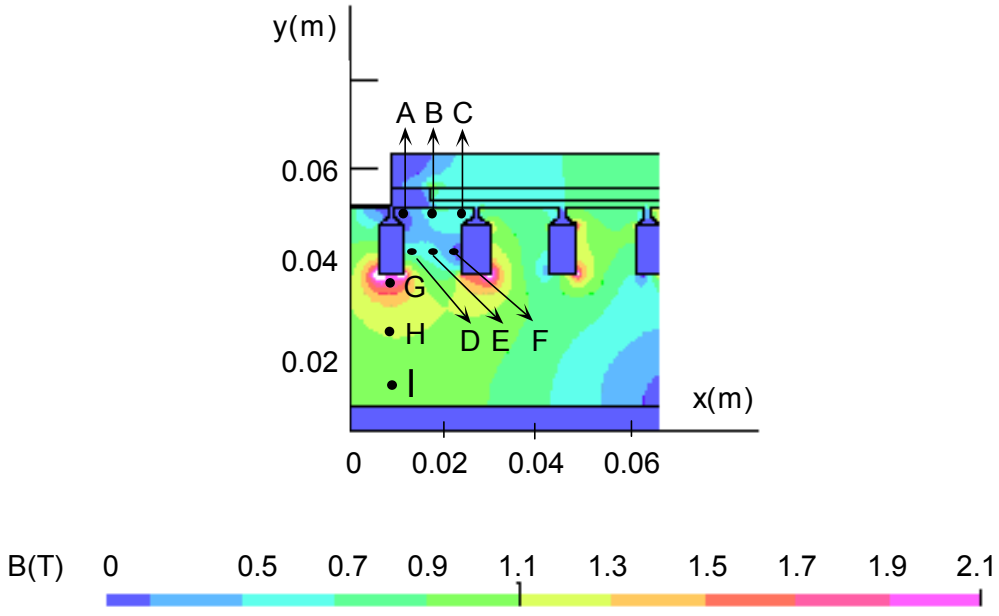

Figure 5.8: Points A, B, C, D, E, F, G, H, and I indicated on a small part of the model and the flux density distribution.

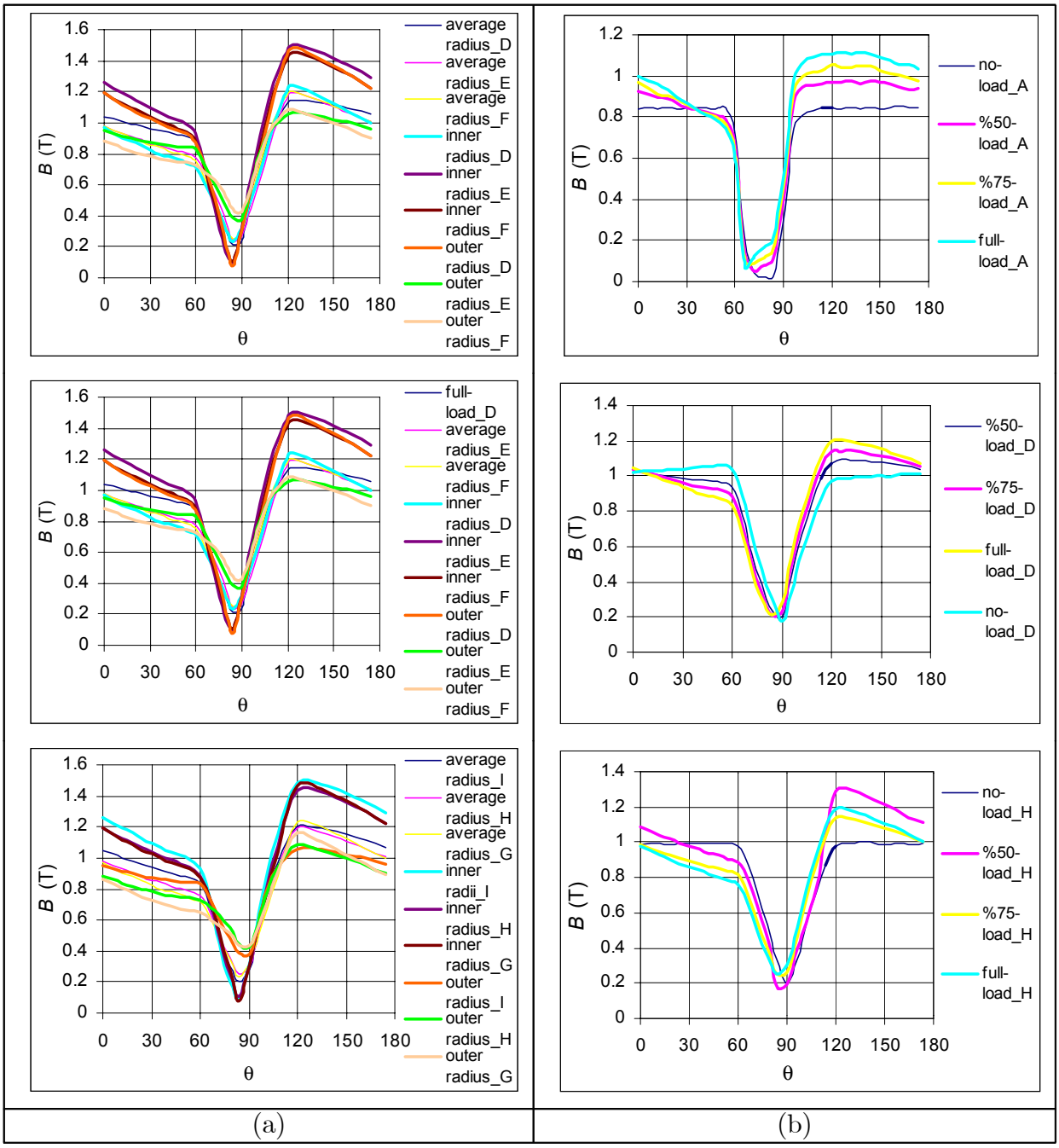

Figure 5.9: Stator flux density variations at points A, B, C, D, E, F, G, H, and I at different radii (a), and at points A, D, and H at several load conditions corresponding to average radius (b).

Fig.5.9, the maximum flux density levels are changing between 0.9 T and 1.5 T depending on the core region and load level. Considering the ultimate condition that a very low-loss steel is used for the stators, core losses can easily be minimized with this design. This is due to the fact that the machine was designed with only four poles, and the maximum frequency was kept around 533 Hz (at 16000 rpm). With modern thin low-loss steel laminations, and with this low level of core flux density, an acceptably low amount of core losses could be achieved at this frequency.

5.5.3 Magnet flux density oscillations

The magnet operating point at several load conditions should be calculated from FE analysis to prevent working with loads exceeding the magnet's demagnetization limits. The magnets used for the prototype have very high demagnetization limits as will be discussed in chapter 7. Therefore, there is no immediate danger of demagnetization due to armature reaction flux at full-load condition. The magnet demagnetization constraint will be included in chapter 7, in relation with the magnet temperature, which determines the overloading capability of the machine.

On the other hand, in order to numerically evaluate the eddy current losses, the amount of flux oscillations that the magnets are exposed to should be verified. The information obtained from static-field analysis (at no-load and several load conditions) enables an easy analytical calculation of the eddy current losses in the rotor iron and magnets[1]. The calculation method will be discussed in section 6.4.

In contrast with the analysis of the stator oscillating fluxes, in this case positional information is collected over a slot pitch instead of a pole pitch. The static FE analysis is repeated 15 times over a slot pitch at several load conditions as well as at different cross-sections of the machine. The oscillating fluxes are calculated along a line near the airgap over a magnet pole pitch.

As an example, Fig.5.10a shows the distribution of the flux density in the magnet as a function of three rotor positions, while the stator current synchronously rotates with the rotor at average radius. It is clear from the figure that, different parts of the magnet are exposed to different values of oscillating flux density. Magnitudes of these oscillations are shown in Fig.5.10b at no-load, full-load and half-load condition. The effect of slotting can be most clearly seen on the no-load waveform. As could be expected the oscillating fluxes are not purely sinusoidal and contain harmonics. Fig.5.11 shows the oscillating flux densities with respect to rotor position at several randomly picked points taken on the magnet span (indicated with an electrical angle in reference to Fig.5.1) as a representative example.

To compute the eddy current losses the average oscillating flux density should be determined as a function of load level considering the fluctuations at several cross-

[1]The oscillating flux density values obtained from the FE program are used in the developed analytical performance analysis program for quick calculations.

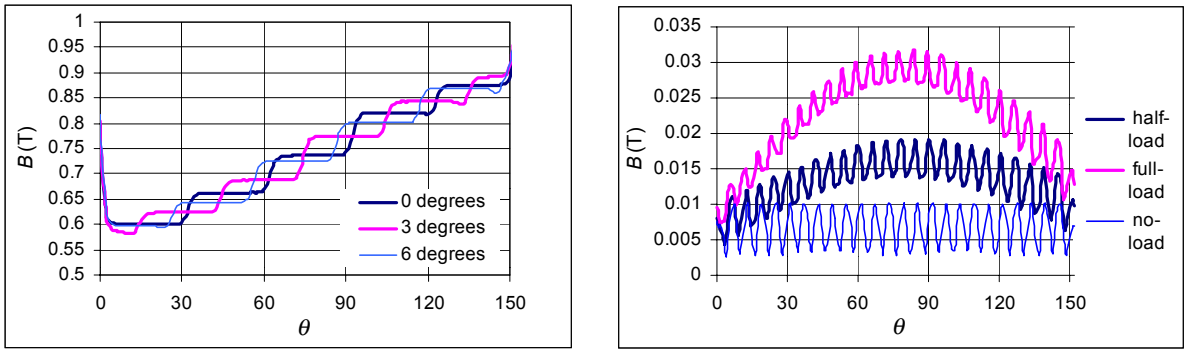

(a) (b)

Figure 5.10: (a) Flux density distribution over the magnet at 0°, 3°, 6° mechanical rotor position. (b) The magnitude of flux density oscillations over the magnet span at no-, half-, and full-load.

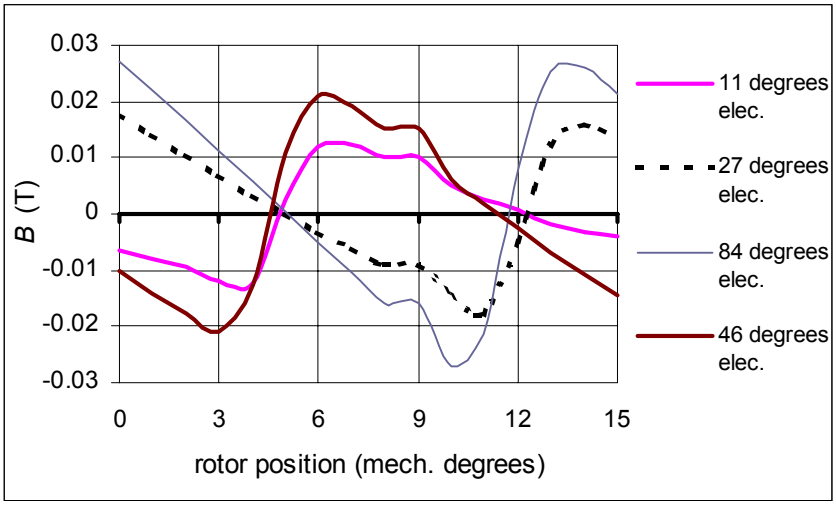

Figure 5.11: Oscillating flux density with respect to rotor position at several points on the magnet span represented with an electrical angle.

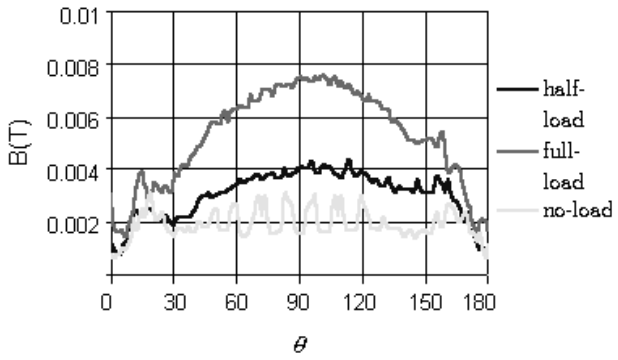

Figure 5.12: The magnitude of flux density oscillations over the rotor polar span at no-, half- and full-load.

sections of the machine. Approximated (root mean square of 200 points over the magnet span) flux density fluctuation levels over the whole magnet span are found to be 0.069 T, 0.026 T, and 0.027 T on the inner, average and outer radii respectively. These values are used later for performance calculations as will be discussed in 6.4.

5.5.4 Rotor flux density oscillations

The same analysis has also been made for the rotor steel which also contributes to the eddy current losses although they are negligible compared to the magnet rotor losses. Fig.5.12 shows the amount of flux density oscillations that the rotor is exposed to. The level of oscillations is not as high as in the magnet.

5.5.5 Magnet leakage flux

The magnet leakage flux coefficient which was discussed in section 3.4, is the ratio of the airgap flux and the magnet flux. The amount of magnet leakage flux can also be calculated from FE analysis through the potential difference on the corners of the magnet where the leakage occurs. Magnet leakage flux is seen in Fig.5.13. In the design stage the amount of magnet leakage was also taken into account for the determination of the required magnet span.

5.6 EMF

FE analysis conducted at incremental rotor positions are also used to calculate the phase-emf waveforms. The curves are deduced from the time derivative of the ob-

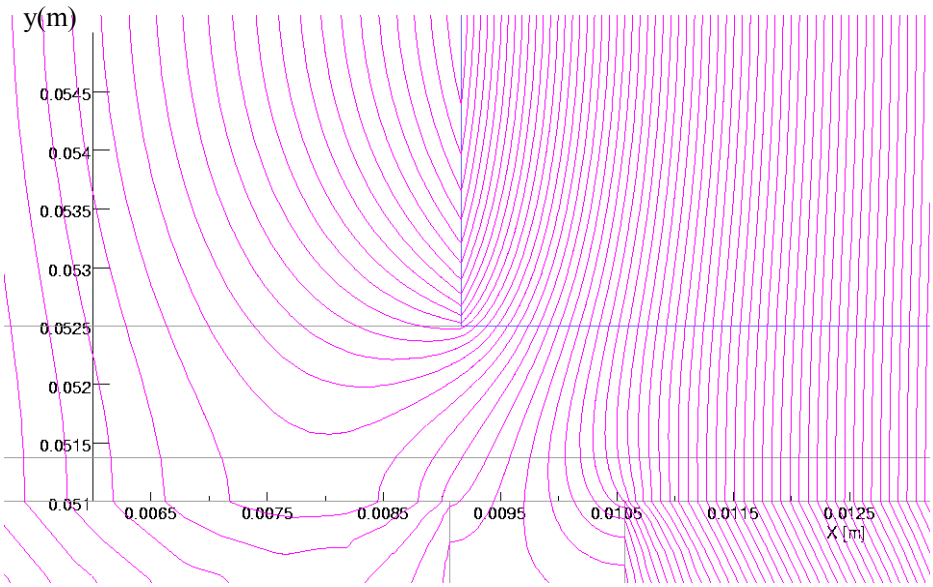

Figure 5.13: Magnet leakage flux.

tained flux variation with respect to rotor position. The effect of the winding distribution into slots should also be taken into account while constructing the emf curves. Fig.5.14a shows the phase-emf waveform calculated from the FE analysis conducted at 30 points over a pole pitch corresponding to the average diameter. Fig.5.14b shows the flux linkages of the four coils belonging to a phase. The phase delay between the coils is due to the distributions of the coils in slots and short pitching as discussed in section 4.3.

5.7 Torque ripple

The torque is computed from FE analysis using the Maxwell stress tensor method. The method is simple from a computational perspective. It only requires the local flux density distribution over a line in the airgap. The accuracy of the method is dependant on the model discretization and on the selection of the integration line. Maxwell stress tensor integration necessitates very fine discretization, consequently a very precise solution of the flux density distribution in the airgap region. The dependence of the resultant accuracy of Maxwell stress tensor method on the airgap discretization is studied in detail in [66].

Using the method, the total electromagnetic force or torque can be determined by the line integral along a closed path ℓ. The normal and tangential forces acting

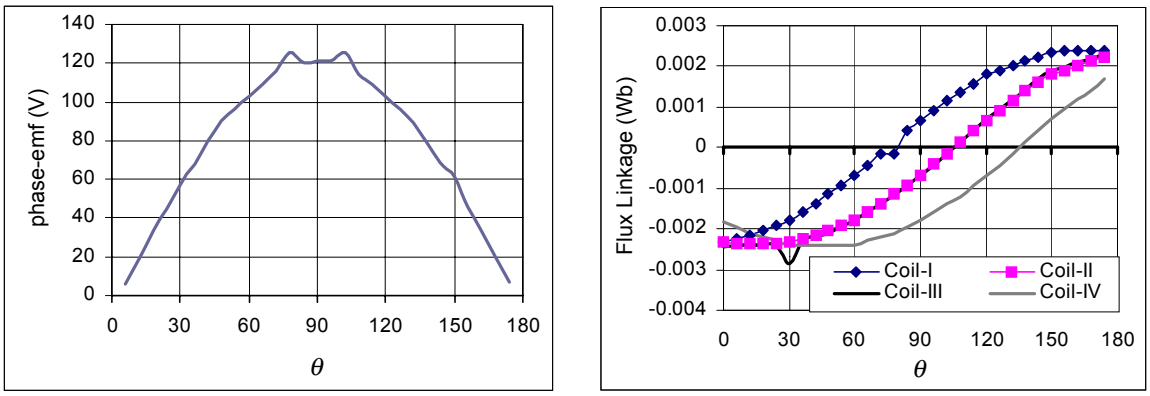

(a) (b)

Figure 5.14: (a) Phase-emf obtained from the incremental position analysis at no-load corresponding to the average radius, (b) Coil flux linkages with respect to rotor position.

on a straight line contour are given by [33]

$$F_n = \frac{L_i}{\mu_o} \int \left(B_n^2 - B_t^2\right) d\ell, \tag{5.16}$$

$$F_t = \frac{L_i}{\mu_o} \int \left(B_n B_t\right) d\ell. \tag{5.17}$$

where L_i is the stack length which is perpendicular to the normal and tangential components of the flux density. The torque at a radius r is given by

$$T = \frac{L_i}{\mu_o} \int B_n B_t r d\ell. \tag{5.18}$$

It should be noted that for AFPM machines every radial cross-section of the model corresponds to a different radius. Considering the finite discritization on the line, the total torque is the sum of the torque contributions of all elements

$$T = \frac{L_i}{\mu_o} \sum_j r \int_{\ell_j}^{\ell_{j+1}} B_{nj} B_{tj} d\ell. \tag{5.19}$$

In section 4.13, torque ripple components of permanent-magnet motors were categorized and the analytical predictions were made. Here, the calculation of these components with FE analysis is presented.

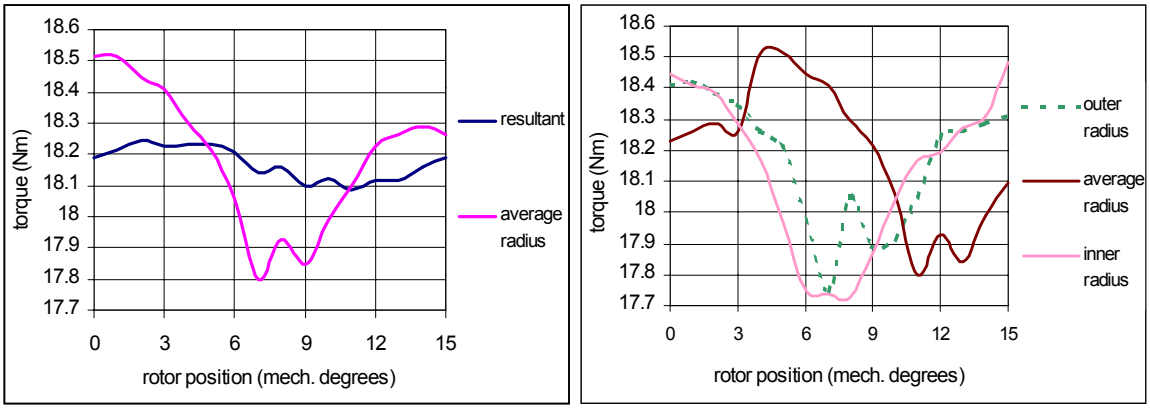

(a) (b)

Figure 5.15: (a) The resultant torque with respect to rotor position taking the effect of the magnet skew into account in comparison with the torque at the average radius (b) The computed torque-position curves at inner, outer and average radius.

5.7.1 Pulsating torque

Pulsating torque is produced due to the spatial components of the windings and permanent magnets. Hence, in order to evaluate the amount of torque ripple, the static analysis is done in 20 incremental rotor positions over a slot pitch, while the stator currents are rotating synchronously with the rotor. The Maxwell stress tensor is calculated along the airgap on three airgap lines to check the accuracy of the analysis [66]. For the sake of accuracy adaptive meshing is used. The resultant torque with respect to rotor position taking the effect of magnet skew into account is shown in Fig.5.15a, in comparison with the torque calculated at the average radius. The computed torque-position curves at the inner, outer and average radii are scaled (normalized) with respect to the average torque for the sake of comparison and they are shown in Fig.5.15b.

5.7.2 Cogging torque

Cogging torque occurs due to the reluctance variations in the airgap mainly because of slotting. This component also exists when there is no armature excitation, so it can be determined with the FE method by calculating the torque for several positions of the rotor at no-load case (as in the case of pulsating torque). The mesh accuracy is especially important in the case of cogging torque calculations [66]. It is also claimed in [66] that calculating the Maxwell stress tensor exactly on the middle line on the airgap increases the accuracy. The results are presented in Fig.5.16.

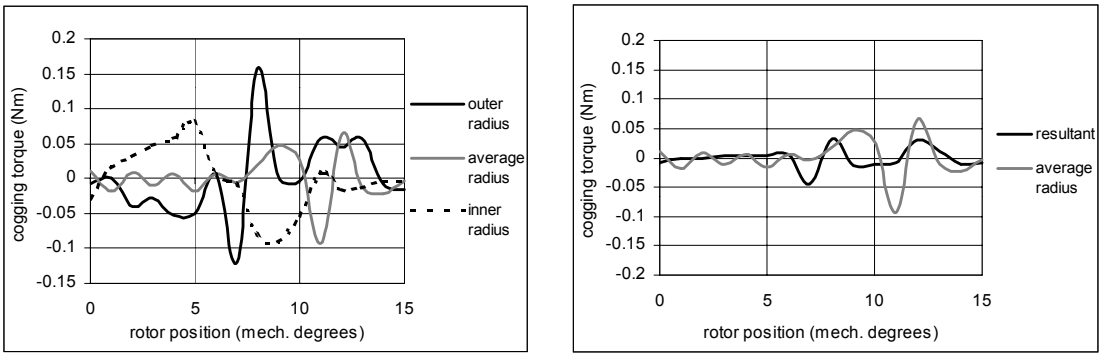

(a) (b)

Figure 5.16: (a) The resultant cogging torque with respect to rotor position taking the effect of magnet skew into account in comparison with the cogging torque contribution at average radius (b) The computed cogging torque-position curves at inner, outer and average radius.

5.7.3 Torque-angle characteristics

The FE analysis is repeated at incremental rotor positions over a polar span with constant stator excitation. Hence, the torque-angle characteristic of the machine is obtained. The result is presented in Fig.5.17, where the slotting effect can be clearly seen.

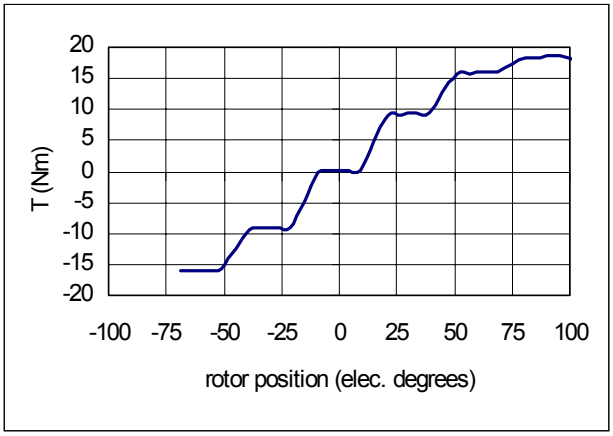

Figure 5.17: Torque with respect to rotor position.

5.8 Inductances

5.8.1 Armature reaction inductance

Since the magnet flux has no contribution to the armature reaction reactance, it is calculated from the field solution that only takes the stator current distribution into consideration. Fig 5.18 depicts the magnetic vector potential distributions in the airgap over a pole pair at full-load and half-load conditions.

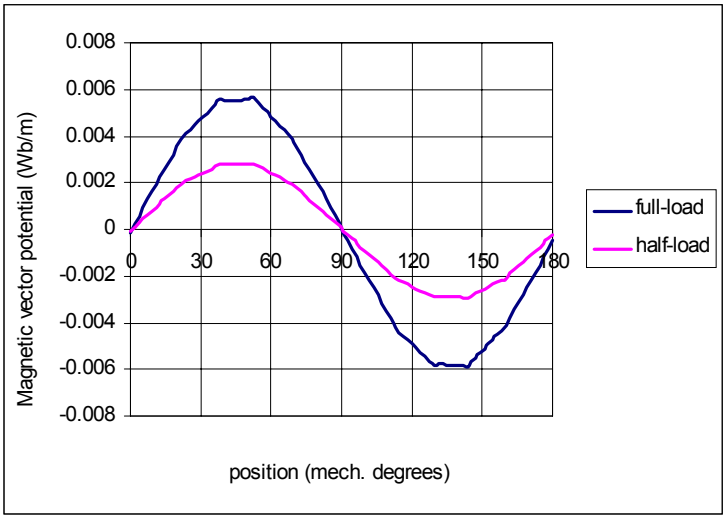

Figure 5.18: Magnetic vector potential distribution in the airgap at full-load and half-load conditions

The flux passing between two points is equal to the integral of the magnetic vector potentials between these points. In this case, the flux per pole may be assumed to be twice the peak value of the magnetic vector potential of the mid-point of the pole as seen in Fig.5.18, because the magnetic vector potential distribution along the neighboring pole exhibits the identical pattern with a negative sign. Since this value is valid for the unit length, it should also be multiplied by the effective length of the stator. Using the flux linkage equation which takes the sinusoidal conductor distribution into account, the armature reaction inductance can be calculated as

$$L_{a1} = \frac{\Psi_{a1}}{\sqrt{2}I} = \frac{k_{w1} N_{ph} 2 A_1 L_i}{\sqrt{2}I} \tag{5.20}$$

where A_1 is the amplitude of the fundamental component of the magnetic vector potential (0.00575 Wb/m for full load). L_{a1} is found as 0.092 mH, while the analytical calculation gives 0.0913 mH. Inductance variation is found to be equal at different load conditions as expected.

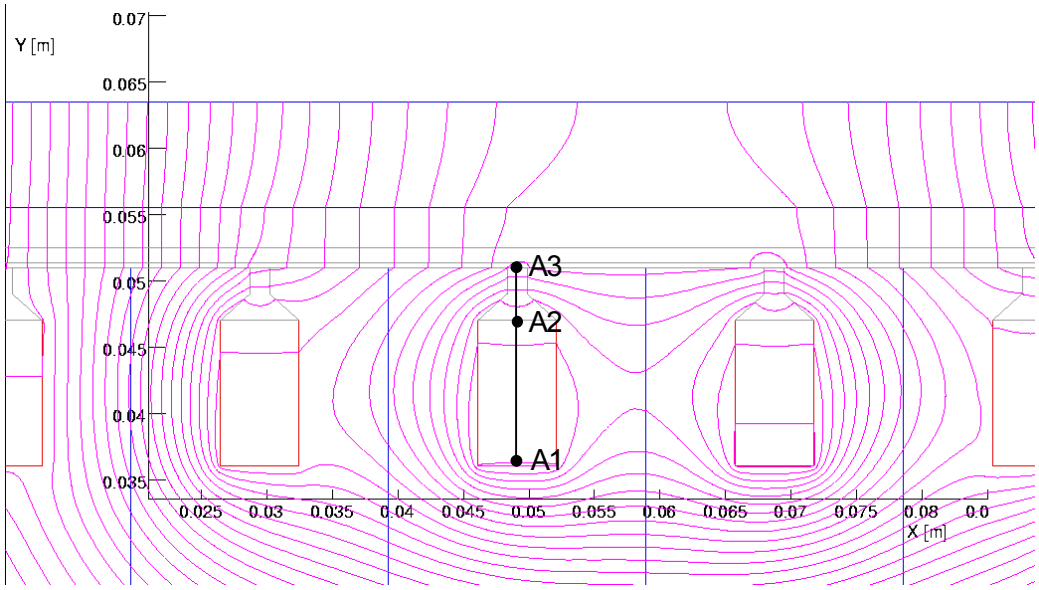

Figure 5.19: Slot leakage flux.

5.8.2 Slot leakage inductance

The slot leakage flux is shown in Fig.5.19 which is obtained using the analysis in which the magnet flux is assumed non-existent. As seen from Fig.5.19, along the conductor regions there are also leakage flux lines, so the method used for the calculation of the armature reaction reactance is not applicable in this case. All conductors which are homogeneously distributed in a slot, are not linked with an equal amount of flux. Hence, two different subregions of the slot area should be considered separately as in the case of the analytical calculation (see section 4.4.2). They are the rectangular area of the conductors and the slot top area.

Fig.5.20 shows the magnetic vector potential distribution along the slot. The three magnetic vector potential values A1, A2, A3 correspond to the vector potential at the slot bottom, at the upper end edge of the conductor area and at the slot top, respectively. The flux passing through the second region (can be defined as the difference between A2 and A3) links all the conductors. But the flux passing through the conductors links only a fraction of the conductors. This can be represented with an integral equation. The contributions of these two regions to the total leakage flux linkage can be represented as follows taking the number of conductors per slot (n_s), and the depth of the slot (d_b) into account

$$\Psi_{sl} = n_s(A_2 - A_3)L_i + \int_0^{d_b} \frac{n_s}{d_b} A(y)dy, \tag{5.21}$$

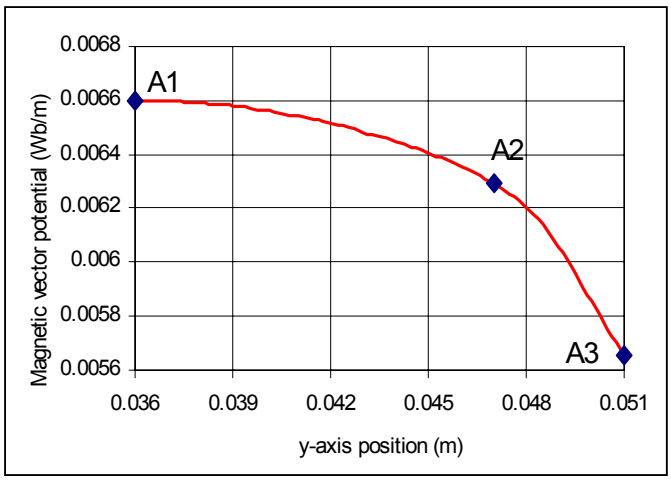

Figure 5.20: Magnetic vector potential distribution along the slot.

where the first part of the equation represents the contribution of the leakage flux in the slot-top region and the integral part is the contribution of the leakage flux in the conductor region. $A(y)$ represents the magnetic vector potential value along the slot. Eq.5.21 reduces to

$$\Psi_{sl} = \frac{n_s L_i}{d_b} \int_0^{d_b} A(y)dy - A_3 n_s L_i. \tag{5.22}$$

The vector potential values and the integral part are obtained from FE analysis. Then, the slot leakage inductance per phase per stator is calculated as

$$\begin{aligned} L_{sl} &= \frac{n_{spp} 2p}{\sqrt{2}I} \left[\frac{n_s L_i}{d_b} \int_0^{d_b} (A(y)dy - A_3 n_s L_i \right] \\ &= \frac{2N_{ph} L_i}{\sqrt{2}I} \left[\frac{1}{d_b} \int_0^{d_b} (A(y)dy - A_3) \right]. \end{aligned} \tag{5.23}$$

The analysis gives the integral value as 0.0000715 Wb and A3 as 0.00628 Wb/m. The resultant slot leakage inductance calculated from FE is 0.015 mH, and the analytical approach gives 0.016 mH.

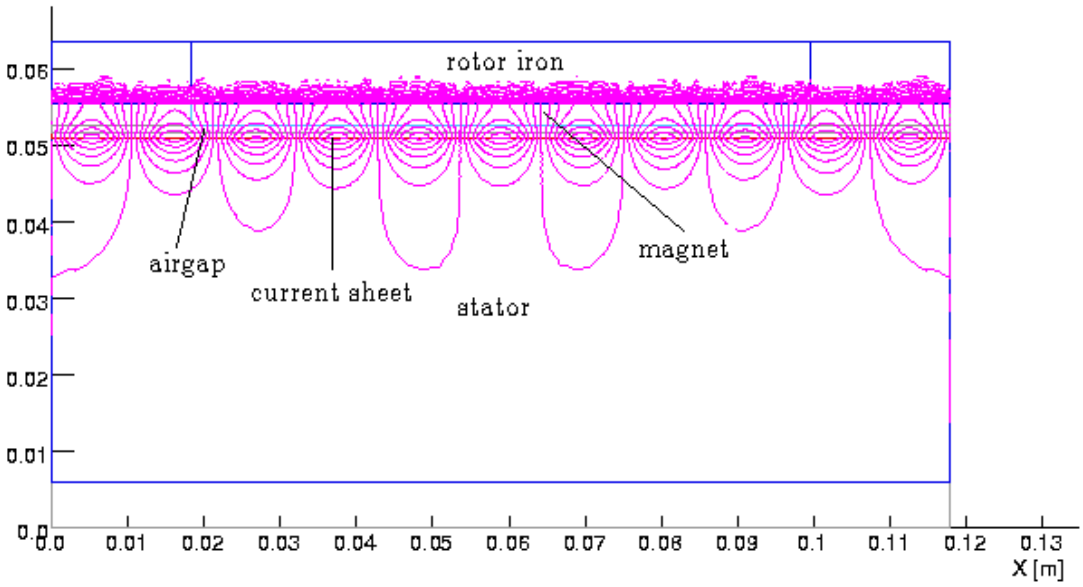

Figure 5.21: Flux lines for the 11^{th} space harmonic component of the winding obtained from FE-AC analysis at 6240 Hz.

5.9 Eddy current loss analysis

Eddy current losses in the magnets and the rotor steel are calculated using FE-AC analysis. The analysis is repeated for every space harmonic component (up to order 49), in combination with the simulated time harmonic components of the current waveform. It should be noted that for a certain space harmonic, the magnet width τ is equivalent to the pole pitch of that space harmonic component (i.e. $\tau = \tau_p/11$ for the 11^{th} harmonic component, where τ_p is the pole pitch of the machine). A flux plot of the AC analysis is shown in Fig.5.21 for the 11^{th} order space harmonic and the fundamental of the current as a representative example. The thin surface current density layer is defined next to the airgap and the effect of slotting is neglected. The frequency is 12×520 Hz in the example representing 15600 rpm. The loss at full load only due to the 11^{th} space harmonic component is 27 W in the magnet and 1 W in the rotor iron.

The flux density distribution along the rotor for the 11^{th} and 13^{th} space harmonic components are shown in Fig.5.22 where the oscillating character can be clearly seen.

The analysis was also repeated for the time harmonic components of the stator current (see Fig.5.23), obtained by means of simulating the equivalent circuit of the converter fed machine using ICAPS. The simulation circuit is derived in Appendix C, and the simulated current waveform is shown in Fig.5.24. The resultant eddy current

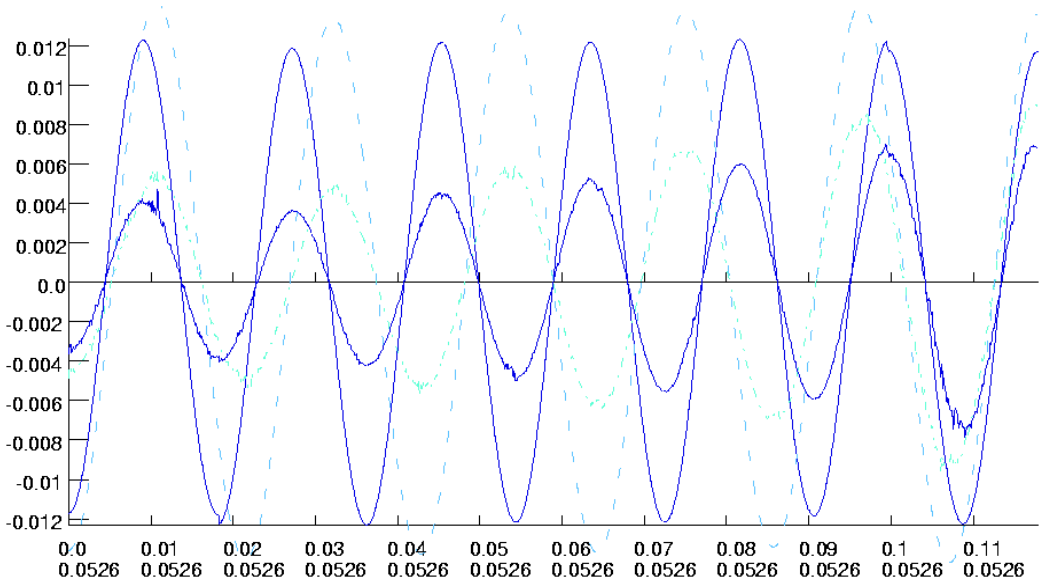

Figure 5.22: Oscillating flux density distribution along the rotor pole pitch for the 11^{th} (dashed line) and 13^{th} (straight line) space harmonic component.

loss values (per unit length per pole) obtained for the dominant time (q), and space (n) harmonic components are presented in Table 5.1.

5.10 Conclusions

An overview of the FEM and the way it is utilized in this study, are presented in this chapter. Many illustrations were included. The effect of discretization on the accuracy was pointed out and an adaptive meshing example was given. The analyses of flux density, emf, torque ripples, inductances and eddy current losses and their results for the designed AFPM machine are presented. Special attention was given to the flux density variations in stator core regions, magnets and rotor steel. The findings of these extensive analyses will be further used in the following chapter for efficiency estimations.

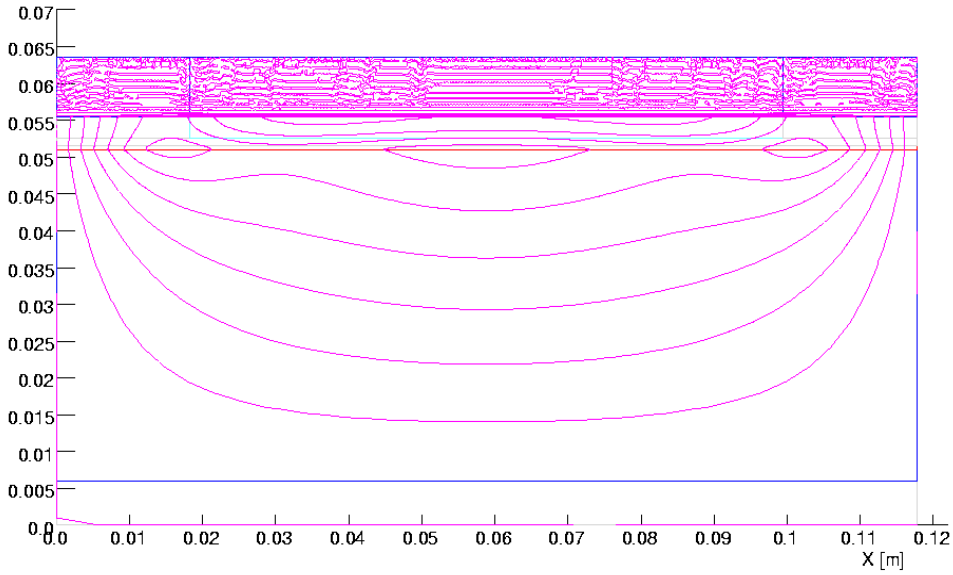

Figure 5.23: Flux lines for the 5^{th} time harmonic component of the stator current obtained from FE-AC analysis at 3120 Hz.

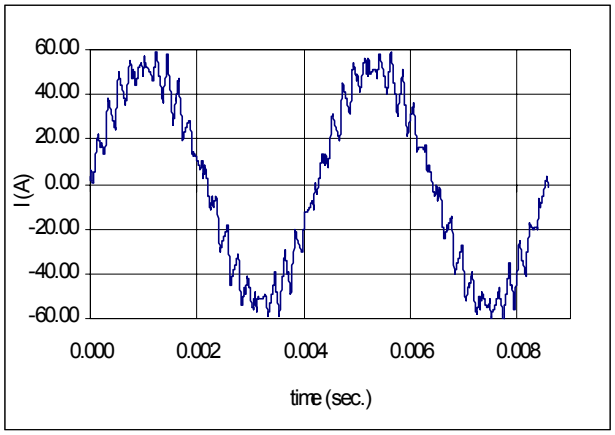

Figure 5.24: Simulated phase current waveform

n	q	P_{magnet}	P_{rotor}
5	1	1.84	0.16
7	1	0.71	0.03
11	1	83	2.13
13	1	42	0.9
17	1	0.14	0.002
19	1	0.08	≈0
23	1	10.8	0.061
25	1	6.9	0.04
29	1	0.025	6.5
31	1	0.02	≈0
35	1	2.5	0.003
37	1	1.74	≈0
41	1	0.007	0

n	q	P_{magnet}	P_{rotor}
43	1	0.005	≈0
47	1	0.71	≈0
49	1	0.53	≈0
1	5	34.9	0.23
1	7	22.3	0.14
1	11	2.67	0.018
1	13	1.44	0.01
1	17	1.48	0.011
1	19	0.6	0.005
1	23	0.079	≈0
1	25	0.51	0.004
1	29	1.02	0.01

n	q	P_{magnet}	P_{rotor}
1	31	0.15	0.001
1	35	1.13	0.011
1	37	0.053	≈0
5	5	0.03	0.002
5	7	0.011	0.001

Table 5.1: Per unit length (1 m), per pole eddy current loss components (W/m) in the magnet and rotor iron.

Chapter 6

Losses

6.1 Introduction

In order to estimate the efficiency and the thermal behavior of the machine accurately, much attention is paid to the calculation of the losses. In this chapter the calculation of the loss components and the prediction of the machine's efficiency map are discussed. The loss components of the machine can be summarized as

$$P_{loss} = P_{cu} + P_{fe} + P_{rotor} + P_{mech} + P_{add}, \tag{6.1}$$

where P_{cu}, P_{fe}, P_{rotor}, P_{mech}, P_{add} are copper losses, stator core (iron) losses, rotor eddy current losses, mechanical losses and additional loss components respectively. The loss components due to the external cooling system are not considered here. Additional loss components should be considered as the sum of the small losses which are not exactly known [67]. Examples of small losses can be considered as the converter related iron and rotor losses, eddy current losses that may occur in the aluminum frame, and losses due to anisotropic effects. The additional losses are assumed in the calculations as 0.5% of the input power.

In sections 6.2 to 6.5 the prediction of the copper, stator core, rotor, and mechanical losses are successively dealt with and their calculation methods are given. In section 6.6, estimated efficiency maps of the machine in normal and reduced inner air pressure conditions are included. Finally, in section 6.7 the effect of design parameters on the efficiency is investigated. These parameters are the stator outside diameter, the inside to outside diameter ratio, and the airgap flux density.

6.2 Copper losses

The I^2R losses cover a large part of the total losses. They depend on the load as well as the temperature of the windings. It should be noted that in an AFPM machine,

Figure 6.1: End windings

the major part of the copper losses is generated in the end windings rather than in the slots. Thus, in order to increase the efficiency, the end winding design deserves special attention. With the use of short-pitched windings, the length of the end-windings is reduced. On the other hand, the relatively longer connections between the coils should correspond to the inner end of the stators in the winding design. The end windings are shown in Fig.6.1. The design of the windings and the dimensions of the slots were discussed in chapter 4.

The calculation of the copper losses is an approximation because the length of the end windings is not exactly known. Using a similar approximation as in the case of end-turn leakage reactance calculation in section 4.4.3, and considering the end-winding shapes shown in Fig.4.5, the length of a turn is written as

$$\ell_{turn} = 2L_i + \ell_{iend} + \ell_{oend} = 2L_i + (\tau_{co} + \tau_{ci})\,\frac{\pi}{2}. \tag{6.2}$$

The phase resistance is

$$R_{ph} = \frac{N_{ph}\ell_{turn}}{\sigma A_c}, \tag{6.3}$$

where σ and A_c are the effective conductance of the copper and the cross-sectional area of the conductor, respectively. The resistance of the conductor is a function of the temperature as

$$R_{ph}(T_2) = R_{ph}(T_1)\left[1 + \alpha_{T_1}(T_2 - T_1)\right], \tag{6.4}$$

where α_{T_1} is the temperature coefficient at a particular temperature T_1. This coefficient can also be converted to another temperature, i.e. T_2, as

$$\alpha_{T_2} = \frac{\alpha_{T_1}}{1 + \alpha_{T_1}(T_2 - T_1)}. \tag{6.5}$$

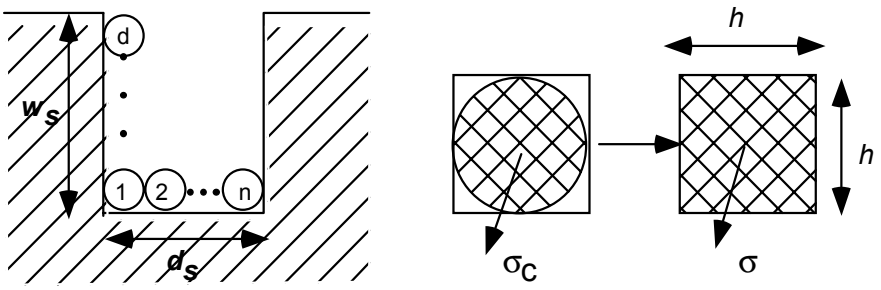

Figure 6.2: Conductor distribution in a rectengular slot

The slots of the machine are filled with small-diameter conductors, in order to decrease the eddy current losses that may occur in the windings at higher frequencies. The eddy factor, which is the ratio of the AC to the DC resistance should be taken into account, which may cause discrepancies with increasing frequency. The dependence of the eddy factor on the frequency is explained in [68], [69]. The method recommended in [68] is used for the calculation of the eddy factor.

Fig.6.2 [68] shows the conductors in a slot and the presentation of a round conductor as a rectangular equivalent just by assuming the effective conductance of the rectangular conductor as $\sigma = \sigma_c k_p$, where σ_c is the conductance of copper and k_p is the slot filling factor. Then the effective resistance, which is a function of the frequency, can be written [68] as

$$R = R_{dc}\left\{\frac{h}{\delta_c}\frac{\sinh 2(h/\delta_c)+\sin 2(h/\delta_c)}{\cosh 2(h/\delta_c)-\cos 2(h/\delta_c)}+\frac{2}{3}(d^2-1)\frac{h}{\delta_c}\frac{\sinh(h/\delta_c)-\sin(h/\delta_c)}{\cosh(h/\delta_c)+\cos(h/\delta_c)}\right\}, \tag{6.6}$$

where δ_c is the skin depth in copper. The high frequency eddy current losses in the windings are reduced to 0.4% of the total copper losses at rated speed (16000 rpm) by dividing the coils into small strands (1mm diameter).

6.3 Core losses

After copper losses, core losses, which are more significant at higher speeds, are generally the second largest loss component in AC machines. Normally, core losses in the stators are viewed as being caused mainly by the fundamental-frequency variation of the magnetic field. However, in addition to the fundamental component, flux variation includes plenty of higher-order frequency components. Their contribution can not be neglected. Moreover, the exposure to the flux density variation at different parts of the core is not the same, especially in an AFPM machine, where the slot to

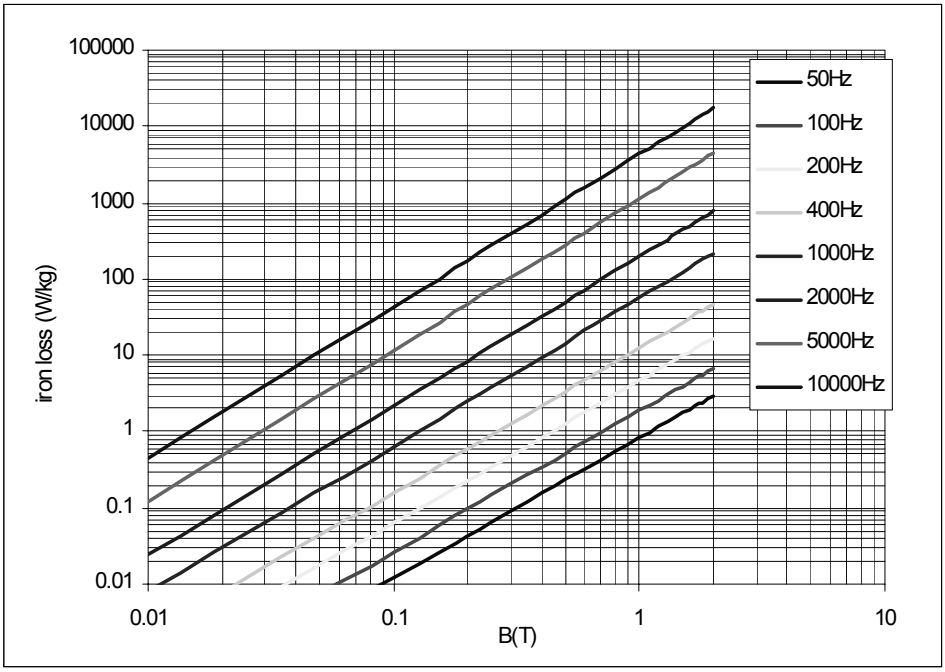

Figure 6.3: Power loss characteristics of M4 steel.

tooth ratio changes with the radius. The core is also exposed to much higher order harmonic components due to switched supply voltage.

Under alternating flux conditions, the stator core loss density p_{fe} in W/kg can be separated into a hysteresis (p_h) and an eddy current component (p_e), and can be written in terms of the Steinmetz equation [43], [70] as

$$p_{fe} = p_h + p_e = c_h \widehat{B}^{n(\widehat{B})} f + c_e \widehat{B}^2 f^2, \tag{6.7a}$$

where c_h, c_e, and n are constants determined by manufacturer's data. Due to the difficulty of purchasing a laminated toroidal core made by thin silicon steel sheets, the M-4 grain-oriented silicon steel is chosen for the prototype machine. The properties and the problems related with this steel will be further discussed in chapter 8. The power loss data of the steel (Fig.6.3), which is only available in the preferred direction of magnetization, is used to fit the Steinmetz equation that describes the specific loss in W/kg as

$$p_{fe} = 0.014492 \widehat{B}^{1.8} f + 0.00004219 \widehat{B}^2 f^2. \tag{6.8}$$

For a fine calculation of the stator core losses, the stators of the AFPM machine are divided into regions. Since the magnitude of the flux density varies over different

cross-sections of the stator (between the inside and the outside diameters), FE analysis is made at several diameters of the stator and at different rotor positions over a pole pitch. The results were presented in section 5.5.2. The resultant flux density waveforms and their higher frequency harmonic components are obtained at different parts of the stator such as slots, slot-tops and stator yoke. From this thorough magnetic field analysis a fine estimation of the core losses is made.

Due to the use of this unconventional steel for the prototype and the consequent fact that extra losses caused by anisotropic effects are not exactly known, the calculated loss do not exactly coincide with the measured one. Nevertheless, an extensive calculation method, aiming at completeness and accuracy, is proposed. This method considers both the flux density variation in different parts of the stator and the harmonic contents of these variations.

In order to take the aforementioned anisotropic effects in the slot direction into account, the calculated losses for these parts are just multiplied with a small coefficient, based on the measurement results presented in [71].

6.4 Rotor losses

In high-speed permanent-magnet machine applications, rotor losses generated by induced eddy currents may amount to a major part of the total losses. The eddy currents are mainly induced in the permanent magnets, which are highly conductive, and also in the rotor steel. The major causes of eddy currents can be categorized into the following three groups:

1. No-load rotor eddy current losses caused by the existence of stator slots. Due to slotting the flux density is stronger under the teeth and weaker under the slots. The frequency of the induced current is equal to the slot frequency of the machine. Having slot-tops, the magnitude of the loss caused by the slot phenomenon can be made very small.

2. On-load rotor eddy current losses induced by the major mmf winding harmonics: For the designed machine (as mentioned in section 4.3) the major winding harmonics are the 11^{th} and the 13^{th}. The contribution of the higher-order winding harmonics is relatively small as discussed and presented in 5.9.

3. On-load rotor eddy current losses induced by the time harmonics of the phase currents. The simulated current waveforms as shown in appendix D, are used to predict these losses.

Since there is no trivial way to remove the heat generated in the magnets, the estimation of the rotor eddy current losses is particularly important in this case. Especially in the case of reduced air pressure inside the machine by means of a

vacuum, where the convection resistances between rotor and frame and rotor and stators are relatively large, rotor heat removal becomes a major problem as will be discussed in section 7.8. Excessive heat may result in the demagnetization of the magnets and possibly rotor destruction. Primarily, the reduction of rotor losses was not chosen as a major objective, and therefore the simplest rotor construction was realized. A substantial reduction of the rotor losses to a negligible level can only be made possible by the choice of a proper low-loss material (low-loss steel or maybe powdered iron) for the rotor iron complemented by a proper lamination of the magnets. The complimentary is quite strong and therefore only one of these methods would not yield a substantial improvement. Extra shielding, such as a copper bandage [72] may not solve the problem due to the loss in the copper itself. The topic of shielding and other less expensive solutions call for proper 3-D field analysis (in order to include end effects) and time stepping. These issues are recommended for future research.

Eddy current losses in the magnets and the rotor steel are calculated using two different methods. The first method includes the use of FE-AC software. The method of calculation wherein the analysis is repeated for every space harmonic component (up to order 49), was explained in section 5.9. The analytical method, which uses the positional magnet flux density waveforms obtained from FE solutions, will be explained later in this section. The advantage of calculating loss from static FE solutions over a FE-AC solution is the fact that the contributions of the stator slotting and the space harmonic flux ripple can both be included. In FE-AC solutions the effect of slotting can not be included due to the fact that the stator is modelled with a thin surface-current layer adjacent to the airgap, instead of a real slotted model. One can also calculate the loss contributions of the current time and winding space harmonics analytically by using the method explained in [72]. The positional-static FE analysis results as discussed in section 5.5.3 can be used to calculate the flux ripple. In fact, this method can be categorized as half analytical/half static FE analysis. It should also be noted that none of these methods is accurate because they neglect the end effects completely, especially in the case of an AFPM machine where there are no laminations in radial direction and the magnet pitch is relatively large.

The eddy current loss problem in a magnet may be explained with the use of Fig.6.4 considering the magnet cube with length L_i, pitch τ_m, and thickness L_m. The eddy current path (c) created by the existence of the time varying flux density $\overrightarrow{B}$ in z-direction is shown. The eddy current problem can be solved one-dimensionally by writing Maxwell Equations

$$\nabla \times \overrightarrow{E} = \frac{\partial \overrightarrow{B}}{\partial t}, \tag{6.9}$$

$$\nabla \times \overrightarrow{H} = \overrightarrow{J}, \tag{6.10}$$

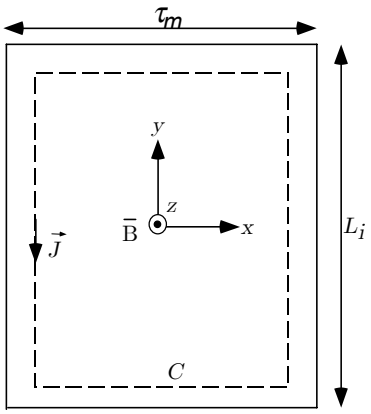

Figure 6.4: Eddy currents in a magnet cube

$$\overrightarrow{J} = \sigma \overrightarrow{E}. \tag{6.11}$$

Integrating both sides of Eq.6.9 and using Stokes' theorem

$$\oint_c \overrightarrow{E} \cdot \overrightarrow{dl} = \int_s \left(\nabla \times \overrightarrow{E} \right) \cdot \overrightarrow{ds}, \tag{6.12}$$

yields

$$\oint_c \overrightarrow{E} \cdot \overrightarrow{dl} = \frac{\partial}{\partial t} \int_s \overrightarrow{B} \cdot \overrightarrow{ds}. \tag{6.13}$$

The flux density equation for a certain harmonic component can be written in rotor coordinates as

$$B(x,t) = \widehat{B} \cos(\omega_e t \pm npx) = \widehat{B} \cos((q \pm n)\omega_s t \pm npx), \tag{6.14}$$

for $(q+n) = 6, 12, 18, ...$ and $(q-n) = 6, 12, 18, .. .$ In order to solve the problem in Cartesian coordinates, the angular variable θ_r is replaced with x, where the pole pitch τ is equivalent to π.

In Eq.6.14 the variable q represents the order of time harmonic components of the current and n represents the order of space harmonic components of the windings. It should be noted that the contribution to the losses should be calculated for every combination. The dominant space harmonics in the designed machine are the 11^{th} and the 13^{th} as explained in section 5.9, so the attention here is only given to the asynchronous components which have a rotor frequency $12\omega_s$.

With the use of the electrical power equation

$$P = \int_V \sigma \overrightarrow{E}^2 dV = \int_V \frac{\overrightarrow{J}^2}{\sigma} dV, \tag{6.15}$$

and considering the time average (over a time period T) of the power, the power loss equation for the magnet cube shown in Fig.6.4 becomes

$$P = \frac{1}{T} \int_0^T \int_0^{L_m} \int_0^{L_i} \int_{-\tau/2}^{+\tau/2} \frac{J^2(x,t)}{\sigma} dxdydzdt. \tag{6.16}$$

Using Eq.6.11 and 6.13, and considering the integral path shown in Fig.6.4, the surface current density can be related to the time-varying flux density of the magnet as

$$J(x) = x\sigma \frac{dB(t)}{dt}. \tag{6.17}$$

It should be noted that the end effects are neglected which means that the current density J has only $y-$axis component (where $J(-x) = J(x)$), and the flux density is one dimensional (z) and homogeneous. A similar approximation can also be found in [73]. In this manner the eddy current loss can be calculated from the static FE solutions.

The integral equation 6.16 can be simplified as

$$\begin{aligned} P &= \frac{1}{T} \int_0^T \int_0^{L_m} \int_0^{L_i} \int_{-\tau/2}^{+\tau/2} \sigma x^2 \left(\frac{dB(t)}{dt} \right)^2 dxdydzdt \\ &= \frac{1}{T} \int_0^T \int_0^{L_m} \int_0^{L_i} \int_{-\tau/2}^{+\tau/2} \sigma x^2 \left(-\frac{\widehat{B}}{\sqrt{2}} \omega_e \sin(\omega_e t) \right)^2 dxdydzdt, \end{aligned} \tag{6.18}$$

where ω_e is the angular frequency of the eddy currents. The integral equation results in

$$P = \frac{\sigma}{48} L_m L_i \tau^3 \widehat{B}^2 {\omega_e}^2. \tag{6.19}$$

It should be emphasized that for a certain space harmonic the magnet width τ is equivalent to the pole pitch of that space harmonic component (i.e. $\tau = \tau_p/11$ for the case of the 11^{th} harmonic component, where τ_p is the pole pitch of the machine). For the power loss calculation explained above the skin depth in the magnet for the relevant harmonic frequency

$$\delta = \frac{1}{\sqrt{\pi f \mu \sigma}}, \tag{6.20}$$

is assumed to be larger than the magnet depth L_m (which is correct for the dominant harmonic components of the machine).

Other approximations for the eddy current loss can be found in the literature [74],[75],[76],[77], [67],[78] . In [79] an equation (including the derivation) which incorporates the skin depth, can be found

$$P = \frac{\sigma L_m L_i \tau^3 \widehat{B}^2 {\omega_e}^2}{8} \left(\frac{\delta}{3\tau} \frac{\sinh(\frac{\delta}{\tau}) - \sin(\frac{\delta}{\tau})}{\cosh(\frac{\delta}{\tau}) - \cos(\frac{\delta}{\tau})} \right). \tag{6.21}$$

The equations 6.19 and 6.21 give similar results. It should always be kept in mind that the total loss calculation should contain all possible combinations of the current time harmonics and the space harmonics as pointed out in section 5.9.

The same method is also applied to the rotor steel where the only differences are the material conductivity and the permeability values. The conductivity of the permanent-magnet material and the steel are taken as $6.25e5\ \Omega^{-1}$ and $50e5\ \Omega^{-1}$respectively, while the permeability values are taken as 1.075 and 1000. The estimated rotor losses with respect to speed and torque are shown in Fig.6.5.

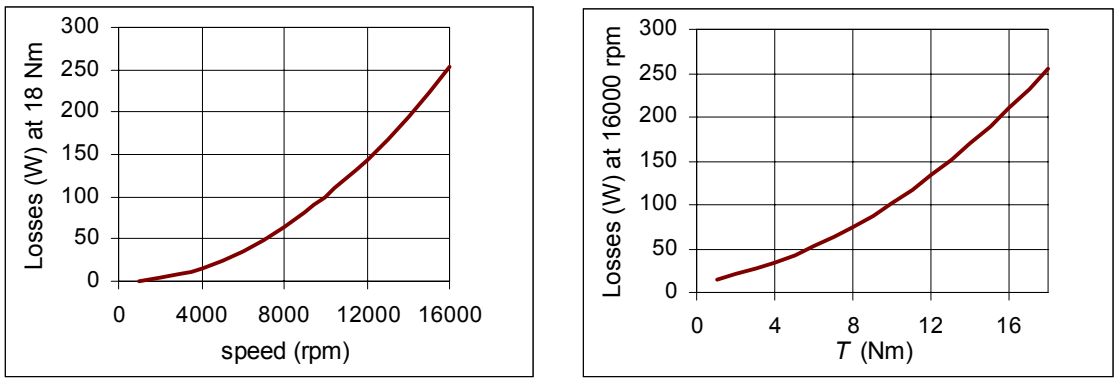

Figure 6.5: Rotor losses with respect to speed and torque.

6.5 Mechanical losses

6.5.1 Windage losses

Friction losses in the air space of high-speed machines largely contribute to the total losses. Especially considering the fact that the circumferential speed of the AFPM machine's rotor is 330 m/sec with, and 217 m/sec without the flywheel (which is many times higher than in standard 50 Hz machines), the heat created by air friction is not tolerable. Hence, the machine frame is sealed and the rotor is designed to run in reduced air pressure conditions.

It is rather important to calculate the friction losses to make good estimations of the efficiency and the thermal behavior of the machine. In order to calculate the loss contribution of the air friction the methods recommended in [80] are used.

The friction torque of a rotating cylinder and rotating disk

The velocity distributions in the airgap of the machine are: a) tangential and axial flows due to the rotation of the rotor disk and b) the Taylor vortices due to the centrifugal forces. The nature of flow is described by the Reynolds number which is the ratio of the inertia and the viscous forces. The tangential flow forced by a rotating rotor with the existence of a stator and a small airgap is described by the Couette Reynolds number [80],

$$RE_g = \frac{\upsilon g}{\vartheta}, \tag{6.22}$$

where υ is the circumferential speed of the rotor, ϑ is the kinematic viscosity of the fluid or gas and g is the airgap length of the machine. The kinematic viscosity of the gas is equivalent to its constant dynamic viscosity over its density. When a disk is rotating in free space the Reynolds number is called the tip Reynolds number and calculated as

$$RE_r = \frac{\upsilon r}{\vartheta}, \tag{6.23}$$

where r is the radius of the disk.

The Reynolds number is an index showing the nature of the flow If it is less than 2000, it means that all particles are flowing in the same direction and the flow is laminar. If the Reynolds number is higher, the particles are not moving in the same direction and it is called turbulence. The flow inside a high-speed electrical machine is usually turbulent. The turbulence also occurs when there is surface roughness [80].

As an illustrative example, the axial and tangential velocity distributions of the airgap flow is shown in Fig.6.6 [80]. The figure also shows the velocity distributions in the case of laminar and turbulent flows. In the tangential flow case, the fluid or particle velocity near the rotor is the same as the rotor speed, and the velocity near the stator is zero. The velocity distribution in the laminar case is linear in the airgap. However, there are regions in the turbulence case: Two viscous layers near the walls and one turbulent layer in the middle flow. "*In the viscous layers, the generation of friction, as well as energy transfer, is determined mainly by the molecular viscosity of the fluid. The thickness of the layer decreases with an increasing Reynolds number. In the middle flow, the chaotic motion of the fluid particles is independent of viscosity. The highest velocity gradients in the mean velocity are in the viscous layers. The lower figures show side views of axial airgap flows. In the laminar flow, the fluid*

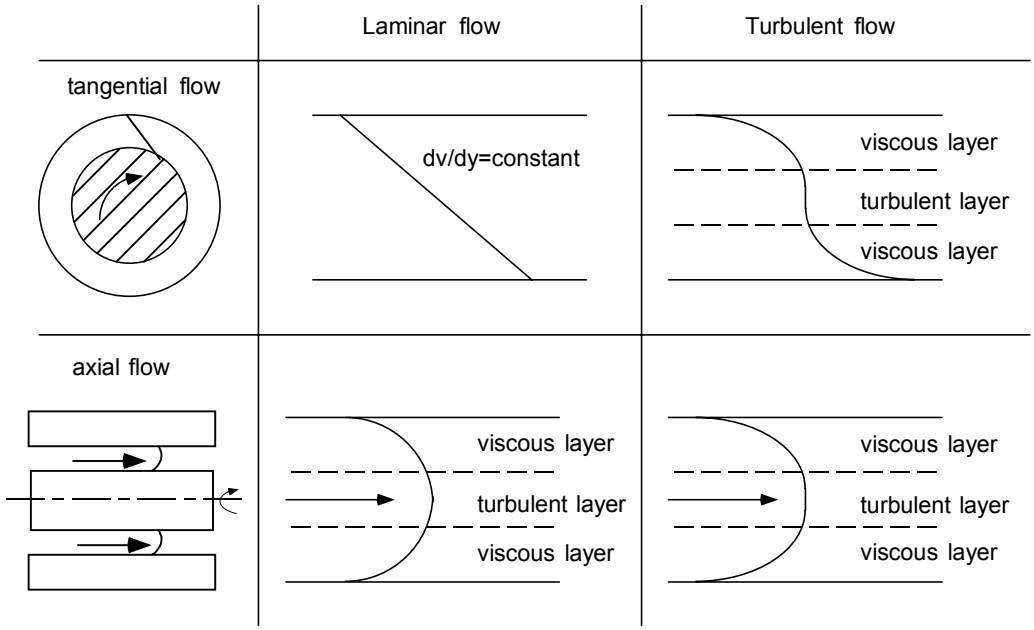

Figure 6.6: Tangential and axial velocity profiles of laminar and turbulent airgap flows.

velocity has a parabolic distributions. In the laminar flow, the fluid velocity has a parabolic distribution. In the turbulent flow, one can separate the same regions as in the tangential flow"[80].

Taylor vortices are circular velocity fluctuations appearing in the airgap as shown in Fig.6.7 [81]. They originate due to the centrifugal force effects on the particles and also depend on the airgap length. The Taylor number is

$$Ta = RE_g^2 \frac{g}{r}. \tag{6.24}$$

In a simple rotor-stator system Taylor vortices occur when the Taylor number exceeds 1700, which is called the critical Taylor number [82]. The critical Taylor number is affected by many factors such as the radius and temperature. Based on Taylor vortices and the turbulence of the flow [80], four flow regimes can be identified as shown in Fig.6.7b.

Since the sheer stresses are difficult to solve, the frictional drag is usually defined by a dimensionless friction coefficient C_f. It is an empirical coefficient depending on many factors such as the nature of the flow and the surface quality. Using this coefficient, the friction torque of a rotating cylinder can be calculated as

$$T = C_f \rho \pi \omega^2 r^4 \ell, \tag{6.25}$$

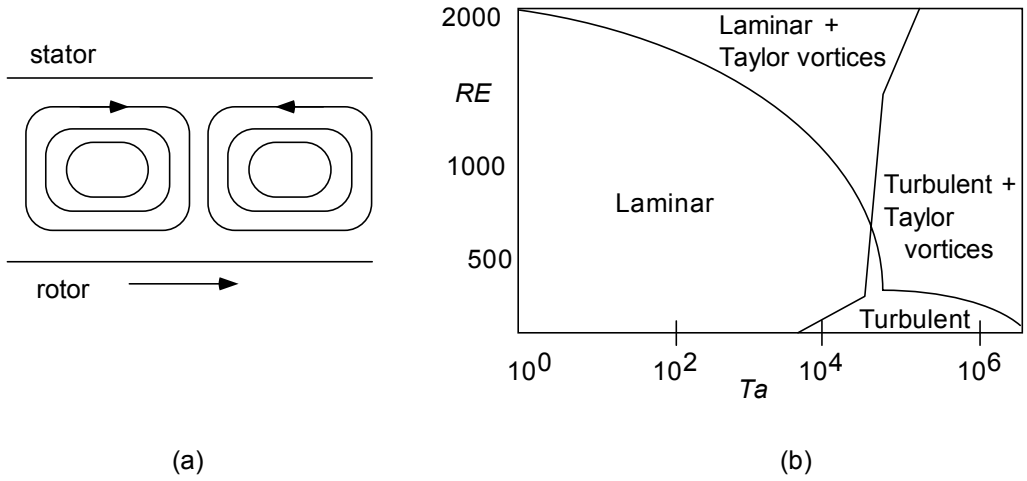

Figure 6.7: (a) Taylor vortices in the airgap (b) Flow regimes with respect to Reynolds numbers and Taylor vortices.

where ℓ is the axial length, r the radius of the cylinder and ρ the density of the material. The friction torque for a rotating disk having inner and outer radii r_i and r_o respectively can be written as

$$T = \frac{1}{2} C_f \rho \pi \omega^2 (r_o^5 - r_i^5), \tag{6.26}$$

The friction coefficient of a rotating cylinder

The friction coefficients of rotating cylinders in an enclosure were formulated by Bilgen and Boules [83] based on the measurements they made corresponding to the Couette Reynolds numbers between 2×10^4 and 2×10^6, and experiments done by other researchers. The coefficients they found are

$$C_f = \left\{ \begin{array}{ll} 0.515 \dfrac{(g/r)^{0.3}}{RE_g^{0.5}} & \text{if } \ 500 < RE_g < 10^4 \\ \\ 0.0325 \dfrac{(g/r)^{0.3}}{RE_g^{0.2}} & \text{if } \ RE_g > 10^4 \end{array} \right\}. \tag{6.27}$$

These coefficients are used in the calculations of the air friction loss caused by the rotor extension (the outer part of the rotor constructed for the flywheel connection) as shown in Fig.7.2.

The friction coefficient of a rotating disk

The rotor of an AFPM machine rotating between two stators may be considered as a rotating disk running in an enclosure. A very detailed study done by Daily and Nece [84] has shown the method of calculation of the friction coefficients for a rotating disk in an enclosure. When the Reynolds numbers and the dimensions of the enclosure and the disk are in certain regimes, apparently the disk operates as a centrifugal pump. Their experiments [84] cover the Reynolds numbers between 10^3 and 10^7 and the spacing ratios (the ratio of airgap length to outer radius of the disk) between 0.0127 and 0.217. They study tangential and radial velocity distributions as well as several pressures in enclosures. Considering the turbulence and the pumping effects they separated four different flow regimes for a rotating disk which are shown in Fig.6.8.

The friction coefficients they find for the corresponding regimes are

$$C_f = \left\{ \begin{array}{ll} \dfrac{2\pi}{(g/r_o)\, RE_r} & \text{regime I} \\ \dfrac{3.7\,(g/r_o)^{0.1}}{RE_r^{0.5}} & \text{regime II} \\ \dfrac{0.08}{(g/r_o)^{0.167}\, RE_r^{0.25}} & \text{regime III} \\ \dfrac{0.0102\,(g/r_o)^{0.1}}{RE_r^{0.2}} & \text{regime IV} \end{array} \right\}. \tag{6.28}$$

Using the theory explained and the analytical expressions written before, the air friction losses for the AFPM machine are calculated considering the fact that the rotor has two parts. The first part is the disk between the stators and the corresponding friction coefficients are calculated using Eq.6.28. The second part of the rotor is the extension which is designed for the flywheel connection as seen in Fig.7.2. The friction coefficients of the inner and outer surfaces of the rotor extension are calculated using Eq.6.27. The results found for the cases of normal and reduced air pressure (100 mBar) are shown in Fig.6.9. It is clear that for higher speeds with normal air pressure, the windage losses are very high.

6.5.2 Bearing Losses

The bearing losses are estimated using the data given by the manufacturer. They calculated the bearing loss at 16000 rpm and at 100 °C as 18 W, corresponding to 200 N radial and 125 N axial forces. The bearing losses at different speeds and torque

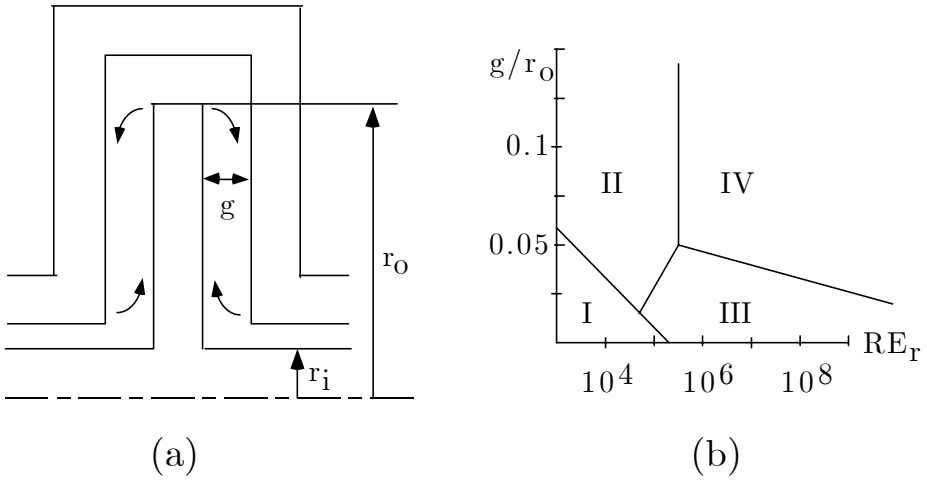

Figure 6.8: (a) Rotating disk in an enclosure, (b) The approximate flow regimes for an enclosed rotating disk.

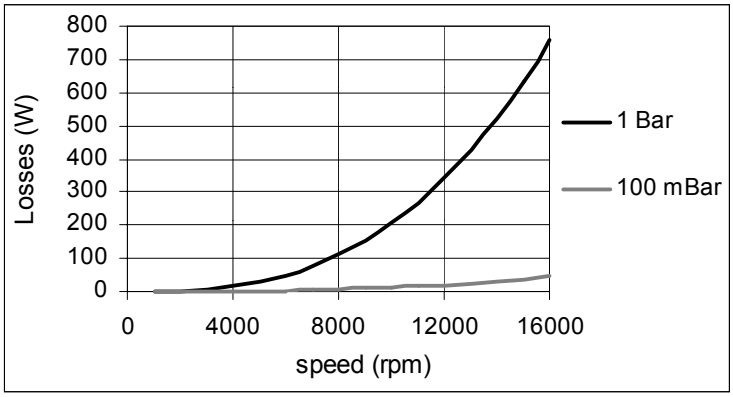

Figure 6.9: Air friction losses at normal and reduced air pressure.

levels are calculated based on this estimation and,

$$P_{br} = C_o d_m^3 \omega \tag{6.29}$$

where C_o is the bearing coefficient and d_m the average diameter of the bearing [67].

6.6 Efficiency map

The variation of the losses and efficiency with respect to torque estimated at 1000, 7000, and 16000 rpm is shown in Fig.6.10 for the rotor running in normal and reduced air pressure (100 mBar) conditions. The corresponding efficiency maps of the AFPM machine at these two conditions are shown in Fig.6.11. The effect of vacuum conditions is clearly visible.

6.7 Effect of the design parameters on efficiency

As it is explained in the previous chapters, the design of the machine is optimized through the use of analytical methods in combination with the finite element analysis. The programma developed is used to investigate the effects of the design parameters on the efficiency of the machine. In this section the results are presented.

6.7.1 Stator outside diameter

Due to the flywheel-machine arrangement the outside diameter D_o is constrained as discussed in section 2.4. The radial length of the space occupied by the outer end turns is estimated to be 25-30 mm by testing the windings on a dummy stator and the maximum possible outside diameter of the stators is determined as 190 mm. The effect of the outside diameter on the losses and the efficiency was simulated for 18 Nm at 7000 rpm and at 16000 rpm which are the inner-city and the highway driving speeds of the flywheel. The inside-to-outside diameter ratio K_r (0.58) and the airgap flux density levels are kept constant. The results are shown in Fig.6.12, where copper, core, rotor and total losses are also shown. The curve of the total losses also contains other loss components such as additional and mechanical losses.

The decreased outside diameter results in higher stator currents, and consequently higher copper losses, which is the most dominating loss component. On the other hand, for higher outside diameter values, core losses increase due to the larger amount of iron, and efficiency eventually decreases. As it is seen from Fig.6.12, the highest efficiency values at rated torque are achieved at higher outside diameters.

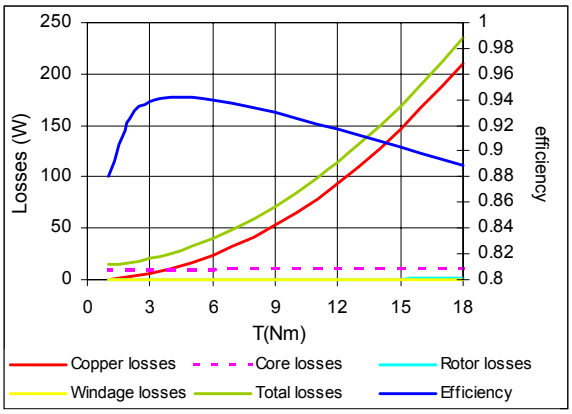

(a) 1000 rpm

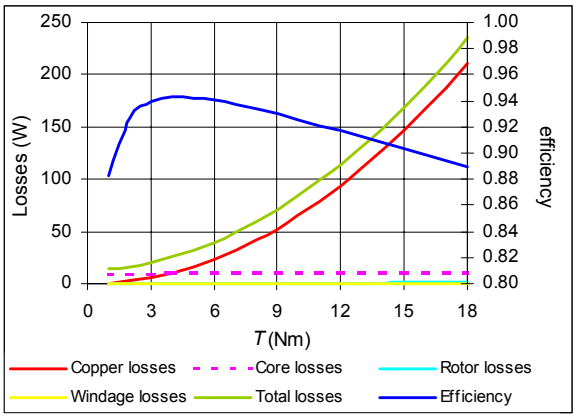

(b) 1000 rpm/100mBar

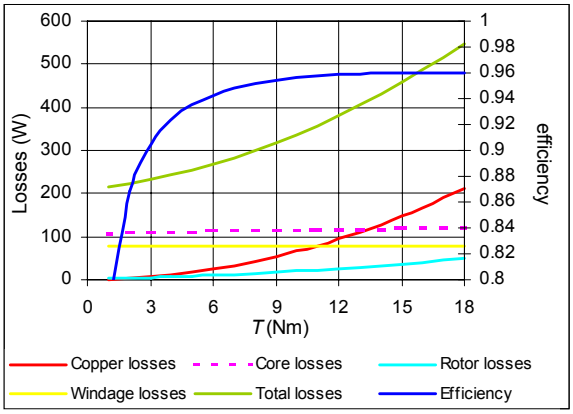

(c) 7000 rpm

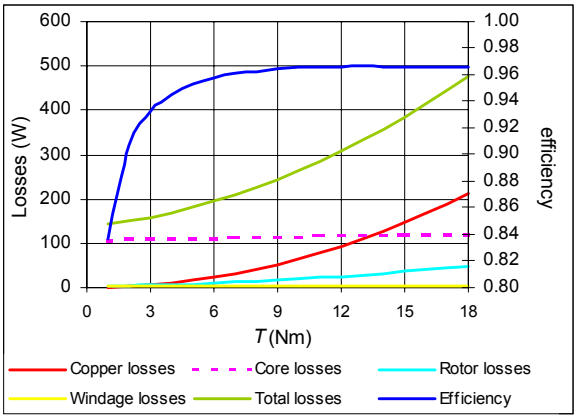

(d) 7000 rpm/100mBar

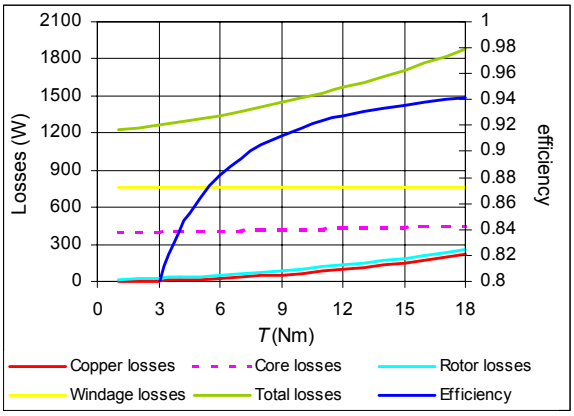

(e) 16000 rpm

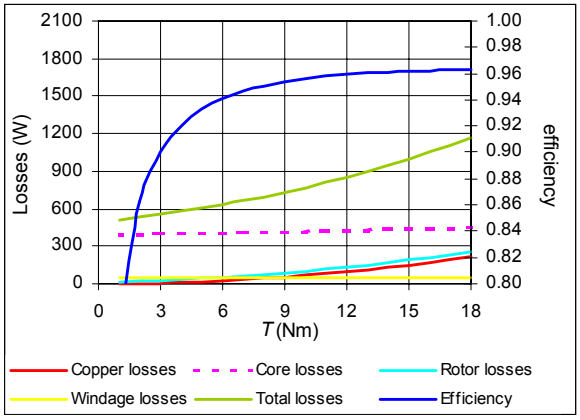

(a) 16000 rpm/100mBar

Figure 6.10: Power losses and efficiency curves of the AFPM machine at 1000, 7000 and 16000 rpm with normal and reduced inner air pressure.

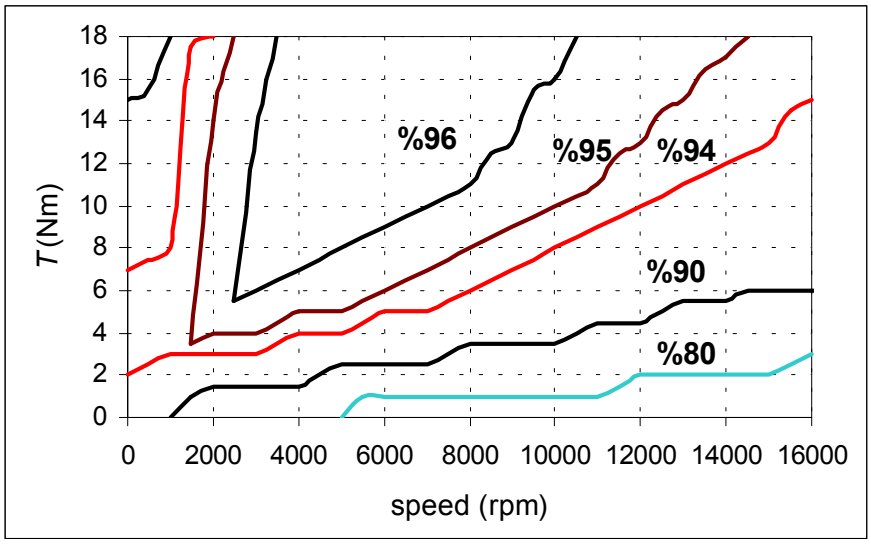

(a) at 1 Bar

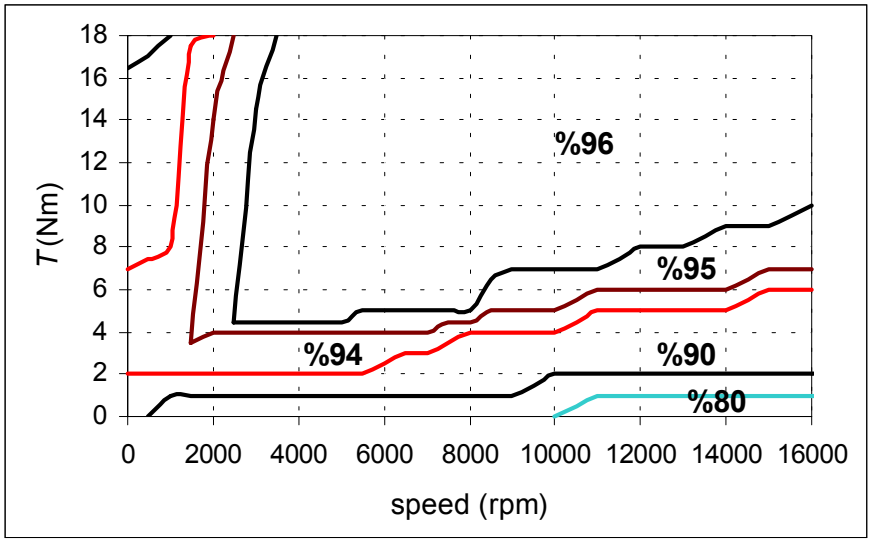

(a) at 100 mBar

Figure 6.11: Efficiency maps at normal and reduced inner air pressure.

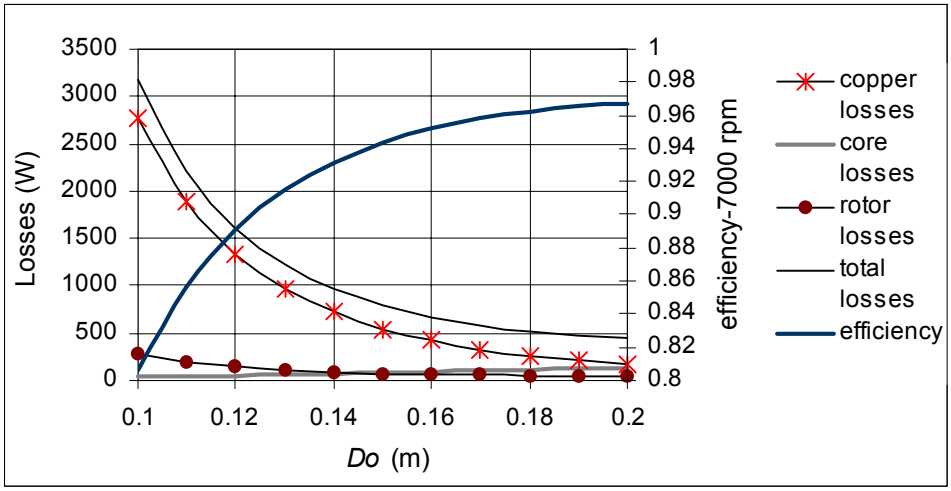

(a) 7000 rpm

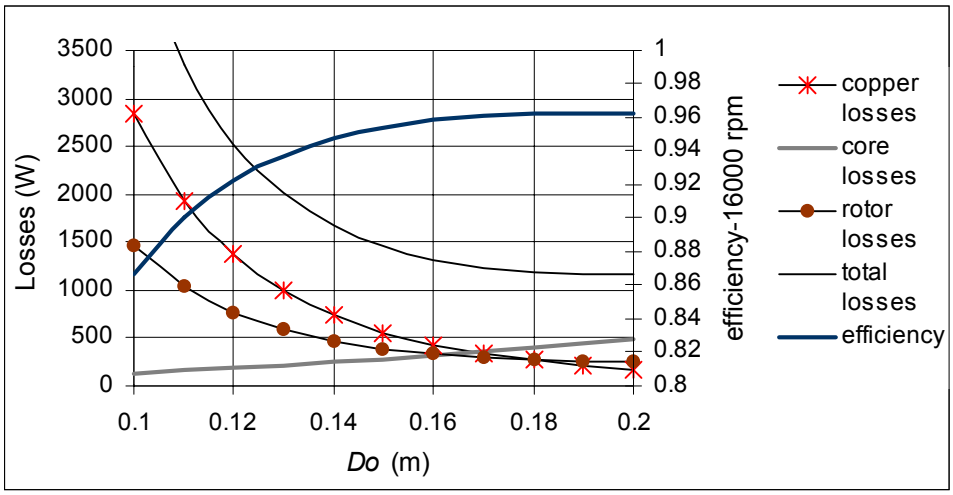

(b) 16000 rpm

Figure 6.12: Effect of outside diameter on efficiency and losses at rated torque (18 Nm).

6.7.2 Inside-to-outside diameter ratio

The inside-to-outside diameter ratio (K_r) is one of the most important parameters in the design of an AFPM machine. In order to show the effect on the design, the torque equation is repeated:

$$T_1 = \frac{h}{4}\pi \widehat{B}_{g1} k_{w1} K_1 r_o^3 (1 - K_r^2)(1 + K_r) \sin(\beta) . \tag{6.30}$$

Assuming constant current density at the stator inside diameter, maximum torque can be obtained for $K_r = 0.578$ [85]. Caricchi et. al. found 0.63 as an optimum value for K_r maximizing both torque and torque density [86]. Actually, the optimum value of K_r depends on the particular application where power ratings also depend upon the loss components. In Fig.6.13, the effect of K_r on losses and efficiency is shown for rated torque at 7000 and 16000 rpm, when the outside diameter of the machine is fixed to 190 mm. As it is seen from the graphs, the highest efficiency values occur at K_r values 0.4 and 0.6, respectively for 7000 and 16000 rpm at rated torque. It can be concluded that for low-speed applications, lower values of K_r will result in relatively higher efficiency levels. On the other hand, a lower limit constraint on the inside diameter should also be taken into account, due to high teeth flux density and mechanical space limitations.

6.7.3 Airgap flux density

The effect of the magnet length consequently the airgap flux density on the efficiency is shown in Fig.6.14 for rated torque at 7000 and 16000 rpm. It can be seen from the figure that at lower speeds relatively higher excitation levels result in higher efficiency. At higher speeds, due to the increased core losses, the optimum efficiency points shift to relatively lower excitation levels. It can be said that, for both speeds, optimum efficiency levels can be achieved at an airgap flux density level around 0.7 T.

6.8 Conclusions

The calculation of losses is essential in terms of an accurate prior estimation of the efficiency and the thermal behavior of the machine. The major types of losses and a detailed discussion on the analysis of each type were presented in this chapter. The chapter also provided an efficiency map and concludes with a discussion on the effects of the design parameters on efficiency.

The high speed and evacuation based thermal problems get worse with the high-frequency related eddy current losses occurring in the rotor magnets and rotor steel

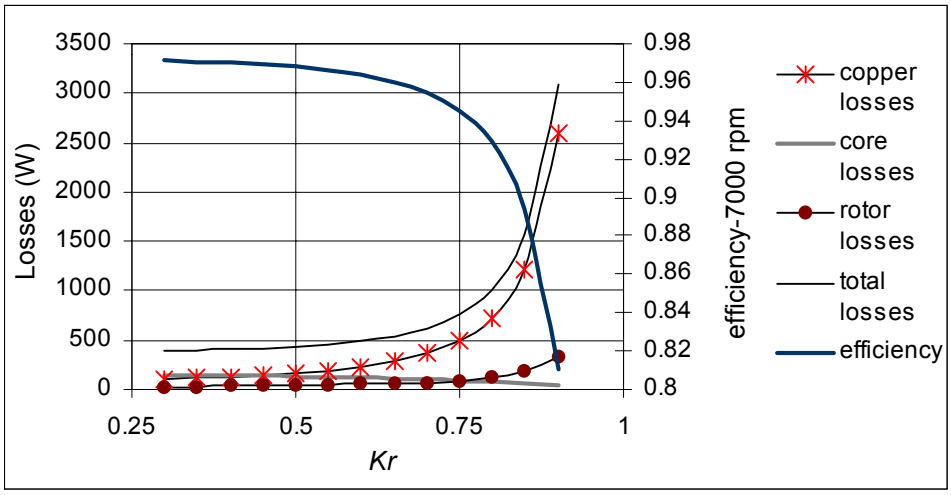

(a) 7000 rpm

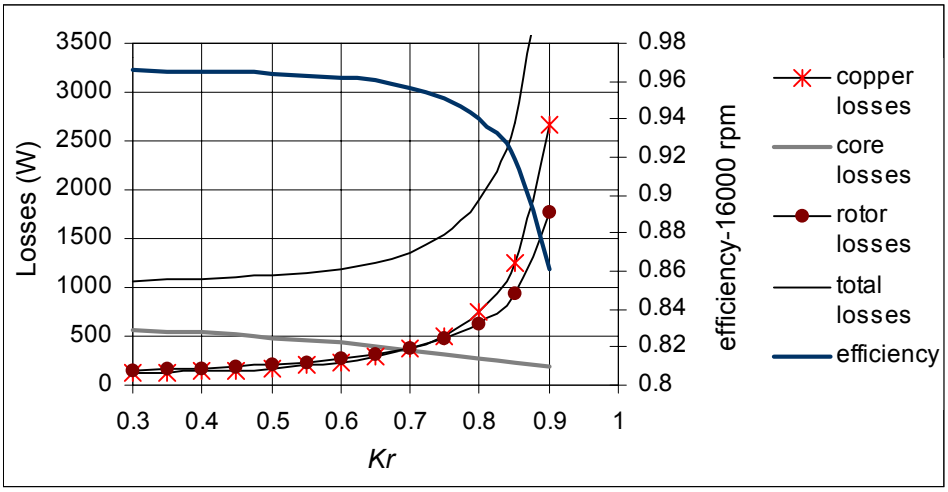

(b) 16000 rpm

Figure 6.13: Effect of inside-to-outside diameter ratio on efficiency and losses at rated torque (18 Nm).

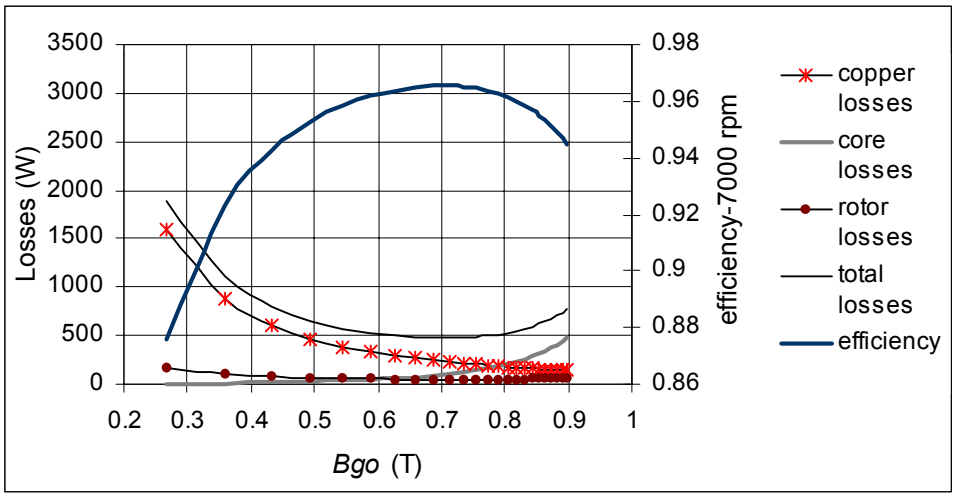

(a) at 7000 rpm

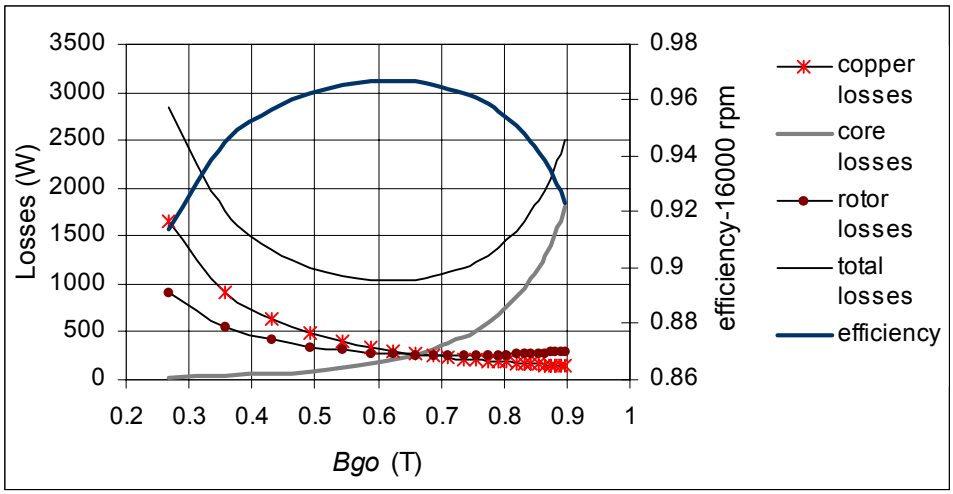

(b) 16000 rpm

Figure 6.14: Effect of airgap flux density on efficiency and losses at rated torque (18 Nm).

as indicated in section 6.4. These losses constitute further heating sources for the magnets. In the theoretical parts of this study, as explained in sections 5.9 and 6.4, particular attention has been paid to the analysis of the rotor losses, which required to be decreased to acceptable levels.

There can be two solutions offered to this problem; either by the lamination of the magnets together with the usage of a low-loss material for the rotor steel, or by eliminating the causes of rotor losses as much as possible during the design process. In this study, considering the potential mechanical problems that it could lead to, the first solution is left aside. This choice can be understood considering the fact that under these high-speed conditions, the rotor structure must be mechanically very robust, at least for this first prototype.

In chapter 4, an extensive space harmonics analysis of possible structures was carried out and the design variables were evaluated in terms of their space harmonic contributions. This study helped to choose a good combination of the design parameters, which eventually resulted in a design with low space harmonics content. Accordingly, the magnitude of the rotor losses, consequently the temperature rise of the magnets were suppressed

The following chapter is devoted to the thermal analysis of the machine. The calculated loss components in this chapter will be used in the analysis of the thermal equivalent circuit.

Chapter 7

Thermal analysis

7.1 Introduction

The dependence of the safe operating conditions and overloading capabilities on the temperature rise makes a prior estimation of the thermal behavior of any electrical machine a very important issue. The temperature tolerance of the materials used in the machine such as the permanent magnets, the winding insulations, and the glue used to attach the magnets determine the safe operating limits of the machine. On the other hand, the temperature dependent characteristics of the winding resistances and consequently the losses, and the temperature dependent permanent magnet flux make the performance analysis of the machine thermally dependent.

It is obvious that an exact prior determination of the thermal behavior of the machine is impossible due to many variable factors, such as unknown loss components and their distribution, and the three-dimensional complexity of the problem. Yet a prior knowledge of the order of magnitude of the temperature rises in various parts of the machine is crucial, especially in the case of a high-speed machine design. It is also important for the designer to know the magnitudes of the thermal parameters and to choose a suitable cooling strategy that will enhance the machine performance.

In the case of a high-speed machine the thermal conditions put more pressure on the designer. The relatively smaller size of high-speed machines which implies smaller cooling surfaces, together with the higher winding current densities required to generate a sufficiently high power density are the major problem sources. Moreover, high speeds introduce additional losses in the machine, such as rotor losses which are almost impossible to be directly cooled through the conventional methods.

There are various methods to analyze the thermal behavior of an electrical machine such as finite difference and finite elements, [87], [88], or alternative numerical techniques such as computational fluid dynamics [89]. Nevertheless, the computation times and the loss of accuracy due to the 2-D cross-section simplification make these methods undesirable. Therefore, the "transient thermal circuit" model is used.

The method is claimed to give very satisfactory results even for the simplified forms [90]. By using this method, as will be made clear in the following sections, a rather complex model that includes a high number of parameters can be made with a rather low cost in terms of computation time. This approach also allows various sensitivity analyses (in terms of thermal parameters and loss magnitudes).

Heat is transferred in an electrical machine by means of conduction in solid and laminated parts and by convection from surfaces which are in contact with the air. Heat transferred by means of radiation is generally small and mostly neglected. The convection coefficients are generally the most difficult ones to predict, although the accuracy and sensitivity of the problem are highly dependent on them. The main problem in making the analytical estimation of the convection coefficients is their nonlinear dependency on the temperature. In addition, it is infeasible to introduce this nonlinearity in the model analytically. This type of nonlinearity is also valid for the radiation coefficients. Therefore, the best way is to use the approximations based on previous experiments on the machines. Unfortunately, for high-speed machines there are not many published results and especially for AFPM machines not many published order of magnitude information about convection coefficients is available. As a result, much emphasis is paid to the thermal analysis during the design procedure, the reasons being:

- Since there are not many published results for thermal analysis of high-speed AFPM machines, the problem is original.

- The accuracy of the current calculation methods for convection coefficients can be judged by means of actual measurements.

- Having the thermal model at hand, the order of magnitude of the thermal convection coefficients can be deduced with the use of measured temperatures in several parts of the machine.

In section 7.2 the thermal magnet demagnetization constraint is investigated. From section 7.3 to 7.5, the theory of heat transfer in electrical machines is summarized and the related equations are given. In section 7.6, the construction of the thermal circuit representation of the machine is discussed and in section 7.7, the calculation method of the parameters is given. In section 7.8, the calculated thermal parameters and the circuit model are presented and finally, section 7.9 summarizes the results of the simulations at critical speed and load conditions, and discusses the temperature rises in various selected parts of the machine.

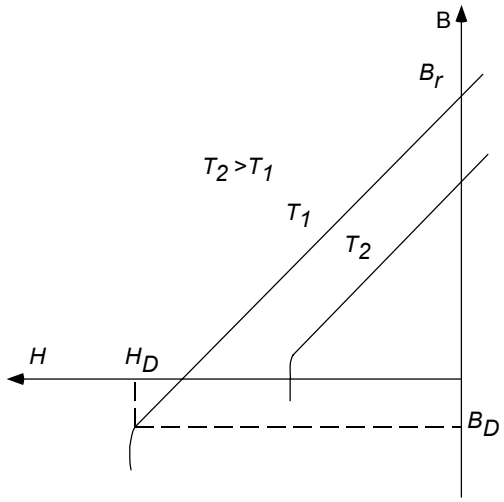

Figure 7.1: Demagnetization characteristic for Nd-Fe-B magnet material at two different temperatures.

7.2 Magnet temperature and demagnetization constraint

The most temperature dependent part of the machine is the magnets. That is due to the fact that, when a machine is operating at a certain load, the stator current density must be constrained so that for any particular part of the magnet, the flux density does not reduce below the knee flux density value B_D as indicated in the magnet demagnetization characteristic shown in Fig.7.1. The value of B_D is a function of the temperature and also increases with increasing temperature. The machine's safe maximum overloading conditions should be initially set from the magnet demagnetization characteristics.

In Fig.3.11, the sinusoidally distributed current sheet and the magnet flux density waveform are shown at maximum torque operating angle ($\beta = 90°$). The three-phase sinusoidal winding distribution as discussed in section 4.4 sets up a flux density in the airgap with the magnitude

$$\widehat{B}_{a1} = \frac{\mu_0}{g'}\frac{3}{\pi} I\sqrt{2}\frac{2k_{w1}N_{ph}}{p}, \tag{7.1}$$

where $g\prime = 2g + L_m/\mu_r$. The magnet on the other hand creates a flux density with the magnitude

$$\widehat{B}_1 = \frac{B_{g0}}{\pi}\sin(\frac{\theta_m}{2}), \tag{7.2}$$

T (in $^\circ C$)	$B_D(T)$	$I_{\max}(A)$
20	≈ -0.6	480
60	≈ -0.4	400
140	≈ 0.2	159

Table 7.1: Knee flux density values at several temperatures for GSN-33SH and corresponding maximum currents.

where θ_m is the magnet span in electrical degrees. Considering the magnet operating point, the demagnetization constraint can be written as

$$\widehat{B}_{a1} \sin(\frac{\theta_m}{2}) \preceq \left(\frac{L_m}{g'} B_r(T) - B_D(T) \right). \tag{7.3}$$

The maximum allowed current at temperature T can be determined using Eq.7.1 and Eq.7.3 as

$$I_{\max}(T) \preceq \frac{\left(\frac{L_m}{g'} B_r(T) - B_D(T) \right) p\pi g'}{6\sqrt{2}\mu_0 k_{w1} N_{ph} \sin(\frac{\theta_m}{2})}. \tag{7.4}$$

The values of B_D for the high temperature Nd-Fe-B magnet (GSN-33SH) chosen for the prototype and the corresponding computed maximum allowable current levels are listed in Table 7.1. Considering the fact that the rated current of the machine at $20^\circ C$ is 53 A, this particular magnet allows 9 times higher overloading capability, while at $140^\circ C$ it is only 3 times. Of course, the magnet demagnetization constraint is not the only limiting factor while dealing with the overloading capability of the machine; also the temperature rise in other parts of the machine, such as winding insulation and bearings should be considered. The short-term overloading capability of the machine will be investigated in section 7.9. with more realistic data.

7.3 Heating of an electrical machine

A part of the energy in an electrical machine is lost as heat. The electrical machine represents a very complex structure and consequently a very complex thermal system, with different materials and distributed heat (loss) sources. The cooling is generally provided to increase the operating range of the machine without exceeding the temperature limits of the parts such as insulations, or magnets. Higher temperature levels are not desirable, to protect the insulation and bearings and to prevent excessive heating of the surroundings. Heating of the surrounding should especially be prevented if the machine is placed in the neighborhood of other temperature sensitive equipment.

The temperature of a machine part is not only dependent on the losses but also on the ambient temperature and the coolant temperature. The temperature difference relative to the ambient is called the temperature rise. The temperature rise limits of various classes of machines are determined by international and some national standards. There exist four classes of machines [91]:

1. Maximum continuous rating: the machine may operate at the load for an unlimited period of time.
2. Short-time rating: the machine may operate at the load conditions for a specific period of time (generally 10, 30, 60, or 90 minutes).
3. Equivalent continuous rating: load conditions at which the machine may be operated without the temperature exceeding a specified value.
4. Duty-type rating: the machine may operate with one of the standard duty types S3-S9 [91].

Intermittent operation is common for permanent-magnet machines, which involves cycles with acceleration, constant speed, deceleration and stops. The cycle T_{cy} has on and off periods as

$$T_{cy} = T_{on} + T_{off}. \tag{7.5}$$

The duty cycle d is defined as

$$d = \frac{T_{on}}{T_{cy}} = \frac{T_{on}}{T_{on} + T_{off}}. \tag{7.6}$$

7.4 Heat transfer

Heat is transferred in the machine by means of conduction, convection and radiation. Heat transfer by means of conduction occurs in the solid parts of the machine such as steel, copper and insulation. Heat transfer by convection appears in the air and cooling water and in other fluids contained in the machine. Heat transfer by radiation is generally insignificant in electrical machines [91]. In some applications the surface is painted or lacquered black to increase the amount of heat transfer by means of radiation [43]. The modes of heat transfer are explained in detail in this paragraph.

7.4.1 Conduction

Under steady-state conditions heat conduction is described by two laws [91]. The first law states that the energy is conserved; i.e. the divergence of the heat flux vector is equal to the heat source density in a region described as

$$\nabla . \overrightarrow{\psi} = w, \tag{7.7}$$

where $\overrightarrow{\psi}$ is the heat flux vector which represents the heat transfer rate per unit area in the normal direction and w is the heat source density. The law of conduction heat transfer states that the heat flux at any point in an isotropic region is proportional to the temperature gradient at the point described as

$$\overrightarrow{\psi} = -k\nabla T, \tag{7.8}$$

where k is the thermal conductivity and T is the temperature. The minus sign satisfies the second law of thermodynamics which says that the heat flows from the higher temperature to the lower temperature regions.

Substituting $\overrightarrow{\psi}$ from Eq.7.8 into Eq.7.7 results in Poisson's equation

$$\nabla^2 T = -\frac{w}{k}. \tag{7.9}$$

It should be noted that this equation is similar to the equation describing the electrostatic field problems replacing T with the electric potential V, w with the electric charge density ρ, and k with the permittivity ε. It gives the opportunity to solve thermal conduction problems with the methods applied in electrostatics.

7.4.2 Convection

Heat removal by convection can be classified as natural and forced (artificial) convection. Natural convection means that neither an external blower nor any coolant liquid exists. This type of convection occurs via the air next to the heated body. The heat dissipation by natural convection is defined with Newton's law

$$Q = \alpha A(T_s - T_a), \tag{7.10}$$

where α is the convection heat transfer coefficient, A is the area of the emitting surface, T_s and T_a are the temperatures of emitting surface and ambient, respectively.

The real difficulty is the calculation of the heat transfer coefficient, which depends on many variables such as the temperature differences between the heated body and air, the geometry and properties of the surface. It is not possible to give accurate values for this parameter since electrical machines are constructed in different manners and shapes. Some advised coefficients for simple geometries can be found in the literature [92].

In many machines heat is removed by means of a ventilator or circulating liquid inside the machine. The calculation method to determine the heat transfer coefficient with forced ventilation can be found in [93]. Other unconventional methods using complicated stator lamination arrangement are discussed in [94]. The water cooling can also be applied in direct [95] or indirect ways according to the design of the channels. As a result, the approximation of the heat transfer coefficient in the case of forced convection is much more complicated, since in addition to the previously

mentioned parameters it is also a function of the velocity and material properties of the liquid and the way it is applied to the machine. Some approximation methods can be found in [91], [96]. The further discussion will take place in section 7.7.

7.4.3 Radiation

Radiation for a black body can be described by Stephan-Boltzmann equation

$$Q = e\sigma A(T_s^4 - T_a^4), \tag{7.11}$$

where σ is the Stephan-Boltzmann constant, 5.67×10^{-8} W/m^{2}C$^{\circ 4}$. Here the black body is assumed as a perfect radiator. Real surfaces are not perfect radiators of course and their effectiveness relative to that of a black body is called emissivity e. A practical value of 0.9 [43] can be assumed in the calculations.

Since the surface of the machine is not covered with a layer with high radiation coefficient and consequently the effect of radiation is very small, this mode of heat transfer will be ignored in the following analyses.

7.5 The diffusion equation

Considering conduction, the partial differential equation describing the three dimensional flow of heat, the so-called diffusion equation is

$$\nabla^2 T = \frac{\partial^2 T}{\partial x^2} + \frac{\partial^2 T}{\partial y^2} + \frac{\partial^2 T}{\partial z^2} = \frac{1}{\zeta}\frac{\partial T}{\partial t} - \frac{1}{k}\frac{\partial q}{\partial t} \tag{7.12}$$

where $\zeta = k/\rho c$ is the diffusivity in m^2/s; k is the thermal conductivity in W/m°C; c is the specific heat capacity in kJ/kg°C, q is heat flow rate, and ρ is the specific density in kg/m^3 [43]. It is obvious that with the inclusion of the convection equations and the three dimensional complexity involved in an electric machine, the problem becomes a very complicated boundary value problem. Thus the construction of a thermal equivalent circuit reduces the problem into an easier one, which can be solved by means of a circuit analysis software.

7.6 The thermal equivalent circuit

The thermal circuit model is an analogy of an electric circuit in which the generated heat is the current source and the temperature is analogous to the voltage. The rate of heat generation in a source is measured in Watts and the heat flow rate which is also measured in Watts is also analogous to current. All loss sources are represented as current sources in the model. All thermal resistances which are expressed in °C/W are represented as resistors and thermal capacitances are represented with capacitors.

In order to analyze the heat transfer in the machine, an idealized geometry must be chosen and divided into basic elements. These elements correspond approximately to areas, which have thermal and physical uniformity, such as:

- temperature within the elements,
- heat generated within the elements,
- material properties of the elements,
- convection conditions through the surfaces of the elements [97].

The division of the machine into small elements is the compromise between the model simplicity and the accuracy. Hence, a good engineering judgement and the knowledge of the properties of the used materials are essential.

All the elements of the machine are described by nodes, having an average surface temperature with respect to the ambient and a thermal capacitance. All nodes are connected to each other by conduction or convection resistances.[67]. Assuming constant thermal parameters and neglecting radiation, the linear differential equation for each node becomes

$$P_i = C_i \frac{dv_i}{dt} + \sum_{j=0}^{n} \frac{1}{R_{ij}}(v_i - v_j), \tag{7.13}$$

where P_i, C_i, R_{ij} and v_i are heat loss in node i, thermal capacitance to ambient, thermal resistance between nodes i and j, and temperature in node i respectively.

The nodes which are used to construct the thermal equivalent circuit of the AFPM machine are indicated on the scaled quarter model of the machine as shown in Fig.7.2. The power loss sources are also indicated. It should be noted that to each loss source node, a current source is connected and each node has a capacitance to the ambient. The proper prediction of the heat transfer in the machine depends on the accurate distribution of the losses [97]. The loss sources in Fig.7.2 are:

- *node* 2-copper losses in the outer-end windings,
- *node* 3-copper losses in the slot windings,
- *node* 4-copper losses in the inner-end windings,
- *node* 5-stator core losses,
- *node* 7-magnet eddy-current losses,
- *node* 8-windage losses,

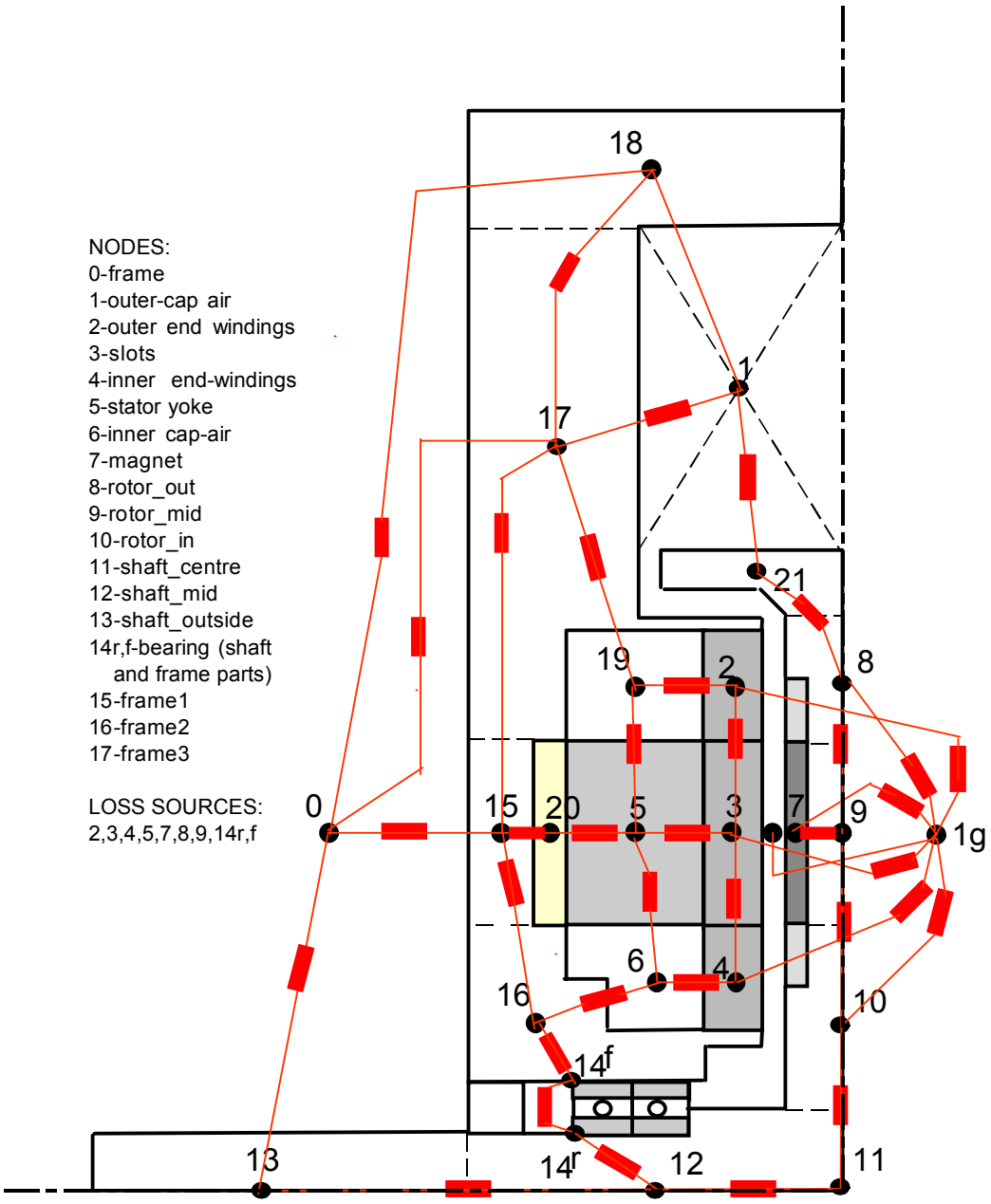

Figure 7.2: Thermal resistances and nodes on a quarter model of the machine.

- *node* 9-rotor eddy-current losses and windage losses,
- *nodes* 14r and 14f-bearing losses,
- *node* 21-windage losses.

It can be observed from Fig.7.2 that the ambient is represented by node 0, the water cooling channel is node 20, the airgap is node 1g and the end-air (the airgap between the rotor and the frame) is node 1.The conduction resistances at one hand and the convection resistances at surface-air interfaces on the other, may be clearly observed. All machine parts have been considered in the construction of the thermal equivalent circuit.

7.7 Method of calculation

The thermal parameters included in Eq.7.13 that should be estimated are thermal capacitances and thermal conduction and convection resistances. The thermal capacitances are calculated as

$$C_i = c_i \rho_i V_i, \tag{7.14}$$

where c_i, ρ_i and V_i are the specific heat capacity, density and the volume of the machine part represented by node i, respectively. The specific heat capacity and specific density values for the related materials are given in Table 7.2.

The thermal conduction resistance can be approximated as

$$R_{ij} = (\frac{d}{kA})_{ij}, \tag{7.15}$$

where k, d, and A are the specific thermal conductivity, the distance between the nodes i and j, and A is the area through which heat is transferred between the nodes. Specific thermal conductivity values of some selected materials are shown in Table 7.2.

Although the formulation of the conduction resistances seems rather simple, the approximations made in the direction of the heat flow should be handled with care. Generally the best assumption is considering only the axial and radial heat flows and determining the conduction resistances accordingly. To obtain simple but adequate assumptions of these conduction components, the following assumptions [98] are made:

- the heat flows in radial and axial directions are independent,
- a single mean temperature defines the heat flow both in radial and axial directions,

Material	Specific heat capacity (kJ/kgC°)	Specific thermal conduct. (W/mC°)	Specific density (kg/m^3)
Copper	0.38	360	8950
Aluminium	0.9	220	2700
%0.1 Carbon steel	0.45	52	7850
Silicon steel	0.49	20-30	7700
Cast iron	0.5	45	7900
Cobalt iron	0.42	30	8000
Ceramic magnet	0.8	4.5	4900
Nd-Fe-B magnet	0.42	9	7400
Kapton	1.1	0.12	1420
Pressboard/Nomex	1.17	0.13	1000
Epoxy resin	1.7	0.5	1400
Water (20°C)	4.18	0.0153	997.4
Air (20°C)	1	0.025	1.2

Table 7.2: Material properties.

- there is no circumferential heat flow,
- the thermal capacity and heat generation are uniformly distributed.

It is also assumed that the whole model is symmetric in both heat flow directions, which is the reason of a quarter thermal model. The calculation methodology related with the axial and radial conduction components can also be found in [98],[80], [99].

The determination of the coordinates of the nodes should be done carefully, considering the fact that the resistance values are dependent on the corresponding machine parts. Furthermore, the direction of the heat transfer should be considered for all parts. In order to calculate the conduction resistances between different parts, some practical values of the contact resistances are required. For instance, the contact resistance between laminated iron and windings, permanent magnet and rotor, slot and conductor (slot liner). Some practical contact resistance values can be found in [91].

The thermal convection resistance is calculated by using

$$R_{ij} = \frac{1}{(\alpha A)ij}, \tag{7.16}$$

where α is the heat transfer coefficient [100], and A the surface area between parts i and j. The calculation of the heat transfer coefficients is not easy and dependent on many approximations and the knowledge accumulated by previous experiments. The types of heat transfer coefficients, which should be calculated in the machine, are;

- heat transfer to the ambient air,
- heat transfer between stator, rotor, windings, epoxy parts, and frame to the end-air,
- heat transfer between rotor and stator through the airgap,
- heat transfer between airgap and end-air,
- heat transfer from the rotating shaft to the ambient,
- heat transfer to the cooling channel.

Since water cooling is applied, it is assumed that there is no fan. It means that, no velocity term is involved while calculating the convection resistance between frame and ambient. Consequently, the corresponding heat transfer coefficient can be taken as a known constant, which is $\alpha = 14W/^{\circ}Cm^2$ [100].

For the calculation of the heat transfer coefficient between the rotating shaft and the ambient, another known formula [100] can be adopted since the circumferential speed of the small shaft is not as high as that of the outer rotor. It can be written as

$$\alpha = 15.5\,(0.39v + 1)\,, \tag{7.17}$$

where v is the velocity of the air if it is lower than 7.5 m/sec.

The heat transfer coefficients in the airgap and in the end-air of the machine depend on many factors such as the speed of the flow, temperature, fluid (or gas) properties, airgap dimensions and even the surface characteristics of the rotating parts. The heat transfer coefficient between the rotor surface and the air can be described with the use of Nusselt number (Nu),

$$\alpha = \frac{Nu.k}{g}, \tag{7.18}$$

where k is the thermal conductivity of the gas (or fluid) and g is the airgap length.

The Taylor vortices and the estimation of the Reynolds numbers were discussed in detail in section 6.5.1 for various structures and will not be repeated here. Yet, it should be noted that the calculation of the Reynolds number for different air regions around the rotating rotor is different. The Taylor number is calculated, as discussed in section 6.5.1 by using

$$Ta = RE_g^2 \frac{g}{r}. \tag{7.19}$$

The Nusselt number is calculated for the three different regimes [67] of Taylor number, based on the measurements conducted by Becker and Kaye, [101] [80]:

$$Nu = \left\{ \begin{array}{ll} 2 & \text{for } Ta < 1700 \\ 0.128Ta^{0.367} & \text{for } 1700 < Ta < 10^4 \\ 0.409Ta^{0.241} & \text{for } 10^4 < Ta < 10^7 \end{array} \right\}. \tag{7.20}$$

The problem of using Eq.7.20 is that the measurements cover the range up to 10^7 for the Taylor number and for the higher speed levels the corresponding Taylor number may exceed this limit.

The heat transfer coefficient between the frame and the cooling water is similar to the heat transfer in turbulent fluids in tubes [100]. It is defined with the Nusselt number, the specific thermal conductivity of the coolant and the hydraulic diameter d_h as[67]

$$\alpha = \frac{Nu.k}{d_h}. \tag{7.21}$$

The Nusselt number for turbulent fluids in tubes is [102]

$$Nu = 0.032RE^{0.8}P_r^{0.37}\left(\frac{d_h}{l_h}\right)^{-0.054}, \tag{7.22}$$

where l_h is the length of the cooling channel and P_r the Prandtl number which describes the relation between the viscosity of the medium at a certain temperature and the thermal conductivity. Another method for the calculation of the Nusselt number can also be adapted [103]. Reynolds number in this case is

$$RE = \frac{\upsilon d_h}{\vartheta}, \tag{7.23}$$

where υ corresponds to the velocity of the water. It is obvious that the machine's overall temperature is also dependent on the flow rate of the cooling water; the sensitivity to this parameter will be shown in the following section. This parameter is also estimated with the help of an experiment made on the stators.

7.8 Thermal parameters

A program code has been written to calculate the thermal parameters. They are calculated with the described methods in section 7.7 and presented in Tables 7.3, 7.4, 7.5, 7.6 including the variations of the convection resistances with respect to rotor speed and reduced air pressure.

The thermal equivalent circuit constructed with the calculated thermal parameters is shown in Fig.7.3. The resultant temperature values for the machine parts will be calculated by analyzing the circuit with ICAPS/PSpice.

$R23 = 0.043$	$R34 = 0.069$	$R35 = 0.31$
$R46 = 5.89$	$R56 = 4.39$	$R519 = 2.55$
$R219 = 2.63$	$R520 = 0.064$	$R1520 = 0.0048$
$R1516 = 0.0027$	$R1517 = 0.0065$	$R1213 = 9.9$
$R1718a = 0.0024$	$R1719 = 1.39$	$R18a18b = 0.01$
$R616 = 6.27$	$R79 = 0.052$	$R1012 = 4.13$
$R14f16 = 0.046$	$R14r14f = 100$	$R14r12 = 0.24$
$R910 = 0.78$	$R821 = 0.203$	$R89 = 0.303$
$R4A = 4.93$	$R2A = 2.05$	$R3A = 0.032$
$R8A = 0.0232$	$R16A = 0.204$	$R10A = 0.0161$
$R15Am = 0.0048$	$R8ACp = 0.11$	$R16Am = 0.021$
$R17ACp = 0.0018$	$R17Am = 0.0015$	$R21ACp = 0.011$
$R18bACp = 0.0021$	$R18bAm = 0.00202$	$R18aAm = 0.0015$
$R21A = 0.0109$		

Table 7.3: Thermal conduction resistances.

$Cfr1 = 298$	$Cfr2 = 320$	$Cfr3 = 4196$
$Cfr41 = 1453$	$Cfr42 = 1660$	$Cwi = 39$
$Cw = 120$	$Cwo = 93$	$Cbe = 50$
$Cm = 88$	$Cr = 1238$	$Csy = 1333$
$CAGp = 4e - 6$	$CACap = 5e - 05$	
$CEpx1 = 785$	$CEpx2 = 967$	$C10 = 188$
$C8 = 289$	$C9 = 261$	$C21 = 499$

Table 7.4: Thermal capacitances.

$R150 = 7.58$	$R160 = 18.6$	$R130 = 3.71$
$R18a0 = 1.69$	$R18b0 = 2.48$	$R170 = 1.38$

Table 7.5: Housing to ambient convection resistances.

Air pressure	1 Bar	1 Bar	1 Bar		100 mBar	100 mBar	100 mBar
Speed (rpm)	3000	7000	16000		3000	7000	16000
$R211g$	0.58	0.39	0.26		1.88	1.25	0.85
$R81g$	0.055	0.037	0.025		0.18	0.12	0.08
$R101g$	0.32	0.21	0.141		1.04	0.69	0.46
$R121g$	67.7	45.3	30.7		221	147	99
$R161g$	13.1	8.8	5.95		43	28	19
$R41g$	0.33	0.22	0.15		1.09	0.72	0.48
$R31g$	0.104	0.08	0.064		0.27	0.19	0.14
$R21g$	0.71	0.53	0.39		1.39	1.14	0.91
$R191g$	4.6	4.4	4.3		6	5.3	4.9
$R71g$	0.072	0.05	0.03		0.24	0.16	0.11
$R211$	0.96	0.64	0.43		3.13	2.09	1.4
$R81$	2.81	1.91	1.32		9	6.02	4.08
$R171$	0.26	0.17	1.12		0.84	0.56	0.38
$R18b1$	0.44	0.30	0.20		1.46	0.97	0.65

Table 7.6: Airgap and end-air convection resistances.

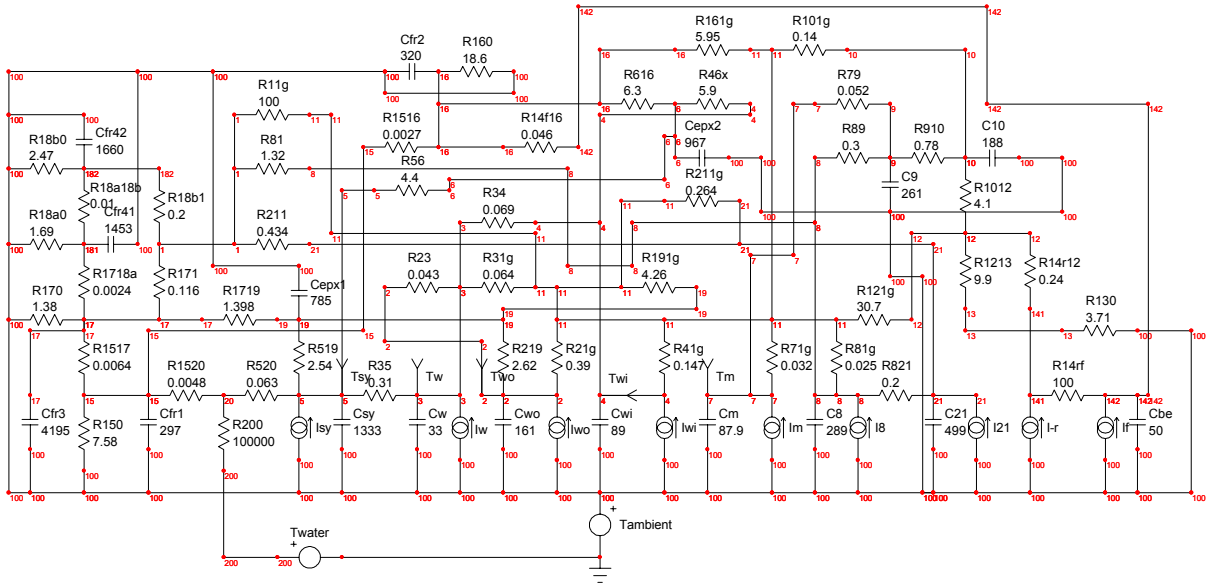

Figure 7.3: The thermal equivalent circuit of the machine at 16000 rpm and 1 Bar.

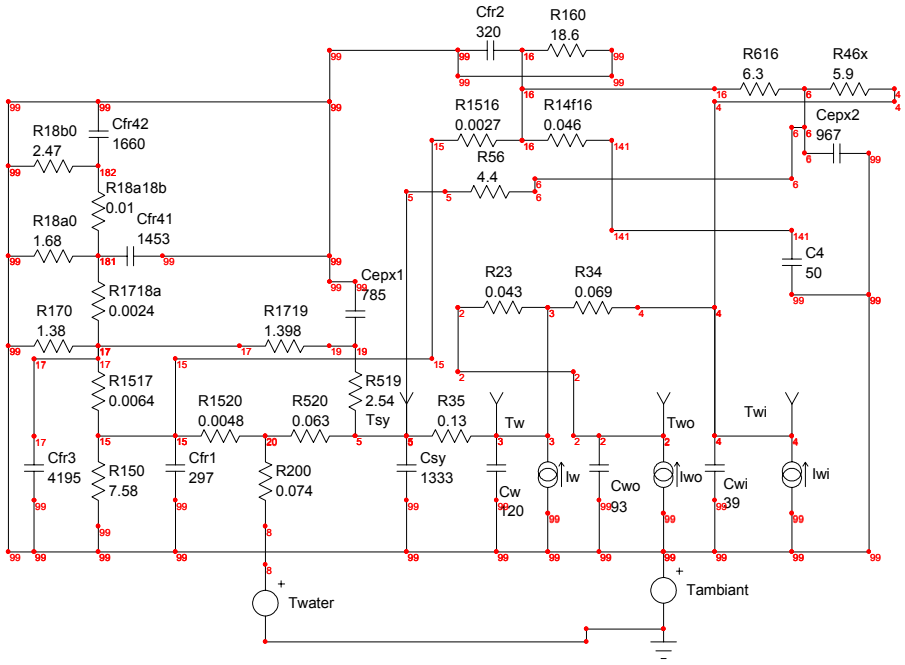

Figure 7.4: Thermal equivalent circuit representing the frame, the stator and the water cooling.

The thermal convection resistance to the cooling water (R200) is calculated as 0.074 considering the speed of the cooling water as 3 l/min. Since this parameter is relatively difficult to estimate, simple temperature tests were conducted on the stators before the machine assembly. In the first step the stator phases were excited with continuous DC current of 55 A. Next, the same experiment is repeated with the cooling water flow rate of 3 l/min. The convection resistance to the water is evaluated from the measured results and those of the thermal equivalent circuit of the tested machine parts (stator, windings, frame and cooling channel), as shown in Fig.7.4 with the same node numbering used in Fig.7.2. It is concluded that the calculation of the convection resistance to water gives fairly good approximates. The thermal convection resistance values estimated with respect to the water flow rate are shown in Fig.7.5.

7.9 Simulations

The thermal equivalent circuit allows various analyses of the machine's thermal behavior at any load conditions. It should again be emphasized that the convection

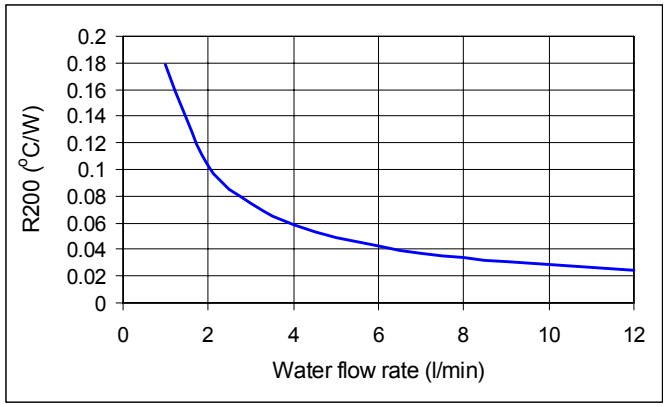

Figure 7.5: Thermal convection resistance between housing and cooling channel with respect to cooling water flow rate.

resistances in the airgap and the end-air regions are function of the rotor speed and the air pressure inside the machine.

The analyses were carried out at various speeds and load conditions in order to obtain the transient and steady-state temperatures in the machine parts, such as magnet, winding, stator yoke etc. It should be noted that the temperature characteristics of all the nodes corresponding to the machine parts, as shown in Fig.7.2, can be obtained through the analysis. Several important cases are included in this section to constitute a basis for comparison.

Naturally, the higher speed conditions are more critical, and should be investigated first. Fig.7.6 shows the rise of some critical machine parts (magnet, winding and stator yoke) under normal air pressure at rated load and speed conditions, and at various cooling conditions (8 and 3 l/min water speed and without water cooling). In the simulations ambient and water temperatures are taken 30°C and 20°C respectively. The figure clarifies the effect of the water cooling. In the absence of water cooling, the temperature of the magnet and the windings exceed their stability limits (140 °C) in less than 30 minutes. With water cooling the maximum temperature limit is not exceeded even in the steady-state. The machine parts under investigation reach their steady-state temperatures in almost one hour. Comparison between the two water flow rate conditions (3 and 8 l/min) shows a 20°C difference in the steady-state temperature values of the magnet and winding.

The same analysis is repeated for the case where the machine is running under reduced air pressure condition (100 mBar). The results are shown in Fig.7.7. In comparison to the previous case, the steady-state temperatures are relatively low due to the fact that at reduced air pressure the air friction losses are not as high. It is also recognizable from the figures that at reduced air pressure condition, the

difference between the magnet and the winding temperatures is larger due to the reduction of the heat convection in the airgap of the machine.

It should also be noted that the estimated temperatures here are the mean temperature values of the particular node corresponding to the related machine part. Hot spot temperatures throughout the machine can exceed the mean values by 10-20 °C.

The thermal conditions in the case of an overloaded machine are also investigated. Fig.7.8 shows the temperature curves at reduced air pressure conditions, the rotor rotating at 7000 rpm, the machine producing twice the value of the rated torque and with 8 l/min cooling water flow rate. It is clear from the figure that it is possible to overload the machine up to this level at lower speeds without exceeding the maximum temperature limit. Fig.7.9, shows the result for a similar condition, with the motor overloaded by four times its rated value and 12 l/min cooling water flow rate. In this case, the maximum limit is exceeded in less than 5 minutes even with the high water flow rate.

Clearly, the overloading capability of the machine is completely dependent on the cooling system. Here, the analysis results only deal with direct cooling, where the water channels are placed between the stator cores and the frame. The manufacturing details will be discussed in detail in the following chapter. Hence, with a better and more complicated cooling system, the overloading capability of the machine can be improved over the whole speed range.

7.10 Conclusions

This chapter summarized the fundamental methodology for the construction of the thermal equivalent circuit of the AFPM machine. The effect of temperature on magnet demagnetization limits was investigated. Throughout the calculations of the thermal parameters of the machine, related material properties and dimensional information of the manufactured machine prototype were used. Simulation results were presented and discussed for several critical machine operating conditions. As will be discussed in chapter 8, several thermocouples are placed in various parts of the prototype machine during manufacturing. A thermochip is also attached to a magnet and the cables are connected through slip rings to measure its temperature accurately. In this way it became possible to compare the measured and calculated temperatures. The thermal measurements will be included in chapter 9.

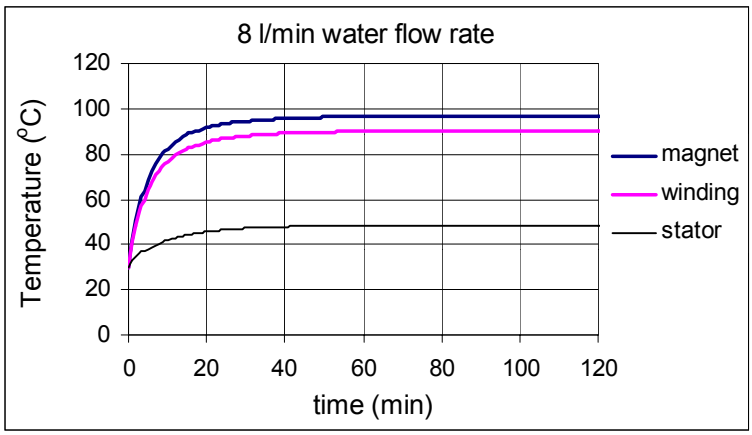

(a)

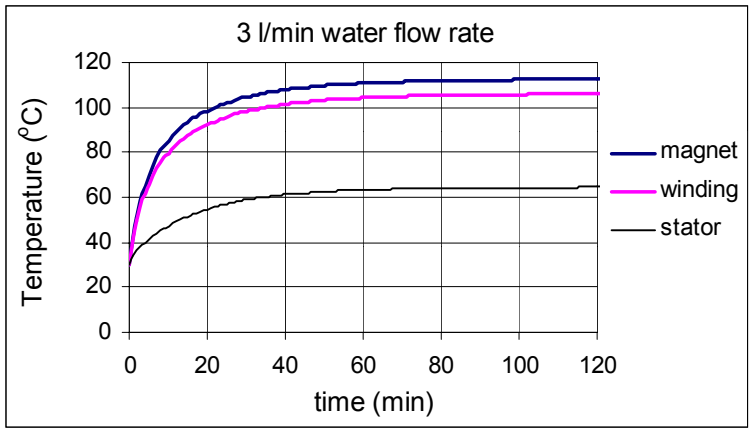

(b)

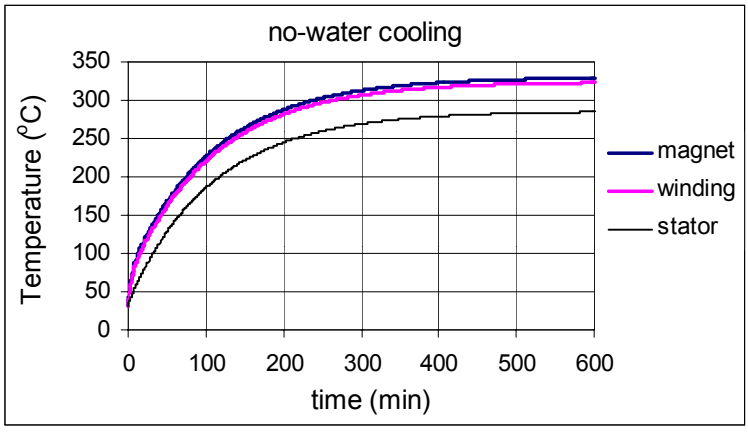

(c)

Figure 7.6: Temperature rise of magnet, winding and stator yoke under normal air pressure, at 16000 rpm and rated load, with 8 l/min (a) and 3 l/min (b) cooling water flow rate and without cooling (c).

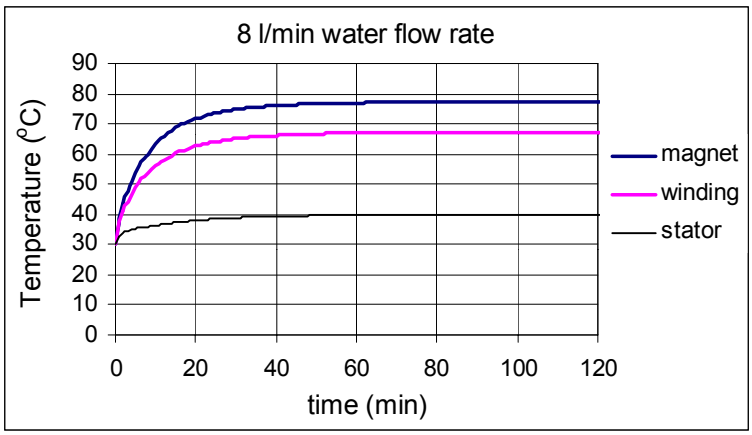

(a)

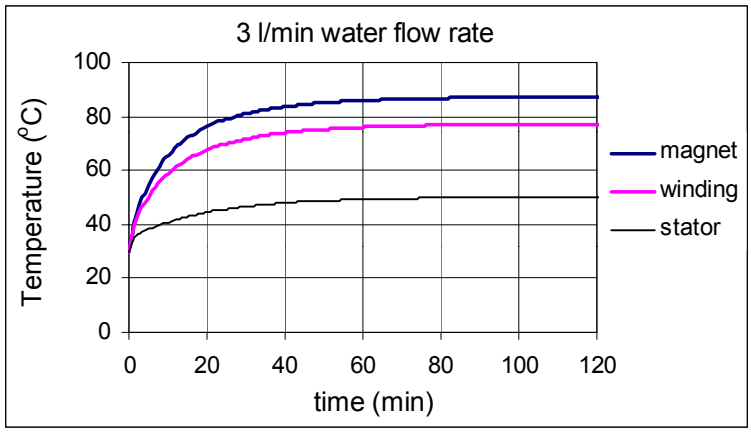

(b)

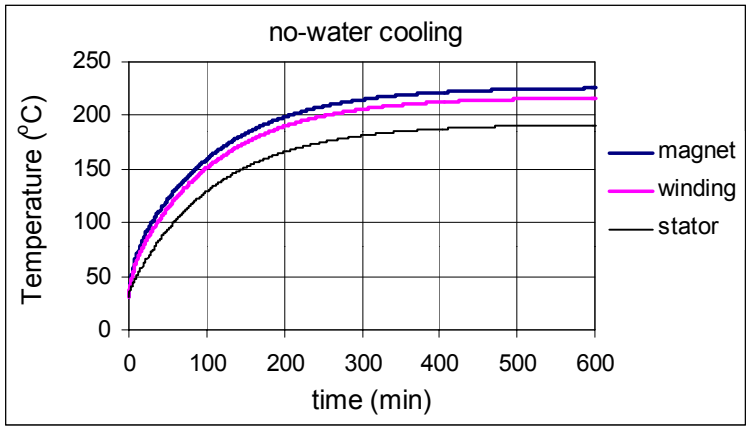

(c)

Figure 7.7: Temperature rise of magnet, winding and stator yoke under 100 mBar air pressure, at 16000 rpm, and at rated load, with 8 l/min (a) and 3 l/min (b) cooling water flow rate and without cooling (c).

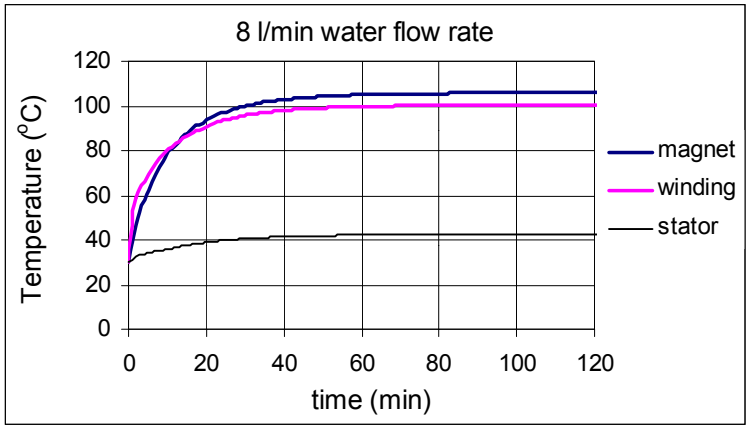

Figure 7.8: Temperature rise of magnet, winding and stator yoke, at 7000 rpm and twice rated current, with 8 l/min cooling water flow rate.

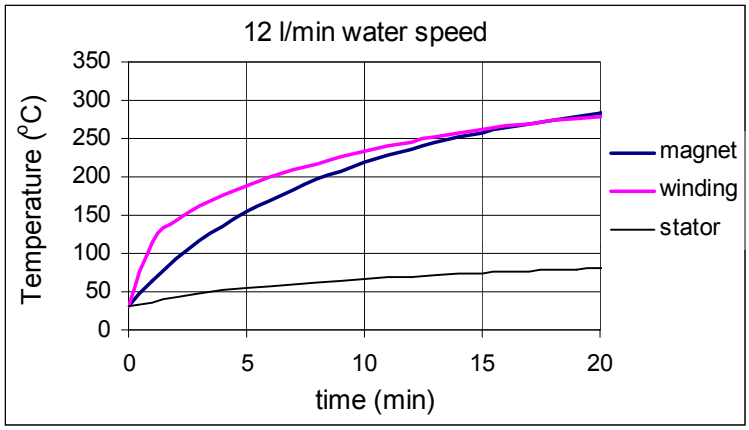

Figure 7.9: Temperature rises of magnet, winding and stator yoke, at 7000 rpm, and four times the rated current, with 12 l/min. cooling water flow rate.

Chapter 8

Manufacturing and mechanical aspects

8.1 Introduction

The theoretical design and the analyses of the AFPM machine have been summarized in the previous chapters. This chapter illuminates the manufacturing procedure and the mechanical aspects of the construction of the machine. The major problems faced during the realization of the machine are discussed as well. Although the theoretical design procedure has its own methodology, it should have been linked to the practical concerns in some way. Of course, when it comes to the realization of the design, the types of problems and the requirements drastically vary from the previous phase. Mostly, the issues of the theoretical and the practical designs do not coincide and proper compromises must be made

The work done in this face of the project can be summarized as follows:

1. Mechanical design;
   (a) determination of the frame and shaft dimensions,
   (b) determination of the critical frequencies by means of modal analysis,
   (c) mechanical stress analysis of the rotor and determination of the safe operating conditions at high speeds,
   (d) design for magnet protection,
   (e) preparation of the technical drawings.
2. Determination and purchasing of the materials which will be used in the prototype construction.
3. Construction of the machine.

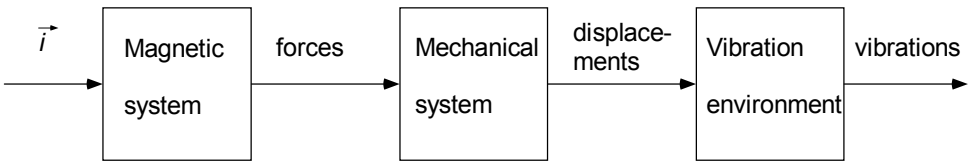

Figure 8.1: Overview of the magneto-mechanical-vibration system.

8.2 Mechanical Design

A high-speed electric machine requires not only a good magnetic design but also an interactive team work between magnetic and mechanical designers. The mechanical design process should not be seen as an incremental advancement on the magnetic design, such as acoustic noise minimization, but a *sine qua non* of the overall design. The safe operating conditions of the machine should be set by means of mechanical constraints. Besides, the overall design can not be realized by the merging of the individual outputs of the magnetic and mechanical designers in isolation. Interaction is inevitable and thus a must. For instance, a magnetic designer can not freely choose a magnet length without considering the centrifugal force effect on the overall design, or the airgap length without considering the effect of the axial attractive forces. During the development process several updates in the magnetic design have been experienced due to the mechanical constraints.

In reference to [104], the overall machine can be illustrated as a magneto-mechanical-vibration system as seen in Fig.8.1. The machine with its currents and permanent magnets represents a magnetic system which creates magnetic related forces. With rotation and centrifugal forces added the overall mechanical system creates displacements which result in vibrations.

The vibration responses of the machine should be investigated and the dimensions of the rotor, shaft and frame should be set accordingly. The vibration phenomenon has lots of dimensions. It is generally known as the cause of acoustic noise. The vibration of the stator laminations caused by electromagnetic forces generates the acoustic noise of an electric machine. There exist methods to determine the resonant frequencies and vibration behavior of the stators, [105],[104], [106], and to analyze the effects of the higher harmonics of electromagnetic forces on vibration [107].

The determination of the vibrations in the scope of this study does not directly aim to reduce or prevent acoustic noise. The main purpose here is to prevent long term damage or immediate failure of the machine due to high magnitude vibrations. Hence, the issue is reliability.

The vibration response in electrical machines is very complicated since the dynamic behavior not only depends on the electromagnetic force amplitudes but also on the relation between the electromagnetic force waves and the eigen modes of the

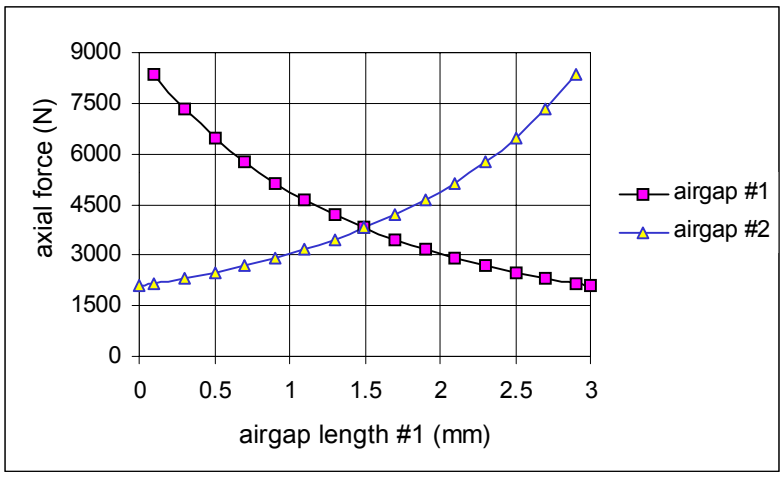

Figure 8.2: Total average axial attractive forces between rotor and stator corresponding to the airgaps #1 and #2.

structure. It is also related to the frequency of the electromagnetic forces and the natural frequencies of the structure [107]. Therefore, it is necessary to analyze the dynamic behavior of the rotor. The first issue which should be discussed here is the determination of the forces acting in the machine.

8.2.1 Forces

The major forces which should be considered in the mechanical analysis of the rotor are the axial attractive forces between the rotor permanent magnets and the stator cores and the centrifugal forces acting on the rotor.

- *Axial attractive forces between the rotor magnets and the stator cores:*

Rotor-stator attraction forces with respect to the airgap length are shown in Fig.8.2. They were calculated by FE analysis considering the total effect of the 4 magnets between one rotor face and the stator core. If the two airgap lenghts on both sides of the rotor are exactly equal (1.5 mm), the net axial force on the bearings will be zero. If the rotor is not precisely positioned in the middle of the machine, there will be a net axial force which will be the difference between the two axial force curves, as shown in Fig.8.2.

- *Centrifugal force acting on the magnets:*

The centrifugal force acting on a magnet piece can be found as

$$F_c = m\omega^2 r, \tag{8.1}$$

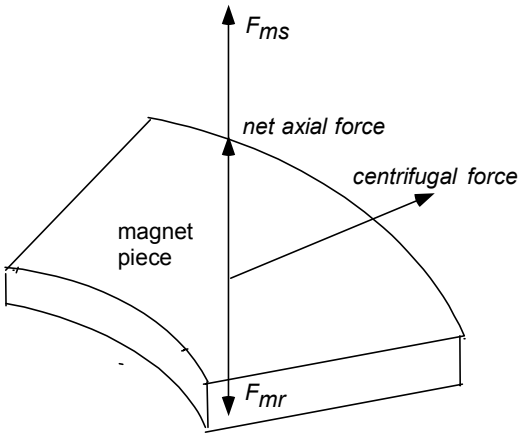

Figure 8.3: Forces acting on a magnet piece.

which results in 20 kN at 16000 rpm.

With this high centrifugal force and also considering the resultant axial attractive force acting on the magnet (the difference of the attractive forces between the magnet and stator F_{ms}, magnet and rotor iron F_{mr}) as shown in Fig.8.3, it is calculated that a glue should withstand a force density around 5 N/mm^2.

The tests conducted on the commercially available glues at several temperatures up to 120 °C show that, the protection of the magnets against such high centrifugal forces is not possible only by means of a glue. The problem is solved by means of a combination of two measures.

1. The nickel coating of the magnet is slightly grinded without causing oxidation of the magnet to increase the adhesive force of the glue.

2. The magnets are ordered with ramped shaped corners (Fig.8.4a). After they are glued on the rotor iron, a fibre glass rim is placed around the rotor magnets (between the magnets and the iron part) as shown in Fig.8.4b.

8.2.2 Dynamical analysis of the rotor

Modal analysis technique, which is commonly used in mechanical engineering is used to obtain the eigen-frequencies of the rotor structure. The modal shapes of the rotor and related displacements or deformation shapes are computed (by Ir. E. Dekkers from GTD) at the eigen-frequencies of the structure. The displacements at four critical frequencies are shown in Fig.8.5. The most important issue here of course is that all of these frequencies are much higher than the operating frequencies.

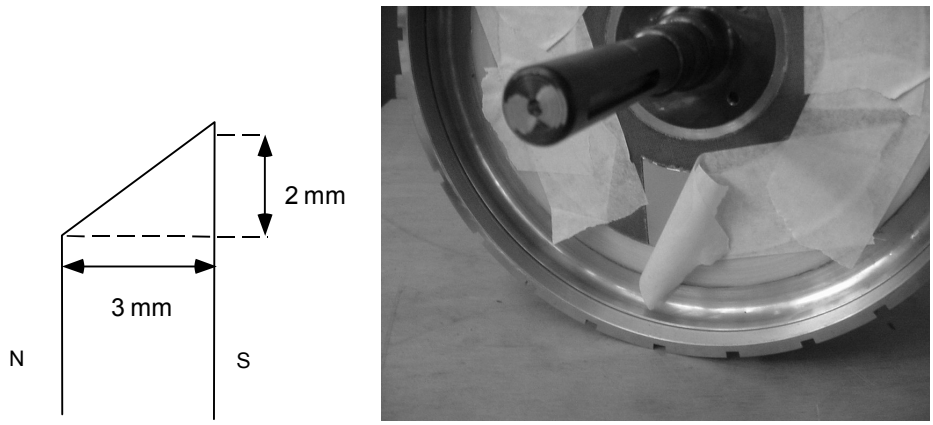

(a) (b)

Figure 8.4: Magnet protection. (a) Magnets side view, and (b) magnets attached on the rotor and the glass fibre rim.

8.2.3 Mechanical analysis of the housing

With reduced air pressure inside the machine, the frame can considerably contribute to the vibration thus reducing reliability. Therefore, the displacements of the frame are computed and used for the determination of its thickness. Fig.8.6 shows two representative examples of the mechanical analyses conducted to determine the frame thickness. Fig.8.6a shows the analysis made on a rather thin frame (quarter model) under 1 Bar pressure; it is assumed that the air inside the machine is completely evacuated. The analysis shows about 1 mm displacement of the frame under this condition. In order to improve this, the frame is thickened on both sides and the end windings of the stator are filled with epoxy. The analysis is repeated for this case and a maximum displacement around 0.01 mm is achieved. The improved frame structure is shown in Fig.8.6b.

8.2.4 Stress analysis of the rotor

Stress analysis of the rotor is also conducted by means of the FE method (in GTD). The centrifugal stresses in the rotor are shown in Fig.8.7. Since the maximum stress occurs at the bottom of the rotor (which is the connection point), the method of shrink fitting between the rotor and the shaft is applied.

The analysis is also repeated for the condition where the flywheel is assumed to be attached to the rotor. The resulting stress values (at 16000 rpm) are shown in Fig.8.8. In this case the maximum stress value lies around 1 GPascals. Due to this very high stress value the rotor outer circumference is slotted to reduce the stress. These outer rotor slots are visible in Fig.8.4. The flywheel is planned to be attached

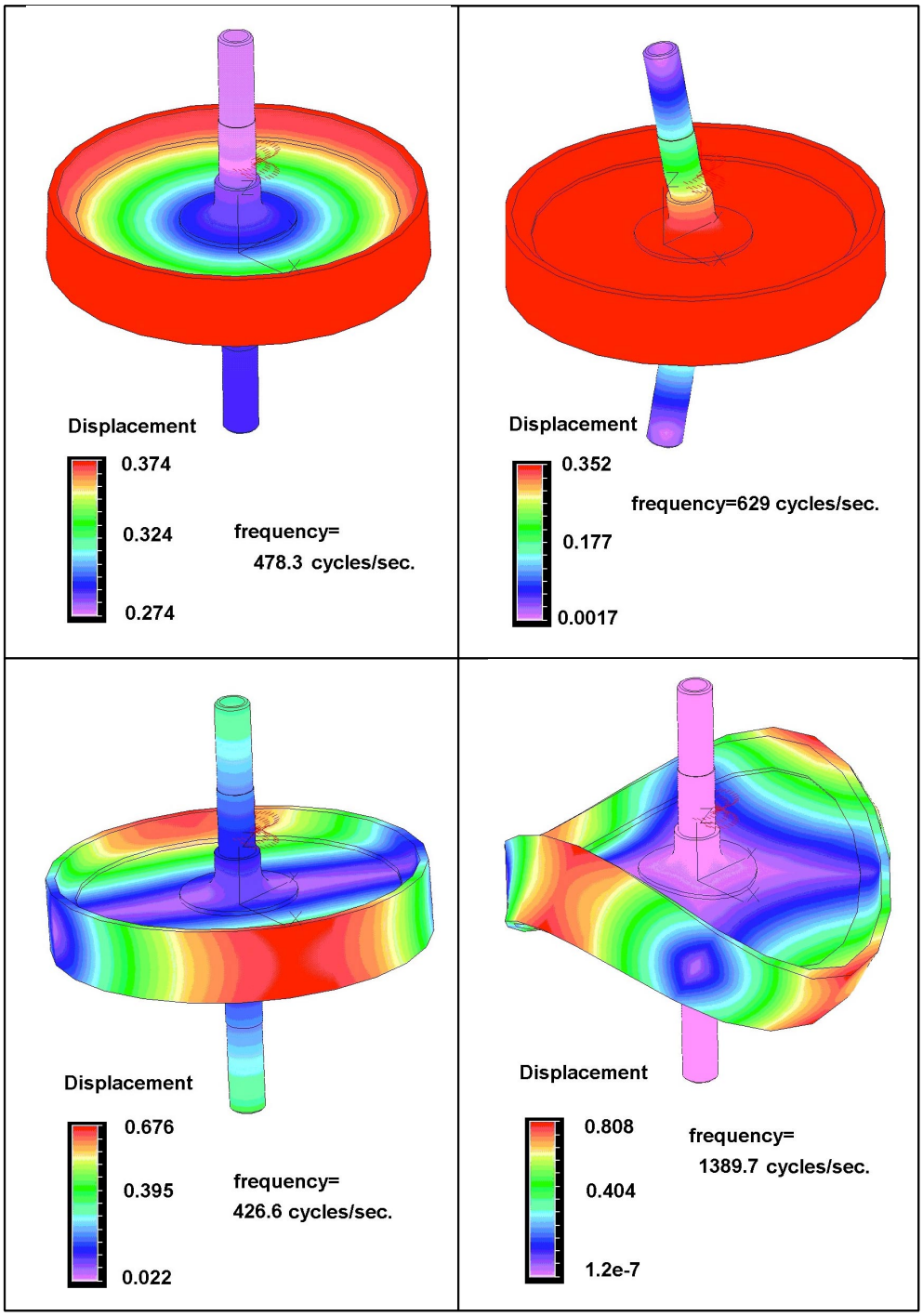

Figure 8.5: Deformation patterns of the rotor at its eigen-frequencies.

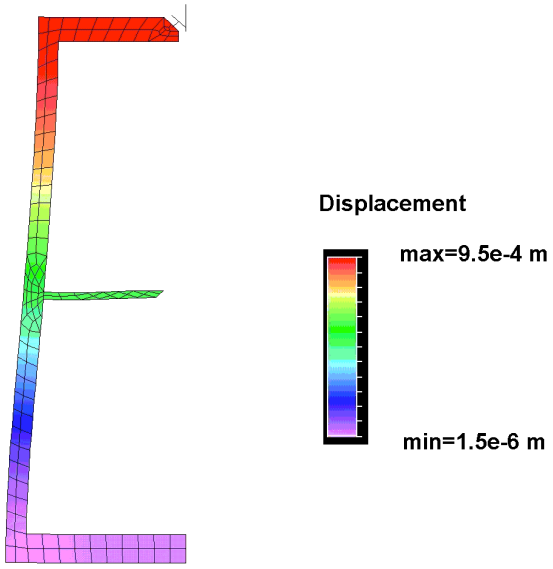

(a) Thin aluminium housing

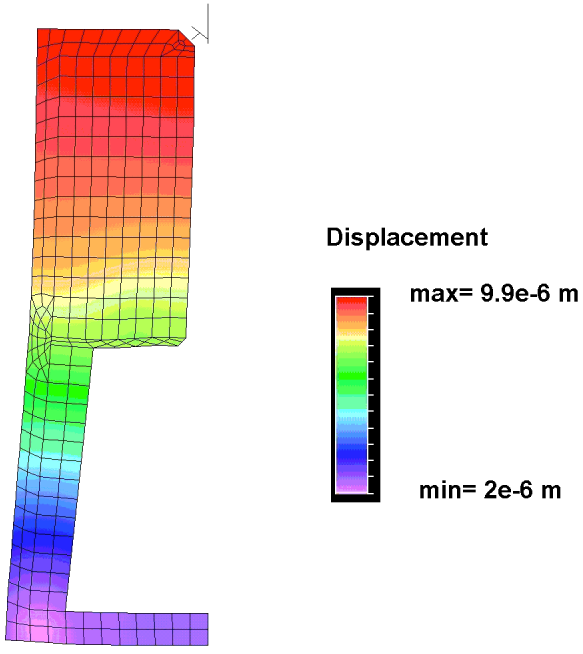

(b) Extra wide aluminium housing with potted stators

Figure 8.6: Deflections of the housing under vacuum for two different dimensions.

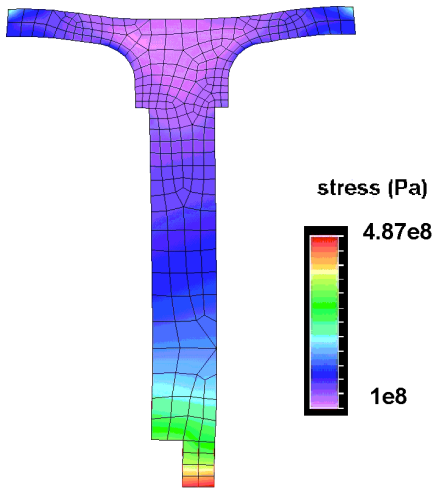

Figure 8.7: Centrifugal stresses in the rotor at 16000 rpm.

to the rotor in these slots. The laminated flywheel and the corresponding FE stress analysis conducted at 16000 rpm is shown in Fig.8.9. During the period of the Ph.D. project the construction of the flywheel has not been realized.

8.2.5 Technical drawings

Finally, as the last phase of the mechanical design the technical drawings were prepared in GTD. The overall drawing of the machine on which the most important parts are indicated, is shown in Fig.8.10. Fig.8.11 shows the technical drawings of the frame.

8.3 Materials

A high-speed machine requires special materials, such as high temperature permanent magnets, high strength steel, etc. The materials used in the production of the machine are listed in Table 8.1 with their properties.

The most binding difficulty is faced during the search for a proper stator lamination. The AFPM machine's stator is a toroid which should be made of a very long and thin lamination segment. Unfortunately, steel manufacturers are no selling such segments. Due to the difficulty of getting a laminated toroidal stator core made of thin silicon and isotrophic steel for a reasonable price, the M-4 grain-oriented silicon steel is chosen for the prototype machine. This can be considered as the weakest

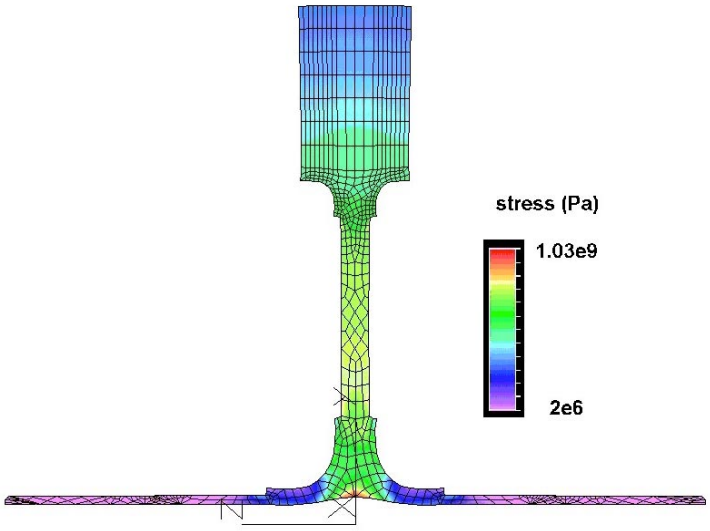

Figure 8.8: Centrifugal stresses in the rotor with the attached flywheel at 16000 rpm.

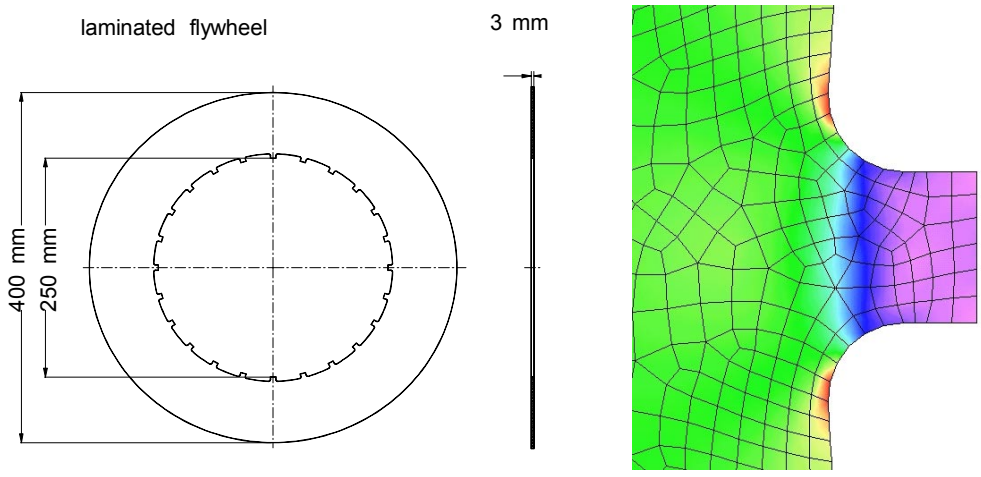

(a) (b)

Figure 8.9: Slots on the laminated flywheel (a), and the corresponding FE stress analysis (b), where the maximum stress of 900 N/mm^2 is found on the edge of the slots at maximum speed.

Machine part	*Material*	*Properties*
Stators	M-4 steel	laminations, 0.27 mm thickness grain-oriented
Rotor and shaft	34CrNiMo6	high strength
Housing	aluminium	high thermal conductivity
Windings	copper	1.06 mm diameter 1.12 mm including the lack layer
Winding insulation	F-class	-
Winding pot	Araldit 5156CW	low thermal expansion high thermal conductivity
Permanent magnets	GSN-33SH	max. temperature 150 °C, at 20°C: $B_r = 1.17T$ $H_c = 1672$ kA/m $(BH)_{\max} = 263$ kJ/m^3
Glue	Araldit 2014	high temperature resistance
Magnet retainer	glass fibre+epoxy	max. temperature 140 °C
Bearings	GMN S6005 ETA	high speed
Seals	PSseal 20×35 × 8	high speed low friction high temperature
Temperature sensors	thermocouples	type K
Magnet temp. sensor	DS1820	digital thermometer max temperature 125 °C
Position encoder	ROD 420	TTL output rated mech. speed 12000 rpm

Table 8.1: Material names and properties.

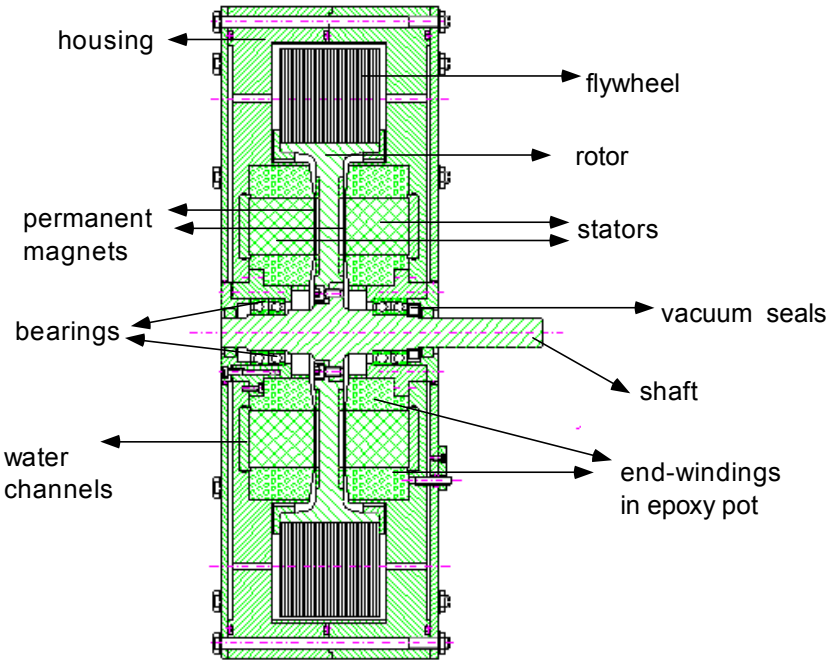

Figure 8.10: Overall technical drawing of the machine.

point of the prototype machine.

Grain-oriented steel is anisotropic, which means the magnetic characteristics, saturation flux density and loss levels are different in two directions. They show very good characteristics in the so-called easy or rolling direction (low loss and high permeability), but in the non-preferred direction quality is very low, B-H characteristic is poor, permeability is lower and the machine may suffer from higher core losses. Hence, they are perfect for a transformer where the magnetic flux has a single direction. However, in an electrical machine flux needs to be guided in both dimensions. For the non-preferred direction, there are no manufacturer's curves.

The stator cores are made by first rolling and pressing the steel (with 0.27 mm thickness) as a toroid with subsequent heat treatment. The shape of the toroidal stator cores is shown in Fig.8.12

Another difficulty faced during the material search phase was related with the glass fibre rim around the magnets. Since the product bought didn't have enough strength, another one was prepared in the mechanical shop of the University.

Insulation for the windings is chosen as F-class material which operates at temperatures up to 150 °C. The material used is relatively thick. It is a disadvantage since the thermal conduction between the windings and stators decreases. On the other hand, it is experienced that during the hand winding process thinner materials

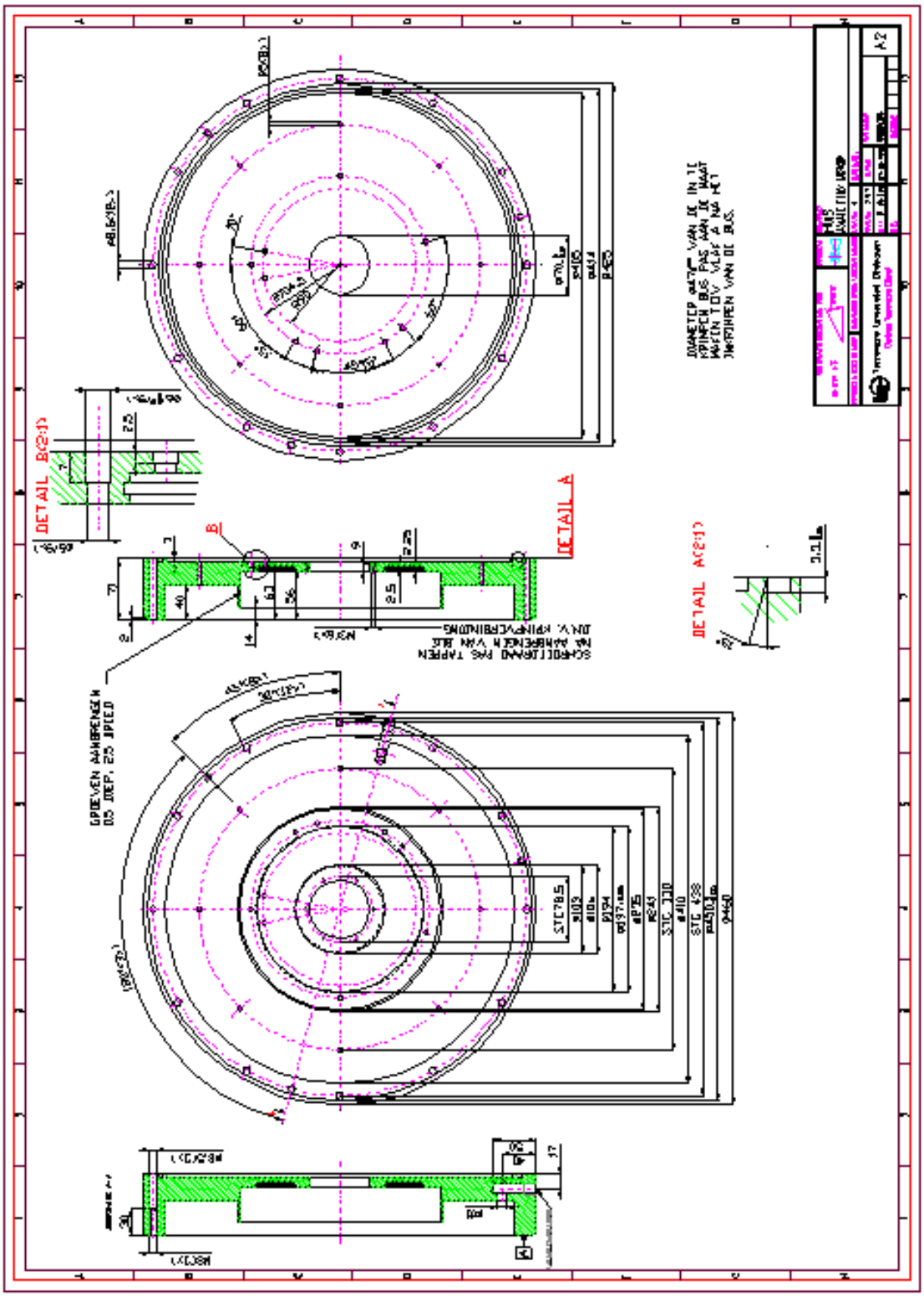

Figure 8.11: Technical drawings of the frame.

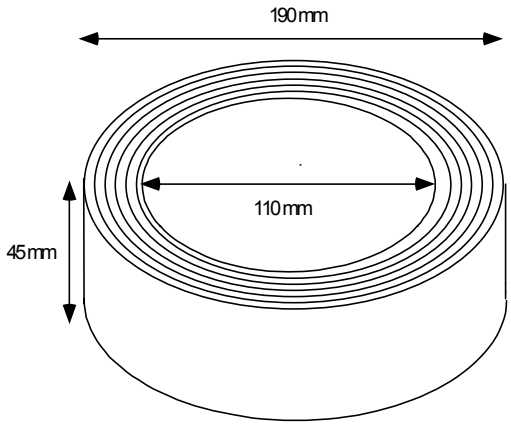

Figure 8.12: Stator core.

(such as Mylar) are totally destroyed. Aluminium is chosen as the material for the frame for its high thermal conductivity.

8.4 Manufacturing

The manufacturing work can be summarized with the following steps:

1. Preparation of the stators.
   (a) Eroding stator slots.
   (b) Placing insulation and windings.
   (c) Placing thermocouples at several possible hot spots inside the windings.
2. Manufacturing of the housing.
3. Attaching the stators with windings into the housing.
4. Epoxy potting of the stator windings.
5. Construction of the rotor.
   (a) Preparation of the retainer ring.
   (b) Gluing the permanent magnets inside the ring on the rotor surface.
   (c) Attaching the digital thermometer adjacent to one of the magnets.
6. Construction of the shaft.

7. Combining shaft and rotor by means of shrink fitting.
8. Balancing the rotor.
9. Placements of thermocouples inside the machine.
10. Placing vacuum seals.
11. Assembling the machine.
12. Inserting slip rings to the shaft for thermometer cables.
13. Constructing the safety ring in which the machine will be placed.

Slots are carved in the laminated stator cores with spark erosion technique. Since it is a very expensive method, punching is also advisable in mass production. Yet with punching, making slot tops with any desirable shape is not possible. In order to have a cost effective design rectangular or round slots should be preferred in that case.

The stators are hand wound while paying special attention to make the end windings shorter and the amount of copper in three phases the same on both stator units. The stator and windings are shown in Fig.8.13. The number of turns of each phase is 16 and each slot contains 4 coil sides. A coil is composed of 11 cylindrical conductors with a diameter of 1.06 mm (1.12 mm including the lack layer). The slot filling factor is 0.56. Considering the rated rms phase current (53 A), the maximum current density in the slot will be around 6 A/mm^2.

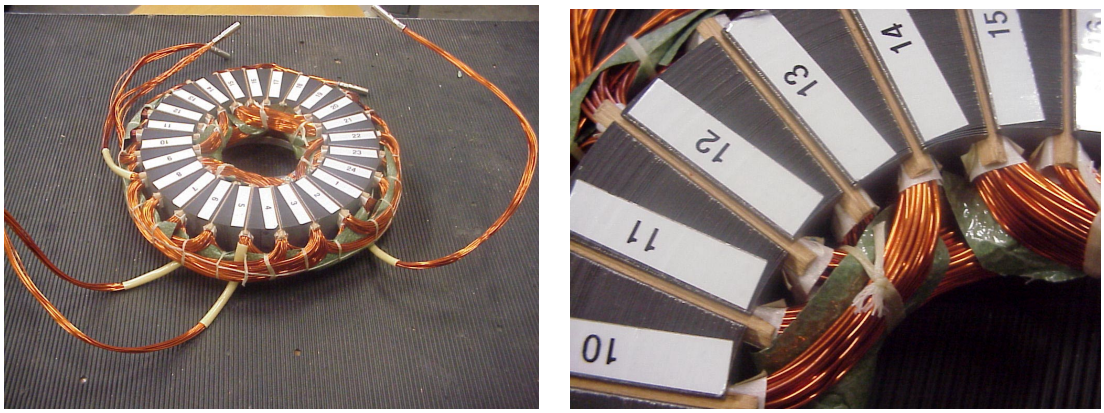

Figure 8.13: Stator and end windings.

The resistance values of the phases for both stator units are measured (after the winding process) at 26 °C and are listed in Table 8.2. The differences between the phase resistance values are very small, which shows the success of the hand winding.

	phase-A	phase-B	phase-C
Stator #1	9.98 mΩ	10.37 mΩ	10.42 mΩ
Stator #2	9.84 mΩ	9.85 mΩ	9.97 mΩ

Table 8.2: Measured phase resistance values.

Water cooling channels are placed between the stator cores and the housing and afterwards the stators are attached to the housing (Fig.8.14). In order to test the thermocouples and the efficiency of the cooling system, thermal tests were conducted on the stators before the motor assembly. Later, epoxy potting is applied to the stator windings since potting creates a more robust structure under reduced air pressure conditions. The major drawback is that the thermal conductivity of the epoxy is rather low, although it is higher than that of air.

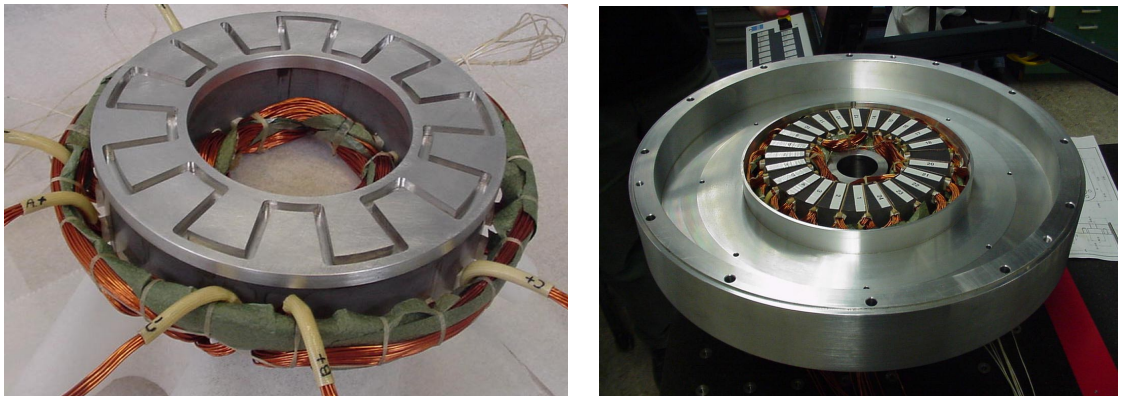

Figure 8.14: Water cooling channels and stator-housing

The thermal expansion and the reduced air pressure can cause a change in the airgap length. The airgap length tolerance is set to ±0.3 mm. This limit is determined considering the fact that different airgap lengths may cause an unbalance. Yet, there is no danger of demagnetization or excess heat within this range as discussed in section 7.2. Of course, it is best to keep the tolerance as low as possible. But the cost of a lower tolerance is a thicker housing. According to this tolerance, the thickness of the housing was computed as discussed in section 8.2.3.

Fig.8.15 shows the parts of the AFPM machine.

8.5 Conclusions

This chapter summarized the mechanical aspects of the design, the materials used and the manufacturing process of the prototype. The problems faced during this phase and the corresponding solutions are included. In the following chapter, the

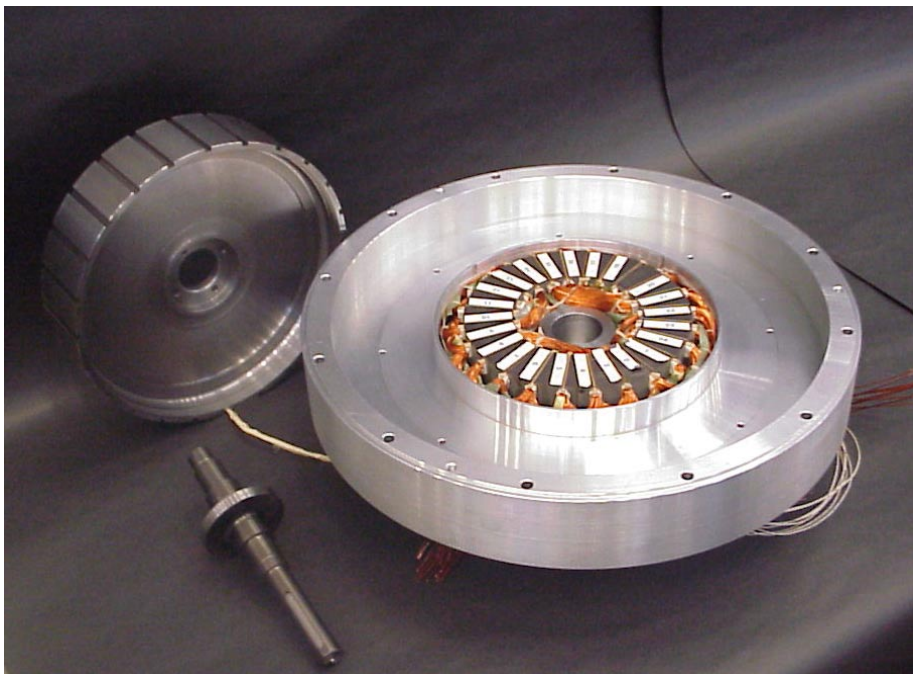

Figure 8.15: Stator, frame, rotor and shaft.

description of the test bench and the measurements conducted on the prototype machine will be given.

Chapter 9

Measurements

9.1 Introduction

This chapter aims to summarize the static performance measurements conducted on the machine and to compare the results with the predictions outlined in the former chapters.

The performance tests are conducted with the use of a test-bench especially developed to test electrical machines with high precision. It is possible to measure the performance of the machine in a broad torque and speed range. In section 9.2 the capabilities of the existing test bench are explained.

In order to evaluate the performance of a PM machine, the required tests can be listed as follows:

1. Measurement of the phase resistances and inductances.
2. Back-emf measurement of the phases at various speeds. This test is done by running the machine as a generator at no-load. From this test also the no-load losses of the machine with respect to speed can be observed.
3. Measurement of torque versus current at various speeds. By means of this test the linearity of the torque with increasing load may be detected.
4. Measurement of the efficiency at various load and speed conditions in order to determine the efficiency map.
5. Measurements of the temperature rise of the machine parts at various speed and load conditions.

The results of these tests are given in section 9.3.

Section 9.4 is devoted to the comparison of measured and predicted results and the explanation of the possible sources of discrepancies. The problems related with the high-speed machine testing are also contained in this section.

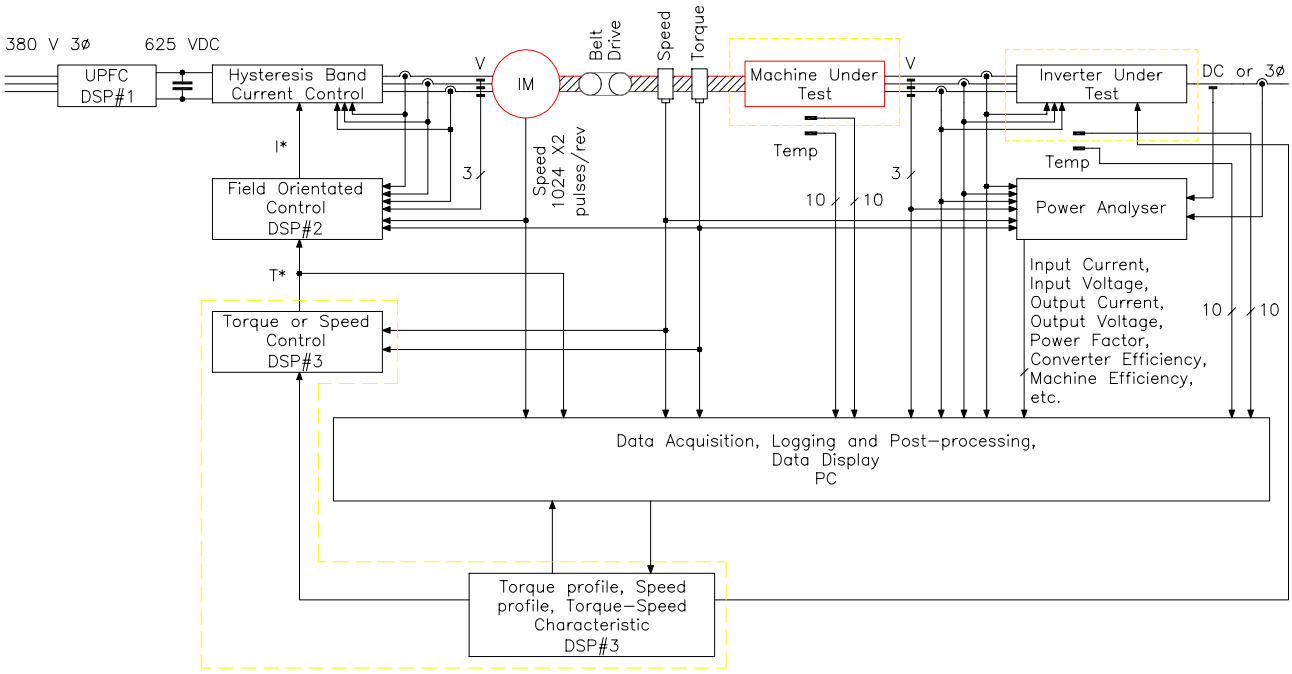

Figure 9.1: The machine test facility.

9.2 Test bench

The schematic of the test bench is shown in Fig.9.1 [108], [109]. This facility consists of an induction type load machine (IM) coupled to the machine under test, the high-speed AFPM machine in this case, through a Poly-V belt drive. The belt drive is designed to allow the machine to be tested at speeds up to 20000 rpm.

Based on Fig.9.1 several units of the test bench can be described as follows:

Computer-controlled mechatronic load (CoCoMeL):

The CoCoMeL unit in the test bench is composed of an induction type load machine (IM), a back to back converter between the mains and the IM, and the data acquisition and control system based on TMS320C40-DSPs.

The back to back converter consists of a pre-conditioner (UPFC) and a current controlled voltage-source inverter (CCVSI), both with a rated power of 30 kW.

The bi-directional preconditioner (universal power flow controller UPFC; see Fig 9.1) converts the AC power from the mains into the DC link and vice versa. It is controlled by means of a field oriented control principle assuming the grid as a synchronous machine. This control requires zero voltage crossover detectors in the

grid lines, an A/D converter for the DC link voltage, and a DSP (DSP#1 in Fig.9.1). The switching patterns of the six gates of the switches (IGBTs) of the rectifier are determined by SIN-PWM (sinusoidal pulse-width modulation).

The induction machine (IM) is driven by a 4-quadrant CCVSI, i.e. a voltage source inverter with a hysteresis band current control. The switch gate signals are obtained by comparing the actual (or measured) phase currents of the IM with the reference currents within a hysteresis or tolerance band. Detailed information related with the hysteresis current controller and its circuitry can be found in [110]. The IM is controlled with a torque or speed control system employing a field oriented control (DSP#2 in Fig.9.1) [111]. In order to ensure the safety of the overall bench, over-current and over-speed protections are built in.

Belt-drive system:

The load IM machine is rated at 19 kW, 45 A (rms) and 3000 rpm, with a maximum speed of 6000 rpm. It can be overloaded up to 34 kW, which corresponds to 76 A rms phase currents, for short periods. Low-speed machines to be tested can be directly coupled to the IM as shown in Fig.9.2a. In order to test high-speed machines a belt drive is used as indicated in Fig.9.2.b [112]. With the use of this belt drive (by means of various pulley/belt combinations) it is also possible to test low-speed/high-torque machines as well. A toothed type belt was chosen for the low speed transmission. The transmission ratio of the Poly-V belt drive which will be used to test the AFPM machine, is 1/3.33, so the maximum speed of 20000 rpm can be theoretically achieved on the high-speed side.

Machine/Inverter under test:

The high-speed machine was initially intended to be driven by a 4-quadrant PWM-VSI (inverter under test in Fig.9.1) where the fundamental frequency of this inverter sets the machine speed. PWM voltage-source inverters are very common in AC drives due to their ease of application, high power factor and good dynamic performance [113].

Since the controller units could not be completed during this project, a hysteresis band current controller similar to the one which is used for the load side is constructed. This gives the flexibility to control the current levels in the phases even at very low speeds and at starting. The dc voltage required for the IGBT-inverter (Semikron-SKiiP 132 GDL Power Pack, 3-phase bridge with a brake chopper, rated at 600 V-150 A) is supplied by a motor-generator set and the bi-directional power flow is established accordingly. During the measurements, the power factor of the AFPM machine is adjusted by controlling the load and dc voltage level.

Overall system torque&speed control unit:

In order to control and measure the torque and speed of the machine under test, torque and speed sensors are coupled at the output shaft of the machine. It is also decided that a digital outer control loop (by means of DSP#3 as shown in Fig.9.1) will be built. This part will ensure an accurate and dynamic torque or speed control.

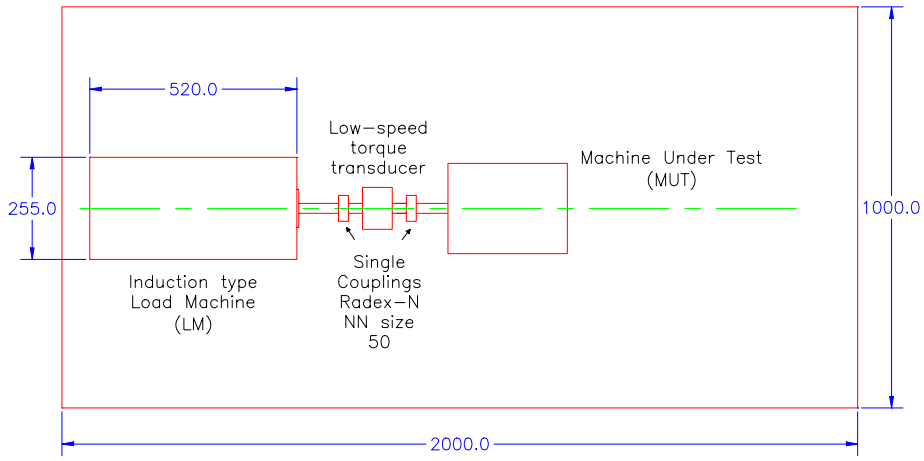

(a) Direct coupling of the machine under test to the IM.

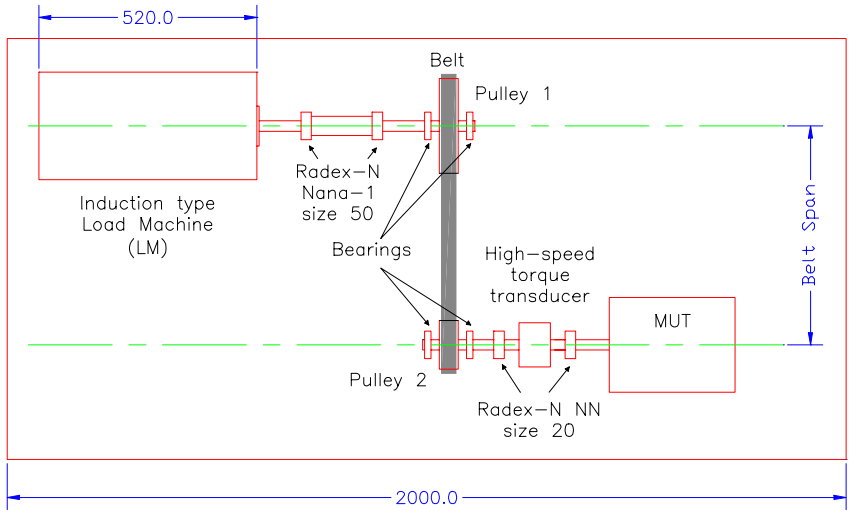

(b) Coupling of the high-speed machine by means of a belt drive.

Figure 9.2: Layout of the mechatronic load test facility (dimensions in mm.).

Post-processing and data acquisition unit:

In order to measure the input/output power of the machine, current and voltage are measured at its three terminals and the power is calculated by an LEM-Norma D6000 power analyzer. Output/input mechanical power is measured via the torque and speed sensors as indicated in Fig.9.1. So the power analyzer can determine the efficiency value. To facilitate the development of efficiency maps, the efficiency at many operating points on the torque-speed plane will be measured. The facility also allows the measurement and storage of the temperatures of various machine parts by means of a thermocouple scanner. In order to get the temperature reading of the digital thermometer (attached to a magnet) a microprocessor is used.

9.3 Performance measurements

9.3.1 Resistance and inductance measurements

After the manufacturing of the machine, the first step in the process of measurements is the measurement of all phase resistances and inductances. It is not only beneficial for determining the machine parameters, but also it is a check for manufacturing. Unexpected differences between the predicted and measured phase resistances and inductances, or unexpected differences between phases may imply a construction error.

The resistances were measured directly after the manufacturing of both stators and were presented in Table 8.2. The phase inductances were measured after the motor assembly with the use of an impedance analyzer and all phase inductance values were found to be approximately 140 μH. This value does not include the mutual inductances between phases. It should again be emphasized that the two stators were connected in series and the phases are connected in Wye scheme. Hence the phase inductance here implies two times one stator phase inductance. The method of calculation of the phase self inductance was explained in detail in section 4.4. The calculated phase self inductance is 152 μH. Considering the fact that the impedance analyzer measures the inductance at relatively high test frequency (1 kHz) with very low phase currents (in mA level) the difference is understandable. The predicted per unit value of the synchronous reactance per phase ($x_{s-pu} = 0.2$) is recommended to be used for the analysis of the machine by means of a phasor diagram in later testing and research steps. It is wise here to remind the relationship between the electromagnetic torque of the cylindrical rotor synchronous machine and the synchronous reactance as

$$T = \frac{P_{elm}}{\omega_m} = \frac{3}{\omega_m} \frac{V_{ph} E_{ph}}{X_s} \sin \delta, \tag{9.1}$$

where δ is the load angle, which is the angle between the phase voltage V_{ph}, and the phase emf E_{ph}.

The measured inductances were at several rotor positions were equal. This test can be seen as a check on the magnets and airgaps. Under normal circumstances, the inductance should not vary with respect to rotor position for surface-mounted PM machines.

9.3.2 Back-emf measurement

This test is important since the relationship between the produced torque and the back-emf is obvious. From this test, the machine's back-emf constant can also be derived. By driving the AFPM test machine with the induction machine at several speeds, the phase-emf (rms) values were recorded and compared with the predictions. Unfortunately, troubling vibrations have been detected in the belt drive system at higher speeds, so that it has been decided to run the machine only up to 10000 rpm.

The measured back-emf versus speed characteristic of the machine in comparison with the predicted one is shown in Fig.9.3. A small difference between the measured and predicted results is recognizable. It is found out later that the machine is mistakenly manufactured with smaller airgaps (around 1.3 mm instead of 1.5 mm) than it is designed. The airgaps are smaller than desired, consequently the airgap flux densities are higher. Back emf is proportional to the airgap flux density magnitude. Therefore, the difference between the measured and predicted emf values is understandable.

A line-emf waveform recorded by means of a digital scope at the speed of 9065 rpm is plotted in comparison with the predicted waveform as shown in Fig.9.4. Except the small difference caused by the airgap lengths, the waveforms coincide. Small hatches on the measured emf waveform are caused by the low precision of the magnet production. The magnets have small dimensional differences between each other.

9.3.3 No-load losses

No-load losses as its name implies cover the losses appearing without armature excitation; they are: friction losses, windage losses (air friction losses), bearing losses, and stator core losses. While doing the back-emf measurement test, the no-load losses of the machine were also measured by means of the torque and speed sensors. Measured losses up to 10000 rpm are compared with the predictions and extreme differences are detected. The results are shown in Fig.9.5. As it can be deduced from the figure, air friction losses are significantly suppressed by air pressure reduction and the differences between the normal and reduced air pressure cases are relatively similar in both measured and predicted cases. In this situation there are only two possible explanations:

1. Excess amount of friction losses, such as friction losses caused by vacuum seals or excess bearing losses: This may be possible up to a certain value, but it

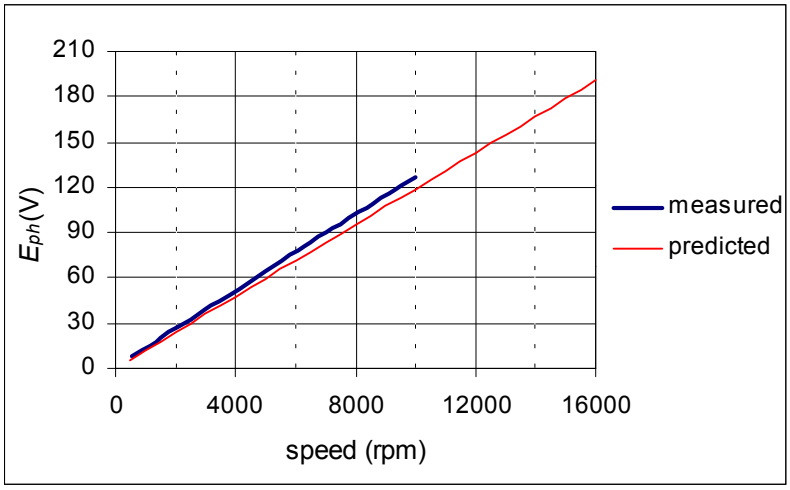

Figure 9.3: Measured and predicted phase-emf values (rms).

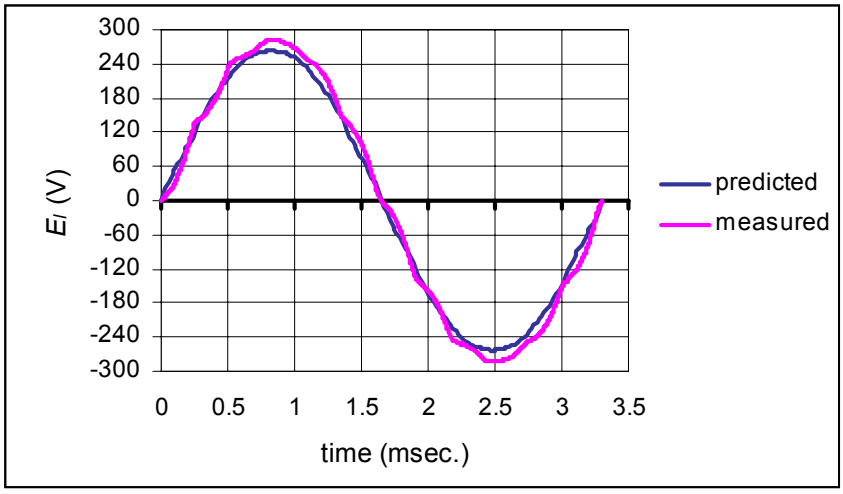

Figure 9.4: Measured and predicted line-emf waveforms at 9065 rpm.

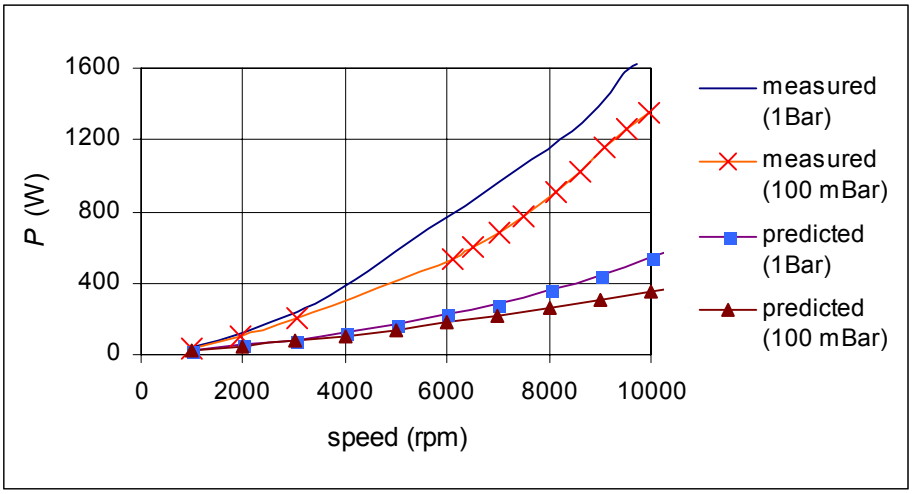

Figure 9.5: Measured and predicted no-load losses with respect to speed at normal and reduced air pressure.

can not explain almost 1000 W of loss difference at 10000 rpm. If there was such an excessive amount of loss caused by the seals, they should have been completely destroyed up to now which did not happen. On the other hand, the bearing manufacturer guaranteed the amount of losses (see section 6.5.2) in the bearings.

2. As it was already predicted during the first stage of the project, the plausible and even only possible explanation is that, the so-far unpredictable loss components are appearing in the stator cores because of the anisotropy of the grain-oriented M-4 steel ([114], [115], [116], [117], [118]), which is not a good alternative to be used in electrical machines, especially in the high-speed ones.

It is also interesting to note that the difference between the measured and predicted no-load loss differences is proportional to the speed (in other words this unexpected no-load torque is not a function of the speed). This directly implies extra hysteresis loss components in the M-4 steel.

9.3.4 Measurement of efficiency and current

To measure the efficiency of the machine at various load and speed conditions, the following experiments are carried out:

1. Using the control program (Assembler code) of the hysteresis-band current-controlled inverter (inverter under test as shown in Fig.9.1), the AFPM test-machine runs in motoring mode at constant (the desired) speed. The frequency

of the machine is set by the control program. The level of the phase currents is adjusted by using a variable resistance directly connected to the controller via the main computer.

2. The torque-control program is run on the DSP#2. The IM then supplies the desired load torque to the AFPM machine.

3. The power factor of the AFPM machine is adjusted as high as possible ($0.95 - 0.98$), by varying the level of the load and the input dc link voltage of the IGBT inverter which drives the AFPM machine. This is accomplished by changing the field excitation of the dc generator which is supplying the dc voltage to the inverter.

4. The machine is let to run in this state for a while till the steady-state temperatures are achieved. This can be detected from the recorded temperature values. Then the measurement data is taken.

Fig.9.6 shows the measured efficiency and phase current values with respect to varying torque at 3000 and 5000 rpm respectively as representative examples. A linear relation between the current and the torque is observed. The necessary currents are a bit higher than required, because of the lack of control of the rotor position. The measured efficiency values are labeled with dots and italics on the predicted efficiency map (as discussed in section 6.6) and shown in Fig.9.7.

Taking into account the amount of core losses observed from the no-load test, the experimental efficiency results and the other loss components are found to coincide with the predictions for the greater part. This means that if a proper stator steel was used instead of an M-4 steel, the desired efficiency levels would have been easily reached. For example, at 7000 rpm and 13.84 Nm, the total loss is measured as 947 W ($P_{out} = 10.15$ kW , $P_{in} = 11.097$ kW, $\cos\phi$=0.988, $\eta = 91.47\%$). If the unexpected loss of 460 W (which can be deduced from Fig.9.5) under reduced air pressure (100 mBar) did not exist, the efficiency value of 95.6% could have been achieved.

9.3.5 Temperature measurements

The temperatures of various machine parts are measured with the use of a thermocouple scanner and a microprocessor (for magnet temperature) at several load and speed conditions. Two examples of the measurements in comparison with the predicted values are shown in Fig.9.8. In the first example (Fig.9.8.a), the temperature rises of the magnet, the stator windings and the stator yoke are shown for the case, where when the machine is excited with a continuous current of 42 A at 6000 rpm, without water cooling, and at normal air pressure. In order to predict the

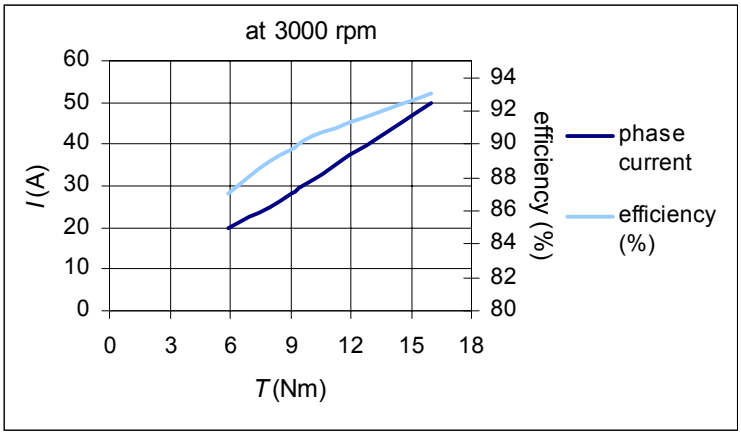

(a) Phase current and efficiency with respect to torque at 3000 rpm.

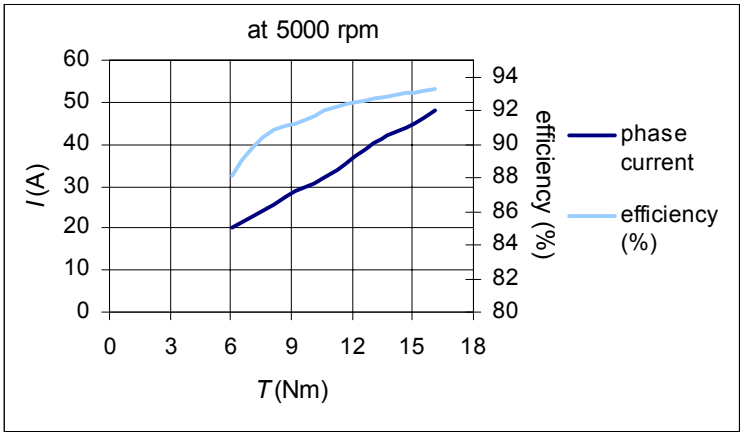

(b) Phase current and efficiency with respect to torque at 5000 rpm.

Figure 9.6: Measured phase current and efficiency with respect to torque.

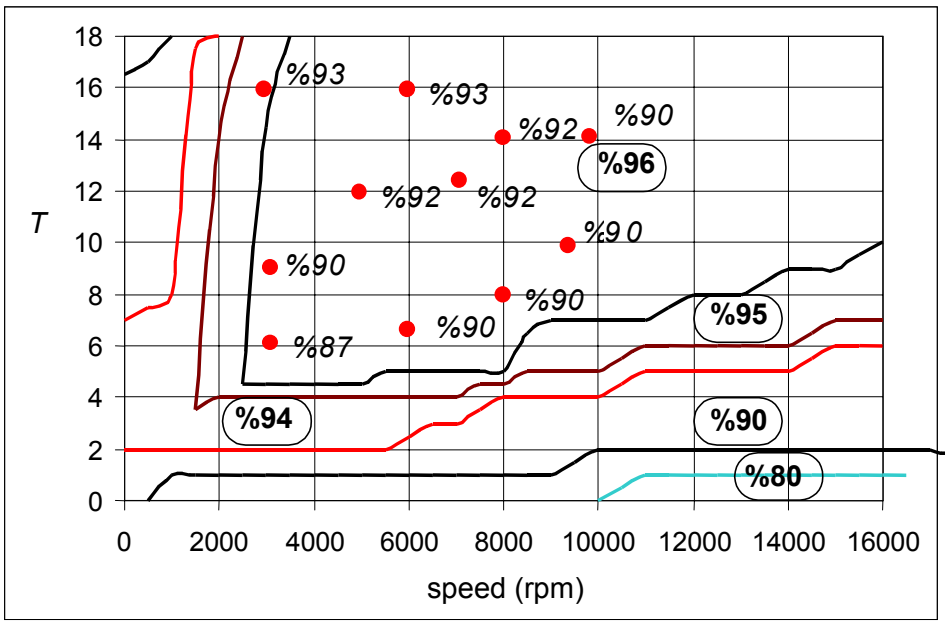

Figure 9.7: Measured efficiency points (indicated with dots and italics) on the predicted efficiency map.

temperature rises for this case, measured losses are applied to the thermal circuit as discussed in section 7.3. In this way the accuracy of the thermal equivalent circuit can be checked. In the second example (Fig.9.8.b), another case with water cooling (4 l/min water flow rate), and reduced air pressure (100 mBar) is investigated. The phase currents are set to 30 A rms, and the speed is 7000 rpm. Steady-state temperatures are reached in this case.

The differences between the measured and the predicted temperatures are generally not more than 12 °C. Stator winding temperatures indicated in the figures are measured from a thermocouple which is placed in a slot. Possibly the hot-spot temperature was measured while the prediction of the winding temperature corresponded to the average one. In the second case, the measured and the predicted steady-state winding temperatures converge to the same level although the slopes of the temperature rise differ.

It is recognized that the thermal equivalent circuit overestimates the magnet temperature values for all test cases. The underlying reason can be related with the approximations done for the calculation of the airgap convection resistances as discussed in section 7.7. The inaccuracy can also be associated with the unknown loss distribution in the machine.

It can be concluded from these tests that the thermal analysis of the AFPM machine through an equivalent circuit gives sufficient information about the thermal

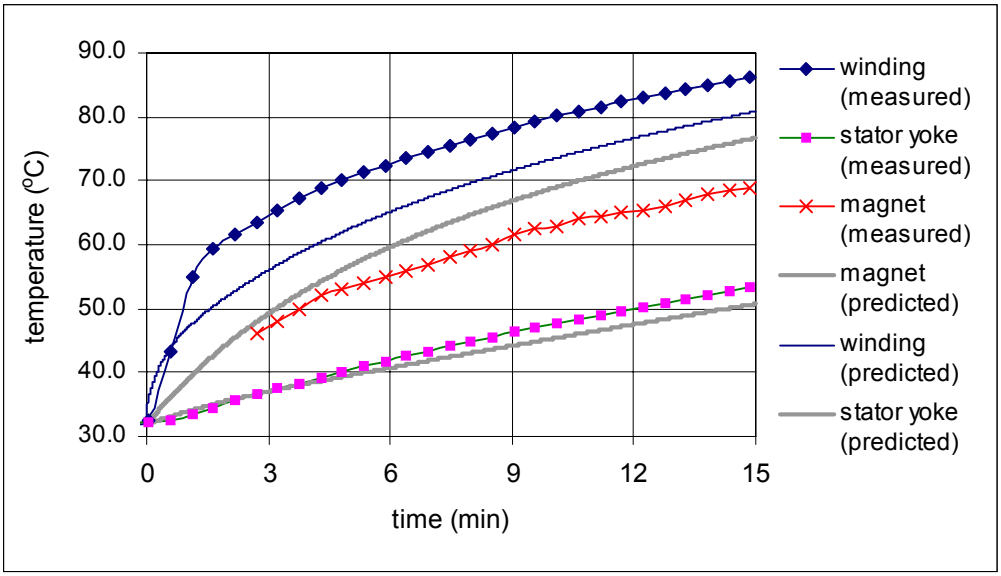

(a) $I = 42$ A, 6000 rpm, no water cooling, normal air pressure.

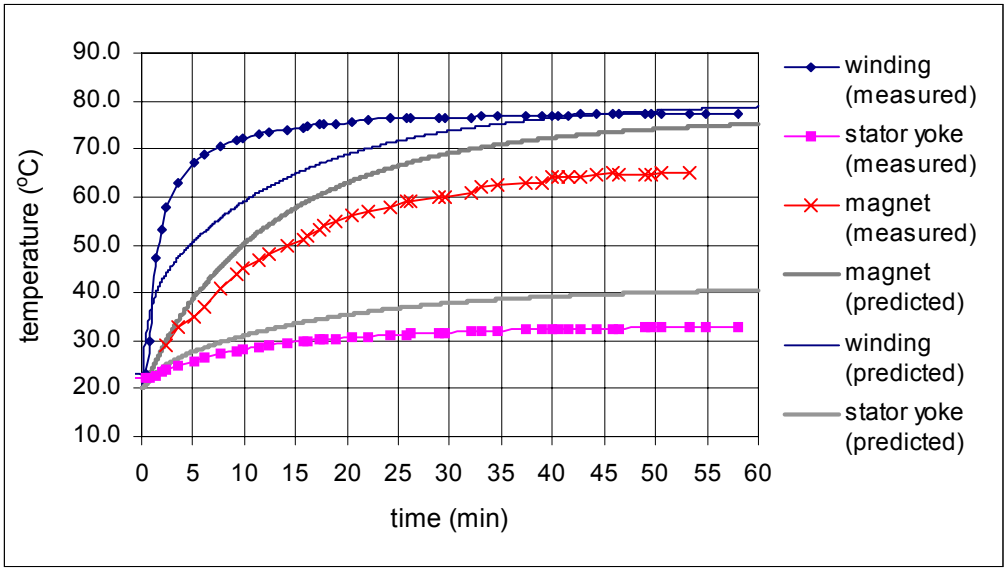

(b) $I = 30$ A, 7000 rpm, water flow rate =4 l/min, 100 mBar air pressure.

Figure 9.8: Measured temperature rises of the magnet, windings and stator yoke in comparison with the predicted results.

behavior of the machine.

9.4 Conclusions

The static performance tests conducted on the AFPM machine are summarized in this chapter. Information regarding the test facility is given. The conclusive remarks regarding the testing phase can be further summarized as follows:

1. The tests could only be carried out up to 10000 rpm, because of the troubling vibration levels in the belt drive at higher speeds. Three different types of belts were tried but the vibration problem could not be solved. It is concluded that a re-design of the belt drive system is necessary.

2. The testing of the machine with flywheel is left as a future study when the safety requirements are fully met in the laboratory.

3. Extreme core losses are detected in the grain-oriented M-4 steel which is used for the stators. As also explained and discussed in section 8.3, this type of steel is used in the production of the prototype since a conventional isotropic, low-loss steel with a modest price could not be found during the period of manufacturing.

4. From the efficiency and no-load tests, it is proven that this particular machine design can achieve the desired efficiency level (96%) if the stator cores are replaced with low-loss steel laminations or with some suitable recent powder-composite material [119].

5. The thermal equivalent circuit is proven to be a sufficient tool to predict the thermal behavior of the AFPM machine.

Chapter 10

Conclusions and recommendations

10.1 Conclusions

This study which is summarized by this dissertation set out with two objectives in mind: First accomplishing a high-speed electric machine exercise. Second, tapping on and contributing to the AFPM machine technologies, which is high on academic and industrial research and development agendas. At the outset, it was possible to make a choice towards carrying out the whole exercise on hypothetical grounds. Nevertheless, the close connections of TU/e with industry made it possible to have access to a real industry application as a well defined starting point. Consequently, the study turned into a real application involving also manufacturing and testing phases in addition to the theoretical design exercise which would constitute the whole study otherwise.

Naturally, the real industry application brought along additional challenges and complications. The usual electromagnetic issues related with high-speed machine design were complemented by additional mechanical engineering considerations. Accordingly, the study involved close interactions with mechanical engineers. The hybrid electric vehicle application that encompasses the research, demanded an electrical machine structure in which the high-speed rotating rotor is to be embedded in a flywheel. The machine is supposed to supply a mechanical torque of 18 Nm in the motoring mode, under normal driving conditions and short-time overloading capacity for cases like starting on the hill or a coupled trailer. In generating mode, while the flywheel energy is recuperated, the machine should be able to supply a power level of 30 kW. Since the electrical machine is integrated within the flywheel, the rotational speed of the machine is the same as that of the flywheel which corresponds to 7000 rpm in city driving and a maximum of 16000 while recuperating the brake energy. Furthermore, the HEV layout requires that the machine (including its frame) is designed small enough to fit in a cylindrical volume of 150mm as height and 240 mm as diameter.

These specifications, among others, lead to one major implication in terms of

electromagnetic requirements; high torque density, which is the main justification of the suitability of the AFPM machine to the surrounding HEV application. Chapter 2 was devoted to the derivation of the sizing equations of the AFPM machine and has demonstrated the torque density advantage of the axial- flux machine in comparison to the radial-flux type, in addition to its shape related advantages and other issues of suitability for the application.

During the theoretical design process, related design parameters have been chosen to increase the machine efficiency under the constraints brought about by high speeds. At this point, the answer to the question *"why is the design of a high-speed machine not straightforward?"* should be clarified.

A high speed rotating rotor with a flywheel tends to generate extremely high air friction losses. Under these circumstances, air pressure reduction inside the machine is inevitable. Reduced air pressure naturally decreases the heat transfer rate from the rotor to the stator which results in a rapid rise of the magnet and rotor temperature in a very short time. Hence, the machine design should carefully take the thermal considerations into account. In chapter 7, the thermal analysis of the designed AFPM machine was explained by a thermal equivalent circuit analysis and the predictions were presented.

The high-speed and evacuation based thermal problems are also aggravated with the high-frequency related eddy current losses occurring in the rotor magnets and rotor steel. These losses constitute further heating sources for the magnets. In the theoretical parts of this study, as explained in chapters 5 and 6, particular attention has been paid to the analysis of the rotor losses, which had to be decreased to acceptable levels.

There can be two solutions offered to this problem; either by the lamination of the magnets together with the usage of a low loss material for the rotor steel, or by eliminating the causes of rotor losses as much as possible during the design process. In this study, considering the potential mechanical problems that it could lead to, the first solution is ruled out. This choice can be understood considering the fact that under these high-speed conditions, the rotor structure must be mechanically very robust, at least for this first prototype. The problems and solutions related with the protection of the magnets against the high centrifugal forces and mechanical stresses in the rotor have been summarized in chapter 8. The mechanical analyses pointed out to the suitability of high-strength rotor steel, which is not an inherently low-loss material. Furthermore, laminated magnets are naturally more difficult to be kept in their places. As it was discussed in chapter 8, the magnets have been ordered with ramp shaped corners and then buried inside glass-fibre rims which support their four sides.

In chapter 3, major causes of rotor losses have been discussed: no-load rotor losses caused by the existence of the stator slots, on-load rotor losses induced by the time harmonics of the stator currents, and on-load rotor losses induced by the winding

space harmonics. The first type, slotting related losses were reduced to a negligible level by endowing the slots with slot-tops. The second type, the time harmonics related rotor losses were analyzed by simulating the PWM-VSI and computing the harmonic contents of the phase currents. The minimization of the current harmonics via the design optimization of the power electronic converter and control is left out of the scope of this study as a future research subject.

In chapter 4, an extensive space harmonic analysis of possible structures was carried out and the design variables were evaluated in terms of their space harmonic contributions. This study helped to choose a good combination of the design parameters, which ultimately resulted in a design with low space harmonic content and consequently low torque ripple. Accordingly, the magnitude of the rotor losses was suppressed. Although the noise and vibration aspects can not be considered as a part of this study and therefore related analyses have not been conducted, higher order harmonics and torque ripple have been associated by many researchers to audible noise and vibration, as a major source [107], [66], [120]. Hence, low torque ripple via low harmonic content design brought along some other advantages as well.

Although the major higher-order harmonic components could be suppressed by design, they have not been fully eliminated, and it has been shown that the 11^{th} and 13^{th} ordered components are still the dominating rotor loss producing mechanisms. Of course, in addition to the losses induced by the time harmonic components caused by the PWM drive scheme, there are other losses in the rotor which eventually result in heat. Under this situation, it is clear that the level of armature excitation should be modest by means of a dominant magnet flux density, which constitutes a trade off. Due to the nature of the application, as low as possible no-load losses are preferred. Since the rotor is integrated into a flywheel, no-load losses always exist and keep on reducing the overall system efficiency. Reduction of the no-load losses can only be made possible via the reduction of the stator core losses, since the air friction losses are suppressed by means of reduced air pressure.

In order to decrease stator core losses, the magnet excitation may be kept very low and a very low flux density may be permitted in the stator cores. Yet, this contradicts with the previous concept, which demands a compromise. In this design, both of these contradicting conditions were tried to be satisfied, by both keeping the magnet excitation dominant (around 0.73 T), and designing the stator cores with lower maximum flux density levels (1.2 T), with the cost of a relatively (to the extent permitted by the volume constraint) thicker stator back-iron. Considering the ultimate condition that a very low-loss steel is used for the stators, core losses can easily be minimized with this design. This is due to the fact that the machine was designed with only four poles, and the maximum frequency was kept around 533 Hz. With modern thin low-loss steel laminations, and with a relatively low level of core flux density, acceptably low amount of core losses could be achieved at this frequency.

Unfortunately, the desired stator steel as described above could not be obtained

due to time and financial restrictions. The stator cores are manufactured from grain-oriented M-4 steel. Measurements, as summarized in chapter 9, have shown an excess amount of core losses due to the anisotropic nature of the material. Yet, from the measurements it can be deduced that, the designed machine is capable of supplying the desired high efficiency with an acceptable temperature rise, if a proper material is chosen for the stators.

Measurements conducted on the machine also proved the correctness of the design and analysis methodology. Measured emf-speed and torque-current characteristics of the machine coincided with the predictions. It is also shown by the measurements that the thermal behavior of the AFPM machine can be successfully predicted with a thermal equivalent circuit analysis.

10.2 Recommendations

Having the design, manufacturing and testing steps completed, finally some recommendations and ideas related with future research subjects can be given. Here the recommendations will cover the further improvement of the designed machine and also the application related topics.

First of all, in order to improve the efficiency of the existing prototype, the stator cores should be replaced with cores made out of low-loss material; e.g. isotropic low loss steel laminations. It will also be a good research subject to replace the prototype machine stators with the ones made out of recent powder composite materials. The comparison between the previous design and the new one will give an insight and experience about this new material which may possibly dominate the future of electrical machines. Additionally, with the use of this material, and with the application of the alternative methods proposed by Jack et. al. [119], slot and end-winding structures can be improved. The stator cores can be produced with tooth elements as explained in [119] and later on pressed together with the windings. This method is claimed (in [119]) to enhance the slot filling factor up to 78%, and to reduce the end-winding length and consequently the copper losses. Hence the machine efficiency may further be enhanced. On the other hand, possible disadvantages of the material such as relatively higher hysteresis losses (in comparison to isotropic steel laminations), should also be evaluated.

This study did not cover the drive circuitry and the required control for the HEV application. The optimization study of the overall drive system including the machine, inverter, control and the battery is advised to be conducted.

Appendices

Appendix A

List of symbols and abbreviations

A.1 Symbols

$A-$magnetic vector potential.
A_g-airgap pole area.
A_m-magnet area.
A_s-slot area.
$B-$flux density.
$\widehat{B}_{a1}-$amplitude of the fundamental component of armature reaction flux density.
$B_{g0}-$airgap flux density
$\widehat{B}_{g1}-$amplitude of the fundamental component of the airgap flux density.
B_m-magnet flux density.
B_r-magnet remanence.
C_f-friction coefficient.
C_o-bearing coefficient.
D_i-stator inside diameter.
D_o-stator outside diameter.
$E_{ph}-$rms value of the phase emf.
$\widehat{E}_n-$amplitude of the n^{th} order emf.
$\%E_{harm}-$percentage harmonic contents of the emf.
$F-$force.
F_n-normal force.
F_t-tangential force.
F_g-mmf.
$H-$magnetic field intensity.
H_m-magnet field intensity.
H_g-airgap field intensity.
$I-$rms value of the phase current.
I_s-slot current.

$J-$current density
K_1-stator surface current density.
K_r-inner to outer diameter ratio of the stators.
L_i-effective length of the stator core in radial direction.
L_m-magnet length.
L_s-self inductance.
$L_{sl}-$slot leakage inductance.
$L_{end}-$end-turn leakage inductance.
$L_{st}-$stator axial yoke length.
L_y-stator axial length excluding slots.
M_s-mutual inductance.
N_p-number of turns per pole.
$N_{ph}-$actual number of series turns per phase.
N_s-sinusoidally distributed series turns per phase.
$Nu-$Nusselt number.
$S_{elm}-$apparent electromagnetic power.
$P-$power.
$P_{add}-$additional losses.
$P_{br}-$bearing losses.
$P_{elm}-$electromagnetic power.
$P_{cu}-$copper losses.
$P_{fe}-$stator core losses.
$P_{loss}-$power loss.
$P_{mech}-$mechanical losses.
$P_{rotor}-$rotor losses.
P_r-Prandtl number.
$R_{ph}-$stator phase resistance
RE_g-Couette Reynolds number.
RE_r-Tip Reynolds number.
$T-$temperature.
$T-$torque.
T_a-Taylor number.
X_a-armature reaction reactance.
$X_{end}-$end-turn leakage reactance.
X_l-leakage reactance.
X_s-synchronous reactance.
$X_{sl}-$slot leakage reactance.
$X_{dif}-$differential leakage reactance.
$c-$specific heat capacity.
$c_\tau-$ratio of the magnet pole pitch to pole pitch.
d_b-slot-depth excluding slot-top.

d_s-total slot depth.
$d_{t1}, d_{t2}-$slot-top depths
$e-$voltage induced in a conductor.
$e-$emissivity.
$f-$frequency.
$g-$airgap length.
$g''-$effective airgap length.
$h-$number of stator faces.
$i-$current.
$\widehat{i}-$amplitude of the phase current.
$k-$thermal conductivity.
$k_{cp}-$conductor packing factor.
$k_{dn} - n^{th}$ order winding distribution factor.
$k_{off-n} - n^{th}$ order stator-offset factor.
$k_{pn} - n^{th}$ order winding pitch factor.
$k_{sn} - n^{th}$ order skew factor.
$k_{wn} - n^{th}$ order winding factor.
$n-$ space harmonic number.
$n_{cs}-$number of conductors per slot
$n_{spp}-$number of slots/pole/phase.
$p-$number of pole pairs.
$p_{fe}-$specific iron (core) loss.
$q-$current time harmonic number.
$r-$radius.
r_i-inside-radii of the stator.
r_o-outside-radii of the stator.
$t-$time.
w_s-slot-top width.
$w_{sb}-$slot bottom width.
$\nu-$volume
$\ell-$conductor length.
$\ell_{end}-$end-turn length.
$\ell_{turn}-$turn length.
$\alpha-$electrical angle between the rotor and the stator magnetic axis.
$\alpha-$convection heat transfer coefficient.
$\beta-$torque angle.
ϕ_a-armature reaction flux per pole.
ϕ_g-airgap flux per pole.
ϕ_y-stator yoke flux.
θ_c-coil pitch in electrical degrees.
θ_p-pole pitch in mechanical degrees.

θ_s−slot pitch in electrical degrees.
θ_m−magnet span in electrical degrees.
Ω−scalar vector potential.
γ−electrical angle of the skew.
δ−load angle.
$\Re$−reluctance.
$\Re_g$−airgap reluctance.
$\Re_m$−magnet reluctance.
σ−conductance.
σ−Stephan-Boltzmann constant.
ζ−torque density.
ζ−diffusivity.
τ_m−magnet span.
τ_p−pole pitch corresponding to average diameter.
μ_0−relative permeability of free space.
μ_r−relative permeability of the magnet.
ρ−specific density.
υ−velocity in.
ϑ−kinematic viscosity.
ω−angular frequency.
ω_m−mechanical angular frequency of the rotor.

A.2 Abbreviations

emf-electromotive force.
mmf-magnetomotive force.
AFPM-axial-flux permanent-magnet.
CoCoMel-computer controlled mechatronic load.
CCVSI-current-controlled voltage source inverter.
DSP-digital signal processor.
EV-electric vehicle.
FE-finite element.
FEA-finite element analysis.
FEM-finite element method.
GTD-gemeenschappelijke technische dienst.
HEV-hybrid electric vehicle.
ICE-internal combustion engine.
IGBT-integrated gate bipolar transistor.
IM-induction machine.
MDS-multiple drive system.
NN-North to north type magnet arrangement.

NS-North to south type magnet arrangement.
PM- permanent magnet.
PWM-pulse width modulation.
RFPM-radial-flux permanent-magnet.
SD-standard deviation.
SDT-standard deviation of torque.
UPFC-universal power flow controller.

Appendix B

Percentage higher order harmonic contents of various structures

In Fig.B.1, the significant harmonic amplitudes of some alternative structures presented in Table 4.2 (corresponding to configuration numbers 13, 12, 11 10, 7, 5, 4, 1 in order of appearance) are shown.

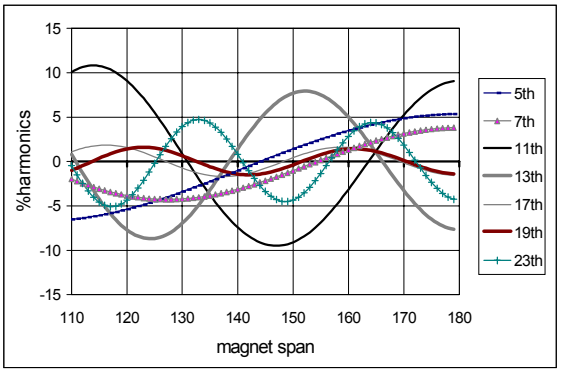

(a) 24 slots, full-pitched

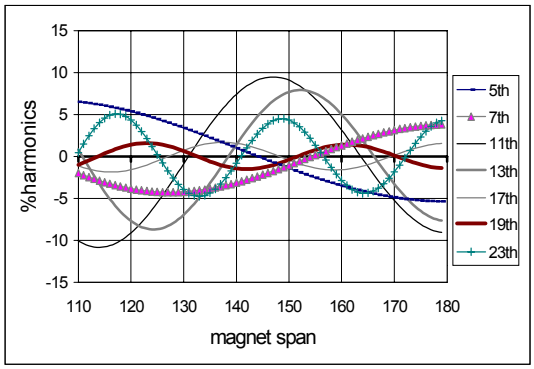

(b) 24 slots, 2/3 full-pitched

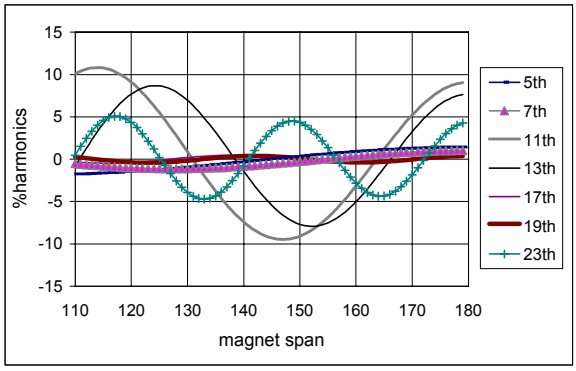

(c) 24 slots, 5/6 full-pitched

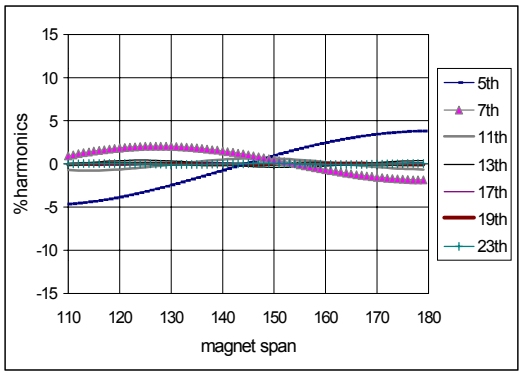

(d) 21 slots

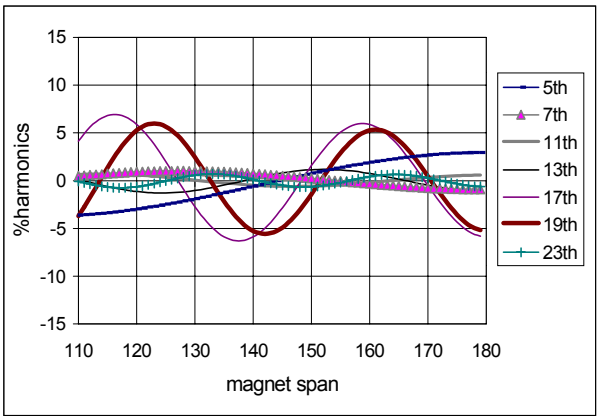

(e) 18 slots

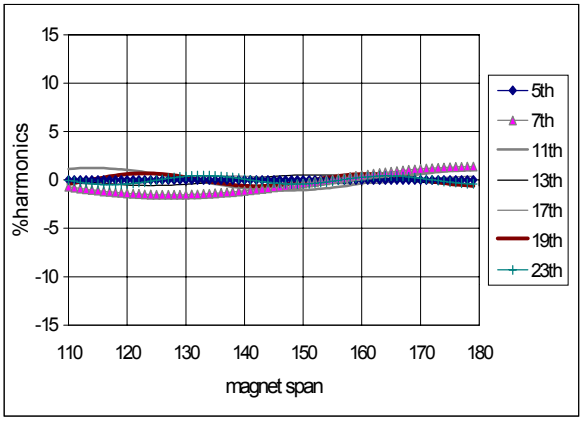

(f) 15 slots

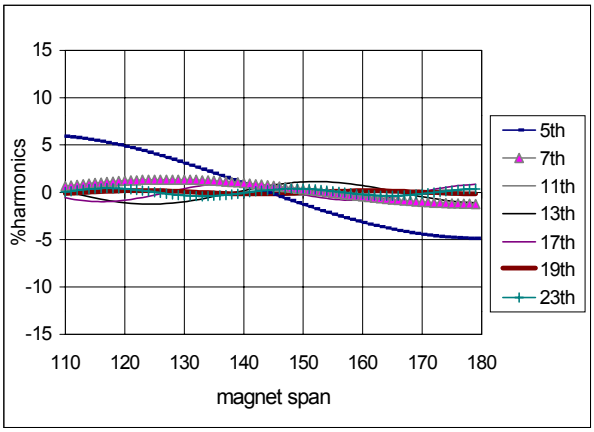

(g) 15 slots, 2/3 full-pitched

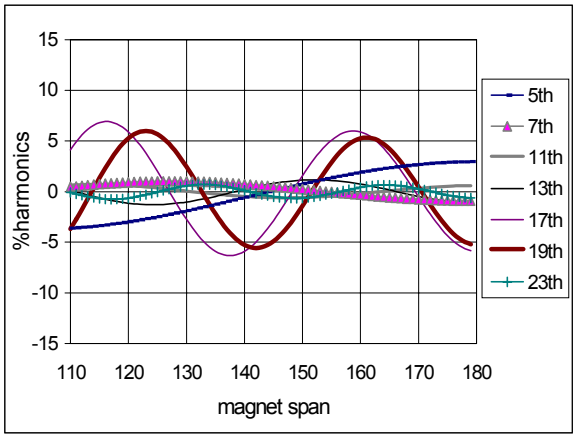

(h) 9 slots

Figure B.1: Percentage higher order emf harmonic components of various alternative structures (slot/winding pitch) as a function of magnet span in electrical degrees.

Appendix C

Standard deviations of torque for various structures

The standard deviation (SD) of the torque for several configurations as presented in Table 4.2 as a function of the magnet span are listed in Table C.1. Specifications of the structures represented with configuration numbers (#13, #12,..etc.) are given in Table 4.2. The mean torque is assumed 18 Nm.

θ_m	#13	#12	.#11	#10	#5	#1	#7	#4	#9	#8
110	1.87	3.09	1.30	0.73	0.59	0.65	0.65	0.99	0.53	0.96
111	1.91	1.60	1.54	0.79	0.56	0.80	0.80	0.98	0.77	1.12
112	1.91	1.57	3.14	0.79	1.41	2.12	2.12	1.74	0.81	1.20
113	1.88	1.80	1.73	0.74	0.40	0.89	0.89	0.90	0.54	0.96
114	1.68	3.39	1.72	0.57	0.27	0.88	0.88	0.83	0.38	0.86
115	1.67	1.97	1.97	0.48	0.42	1.10	1.10	0.90	0.45	0.89
116	1.67	1.95	3.57	0.49	1.42	2.43	2.43	1.74	0.50	0.97
117	1.65	2.20	2.17	0.58	0.58	1.28	1.28	0.98	0.42	0.85
118	1.39	3.89	2.15	0.56	0.61	1.28	1.28	0.98	0.44	0.86
119	1.31	2.35	2.42	0.66	0.83	1.53	1.53	1.14	0.67	0.98
120	1.31	2.21	4.69	0.84	2.33	3.45	3.45	2.56	0.90	1.21
121	1.30	2.32	2.39	0.70	0.82	1.51	1.51	1.12	0.64	0.92
122	1.26	3.83	2.09	0.51	0.59	1.24	1.24	0.93	0.44	0.79
123	1.41	2.10	2.10	0.42	0.56	1.23	1.23	0.90	0.46	0.79
124	1.41	1.83	3.49	0.43	1.41	2.37	2.37	1.67	0.49	0.85
125	1.40	1.83	1.86	0.46	0.40	1.00	1.00	0.78	0.40	0.70
126	1.33	3.24	1.60	0.43	0.28	0.77	0.77	0.68	0.41	0.68
127	1.43	1.60	1.60	0.54	0.42	0.79	0.79	0.75	0.60	0.81
128	1.43	1.35	3.05	0.76	1.42	2.06	2.06	1.63	0.78	1.00
129	1.42	1.38	1.40	0.74	0.58	0.69	0.69	0.81	0.72	0.85
130	1.33	2.91	1.16	0.52	0.61	0.54	0.54	0.80	0.54	0.69

θ_m	#13	#12	#11	#10	#5	#1	#7	#4	#9	#8
131	1.38	1.23	1.23	0.43	0.83	0.71	0.71	0.98	0.51	0.66
132	1.38	1.01	2.81	0.46	2.34	2.07	2.07	2.43	0.50	0.71
133	1.37	1.12	1.13	0.44	0.82	0.82	0.82	0.94	0.39	0.53
134	1.26	2.78	0.95	0.36	0.59	0.80	0.80	0.73	0.38	0.48
135	1.28	1.11	1.11	0.47	0.56	1.04	1.04	0.69	0.57	0.60
136	1.28	0.98	2.78	0.68	1.41	2.39	2.39	1.53	0.70	0.81
137	1.27	1.18	1.16	0.82	0.40	1.24	1.24	0.53	0.75	0.81
138	1.14	2.86	1.08	0.60	0.26	1.24	1.24	0.40	0.60	0.64
139	1.13	1.30	1.30	0.50	0.40	1.50	1.50	0.49	0.59	0.58
140	1.13	1.26	2.95	0.50	1.41	3.43	3.43	1.49	0.54	0.61
141	1.12	1.50	1.46	0.45	0.56	1.49	1.49	0.60	0.38	0.44
142	0.95	3.12	1.44	0.35	0.59	1.22	1.22	0.60	0.33	0.40
143	0.90	1.69	1.69	0.43	0.82	1.21	1.21	0.82	0.51	0.49
144	0.90	1.68	3.29	0.62	2.33	2.36	2.36	2.32	0.67	0.67
145	0.89	1.94	1.90	0.73	0.81	1.00	1.00	0.81	0.66	0.72
146	0.66	3.55	1.89	0.69	0.58	0.76	0.76	0.58	0.64	0.73
147	0.55	2.15	2.15	0.60	0.54	0.78	0.78	0.56	0.64	0.64
148	0.56	2.13	3.85	0.56	1.39	2.05	2.05	1.46	0.61	0.62
149	0.55	2.41	2.33	0.48	0.37	0.68	0.68	0.42	0.41	0.47
150	0.20	4.69	2.20	0.37	0.22	0.53	0.53	0.30	0.29	0.45
151	0.43	2.39	2.32	0.42	0.37	0.70	0.70	0.45	0.44	0.54
152	0.44	2.11	3.83	0.57	1.40	2.07	2.07	1.49	0.61	0.65
153	0.43	2.12	2.12	0.66	0.54	0.82	0.82	0.62	0.61	0.66
154	0.49	3.51	1.85	0.69	0.57	0.80	0.80	0.65	0.63	0.78
155	0.68	1.88	1.85	0.69	0.81	1.04	1.04	0.87	0.68	0.82
156	0.68	1.63	3.25	0.63	2.32	2.39	2.39	2.37	0.65	0.75
157	0.68	1.63	1.63	0.52	0.80	1.24	1.24	0.89	0.45	0.56
158	0.71	3.07	1.38	0.39	0.57	1.25	1.25	0.70	0.28	0.54
159	0.83	1.44	1.41	0.41	0.53	1.51	1.51	0.70	0.39	0.63
160	0.84	1.20	2.91	0.52	1.39	3.45	3.45	1.55	0.53	0.76
161	0.84	1.25	1.25	0.60	0.36	1.51	1.51	0.62	0.54	0.68
162	0.86	2.82	1.03	0.64	0.22	1.24	1.24	0.55	0.58	0.77
163	0.96	1.15	1.13	0.77	0.37	1.24	1.24	0.66	0.76	0.97
164	0.96	0.96	2.77	0.69	1.40	2.38	2.38	1.60	0.70	0.95
165	0.96	1.11	1.10	0.57	0.55	1.03	1.03	0.81	0.50	0.72

θ_m	#13	#12	#11	#10	#5	#1	#7	#4	#9	#8
165	0.96	1.11	1.10	0.57	0.55	1.03	1.03	0.81	0.50	0.72
166	0.97	2.77	0.97	0.43	0.58	0.80	0.80	0.83	0.32	0.65
167	1.05	1.15	1.16	0.41	0.81	0.82	0.82	1.03	0.39	0.72
168	1.06	1.06	2.84	0.48	2.33	2.07	2.07	2.48	0.50	0.85
169	1.05	1.28	1.27	0.54	0.81	0.71	0.71	1.05	0.47	0.77
170	1.07	2.93	1.23	0.58	0.59	0.57	0.57	0.88	0.51	0.80
171	1.14	1.44	1.47	0.73	0.55	0.72	0.72	0.88	0.73	0.97
172	1.14	1.42	3.09	0.75	1.40	2.07	2.07	1.66	0.78	1.09
173	1.14	1.66	1.66	0.62	0.39	0.83	0.83	0.81	0.56	0.87
174	1.16	3.27	1.65	0.48	0.26	0.81	0.81	0.75	0.38	0.76
175	1.22	1.88	1.91	0.44	0.40	1.04	1.04	0.83	0.41	0.79
176	1.23	1.88	3.53	0.45	1.41	2.39	2.39	1.70	0.49	0.90
177	1.23	2.14	2.14	0.49	0.56	1.25	1.25	0.94	0.43	0.81
178	1.24	3.84	2.12	0.53	0.60	1.26	1.26	0.95	0.44	0.82
179	1.31	1.94	2.40	0.67	0.83	1.52	1.52	1.13	0.65	0.95

Table C.1: SDT values for various structures with respect to magnet span.

Appendix D

Simulation of the PWM inverter

The circuit shown in Fig.D.2 is used to simulate the PWM inverter by means of sine-triangle approach, in order to analyse the time harmonic components of the stator currents. Fig.D.1.a shows the sine-triangle waveforms which are the inputs of the comparators indicated in Fig.D.2. The three comparator inputs are 120° phase shifted and the frequency of the sinusoid determines the fundamental frequency of the voltages and currents of the machine which are shown in Fig.D.1.b. The triangle frequency is 5 kHz which is the constant sampling frequency of the inverter that will be used to test the prototype machine. The space vector PWM technique explained in [121] is used. The frequency of the reference sinusoid shown in Fig.D.1.a is 520 Hz and the harmonic content is high due to the relatively low sampling frequency used.

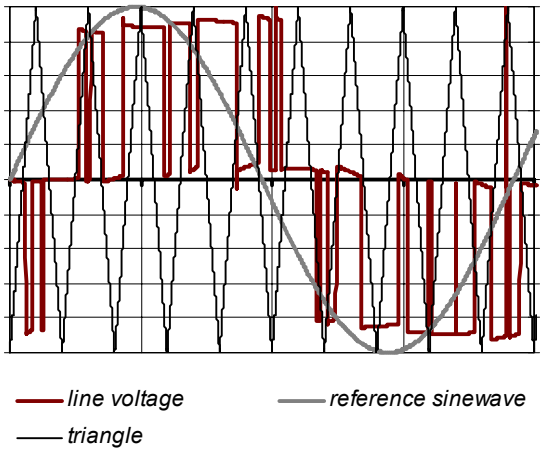

(a) Sine-triangular approach.

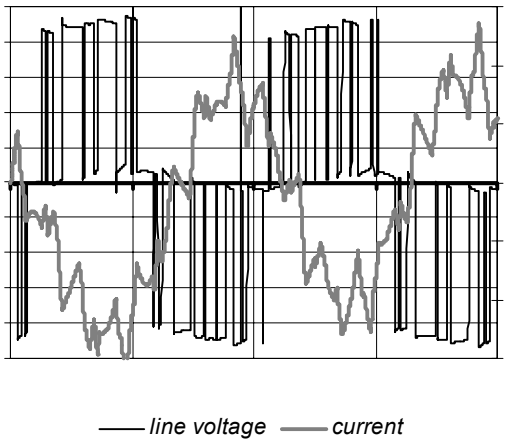

(b) Line to line voltage and current.

Figure D.1: PWM modulation.

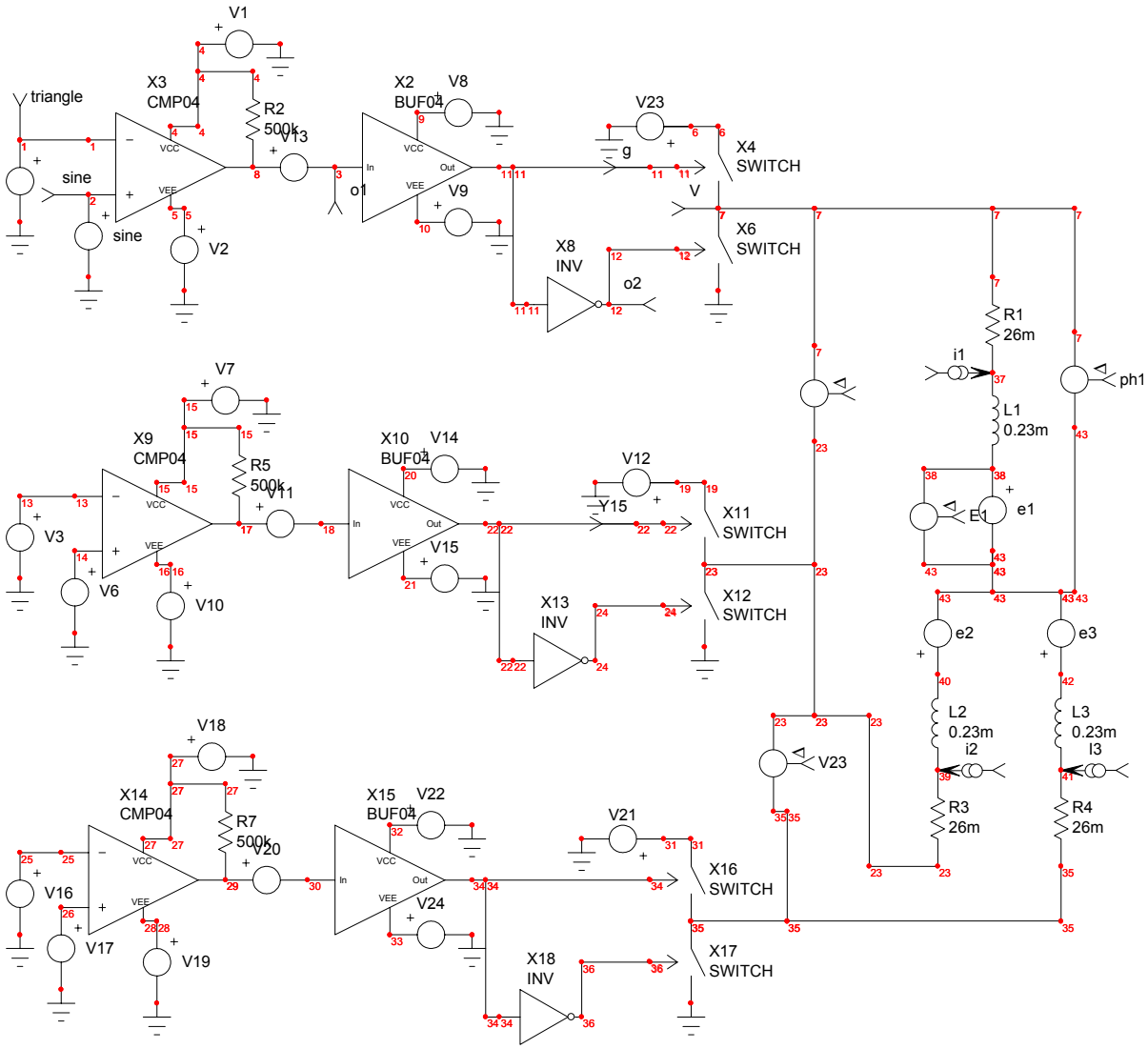

Figure D.2: Simulation circuit.

Bibliography

[1] W.W. Gibbs. Transportation's perennial problems. *Scientific American*, pages 32–35, October 1997.

[2] A. Schafer and D. Victor. The past and future of global mobility. *Scientific American*, pages 36–39, October 1997.

[3] B. Szabados and U. Schaible. Peak power bi-directional transfer from high speed flywheel to electrical regulated bus voltage system: A practical proposal for vehicular technology. *IEEE Trans. on Energy Conversion*, 13(1):34–41, March 1998.

[4] M.J. Riezenman. Engineering the EV future. *IEEE Spectrum*, pages 19–28, November 1998.

[5] G.J. Hoolboom and B. Szabodos. Nonpolluting automobiles. *IEEE Trans. on Vehicular Technology*, 43(4):1136–1144, 1994.

[6] G.L. Hunt. The great battery search. *IEEE Spectrum*, pages 21–28, November 1998.

[7] J.A. McDowall. Substation battery options: Present and future. *IEEE Power Engineering Review*, pages 4–7, November 2000.

[8] R.C. Stempel, S.R. Ovshinsky, P.R. Gifford, and D.A. Corrigan. Nickel-methal hybrid: Ready to serve. *IEEE Spectrum*, pages 29–34, November 1998.

[9] T. Gilchrist. Fuel cells to the fore. *IEEE Spectrum*, pages 35–40, November 1998.

[10] R.C. Flanagan and M. Keating. Evaluation of a flywheel hybrid electric vehicle drive. *Prof. of the 25th Intersociety Energy Conversion Conference*, 4:205–210, 1990.

[11] C. Mendler. Electric drive for flywheel energy storage. *IECEC'96*, 4:2199–2202, 1996.

[12] R.C. Flanagan and C. Aleong. Design of a flywheel surge power unit for electric vehicle drives. *Proc. of the 25th Intersociety Energy Conversion Conference*, 4:211–217, 1990.

[13] P. Acarnly, J. Mecrow, J.S. Burdess, J.N. Fawchett, J.G. Kelly, and P. G. Dickinson. Design principles for a flywheel energy store for road vehicles. *IEEE Trans. on Industry Applications*, 32(6):1402–1407, November 1996.

[14] G. Heidelberg and G. Reiniger. The magnetodynamic storage unit test results of an electrical flywheel storage system in a local public transport bus with a diesel electrical drive. *Proc. of the 23rd Intersociety Energy Conversion Engineering Conference*, 2:75–80, 1988.

[15] S.C. Triphaty. Electric drive for flywheel energy storage. *Energy Conversion and Management*, 35:127–138, February 1994.

[16] S.C. Triphaty. Simulation of flywheel energy storage unit for city busses. *Energy Conversion and Management*, 33:243–250, April 1992.

[17] H.A. Rosen and D.R. Castleman. Flywheels in hybrid vehicles. *Scientific American*, pages 49–51, October 1997.

[18] V. Wouk. Hybrid electric vehicles. *Scientific American*, pages 44–48, October 1997.

[19] T.P.M Cadee and J.H.M van Rooij. Hybrid driving system. In *Europian Patent Specification, Patent Number: EP 0 665 B1*, 1997. bulletin 04.

[20] A. Van Zyl and R. Spee. Short term energy storage for ASD ride-through. *IEEE IAS'98*, pages 1162–1167, 1998.

[21] Z. Zhang, F. Profumo, and A. Tenconi. Axial flux wheel machines for electric vehicles. *Electric Machines and Power Systems*, 24:883–96, 1996.

[22] K.R. Pullen, M.R. Etemad, and M.R. Fenocchi. The high speed axial flux disk generator unlocking the potential of automative gas turbine. *IEE Colloquium on Machines and Drives for Electric and Hybrid Vehicles*, pages 1–4, June 1996.

[23] F. Caricchi, F. Crescimbini, O. Honorati, and E. Santini. Compact wheel direct drive for EVs. *IEEE Industry Application Magazine*, pages 25–32, November-December 1996.

[24] A. Di Napoli, F. Caricchi, F. Crescimbini, and G. Noia. Design criteria of a low speed axial flux synchronous machine. *Int. Conf. On Evolution and Modern Aspects of Synchronous Machines*, pages 1119–1123, 1991.

[25] F. Profumo, Z. Zhang, and A. Tenconi. Axial flux machine drives: A new viable solution for electric cars. *IEEE Trans. on Industrial Applications*, 44(1):39–45, February 1997.

[26] F. Caricchi, F. Crescimbini, F. Mezzetti, and E. Santini. Multistage axial flux PM machine for wheel direct drive. *IEEE Trans. on Industry Applications*, 32(4):882–887, July 1996.

[27] F. Caricchi, F. Crescimbini, A. Di Napoli, and M. Marcheggiani. Prototype of electric vehicle drive with twin water cooled wheel direct drive motors. *PESC'96*, 2:1926–1932, 1996.

[28] F. Caricchi, F. Crescimbini, and A. Di Napoli. Prototype of innovative wheel direct drive with water cooled axial flux pm motor for electric vehicle applications. *APEC'96*, 2:764–770, 1996.

[29] E. Spooner and B.J. Chalmers. TORUS: A slotless toroidal-stator, permanent magnet generator. *IEE-Proc.-B*, 139(6):497–506, November 1992.

[30] M.M. El-Missiry, Z. Zuncheng, and E. Spooner. The electrical performance of anaxial flux, slotless, toroidally wound, permanent magnet alternator with rectified output. *Proc. of the 25th Universities Power Engineering Conference*, 2:293–296, September 1990.

[31] F. Caricchi, F. Crescimbini, and O. Honorati. Low cost compact PM machine for adjustable speed pump application. *IEEE IAS'96*, 1:464–470, 1996.

[32] F. Caricchi, F. Crescimbini, and E. Santini. Basic principle and design criteria of axial-flux PM machines having counter rotating rotors. *IEEE Trans. on Industry Application*, 31(5):1062–68, September 1995.

[33] J. F. Gieras and M. Wing. *Permanent Magnet Motor Technology, Design and Applications*. Marcel Dekker, Inc., 1997.

[34] M. Van Dessel, R. Belmans, and E.A. Hemead. Design of a small, axial-flux permanent-magnet motor. *ETEP'96*, 6(2):81–90, March/April 1996.

[35] A.G. Jack, B.C. Mecrow, and C.P. Madison. Combined radial and axial permanent magnet motors using soft magnetic composites. *IEE Ninth International Conference on Electrical Machines and Drives*, (468):25–29, 1999.

[36] D. Petterson and R. Spee. The design and development of an axial flux permanent magnet brushless DC motor for a wheel drive in solar powered vehicle. *IEEE Trans. on Industry Applications*, 31(5):1054–1061, September 1995.

[37] D. Platt. Permanent magnet synchronous motor with axial flux geometry. *IEEE Trans. on Magnetics*, 25(4):3076–3079, 1989.

[38] J.F. Eastham, M. J. Balchin, T. Betzer, H.C. Lai, and S. Gair. Disk motor with reduced unsprung mass for direct EV wheel drive. *IEEE Int. Symp. on Industrial Electronics*, 2:569–573, 1995.

[39] K.J. Binns and D.W. Shimmin. Relationship between rated torque and size of permanent magnet machines. *IEE Proc. Electr. Power Appl.*, 143(6):417–422, November 1996.

[40] J. Jensen, F. Profumo, and A. Tenconi. A low loss permanent magnet brushless DC motor utilizing tape-wound amorphous iron. *IEEE Industry Applications Society Annual Meeting*, pages 281–286, 1990.

[41] G.R. Slemon. On the design of a high-performance surface-mounted PM motors. *IEEE Trans. on Industry Applications*, 30(1):134–140, January/February 1994.

[42] T.J.E. Miller. *Brushless Permanent Magnet and and Reluctance Motor Drives*. Clarendon Press, Oxford, UK, 1989.

[43] TJE Miller and J.R. Hendershot Jr. *Design of Brushless Permanent Magnet Motors*. Oxford University Press, 1995.

[44] F. Caricchi, F. Crescimbini, A. Di Napoli, and E. Santini. Optimum CAD-CAE design of axial-flux permanent-magnet motors. In *ICEM'92*, volume 3, pages 637–641, 1992.

[45] D.C. Hanselman. *Brushless Permanent-Magnet Motor Design*. Number 2. McGraw-Hill, Inc., 1994.

[46] T.A. Lipo and F.X. Wang. Design and performance of a converter optimized AC machines. *IEEE Trans. on Industry Applications*, IA-20(4):834–844, 1984.

[47] S. Huang, J. Luo, F. Leonardi, and T.A. Lipo. A general approach to sizing and power density equations for comparison of electric machines. *IEEE Trans. on Energy Conversion*, 34(1):92–97, January/February 1998.

[48] S. Huang, J. Luo, F. Leonardi, and T.A. Lipo. A comparison of power density for axial flux machines based on general purpose sizing equations. *IEEE Trans. on Energy Conversion*, 14(2):185–192, June 1999.

[49] A.G. Jack. Drives and control strategies for permanent magnet machines. *IEE Colloquium on PM machines and Drives*, pages 3/1–3/13, 1993.

[50] G. Friedrich and M. Kant. Choice of drives for electric vehicles: A comparison between two permanent magnet AC machines. *IEE Proc. Electr. Power Applications*, 145(3):247–252, May 1998.

[51] Z. Zhang, F. Profumo, and A. Tenconi. Axial-flux versus radial-flux permanent magnet machines. *Electromotion*, 3:134–140, 1996.

[52] F. Sahin and A.J.A. Vandenput. Design considerations of the flywheel-mounted axial-flux permanent-magnet machine for a hybrid electric vehicle. *EPE'99*, page CD, September 1999.

[53] B. Chalmers and A. Williamson. *AC Machines Electromagnetics and Design*. John Wiley and Sons INC., England, 1991.

[54] J. Hsu and et al. Nature and assesments of torque ripples of permanent magnet adjustable speed motors. *IEEE IAS'95*, pages 2696–2702, 1995.

[55] D.C. Hanselman. Effect of skew, pole count, slot count on brushless motor radial force, cogging torque and back emf. *IEE Proc. on Elec. Power Appl.*, 144(5):325–330, September 1997.

[56] F. Sahin, H.B. Ertan, and K. Leblebicioglu. Optimum geometry for torque ripple minimization of switched reluctance motors. *IEEE Trans. on Energy Conversion*, 15(1):30–39, 2000.

[57] Z.Q. Zhu, D. Howe, E. Bolte, and B. Ackermann. Instanteneus magnetic field distribution in brushless permanent magnet dc motors, part i: Open circuit field. *IEEE Trans. on Magnetics*, 29(1):124–135, January 1993.

[58] Z.Q. Zhu and D. Howe. Instanteneus magnetic field distribution in brushless permanent magnet dc motors, part II: Armature reaction field. *IEEE Trans. on Magnetics*, 29(1):136–142, January 1993.

[59] Z.Q. Zhu and D. Howe. Instanteneus magnetic field distribution in brushless permanent magnet dc motors, part III: Effect of stator slotting. *IEEE Trans. on Magnetics*, 29(1):143–151, January 1993.

[60] Z.Q. Zhu and D. Howe. Instanteneus magnetic field distribution in brushless permanent magnet dc motors, part IV: Magnetic field on load. *IEEE Trans. on Magnetics*, 29(1):152–, January 1993.

[61] Y. N. Zhilichev. Three dimensional analytical model of permanent magnet axial flux machine. *IEEE Trans. on Magnetics*, 34(6):3897, November '1998.

[62] A.B.J. Reece and T.W. Preston. *Finite Element Methods in Electrical Power Engineering*. Oxford University Press, 2000.

[63] *Opera Users Manual.*

[64] P.P. Silvester and R. L. Ferrari. *Finite Elements for Electrical Engineers.* Cambrige University Press, 1990, 2nd edition.

[65] D.J. Patterson. Contemporary finite element analysis techniques for permanent magnet brushless DC machines, with application to axial flux traction systems for electric vehicles. *PEDES'99*, pages 1–5, 1999.

[66] Zi-Qiang Zhu. *The Electromagnetic Performance of Brushless Permanent Magnet DC Motors - with Particular Reference to Noise and Vibration.* PhD thesis, University of Sheffield, 1991.

[67] S. Henneberger. *Design and Development of a Permanent Magnet Synchronous Motor for a Hybrid Electric Vehicle Drive.* PhD thesis, May 1998.

[68] D.C. Hanselman and W.H. Peake. Eddy-current effects in slot bound conductors. *IEE Proc. Elec. Power. Appl.*, 142(2):131–136, March 1995.

[69] S.J. Salon and L. Ovacik. Finite element calculation of harmonic losses in AC machine windings. *IEEE Trans. on Magnetics*, 29(2):1442–1445, March 1993.

[70] Fang Deng. An improved iron loss estimation for permanent magnet brushless machines. *IEEE Trans. on Energy Conversion*, 14(4):1391–1395, December 1998.

[71] A.J. Moses. Problems in modelling anisotrophy in electrical steels. *International Journal of Applied Electromagnetics in Materials*, 3:193–197, 1992.

[72] J.L.F. Van der Veen, L.J.J. Offringa, and J.A. Vandenput. Minimising rotor losses in high-speed high-power permanent-magnet synchronous generators with rectifier load. *IEE Proc. Elec. Power Appl.*, 144(5):331–337, September 1997.

[73] H. Polinder and M.J. Hoeimakers. Eddy-current losses in the permanent magnets of a PM machine. *IEE Int. Conf. on Electrical Machines and Drives*, pages 138–142, 1-3 September 1997.

[74] K. Atallah, D. Howe, P.H. Mellor, and D.A. Stone. Rotor losses in permanent magnet brushless AC machines. *IEEE Trans. on Industry Applications*, 36(6):1612–1618, 1999.

[75] H. Hofmann and S.R. Sanders. High-speed synchronous reluctance machine with minimized rotor losses. In *IEEE IAS'98*, volume 1, pages 118–125, 1998.

[76] Z.Q. Zhu K. Ng, N. Schofield, and D. Howe. Analytical prediction of rotor eddy current loss in brushless permanent magnet motors. In *UPEC'97*, pages 49–52, 1997.

[77] J. Gynselinck, L. Vandevelde, and J. Melkebeek. Calculation of eddy currents and associated losses in electrical steel laminations. *IEEE Trans. on Magnetics*, 35(3):1191–1195, May 1999.

[78] S.M. Abu Sharkh, M.R. Harris, and N. Taghizadeh Irenji. Calculation of rotor eddy current losses in high-speed PM alternators. In *IEE-EMD No.444*, pages 171–174, 1-3 September 1997.

[79] C. P. Cho and B.K. Fussell. Eddy current loss calculation in the permanent magnet of a large horse power axial-field motor. *Incremental Motion Control Systems and Devices Proc.*, pages 245–254, 1993.

[80] J. Saari. *Thermal Analysis of High-Speed Induction Machines*. PhD thesis, Acta Polytechnica Scandinavica, 1998.

[81] L.A. Dorfman. *Hydrodynamic Resistance and the Heat Loss of Rotating Solids*. Oliver and Boyd, Edinburgh and London, 1963.

[82] Jr. C. Gazley. Heat transfer characteristics of the rotational and axial flow between concentric cylinders. *Trans. of ASME*, 80:79–90, 1958.

[83] E. Bilgen and R. Boulos. Functional dependence of torque coefficient of coaxial on gap width and reynold numbers. *Trans. of ASME, Journal of fluid engineering, series.1*, 95(1):122–126, 1973.

[84] J.W. Daily and R.E. Nece. Chamber dimension effects on induced flow and frictional resistance of enclosed rotating disks. *Trans. of ASME, Journal of Basic Engineering*, 82(1):217–232, March 1960.

[85] P. Campbell. Principle of a permanent magnet axial field DC machine. *Proc. IEE*, 121(12):1489–1494, December 1974.

[86] F. Caricchi, E. Crescimbini, E. Edeli, and G. Noia. Design and construction of a wheel-directly-coupled-axial-flux PM motor prototype for evs. *IEEE IAS'94*, pages 254–261, October 1994.

[87] G. Cannistra and M.S. Labini. Thermal analysis in an induction machine using thermal network and finite element method. *Fifth International Conference on Electrical Machines and Drives*, pages 300–304, 1991.

[88] G. Cannistra, V. Dattoma, and M.S. Labini. Analysis of thermal and mechanical stresses in the stator of a direct-current motor by finite element method. *Sixth International Conference on Electrical Machines and Drives*, pages 49–54, 1993.

[89] D.A. Staton and E. So. Determination of optimal thermal parameters for brushless permanent magnet motor design. *IEEE IAS'98*, 1:41–49, 1998.

[90] G. Bellenda, L. Ferraris, and A. Tenconi. A new simplified thermal model for induction motors for EVs applications. *IEE Int. Conf. on Electrical Machines and Drives*, pages 11–15, September 1995.

[91] E.S. Hamdi. *Design of Small Electrical Machines*. John Wiley and Sons, 1994.

[92] V.T. Morgan. *The Overal Convective Heat Transfer from Smooth Circular Cylinders (in Advances in Heat Transfer, T.F. Irvine and J.P. Harntnett, Eds)*, volume 11. Academic Press, Newyork, 1975.

[93] A. Farschtschi. Temperature calculation in electrical machines. *ETEP'92*, 2(3):153–159, May-June 1992.

[94] Y.G. Dessouky, B.W. Williams, and J.E. Fletcher. Cooling enhancement of electric motors. *IEE Proc. Electr. Power Applications*, 145(1):57–60, 1998.

[95] A.G. Jack, B.C. Mecrow, and K. Cowan. Calculation of temperature in directly cooled electrical machines. *IEE Colloquium on Thermal Aspects of Machines*, pages 6/1–6/4, 1992.

[96] R. Smyth. The thermal analysis of fluid flow parallel to rotating surfaces. *Proc. of 32.nd Intercociety Conference on Energy Conversion Engineering*, 2:1531–1536, 1997.

[97] A. Bousbaine. Thermal modelling of induction motors based on accurate loss density distribution. *Electric Machines and Power Systems*, 27:311–324, 1998.

[98] P.H. Mellor. Lumped parameter thermal model for electrical machines of TEFC design. *IEE Proc.-B*, 138(5):205–218, 1991.

[99] I.J. Perez and J.G. Kassakian. A stationary thermal model for smooth airgap rotating electric machines. *Electric Machines and Electromagnetics*, 3:285–303, 1979.

[100] G. Henneberger and K. Ben Yahia. Calculation and identification of a thermal equivalent circuit of a water cooled induction motor for electric vehicle applications. *IEE Int. Conf. on Electrical Machines and Drives*, pages 6–10, September 1995.

[101] K.M. Becker and J. Kaye. Measurements of diabatic flow in an annulus with an inner rotating cylinder. *Trans. of ASME, Journal of Heat Transfer*, 84:97–105, May 1962.

[102] G. Gotter. *Erwrmung and Khlung Elektrischer Maschinen*. Springer Verlag, Berlin, 1954.

[103] K.J. Binns and D.W. Shimmin. The relationship between performance characteristic and size of permanent magnet motors. *IEE Int. Conf. on Electric Machines and. on Drives*, (412):423–426, 1995.

[104] D. Verdyck and R.J.M. Belmans. An acoustic model for a permanent magnet machine: Modal shapes and magnetic forces. *IEEE Trans. on Industry Applications*, 30(6):1625–1631, November/December 1994.

[105] R.S. Girgis, P. Eng, and S.P. Verma. Method for accurate determination of resonant frequencies and vibration behaviour of stators of electrical machines. *IEE Proc. B*, 128(1):1–11, January 1981.

[106] W.R. Finley, M.M. Hodowanec, and W.G. Holter. Diagnosing motor vibration problems. *Pulp and Paper Industry Technical Conference*, pages 165–180, 2000.

[107] S. Sakamoto and T. Hirata. Vibration analysis considering higher harmonics of electromagnetic forces for rotating electric machines. *IEEE Trans. on Magnetics*, 35(3):1662–1665, 1999.

[108] A. Tuckey. Mechatronic load-meetings summary. Interim report, Technical University Eindhoven Group EPE, November 1998.

[109] F. Sahin, A. Tuckey, and A.J.A. Vandenput. The design of a high speed flywheel mounted axial-flux permanent-magnet machine. In *ICEM'2000*, pages 807–811, Espoo, August 2000.

[110] P.M. Risseeuw. Development of a hysteresis current controller. Master's thesis, Technical University Eindhoven Faculty of Electrical Engineering, October 1998.

[111] R. Derfiora. Comprehensive design of a universal mechatronic load. Master's thesis, Technical University Eindhoven Faculty of Electrical Engineering, December 1995.

[112] A. Tuckey. Mechatronic load-decisions. Interim report, Technical University Eindhoven Group EPE, June 1999.

[113] P. Vas and W. Drury. Electrical machines and drives: Present and future. *MELECON'96*, 1:67–74, 1996.

[114] H. Pfutzner. Rotational magnetization and rotational losses of grain oriented silicon steel sheets-fundamental aspects and theory. *IEEE Trans. on Magnetics*, 30(5):2802–2807, September 1994.

[115] T. Waeckerle and B. Cornut. Influence of texture in grain oriented steel on magnetization calculated curve in the range of rotation process. *IEEE Trans. on Magnetics*, 30(5):2793–2795, September 1992.

[116] M. Enokizono and N. Soda. Magnetic field analysis by finite element method using effective anisotropic field. *IEEE Trans. on Magnetics*, 31(3):1793–2795, 1995.

[117] A. K. Lebouc, S. Zouzou, and P. Brissonneau. Anisotropy influence on the rotational and alternating field behavior of soft magnetic materials. *IEEE Trans. on Magnetics*, 28(5):2796–2798, September 1992.

[118] H. Warlimont. Magnetic property assesment: Between physical maximum and economic minimum. *IEEE Trans. on Magnetics*, 26(5):1313–1321, September 1990.

[119] A.G. Jack, B.C. Mecrow, P.G. Dickinson, J.S. Burdess, N. Fawcett, and J.T. Ewans. Permanent-magnet machines with powdered iron cores and prepressed windings. *IEEE Trans. on Industry Applications*, 36(4):1077–1084, July/August 2000.

[120] M. Yoshida, Y. Murai, and M. Takada. Noise reduction by torque ripple suppression in brushless DC motors. *PESC'98*, pages 1397–1401, 1998.

[121] J. Granado, R.G. Harley, and G. Diana. Understanding and designing a space vector pulse-width-modulater to control a three phase inverter. *The Trans. of the SA Institude of Electrical Engineers*, pages 29–37, september 1989.

Summary

Numerous electric vehicle (EV) and hybrid electric vehicle (HEV) applications have proved to be successful in reducing the global CO_2 emission. Consequently, the improvement of such vehicle drives has become a major research topic, and HEVs are especially favorable in the short term considering the difficulties introduced by batteries and the current lack of an EV charging infrastructure.

The hybrid electric vehicle application that encompasses this thesis, demands an electrical machine structure in which a high-speed rotor is to be embedded in a flywheel. Due to its shape and compactness an axial-flux permanent-magnet (AFPM) machine is proposed. The inner city and highway driving speeds of the flywheel are specified to be 7000 rpm and 16000 rpm respectively, at a torque level of 18 Nm. The total drive system is highly demanding in terms of electrical machine efficiency and furthermore the HEV layout specifies that the machine including its frame must be designed small enough to fit in a cylindrical volume of 240 mm diameter with 150 mm height.

These specifications, among others, lead to one major implication in terms of electromagnetic requirements, namely a high torque density, which is the main justification of the suitability of an AFPM machine in a HEV application. In addition to the shape related advantages and other issues of suitability for the application, the sizing equations of the AFPM machine derived at the outset of this study, demonstrate the torque density advantage of the axial-flux machine in comparison with the radial-flux type.

A high-speed rotor with a flywheel tends to generate extremely high air friction losses. Under these circumstances an air pressure reduction inside the machine is inevitable. Reduced air pressure naturally decreases the heat transfer from the rotor to the stator, which results in a rapid rise of the magnet and rotor temperatures. Hence, a special emphasis is placed on thermal considerations. A preliminary verification of the thermal behavior with respect to given constraints was accomplished by analyzing a thermal equivalent circuit of the designed AFPM machine.

The thermal problems due to high speed and reduced inner air pressure are also aggravated by high-frequency eddy current losses emerging in the rotor magnets and rotor steel. These losses constitute additional heating sources for the magnets. In the theoretical parts of this study particular attention has been paid to the analysis

of the rotor losses, which, together with other loss components, had to be decreased to acceptable levels.

An extensive analysis of the space harmonics was carried out and the design variables were evaluated in terms of their contribution to space harmonics. This effort helped to choose a better combination of the design parameters, which ultimately resulted in a design with low space harmonics content and consequently low torque ripple. Accordingly, the amount of rotor losses was suppressed.

The theoretical design and analysis of the AFPM machine are followed by manufacturing. The manufacturing process is reported in relation to several critical aspects, such as the choice of materials, the accuracy and tolerance, the mechanical forces and stresses on components, and the dynamical analysis of the rotating parts.

An accurate test bench made it possible to test and measure the machine under varying load and speed conditions. Various experiments have been carried out, the main focus being on the stationary performance and the thermal behavior. Measured and calculated results were compared and the possible causes of discrepancy between the two were investigated.

An evaluation of the overall study, together with a reference to the most recent literature, points towards further development possibilities by using better materials for the stator core, especially the recent powder composite materials.

Samenvatting

Talrijke toepassingen van elektrische voertuigen (EV) en hybride elektrische voertuigen (HEV) hebben bewezen succesvol te zijn in de reductie van de globale CO_2 uitstoot. Bijgevolg is de verbetering van dergelijke voertuigaandrijvingen een belangrijk onderzoeksonderwerp geworden, en zijn HEVs in het bijzonder veelbelovend op korte termijn gezien de moeilijkheden in de batterijtechnologie en het huidige gebrek aan een infrastructuur om EVs op te laden.

De toepassing van een hybrid elektrisch voertuig, dat het onderwerp uitmaakt van deze thesis, vereist een elektrische machine structuur waarin de hoge snelheid rotor moet worden ingebed in een vliegwiel. Omwille van de vorm en de compactheid wordt een axiale-flux permanent-magneet (AFPM) machine voorgesteld. De snelheden van het vliegwiel in het stedelijk en snelweg verkeer zijn respectievelijk 7000 en 16000 omw/min bij een koppelwaarde van 18 Nm. Het totale aandrijfsysteem stelt hoge eisen aan het rendement van de elektrische machine, en bovendien bepaalt het ontwerp van het HEV dat de machine, inclusief het statorhuis, voldoende klein moet worden ontworpen zodat ze past in een cilindrisch volume van 240 mm diameter en 150 mm hoogte.

Deze specificaties, en andere, leiden tot een belangrijke implicatie op elektromagnetisch gebied, namelijk een hoge koppeldichtheid, dat de voornaamste rechtvaardiging is van de geschiktheid van een AFPM machine in een HEV toepassing. Naast de aan de vorm gerelateerde voordelen en andere punten van geschiktheid voor de toepassing, tonen de vergelijkingen van de AFPM machine, die betrekking hebben op de afmetingen en die afgeleid zijn in het begin van deze studie, aan dat de axiale-flux machine een hogere koppeldichtheid heeft dan het radiale-flux type.

Een hoge snelheid rotor met een vliegwiel doet extreem hoge luchtwrijvingsverliezen ontstaan. Onder deze omstandigheden is een reductie van de luchtdruk in de machine onvermijdelijk. Een gereduceerde luchtdruk vermindert uiteraard de warmte overdracht van de rotor naar de stator, wat resulteert in een snelle stijging van de magneet en rotor temperatuur. Bijgevolg wordt een speciaal accent gelegd op thermische beschouwingen. Een voorafgaandelijke verificatie van het thermische gedrag met betrekking tot gegeven randvoorwaarden werd uitgevoerd door een thermisch equivalent schema van de ontworpen AFPM machine te analyseren.

De thermische problemen ten gevolge van de hoge snelheid en de gereduceerde

inwendige luchtdruk worden nog verergerd door hoogfrequente wervelstroomverliezen die in de magneten en het rotorijzer ontstaan. Deze verliezen vormen bijkomende warmtebronnen voor de magneten. In de theoretische delen van deze studie wordt speciale aandacht besteed aan de analyse van de rotorverliezen, die, samen met andere verliescomponenten, moesten worden verkleind tot aanvaardbare niveaus.

Een uitvoerige analyse van de ruimteharmonischen werd uitgevoerd en de ontwerpvariabelen werden geëvalueerd met betrekking tot hun bijdrage aan de ruimteharmonischen. Door deze inspanning kon een betere combinatie van de ontwerpparameters worden gekozen, hetgeen uiteindelijk resulteerde in een ontwerp met een laag gehalte aan ruimteharmonischen en bijgevolg kleine koppelrimpel. Dienovereenkomstig werden de rotorverliezen onderdrukt.

Na het theoretische ontwerp en de analyse van de AFPM machine volgt de constructie. Meerdere kritische aspecten tijdens het constructieproces worden beschreven, zoals de keuze van de materialen, de nauwkeurigheid en tolerantie, de mechanische krachten op en spanningen in componenten, en de dynamische analyse van de roterende delen.

Een nauwkeurige testbank maakte het mogelijk de machine onder variërende condities van belasting en snelheid te testen en te meten. Verscheidene experimenten werden uitgevoerd, waarbij vooral werd gefocusseerd op de stationaire prestaties en het thermische gedrag. Gemeten en berekende resultaten werden vergeleken en mogelijke oorzaken voor de onderlinge verschillen werden onderzocht.

Een evaluatie van de globale studie, alsmede een referentie aan de meest recente literatuur, duidt verdere ontwikkelingsmogelijkheden aan door gebruik te maken van betere materialen voor de statorkern, in het bijzonder de recente poeder composietmaterialen.

Curriculum vitae

Funda Sahin was born in 1970 in Turkey. After completing her B.Sc. study in electrical and electronics engineering in 1991, she started working as a research and teaching assistant in the Department of Electrical and Electronics Engineering of Middle East Technical University, Ankara. Between 1992 and 1995, she was also a member of the research team in the project titled as "Development of an adjustable speed switched-reluctance motor drive system" of Turkish Scientific and Technical Research Council". She completed her M.Sc. study titled as "Optimum geometry for torque ripple minimization of switched reluctance motor " under the supervision of Prof.dr. H.B. Ertan in 1996. In May 1997, she started the Ph.D. research project that led to this thesis. Under the supervision of Prof.dr.ir. A.J.A. Vandenput, the research was performed in the Electromechanics and Power Electronics Group in Electrical Engineering Faculty of TU/e.